Frequency extension of solid-state terahertz lasers

By

Tiago Almeida Ortega

A thesis submitted to Macquarie University for the degree of

Doctor of Philosophy

Department of Physics and Astronomy

July 2017

MACQUARIE
University
SYDNEY·AUSTRALIA

This thesis is submitted in fulfilment of the requirements of the degree of Doctor of Philosophy at Macquarie University, and has not been submitted in whole or part for a higher degree in any other university or institution. I certify that, to the best of my knowledge, all sources used and assistance received in the preparation of this thesis have been acknowledged in the customary manner.

_____

Tiago Almeida Ortega

Acknowledgements

The challenges of a PhD candidature are technically and emotionally demanding, and one is very unlikely to succeed without the assistance and support of others. First and foremost, I would like to thank my supervisor Dr. Andrew Lee, and my co-supervisor Dr. Helen Pask. Thank you for giving me the opportunity to be part of your research group, and for sharing the passion for solid state laser design. Thank you for always fostering my creativity and for being so genuinely interested in my professional growth. You were always available, and never failed to guide me throughout my candidature, and always provided the required resources to conduct my research work. I also wish to express my gratitude to Dr. David Spence for being so generous in sharing his knowledge with me, often shedding light on the most complicated aspects of laser theory. The three of you have my deepest respect and gratitude.

I also would like to express my appreciation to M-Squared Lasers for supporting our research projects.

To all those work colleagues who helped me along the way, and enriched the academic experience: Yameng, Ran, Andréa, Chris, Ondrej, Varun, Jipeng, Rob, Aaron, Josh, Martin, Pete, Simon, and all the others. Thank you.

Thank you Giuliano, for introducing me to the concept of genetic algorithms, and the valuable programming tips. You are one of the best electronic engineers I have ever met. Thank you very much.

I would like to thank my family, living on the other side of the world, for all the emotional support. To my parents Rubens and Celia, for all the love and care. You provided me access to a privileged level of education, despite the social inequalities in our country. I am conscious of all the sacrifices you had to make, and how much of your lives you dedicated for that purpose. Words will never be sufficient to describe my gratitude. My love for you is unconditional. My sister Gabi, my grandparents, cousins, uncle, aunties, thank you for always supporting me and always filling my heart with positiveness.

Thank you to all my brothers of choice, from Piracicaba and “Fura Zóio”. The geographical distance between us will never diminish our love and friendship. Thank you my friends from Goulburn and the Northern Beaches. My weekends could not have been better.

Finally, I want to thank my wife Charlotte, for being so patient, loving and caring. Thank you for supporting me so much. For bringing me calm and confidence in the most challenging days. For shining my days with your smile and warming my heart with your love. I love you very much.

Thank you!

Abstract

Terahertz radiation has the potential to impact revolutionary real-world applications through THz spectroscopy and spectral imaging in various fields such as life-sciences, medicine, homeland security and in manufacturing. Terahertz laser sources based on intracavity stimulated polariton scattering (SPS) in magnesium oxide-doped lithium niobate crystals ($MgO:LiNbO_3$; MgO:LN) have been extensively reported in the literature, typically producing terahertz radiation continuously tunable from 1 – 3 THz. This technology has proven to produce truly compact, reliable and cost-effective THz sources with frequency tunable output which can be interfaced with relatively simple detection mechanisms (portable spectrometers, Golay cells, and robust pyroelectric detectors). What is of particular significance is that the core technology is based on solid state laser design, which is well established, and the components are well developed.

This thesis offers new insights into the design and operation of intracavity THz lasers based on stimulated polariton scattering. Contributions to the knowledgebase have been made with regards to the understanding of SPS material properties, terahertz frequency coverage and terahertz output power. The SPS crystals are investigated from first principles, with their vibrational spectra (spontaneous Raman and infrared reflection) and dispersion properties being examined. Their polariton dispersion curves, refractive index and absorption coefficient are calculated, providing valuable tools to guide the design of these sources.

Exploring $MgO:LiNbO_3$, and also two other SPS-active crystals never explored in the intracavity design, potassium titanyl phosphate ($KTiOPO_4$; KTP) and rubidium titanyl phosphate ($RbTiOPO_4$; RTP), significant contributions to the area of SPS laser design have

been made. The use of KTP and RTP in the novel intracavity surface-emitted geometry expanded the terahertz tuning range of intracavity SPS sources up to 5.98 THz. The average output power of the terahertz field was also greatly enhanced, reaching 125 μW for a modest 6 W diode pump power. This remarkable power level is the highest ever reported from an intracavity SPS laser source, and breaks the 0.1 mW THz power barrier. Moreover, this represents an increase in one order of magnitude in output power, and two orders of magnitude in diode-to-THz conversion efficiency from previously reported intracavity SPS laser systems. The beam quality parameter of the terahertz output was also measured to be excellent in comparison to previously reported linear THz SPS sources, being M_H^2~1.57 and M_V^2~1 in the horizontal and vertical dimensions respectively, indicating a substantial increase in brightness.

This research has resulted in two peer reviewed papers in high impact-factor journals, three international conference papers, and a third manuscript is under preparation.

This project was supported under Australian Research Council's Linkage Projects funding scheme (LP140100724).

List of acronyms

DFG	Difference-frequency generation
EFL	Effective focal length
FEA	Finite element analysis
FTIR	Fourier-transform infrared reflectance spectroscopy
Is-TPG	Injection seeded terahertz parametric generator
KTA	Potassium titanyl arsenate ($KTiOAsO_4$)
KTP	Potassium titanyl phosphate ($KTiOPO_4$)
LN	Lithium niobate ($LiNbO_3$)
MgO:LN	Magnesium oxide-doped lithium niobate ($MgO:LiNbO_3$)
Nd:YAG	Neodimium-doped yttrium aluminium garnet
NIR	Near-infrared
OC	Output coupler
OCT	Optical coherence tomography
OR	Optical rectification
QCL	Quantum cascade laser
RTP	Rubidium titanyl phosphate ($RbTiOPO_4$)
SE	Surface-emitted
SPS	Stimulated polariton Scattering
SRS	Stimulated Raman Scattering
TDS-THz	Terahertz time-domain spectroscopy
TEC	Thermoelectric cooler
TIR	Total internal reflection
TPG	Terahertz parametric generator
TPO	Terahertz parametric oscillator
TPX	Polymethylpentene
VECSEL	Vertical-external-cavity surface-emitting-laser

Table of contents

1. Introduction

In this chapter the basic concepts of terahertz radiation and its ability to address real-word applications are introduced; an overview of the main optical techniques to produce THz radiation is given, and the intracavity THz polariton laser is presented as a viable technology meeting the requirements of such applications. The structure of this thesis is outlined at the end of the chapter.

1.1. Terahertz radiation: mind the gap

Terahertz (THz) radiation is the most accepted nomenclature to refer to electromagnetic fields with frequency spanning from 0.3 to 10 THz (1 mm to 30 μm in wavelength), a portion of the electromagnetic spectra situated between microwaves and near-infrared (NIR). Photon energies in this frequency region correspond to vibrational and rotational modes of various substances and molecules, and the relatively long wavelength enables THz radiation to penetrate particularly well through non-polar and non-metallic materials such as papers, textiles, cardboards and polymers. This convenient scenario confers to terahertz radiation the

potential to address revolutionary real-world applications through THz spectroscopy and spectral imaging, as extensively reported in the literature [1–22].

In life sciences and medicine for example, THz pulse imaging in reflection geometry was capable of differentiating normal human tissue from basal cell carcinoma and from inflammation and scar tissue [9]; another study demonstrated the ability to differentiate tumour from several cell types in mice with THz molecular imaging via differential modulation of surface plasmons induced on nanoparticles [13]. Terahertz optical coherence tomography (THz OCT) is another promising diagnosis tool in medicine, with in-depth measurements of human sweat ducts being recently reported with remarkable detail [14]. In homeland security, illicit drugs (MDMA and methamphetamine) concealed in envelopes were detected and differentiated from aspirin in a non-destructive and non-invasive procedure [15], and standoff explosive detection was demonstrated [18] using THz radiation. In industry, terahertz radiation is a great candidate for non-destructive testing. Non-contact thickness measurements of multi-layered automotive paints were performed via terahertz time-domain spectroscopy TDS-THz in reflection geometry with high accuracy [22]. Simultaneous measurement of thickness and moisture content in paper were also demonstrated with a similar technique [19]. Real-time measurements of coatings on pharmaceutical tablets were also performed [20]. These selected examples glimpse how terahertz technologies can revolutionise medical diagnostics, border protection control mechanisms and quality control across a range of industries.

Despite numerous proposed applications across different fields, and proof-of-concepts demonstrated in the literature, real-world solutions using terahertz sources are not yet a reality. This is because THz frequencies are probably the least developed portion of the electromagnetic spectrum with regards to radiation sources, manipulation optics, and detectors [1].

With respect to currently established radiation sources, the output power in the terahertz range is drastically lower when compared to the surrounding microwave and near infrared, giving rise to the so-called “THz gap”, shown in Figure 1.1 [1]. For this reason, enormous research effort has been dedicated worldwide to close this gap [1,23] and deliver viable terahertz sources with appreciably-high output power. This being the motivation for this thesis. Different approaches can be utilised to produce such sources, and they can be broadly classified as electronic or optical, if they present similarities with the technologies utilised in microwave

or near-infrared sources, respectively [1]. This work is situated in the context of optical sources of THz radiation.

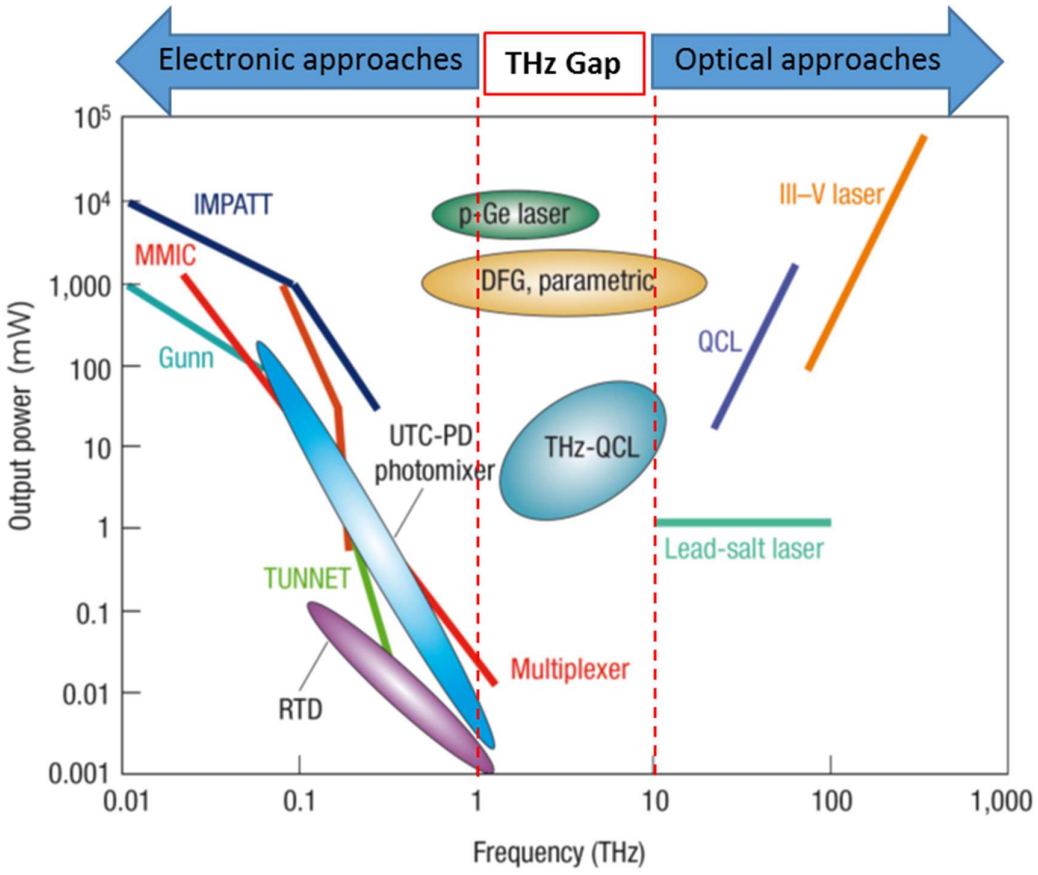

Figure 1.1 -THz-emission power as a function of frequency. Solid lines are for the conventional THz sources; IMPATT diode stands for impact ionization avalanche transit-time diode, MMIC stands for microwave monolithic integrated circuit, TUNNET stands for tunnel injection transit time and the multiplexer is an SBD (Schottky barrier diode) frequency multiplier. Ovals denote more recent THz sources. The values of the last two (multiplexer and ovals) are indicated by peak power, and the others are by c.w. power. (Adapted from [1]).

1.2. Optical sources of terahertz radiation

Terahertz radiation can be generated via different techniques, many of them based on optical phenomena. This section provides an overview of some common optical approaches currently used to produce broadband and narrowband THz sources with compact form factors.

1.2.1. Sources producing broadband THz emission

The technologies presented in this subsection produce terahertz fields with spectral bandwidth greater than 1 THz (and ultra-short pulse duration), hence being classified in this thesis as broadband.

Photoconductive antennas

A photoconductive antenna consists of two metal electrodes with a gap in between them [24] that are coated on a semiconductor substrate (typically GaAs). Irradiating a focused femtosecond laser pulse on a photoconductive antenna produces a transient of photo carriers generating a very short pulse (few picoseconds) of broadband terahertz radiation. Typically these antennas based on GaAs emit a terahertz peak below 1 THz, and exhibit low spectral brightness (emission is around 3 to 5 THz wide) as illustrated in Figure 1.2. This a successful technology, forming the basis for time-domain THz spectroscopy (TDS-THz), allowing simultaneous detection of the real and imaginary components of the electric field. TDS-THz is probably the most widely used terahertz spectroscopic technique [2,19–21] with a variety of sources commercially available in the market. However, these systems require high-power and expensive femtosecond pump lasers, and produce highly diverging beams that are not simple to manipulate. They also require complex electronic control and synchronisation of a delay line for detection which makes the detection fairly slow (of order of minutes depending on required resolution). This is because the signal is generated and collected in the time-domain, and has to be later converted into the frequency domain using Fourier-transform. It is also important to note that, while this technique produces relatively broad THz emission, the spectral power drops dramatically at the high frequencies, as seen in Figure 1.2.

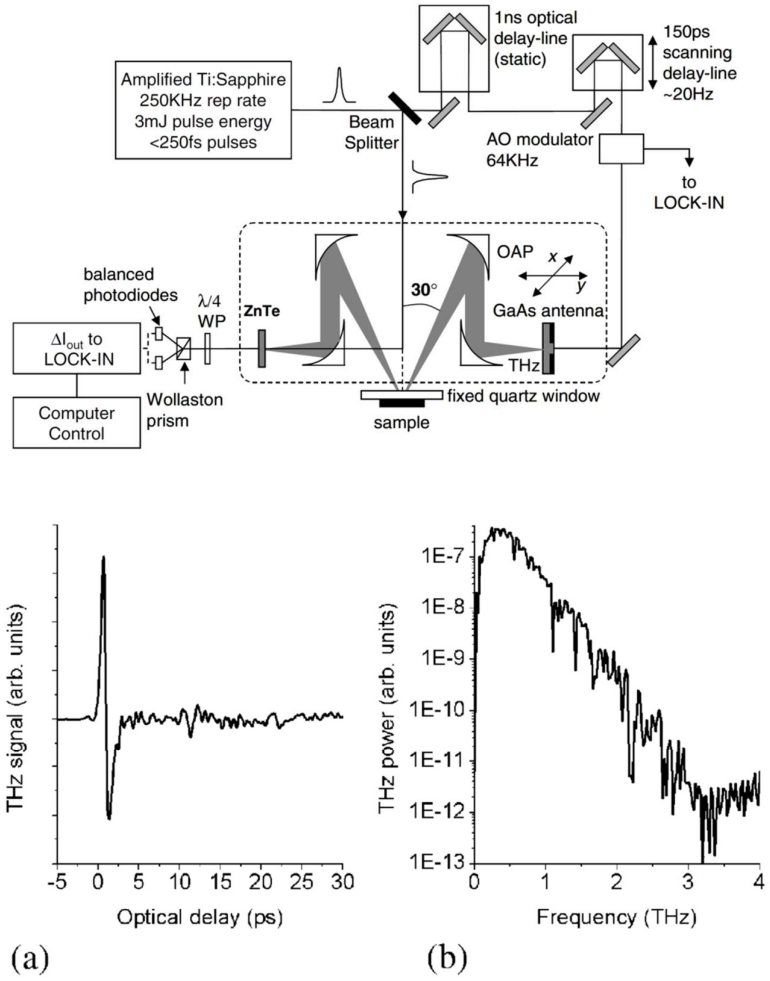

Figure 1.2 – Typical time-domain terahertz spectroscopy system (reproduced from [9]): TOP: The components of the THz pulsed imaging system in reflection geometry shown in schematic form: the NIR beam path is shown as a solid black line, the THz path as a shaded grey line. Shaded boxes indicate mirrors. Abbreviations: OAP: off-axis parabolic mirrors, λ/4 WP: quarter wave plate. The static delay line ensures that the path length of the pump and probe beam are equal. BOTTOM:(a) A typical THz pulse waveform, prior to signal conditioning (raw), as measured in the imaging system using the step-scan delay. (b) The corresponding THz power spectrum. The fine structure in the spectrum is due to atmospheric water absorption. Adapted from [9]

Optical rectification

Optical rectification (OR) is a second-order nonlinear effect resulting from a quasi-DC component of the nonlinear polarization [25] and can also be utilised to generate broadband THz pulses [24]. When an ultrafast laser pulse impinges on an electro-optical crystal, the quasi-DC component of the nonlinear polarization oscillates rapidly. As a consequence, a broadband THz pulse can be emitted. Optical rectification also enables simultaneous detection of the amplitude and phase of the electric field, being another basic technique to produce TDS-THz

systems. The most favourable materials for THz generation via OR are Zinc telluride (ZnTe) and the organic crystal DAST (4-dimethylamino-N-metyl-4-stilbazolium tosylate) [24,26]. Optical rectification is another technique producing sources with low spectral brightness, with typical emission peak between 1 – 3 THz and 3 – 5 THz bandwidth [24,26]. The high absorption of the femtosecond laser pulse and the THz pulse inside the OR material, and the restrictions around the coherence length of the nonlinear phenomena in the nonlinear crystals are the main limiting factors for optical rectification.

Optical Cherenkov radiation

The optical Cherenkov effect is another second order nonlinear optical phenomena by which broadband THz pulses can be produced from the interaction of a femtosecond laser pulse with an electro-optical crystal such as lithium niobate ($LiNbO_3$; LN)and lithium tantalate ($LiTaO_3$) [27]. In this process a pulse of terahertz radiation is produced in a cone resembling classical Cherenkov radiation [27] arising from the inverse electro-optic effect, as a consequence of the fast electromagnetic transient induced by the pump laser. The process is suitable for bulk crystals or domain inverted materials [28,29] and also generates broadband terahertz pulses with typical emission peak around 1 THz and low spectral brightness (1 – 5 THz wide) [27,29,30]

1.2.2. Sources producing narrowband THz emission

The technologies presented in this subsection are classified in this thesis as narrowband because they produce terahertz fields with spectral bandwidth of the order of a few GHz or narrower. Their temporal modalities range from pulsed to continuous-wave operation.

Quantum cascade lasers (QCL)

Quantum cascade lasers (QCL) are semiconductor devices available now for more than 20 years [31]. Different from conventional diode lasers, QCLs are created in the form of nanometric quantum wells having different energy levels, as shown in Figure 1.3 [32]. An electron transitioning from a more energetic level to another with lower energy will thus emit a photon at the energy difference. These small devices with great potential for mass production,

have had substantial development in the past decade resulting in high-performance the mid-infrared [33]. These developments extended to longer wavelengths, with QCL in the terahertz capable of delivering over 100 mW continuous-wave (CW) output power [34] and peak powers in excess of 1 W in the pulsed regime [35], which can be engineered to operate from 1.2 to 5 THz output frequency [32]. However, to this date, the applications of THz QCLs is rather limited. This is because their emission bandwidth do not allow coherent spectroscopy, and their frequency tunability is limited to a few hundred GHz, requiring cryogenic cooling [32,36,37].

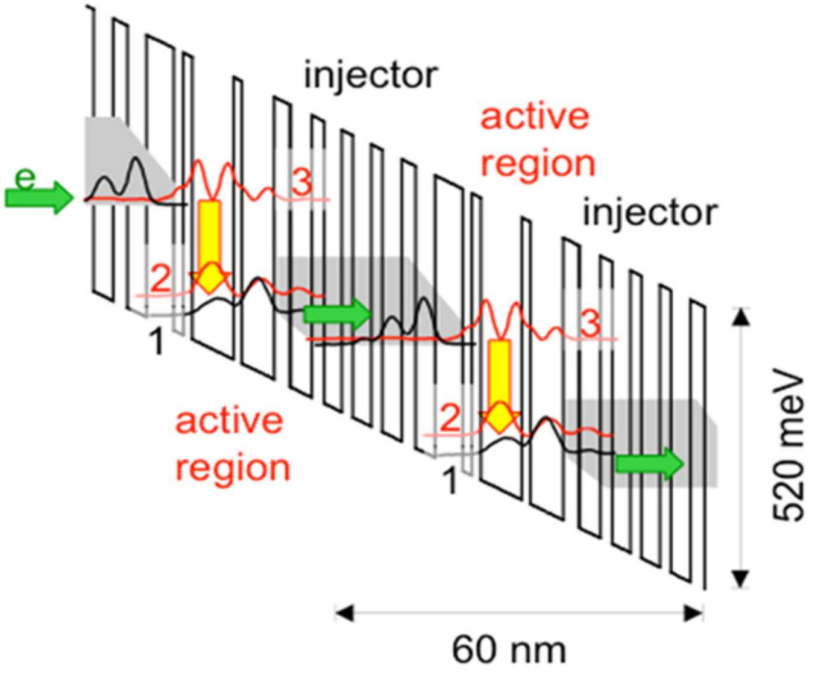

Figure 1.3 – Band diagram of a quantum cascade laser emitting at λ = 7.5 µm. The injector plus the active region is 60 nm thick. The energy levels and the calculated electron probability distributions obtained are shown. The quantum wells and barriers are made of AlInAs and GaInAs semiconductor alloys respectively. (Adapted from [32]).

Difference-frequency generation sources (DFG)

Difference-frequency generation is a well-known second order ($\chi^{(2)}$) nonlinear effect by which two electromagnetic waves with different frequencies (ω_1 and ω_2) interact in a nonlinear media to generate a third wave at the frequency difference ($\omega_3 = \omega_1 - \omega_2$). By combining two near-infrared lasers with wavelength around 1 µm with slightly different wavelengths (a few

nm apart) in a photomixer or in a nonlinear crystal it is possible to generate terahertz output at the frequency difference by means of DFG [38,39], and modifying the wavelength of at least one of the two pump lasers produces frequency tunable THz, typically at frequencies below 2 THz, with power levels in the order of several microwatts [40].

Using a dual-wavelength vertical-external-cavity surface-emitting-laser (VECSEL) a continuous wave THz source based on DFG in magnesium oxide-doped lithium niobate was also demonstrated operating at the discrete frequencies of 1 THz and 1.9 THz exceeding 2 mW output power [41]. These approaches are promising but are still limited in terahertz tunable bandwidth.

Parametric sources based on stimulated polariton scattering (SPS),

Stimulated polariton scattering is a mixed second-order ($\chi^{(2)}$) and third-order ($\chi^{(3)}$) nonlinear optical process by which narrowband, frequency-tunable THz radiation can be produced. The most common THz-SPS laser configurations are the terahertz parametric generator (TPG) and the terahertz parametric oscillator (TPO) [42]. In SPS, a fundamental pump laser field (typically from a Nd:YAG laser at 1064 nm) incident on a nonlinear crystal generates two other optical fields: Stokes (also in the NIR) and THz [43,44] (analogous to optical parametric generation's idler and signal fields, respectively), under non-collinear phase matching. Conservation of energy and momentum among fields in the scattering process dictates the frequency of the THz field (and Stokes field wavelength), and by adjusting the interacting angle between the fundamental and Stokes fields, it is possible to produce narrowband THz output. The most explored materials for use in SPS sources are LN and MgO:LN, which typically produce output continuously tunable from 1 – 3 THz (with linewidth <100 GHz) with microwatt-level average power [44] and in pulsed or CW temporal operation [45,46]. The presence of infrared absorbing modes in the SPS crystal structure may induce discontinuities in the THz emission band, as will be investigated in this thesis. However with the use of different SPS active materials new frequency ranges can be accessed increasing the overall coverage of such sources as detailed in Chapter 4 and Chapter 5. The principles of SPS are presented in more detail in Section 1.3, along with an overview of the main achievements in the field. An in-depth theoretical description of the SPS process is conducted in Chapter 3.

1.2.3. Desirable features of optical THz sources

Different optical technologies produce THz sources with different output characteristics and it is important to identify these differences and how they might affect real-world applications. As detailed in the previous section, most applications are based around the identification of spectral features of different materials in the THz range. There is simply a lack of available sources capable of producing radiation in this feature-rich portion of the electromagnetic spectrum. Hence, to maximise the potential use of a THz source in applications such as spectroscopy it is desirable that it emits narrowband radiation which is tunable over a broad frequency range with high average output power at discrete THz frequencies (high spectral brightness).

TDS-THz systems based on photoconductive antennas have had great development and yet do not have particularly high spectral brightness. Terahertz sources based on SPS exhibit these desirable features and for this reason experienced rapid development over the past decade. Terahertz sources based on SPS are particularly attractive because of their frequency-domain nature, wherein the actual frequency of the THz field is easily tuned and has narrow linewidth. It also eliminates the need for delay lines and simplifies detection. Moreover, SPS sources are versatile with respect to temporal regime, having capability to produce THz radiation with temporal properties ranging from picosecond pulsed to continuous-wave [45,46].

1.3. Terahertz sources based on SPS

1.3.1. Stimulated Raman scattering phenomena

The concepts of stimulated Raman scattering (SRS) are important for the understanding of the SPS process. For this reason, the basic concept of SRS is introduced in this section. A more thorough analysis of the SRS can be found in [47].

Stimulated Raman scattering is a third-order nonlinearity which is effectively inelastic scattering of light which interacts with an optical medium. In crystalline SRS, an intense electromagnetic field (with frequency υ_P) interacting with a Raman-active crystal may excite

a vibration mode within the crystal (phonon), scattering photons exhibiting lower energy levels (with frequency υ_S). The scattered light is typically referred to as the Stokes field, and for sufficiently intense Stokes fields, they too can experience SRS, leading to cascading and generation of a second-Stokes field and so on [47]. The energy difference between the incident and scattered Stokes fields corresponds to the crystal vibrational energy, or that of the phonon (with frequency υ_{ph}). The diagram in Figure 1. 4 illustrates the energy levels involved in the SRS process.

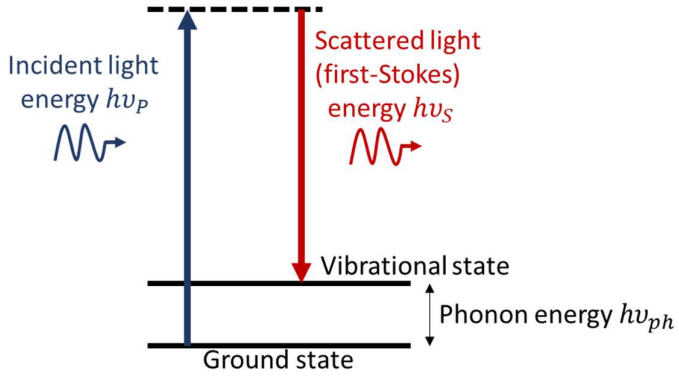

Figure 1. 4 - Stimulated Raman Scattering.

1.3.2. Stimulated polariton scattering phenomena

The first experimental observation of stimulated polariton scattering dates back to 1969, when tunable Stokes (idler) radiation was detected from lithium niobate [48]. In the following years an extensive theory describing the scattering process was developed by Sussman [43] which was revisited by Kawase *et al.* [44] about 25 years later.

A polariton, as it relates to this work, is a coupled photon-phonon transverse wave field which may be accessed in crystalline materials having vibrational modes that are both infrared-active and Raman-active. The dispersion relation of such a mode with frequency ω_0 is illustrated in Figure 1.4. Close to resonance (ω), the polariton mode behaves like a pure phonon, but in the lower frequency region it manifests like a photon. Polar crystals such as MgO:LN, lithium iodate ($LiIO_3$), KTP, RTP, potassium titanyl arsenate ($KTiOAsO_4$; KTA) and many others have transverse optical (TO) A_1 –symmetry modes (symmetric stretching modes) satisfying these conditions, and may exhibit SPS. Semiconductors such as gallium phosphate (GaP) and gallium selenide (GaSe) and others can also exhibit SPS.

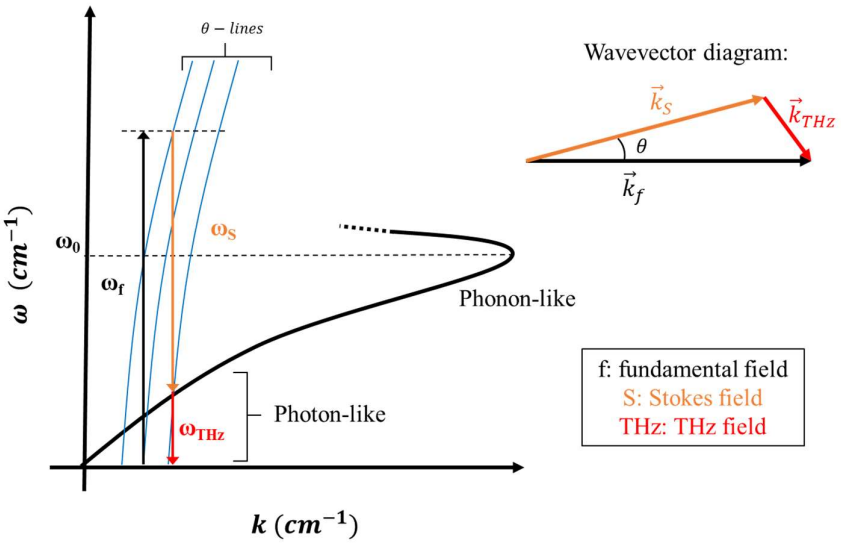

Figure 1.5 – Diagram illustrating the dispersion relation close to a polariton mode in a crystal. Close to resonance (upper frequency limit) the polariton behaves like a phonon. At lower frequencies, the polariton exhibits a photon behaviour. The wavevector diagram represents the fundamental ($\vec{k}_f$), Stokes ($\vec{k}_S$) and THz ($\vec{k}_{THz}$) fields interacting via SPS in a noncollinear phase matching condition. For every interacting angle θ there is a pair of Stokes and THz frequencies satisfying energy and momentum conservation laws, given by the intersection of the angle tuning lines ("θ-curves") with the dispersion curve.

In stimulated polariton scattering, a fundamental electromagnetic field is parametrically scattered into two other fields subject to a phase matching condition represented in Figure 1.4 (wavevector diagram in the top right). Here it will assumed the fundamental is in the near-infrared (NIR). The scattered fields are named here as Stokes (also in the NIR; called idler in TPO nomenclature) and THz (also called signal in TPOs). The SPS fields are strongly coupled, and must obey energy and momentum conservation laws (i. e., $h\nu_f = h\nu_S + h\nu_{THz}$ and $\vec{k}_f = \vec{k}_S + \vec{k}_{THz}$ respectively; where $h\nu_f$, $h\nu_S$, $h\nu_{THz}$ are the energies and $\vec{k}_f$, $\vec{k}_S$, $\vec{k}_{THz}$ are the wave vectors of the fundamental, Stokes and THz fields). For every interacting angle between the fundamental and Stokes fields, there would be an infinite number of THz and Stokes wavevector pairs satisfying these energy conservation laws, represented in Figure 1.4 as the different "θ-lines" for different angles θ. Since the material dispersion relation must also be respected in the process, the intersecting point between the "θ-line" with the dispersion curve will dictate the Stokes and THz wavevectors (and corresponding frequencies) for a particular interacting angle θ. For every different interacting angle, the intersection between the two curves will represent the Stokes and THz wavevector pair that simultaneously satisfies energy

and momentum conservation laws in the scattering process and the material dispersion relation as well. For this reason, different interacting angles between fields result in different THz and Stokes frequencies and wavevectors, as schematically represented in Figure 1.5. As a consequence, SPS is a suitable process for producing THz sources with frequency-tunable output by means of adjusting the interacting angle between fields.

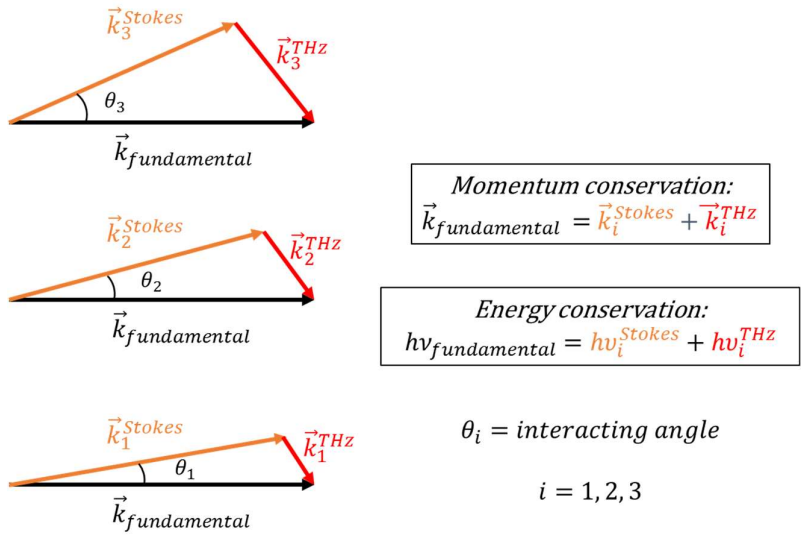

Figure 1.6 – Conservation of energy ($h\nu_{fundamenatal} = h\nu_i^{Stokes} + h\nu_i^{THz}$) and momentum ($\vec{k}_{fundamental} = \vec{k}_i^{Stokes} + \vec{k}_i^{THz}$) in stimulated polariton scattering (SPS), where $h\nu_{fundamenatal}$, $h\nu_i^{Stokes}$, $h\nu_i^{THz}$, are the energies and $\vec{k}_{fundamental}$, $\vec{k}_i^{Stokes}$, $\vec{k}_i^{THz}$ are the wave vectors of the fundamental, Stokes and terahertz fields for different interacting angles (θ_i). Every different interacting angle generates different THz and Stokes wavevectors.

1.3.3. Linear and surface emitted geometries

The angles at which the terahertz field is generated inside the nonlinear crystal exceed the critical angle for total internal reflection (TIR) in the crystal-air interface [44], in case the SPS material has a conventional cuboid geometry. To avoid TIR of the THz field in this linear geometry, silicon prisms are typically bonded to the crystal's side face enabling the extraction of the terahertz field from the material [49]. Here the refractive index of silicon is such that the angle for TIR at the SPS-crystal/Si-prism interface is greater than all angles of incidence of the THz field, and hence the terahertz field is effectively coupled into the Si-prisms and then refracted into the air. Another efficient technique is called the surface-emitted configuration (SE), at which the SPS material is cut at angles, promoting TIR for the fundamental and Stokes

fields, and enabling the THz radiation to be refracted directly into the air [50]. The linear configuration with silicon prisms and the surface emitted configuration are shown in Figure 1.6. These configurations will be explored in detail in Chapter 2 within the context of an intracavity resonator configuration.

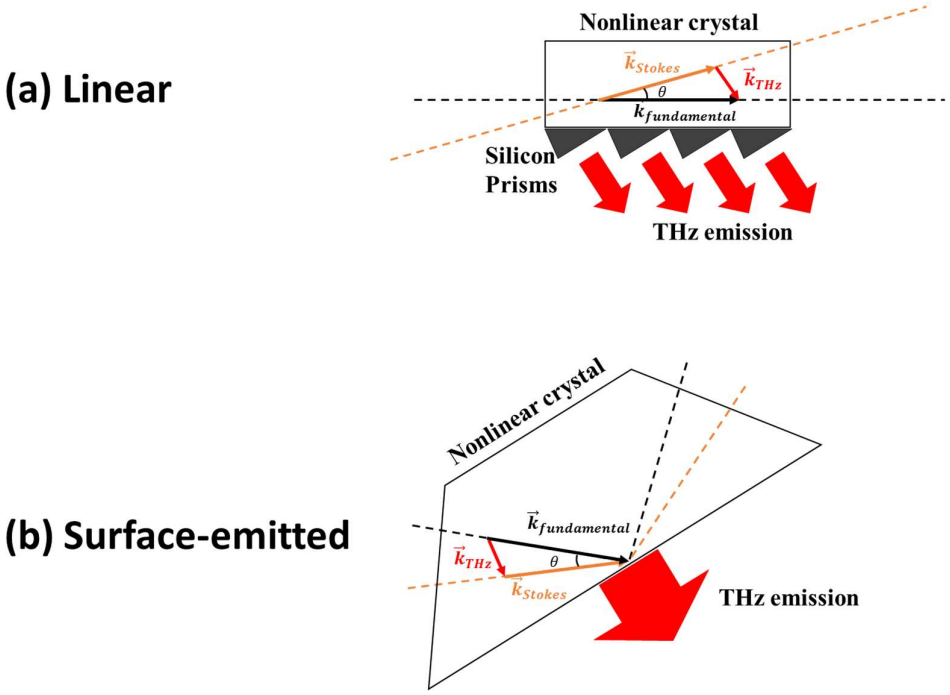

Figure 1.7 – The linear and surface-emitted (SE) configurations.

1.3.4. Resonator configurations for SPS sources

Terahertz parametric sources based on SPS can be divided into two main categories based on their resonator configuration: extracavity (externally pumped) and intracavity systems.

Extracavity sources

Most systems developed to-date are externally pumped by 1064 nm lasers. The simplest design is a terahertz parametric generator (TPG) outlined in Figure 1.7(a). This configuration was mainly adopted in the early work on the field [43,51], in which the nonlinear crystal is pumped in a single-pass by a fundamental laser source producing THz emission with broad linewidth [52].

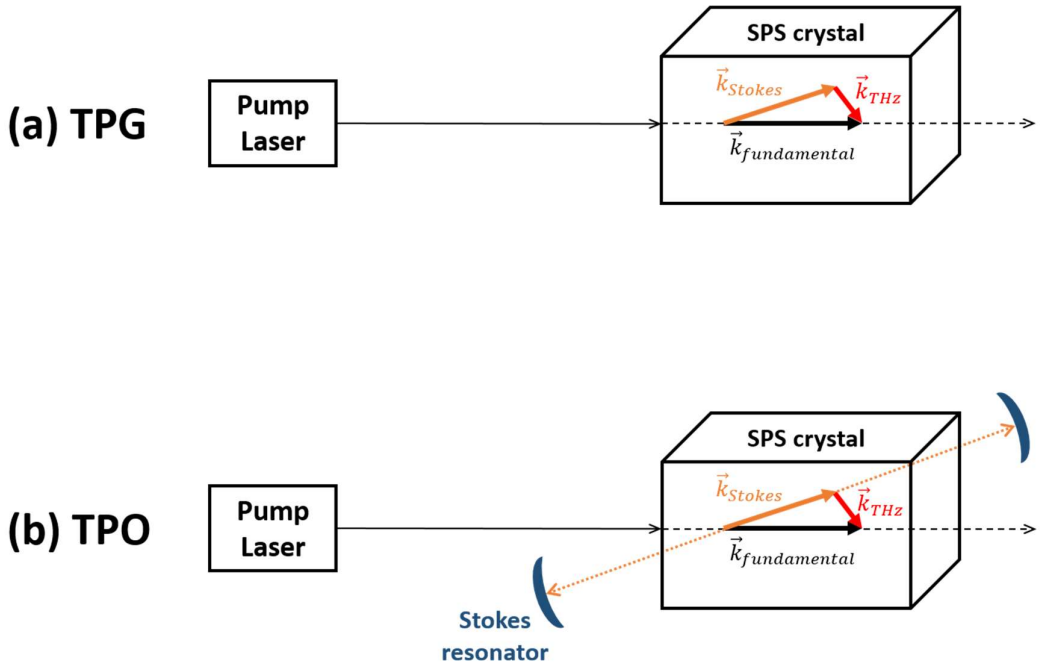

Figure 1.8 – Externally pumped THz parametric sources configurations. (a) Terahertz parametric generator (TPG). (b) Terahertz parametric oscillator (TPO). Typically the pump laser is a high-energy pulsed 1064 nm laser.

More narrowband terahertz radiation can be generated by forming an optical cavity around the SPS crystal to resonate the Stokes field, constituting a terahertz parametric oscillator (TPO), illustrated in Figure 1.7(b). The angle between the Stokes resonator and the fundamental laser in the TPO is adjusted to produce frequency-tunable THz output. With the resurgence of SPS research in the mid-90's, a massive effort was directed towards developing TPOs. There is an extensive literature available reporting high energy (mJ-level) pump lasers generating hundreds-of-nanojoules THz pulses in linear and surface-emitted configuration and different nonlinear crystals [44,49,52–56].

The most common SPS material is MgO:LN, which typically generates output continuously tunable from 1 – 3 THz [44]. In a representative example (reported in [53]) a TPO based on MgO:LN in surface-emitted configuration exhibited an energy per pulse of 854 nJ at 1.62 THz and was tunable from 0.75 – 2.81 THz.

More recently, utilising different nonlinear crystals such as KTP and KTA the spectral coverage of externally pumped TPOs was expanded to the 3 – 6 THz range. In [55], a TPO based on surface-emitted KTP as the nonlinear material delivered 336 nJ at 5.72 THz, and was continuously tunable from 3.17 – 3.44 THz, 4.19 – 5.19 THz and 5.55 – 6.13 THz. Replacing the nonlinear material by a KTA crystal, that same research group demonstrated 627 nJ at 4.30 THz, and the output frequency was continuously tunable from 3.59 – 3.96 THz, 4.21 – 4.50 THz, 4.90 – 5.16 THz, 5.62 – 5.66 THz and 5.92 – 6.43 THz [56]. The terahertz emission gaps in KTP and KTA terahertz parametric oscillators are due to suppression of the SPS process induced by infrared absorbing modes in those crystals.

Injection-seeding has also been explored as a technique to increase the output power and narrow the THz linewidth of TPOs, at the expense of increased system complexity [44,57,58]. The is-TPG reported in [58] is based on a microchip Nd:YAG laser amplified in a double-pass configuration, producing 20 mJ pulses, and used a 800 mW CW seed Stokes laser (itself producing 5.5 μJ pulses at 1.80 THz). From this system, 50 kW peak power was achieved, with output tunable from 0.7 – 3 THz in MgO:LN, with the Si-prisms extraction mechanism.

Intracavity sources

Externally pumped THz parametric sources combine wide frequency tunability with high output power when compared to other optical THz sources, as can be noted from the literature review provided here. However, these systems in-general require high pulse-energy fundamental pump lasers which may be costly and in most cases, have a large footprint and intricate setup, restricting their potential applicability in real-world devices. To overcome these issues and produce more attractive THz parametric sources the intracavity configuration was designed. In the intracavity approach, the nonlinear crystal is placed inside the fundamental resonator, and a separate pair of mirrors is responsible for resonating the Stokes field, as illustrated in Figure 1.8. The intense fundamental field inside the resonator may be considered analogous to the pump laser field in the externally pumped systems and is of sufficient intensity to achieve threshold for the SPS process.

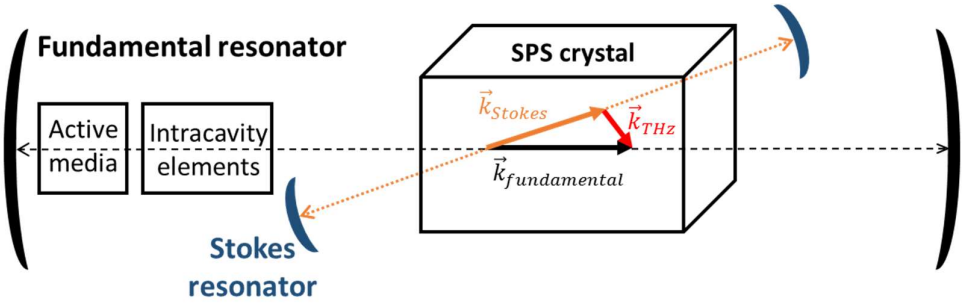

Figure 1.9 – The intracavity configuration. The nonlinear material is placed inside the fundamental resonator, and a separate pair of mirrors form a secondary resonator for the Stokes field.

The first intracavity terahertz parametric oscillator was demonstrated in 2006 at the University of St. Andrews (UK) [59] and was based on a conventional Q-switched 1064 nm Nd:YAG fundamental laser with an intracavity MgO:LN as the SPS crystal in linear configuration making use of Si-prisms for THz out-coupling. The system was continuously tunable from 1.2 – 3.05 THz, and exhibited 5 nJ pulse energies (75 nW average output power) with peak powers greater than 1 W for a modest 36 W pump power from a quasi-CW diode laser. As illustrated in Figure 1.9 (reproduced from [59]), in this novel configuration the nonlinear material is placed inside the fundamental resonator, making use of the high intracavity fields (>10 MW/cm^2) to achieve SPS threshold, removing the need for a high power pump source. The terahertz output frequency was tuned via rotating the Stokes cavity (mirrors M3 and M4 in Figure 1.9). (To avoid confusion with nomenclature from this point, in intracavity systems the SPS fields will simply be referred to as fundamental, Stokes and THz; the term "pump" will be exclusively used to refer to the pump laser diode.)

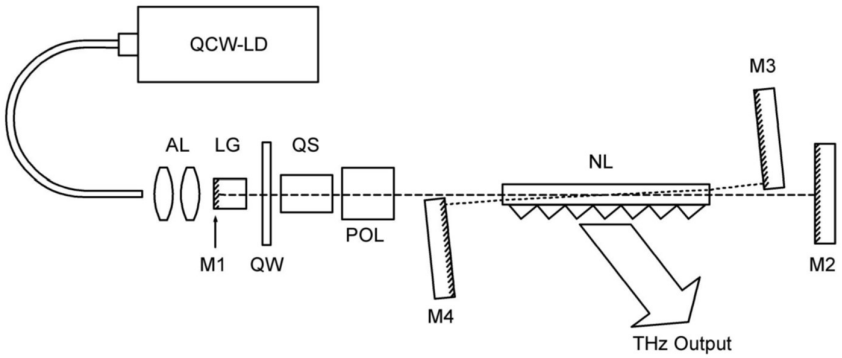

Figure 1.10 – Schematic diagram of the non-collinear phasematched THz OPO (reproduced from [59])

The first intracavity TPO demonstration was followed by rapid improvements in output power and reductions to the THz laser linewidth, which culminated in a compact source continuously tunable from 1 – 3 THz, delivering ~30 nJ/pulse around 1.6 THz for a 400 Hz repetition rate (>10 μW average output power and peak powers around 3 W for similar pump power levels) with ~1 GHz linewidth when etalons were placed in fundamental and Stokes cavities [60]. This technology was successfully translated to a commercial product produced by Scottish laser company M-Squared Lasers. This same research group successfully demonstrated further reduction in the THz linewidth below 100 MHz via seeding the Stokes field by a single-frequency external-cavity diode laser [61].

The surface-emitted configuration was also reported in an intracavity TPO by a separate research group [62]. In that report, terahertz pulses of 283 nJ were measured at 1.54 THz for a 595 mJ diode pump, and was continuously tunable from 0.75 – 2.75 THz.

Mindful of these recent developments and the important potentials of THz research, the Raman Laser group from Macquarie University decided pursue its own research line in terahertz in 2012. The Raman laser group at Macquarie University accumulates more than 20 years' experience on research and development of cutting-edge solid-state laser technology, particularly on intracavity SRS lasers [47,63–70]. This research group has also actively engaged with commercial partners, having successfully transferred in 2008 a yellow laser operating at 586 nm for the company Opto Global Pty (today part of Optos Inc.), a global player in the ophthalmic market.

The interplay between fields in SPS and SRS phenomena in intracavity systems requires similar laser design expertise, reason for which research on intracavity terahertz lasers was a natural initiative for Macquarie University, and a collaboration with the company M-Squared Lasers was initiated. Macquarie University's first terahertz source was reported in 2013 as a laser tunable from 1.53 – 2.82 THz and delivering 6.45 μW average output power at 1.82 THz (2.15 nJ/pulse) for only 5 W input diode pump power [71]. Shortly thereafter the versatility of intracavity SPS lasers was demonstrated by Macquarie University, with the construction of a continuous-wave THz source yielding 2.3 μW average output power at 1.8 THz (0.77 nJ/pulse) for 6 W diode pump and tunable from 1.5 – 2.3 THz using a high-Q resonator [46].

Over the last decade, terahertz sources based on intracavity SPS have experienced substantial development with regards to output power and system efficiency. However, little work has been dedicated to extend the spectral coverage of these sources.

1.4. Thesis outline

This research intends to push the frontiers of terahertz laser sources based on intracavity SPS; a technology capable of producing truly compact, reliable and cost-effective THz sources with frequency tunable output which can be interfaced with relatively simple detection mechanisms (portable spectrometers and Golay cells). What is of particular significance is that the core technology is based on solid state laser design, which is well established, and the components are well developed. More specifically, this research project evaluates different nonlinear materials (which exhibit distinctly different polariton dispersion relations and as a result, different SPS fields frequencies) with the objective of extending the range of tunable frequencies of such technologies, limited to ~1 – 3 THz at the time this work was initiated. Exploring three different nonlinear materials (MgO:LN, KTP and RTP) and clever resonator designs, this research work has produced original contributions to the knowledgebase. The primarily objective of the research was successfully achieved, as this research work demonstrated a substantial increase in the accessible frequency range of intracavity sources, covering the broad region from 1.4 – 6.0 THz when combining all laser configurations as per March 2017. Another important outcome of this research was the significant increase in average output power, reaching 0.125 mW at 4.1 THz (43 nJ/pulse) for only 6 W diode pump, a 20-fold increase over the previous work reported by this research group in [71], and also breaking the 0.1 mW average output power barrier. All the materials, research methods and original contributions of this work to the knowledge base are detailed in the following chapters. In this thesis the laser resonator designed to produce frequency-tunable terahertz radiation based on intracavity SPS is referred to as a THz polariton laser. This simplified nomenclature (instead of intracavity terahertz parametric oscillator) acknowledges the fact that the key nonlinear optical phenomena responsible for producing the desired output is stimulated polariton scattering, and this was also adopted in our publications.

Chapter 2 describes the design and optimization of the fundamental 1064 nm laser, the Nd:YAG resonator for intracavity SPS; the general diagnostic equipment (spectrometers, beam profilers, laser powermeters, etc.) and the terahertz-specific optics and diagnostic equipment (silicon-prisms, Golay cell, THz optics, THz camera, etc.) used in this project.

In Chapter 3 SPS theory is presented in-depth, and due to the lack of information available in the literature, the vibrational spectra (Raman and infrared reflection) of the nonlinear crystals investigated in this thesis are characterised experimentally. The classical coupled-wave equations for the interacting SPS fields are solved to obtain an analytical expression for the terahertz gain coefficient, and a methodology is described to calculate the dispersion curve for the SPS materials based on information obtained from Raman and Fourier-transform infrared reflectance spectroscopy (FTIR). The three different materials evaluated are then presented: MgO:LN, KTP and RTP. A literature review of these materials is provided, followed by an investigation of their properties relevant to polariton scattering. The Raman and FTIR spectra of MgO:LN, KTP and RTP were collected and the dispersion curve, refractive index and absorption coefficient in the THz are calculated for each material, to make predictions around the THz output characteristics. The high absorption coefficients calculated predicts serious limitations for KTP and RTP crystals in the linear design to operate at frequencies above ~4 THz. The SPS gain curve for MgO:LN is also calculated.

The experimental results with linear resonators are presented in Chapter 4. First, competition effects between SRS (in the fundamental cavity) and SPS in the Stokes cavity with the intracavity KTP crystal is observed, which required the introduction of selective losses for the competing Raman lines to produce stable SPS fields. With stable SPS fields, the linear THz polariton lasers based on KTP and RTP are evaluated and the limitations in terahertz detection predicted in Chapter 3 are observed experimentally. It was not possible to detect THz radiation above 4.2 THz, confirming the prediction from Chapter 3. Continuously tunable terahertz output from an intracavity RTP was detected for the first time, yet on a limited range (below 4.2 THz) when compared to the THz fields generated internally (as high as 7 THz). Despite the strong Stokes signal obtained in KTP corresponding to ~4 – 6 THz fields being generated, no terahertz radiation was detected. The main factors influencing the absence of terahertz detection were investigated with the experimental device: the losses associated with the extraction of the THz fields from the SPS crystal, transmission losses through propagation and transmission losses on the detection system. The high absorption coefficient of KTP and RTP in the THz range which was being generated was then confirmed to be a limiting factor in terahertz detection above ~4 THz from the linear design, which led to the construction of the surface-emitted configuration.

In Chapter 5 the results obtained with MgO:LN, KTP and RTP in a surface-emitted configuration are presented, showing that the limitations of THz detection encountered in the

linear configuration were overcome. In this layout it was possible to detect THz radiation for all interacting angles producing wavelength-tunable Stokes radiation. An experimental investigation of laser damage threshold in MgO:LN crystal is conducted which resulted in an enhancement in the performance of the system after the deposition of a protective Teflon coating on the crystal to avoid laser induced damage. The Teflon-coated MgO:LN is reported to deliver 56.8 μW at 1.76 THz (19 nJ/pulse) for 6.5 W diode pump power and was tunable from 1.46 – 3.84 THz, a record output power level and frequency range. The first terahertz detection from an intracavity KTP crystal is also demonstrated, with 71 μW at 5.57 THz (24 nJ/pulse) being measured for 6.5 W diode input power, and terahertz tunability from 4.30 – 5.20 THz and 5.50 – 5.90 THz (limited by strong SRS competition in the Stokes cavity). The highest output power among all systems evaluated was achieved was when using the RTP crystal in SE configuration, in which 0.125 mW average output power is reported at 4.1 THz (43 nJ/pulse) for only 6 W diode pump, with terahertz field tunable from 3.05 – 3.16 THz, 3.50 – 4.25 THz, 4.57 – 4.75 THz and 5.40 – 5.98 THz and free from SRS competition.

Chapter 6 summarises the key findings and contributions of this research work to the knowledgebase and presents an outlook for future work.

1.5. List of publications

The following paper and conference manuscripts were published as a consequence of this research work:

Papers

1. Tiago A. Ortega, Helen M. Pask, David J. Spence, and Andrew J. Lee, "Stimulated polariton scattering in an intracavity RbTiOPO4 crystal generating frequency-tunable THz output," Opt. Express 24, 10254-10264 (2016)

2. Tiago A. Ortega, Helen M. Pask, David J. Spence, and Andrew J. Lee, "THz polariton laser using an intracavity MgO:$LiNbO_3$ crystal with protective Teflon coating," Opt. Express 25, 3991-3999 (2017)

3. Tiago A. Ortega, Helen M. Pask, David J. Spence, and Andrew J. Lee, "Tunable 3-6 THz polariton laser exceeding 0.1 mW average output power based on crystalline $RbTiOPO_4$," IEEE J. Sel. Top. Quantum Electron. DOI: 10.1109/JSTQE.2018.2810380 (2018)

Conference manuscripts

1. T. Ortega, H. M. Pask, D. Spence, and A. Lee, "Competition Effects Between Stimulated Raman and Polariton Scattering in Intracavity KTiOPO4 Crystal," in Advanced Solid State Lasers, OSA Technical Digest (online) (Optical Society of America, 2015), paper ATu3A.3.

2. T. A. Ortega, H. M. Pask, D. J. Spence and A. J. Lee, "Frequency-tunable THz polariton laser based on intracavity $RbTiOPO_4$ crystal," 2016 41st International Conference on Infrared, Millimeter, and Terahertz waves (IRMMW-THz), Copenhagen, 2016, pp. 1-2.

3. T. A. Ortega, H. M. Pask, D. J. Spence and A. J. Lee, "MgO:$LiNbO_3$ crystal generating frequency-tunable THz output in intracavity surface-emitted configuration" Joint 13th Asia Pacific Physics Conference and 22nd Australian Institute of Physics Congress, Brisbane 2016,

References

1. M. Tonouchi, "Cutting-edge terahertz technology," Nat. Photon. **1**, 97–105 (2007).

2. I. Hosako, N. Sekine, M. Patrashin, S. Saito, K. Fukunaga, Y. Kasai, P. Baron, T. Seta, J. Mendrok, S. Ochiai, and H. Yasuda, "At the dawn of a new era in terahertz technology," Proc. IEEE **95**, 1611–1623 (2007).

3. W. L. Chan, J. Deibel, D. M. Mittleman, B. Ferguson, S. Wang, D. Gray, and X. Zhang, "Terahertz wave imaging : horizons and hurdles," Phys. Med. Biol. **47**, 3667–3677 (2002).

4. J. Federici, B. Schulkin, F. Huang, D. Gady, R. Barat, F. Oliveira, and D. Zimdars, "THz imaging and sensing for security applications — explosives, weapons and drugs," Semicond. Sci. Technol. **20**, S266–S280 (2005).

5. W. L. Chan, J. Deibel, and D. M. Mittleman, "Imaging with terahertz radiation," Reports Prog. Phys. **70**, 1325–1379 (2007).

6. J. A. Zeitler, P. F. Taday, D. A. Newnham, M. Pepper, K. C. Gordon, and T. Rades, "Terahertz pulsed spectroscopy and imaging in the pharmaceutical setting – a review," J. Pharm. Pharmacol. **59**, 209–223 (2007).

7. I. Amenabar, F. Lopez, and A. Mendikute, "In Introductory Review to THz Non-Destructive Testing of Composite Mater," J. Infrared Millimiter Terahertz Waves **34**, 152–169 (2013).

8. B. Recur, L. Frederique, B. Bousquet, L. Canioni, and P. Mounaix, "Review of Terahertz Tomography Techniques," J. Infrared Millimiter Terahertz Waves **35**, 382–411 (2014).

9. A. J. Fitzgerald, E. Berry, R. E. Miles, C. B. Reid, A. Fitzgerald, G. Reese, S. Fan, Y. He, B. S. Ung, W. L. Chan, J. Deibel, D. M. Mittleman, B. Ferguson, S. Wang, D. Gray, R. M. Woodward, B. E. Cole, and V. P. Wallace, "Terahertz pulse imaging in reflection geometry of human skin cancer and skin tissue," Phys. Med. Biol. **47**, 3853–3863 (2002).

10. S. Nakajima, H. Hoshina, M. Yamashita, and C. Otani, "Terahertz imaging diagnostics of cancer tissues with a chemometrics technique," Appl. Phys. Lett. **90**, 2007–2009

(2007).

11. A. R. Orlando and G. P. Gallerano, "Terahertz Radiation Effects and Biological Applications," J. Infrared Millim Terahertz Waves **30**, 1308–1318 (2009).

12. Y. Sun, M. Y. Sy, Y. J. Wang, A. T. Ahuja, Y. Zhang, and E. Pickwell-MacPherson, "A promising diagnostic method: Terahertz pulsed imaging and spectroscopy," World J. Radiol. **3**, 55–65 (2011).

13. S. J. Oh, J. Choi, I. Maeng, J. Y. Park, K. Lee, Y. Huh, J. Suh, S. Haam, and J. Son, "Molecular imaging with terahertz waves," Opt. Express **19**, 4009–4016 (2011).

14. S. R. Tripathi, E. Miyata, P. Ben Ishai, and K. Kawase, "Morphology of human sweat ducts observed by optical coherence tomography and their frequency of resonance in the terahertz frequency region," Sci. Rep. **5**, 1–7 (2015).

15. K. Kawase, Y. Ogawa, and Y. Watanabe, "Non-destructive terahertz imaging of illicit drugs using spectral fingerprints," Opt. Express **11**, 2549–2554 (2003).

16. M. R. Leahy-Hoppa and M. J. Fitch, "Terahertz spectroscopy techniques for explosives detection," Anal. Bioanal. Chem. **395**, 247–257 (2009).

17. K. B. Cooper, R. J. Dengler, N. Llombart, and T. Bryllert, "An Approach for Sub-Second Imaging of Concealed Objects Using Terahertz (THz) Radar," J. Infrared Millimiter Terahertz Waves **30**, 1297–1307 (2009).

18. D. M. Sheen, T. E. Hall, R. H. Severtsen, D. L. Mcmakin, B. K. Hatchell, and P. L. J. Valdez, "Active wideband 350 GHz imaging system for concealed-weapon detection," Proc. SPIE 7309, Passiv. Millimeter-Wave Imaging Technol. XII **7309**, 1–10 (2009).

19. P. Mousavi, F. Haran, D. Jez, F. Santosa, and J. S. Dodge, "Simultaneous composition and thickness measurement of paper using terahertz time-domain spectroscopy," Appl. Opt. **48**, 6541–6546 (2009).

20. R. K. May, M. J. Evans, S. Zhong, I. A. N. Warr, L. F. Gladden, Y. Shen, and J. A. Zeitler, "Terahertz In-Line Sensor for Direct Coating Thickness Measurement of Individual Tablets During Film Coating in Real-Time," J. Pharm. Sci. **100**, 1535–1544 (2011).

21. E. V Yakovlev, K. I. Zaytsev, I. N. Dolganova, and S. O. Yurchenko, "Non-Destructive

Evaluation of Polymer Composite Materials at the Manufacturing Stage Using Terahertz Pulsed Spectroscopy," IEEE Trans. Terahertz Sci. Technol. **5**, 810–816 (2015).

22. S. Krimi, J. Klier, J. Jonuscheit, G. Von Freymann, R. Urbansky, and R. Beigang, "Highly accurate thickness measurement of multi-layered automotive paints using terahertz technology," Appl. Phys. Lett. **109**, 21105 (2016).

23. G. L. Carr, M. C. Martin, W. R. Mckinney, S. V Benson, D. Douglas, and G. R. Neil, "Filling the THz gap — high power sources and applications," Reports Prog. Phys. **69**, 301–326 (2005).

24. X. Zhang and Z. Xu, *Introduction to THz Wave Photonics* (Springer, 2010).

25. F. Ward, G. Weinreich, M. Bass, and P. A. Franken, "Optical Rectification," Phys. Rev. Lett. **9**, 28–31 (1962).

26. P. Y. Han and M. Tani, "Use of the organic crystal DAST for terahertz beam applications," Opt. Lett. **25**, 675–677 (2000).

27. H. Auston, T. American, and P. Society, "Cherenkov Radiation from Femtosecond Optical Pulses in Electro-Optic Media," Phys. Rev. Lett. **53**, 1555–1558 (1984).

28. J. A. L'Huillier, G. Torosyan, M. Theuer, C. Rau, Y. Avetisyan, and R. Beigang, "Generation of THz radiation using bulk, periodically and aperiodically poled lithium niobate -- Part 2: Experiments," Appl. Phys. B **86**, 197–208 (2007).

29. J. A. L'Huillier, G. Torosyan, M. Theuer, Y. Avetisyan, and R. Beigang, "Generation of THz radiation using bulk, periodically and aperiodically poled lithium niobate -- Part 1: Theory," Appl. Phys. B **86**, 185–196 (2007).

30. K. Suizu, T. Tsutsui, T. Shibuya, T. Akiba, and K. Kawase, "Cherenkov phase matched THz-wave generation with surfing configuration for bulk Lithium Nobate crystal," Opt. Express **17**, 7102–7109 (2009).

31. J. Faist, F. Capasso, D. L. Sivco, C. Sirtori, A. L. Hutchinson, and A. Y. Cho, "Quantum Cascade Laser," Science. **264**, 553–556 (1994).

32. M. A. Belkin and F. Capasso, "New frontiers in quantum cascade lasers : high performance room temperature terahertz sources," Physi. Scr. **90**, 118002 (2015).

33. F. Capasso and F. Spie, "High-performance midinfrared quantum cascade lasers," Opt.

Eng. **49**, 1–9 (2017).

34. B. S. Williams, S. Kumar, Q. Hu, and J. L. Reno, "High-power terahertz quantum-cascade laser," Electron. Lett. **42**, 18–19 (2006).

35. L. Li, L. Chen, J. Zhu, J. Freeman, P. Dean, A. Valavanis, A. G. Davies, and E. H. Linfield, "Terahertz quantum cascade lasers with >1 W output powers," Electron. Lett. **50**, 309–311 (2014).

36. Q. Qin, J. L. Reno, and Q. Hu, "MEMS-based tunable terahertz wire-laser over 330 GHz," Opt. Express **36**, 692–694 (2011).

37. Q. Qin, B. S. Williams, S. Kumar, J. L. Reno, and Q. Hu, "Tuning a terahertz wire laser," Nat. Photon. **3**, 732–737 (2009).

38. A. J. Deninger, T. Göbel, D. Schönherr, T. Kinder, A. Roggenbuck, M. Köberle, F. Lison, T. Müller-Wirts, and P. Meissner, "Precisely tunable continuous-wave terahertz source with interferometric frequency control," Rev. Sci. Instrum. **79**, 1–6 (2008).

39. K. Miyamoto, A. Lee, T. Saito, T. Akiba, K. Suizu, and T. Omatsu, "Broadband terahertz light source pumped by a 1 μm picosecond laser," Appl. Phys. B **110**, 321–326 (2013).

40. D. Stanze, A. Deninger, and A. Roggenbuck, "Compact cw Terahertz Spectrometer Pumped at 1.5 μm Wavelength," J. Infrared Millim Terahertz Waves **32**, 225–232 (2010).

41. M. Scheller, J. M. Yarborough, J. V Moloney, M. Fallahi, M. Koch, and S. W. Koch, "Room temperature continuous wave milliwatt terahertz source," Opt. Express **18**, 27112–27117 (2010).

42. K. Kawase, J. I. Shikata, and I. Hiromasa, "Terahertz wave parametric sources," J. Phys. D Appl. Phys **35**, R1–R14 (2002).

43. S. Sussman, "Tunable Light Scattering from Transverse Optical Modes in Lithium Niobate," Microw. Lab. Rep. No1851, Stanford Univ. (1970).

44. K. Kawase, J. Shikata, and H. Ito, "Terahertz wave parametric source," J. Phys. D. Appl. Phys. **35**, R1–R14 (2002).

45. A. M. Warrier, R. Li, J. Lin, A. J. Lee, H. M. Pask, and D. J. Spence, "Tunable terahertz generation in the picosecond regime from the stimulated polariton scattering in a

$LiNbO_3$ crystal," Opt. Lett. **41**, 4409–4412 (2016).

46. A. J. Lee and H. M. Pask, "Continuous wave, frequency-tunable terahertz laser radiation generated via stimulated polariton scattering," Opt. Lett. **39**, 442–445 (2014).

47. H. M. Pask, "The design and operation of solid-state Raman lasers," Prog. Quantum Electron. **27**, 3–56 (2003).

48. J. Gelbwachs, R. Pantell, H. Puthoff, and J. Yarborough, "A Tunable Stimulated Raman Oscillator," Appl. Phys. Lett. **14**, 258–262 (1969).

49. K. Kawase, J. Shikata, H. Minamide, K. Imai, and H. Ito, "Arrayed silicon prism coupler for a terahertz-wave parametric oscillator," Appl. Opt. **40**, 1423–1426 (2001).

50. T. Ikari, X. Zhang, and H. Minamide, "THz-wave parametric oscillator with a surface-emitted configuration," Opt. Express **14**, 1604–1610 (2006).

51. J. M. Yarborough, S. S. Sussman, H. E. Purhoff, R. H. Pantell, and B. C. Johnson, "Efficient, tunable optical emission from $LiNbO_3$ without a resonator," Appl. Phys. Lett. **15**, 102–105 (1969).

52. S. Hayashi, K. Nawata, K. Kawase, and H. Minamide, "Terahertz parametric oscillator sources," Adv. Solid State Lasers, OSA Tech. Dig. Pap. AW2A.1. Opt. Soc. Am. (2014).

53. Y. Wang, Z. Li, J. Li, C. Yan, T. Chen, D. Xu, W. Shi, H. Feng, and J. Q. Yao, "Energy scaling of a tunable terahertz parametric oscillator with a surface emitted configuration," Laser Phys. **24**, 125402 (2014).

54. W. Wang, X. Zhang, Q. Wang, Z. Cong, X. Chen, Z. Liu, Z. Qin, P. Li, G. Tang, N. Li, C. Wang, Y. Li, and W. Cheng, "Multiple-beam output of a surface-emitted terahertz-wave parametric oscillator by using a slab MgO:$LiNbO_3$ crystal," Opt. Lett. **39**, 754–757 (2014).

55. W. Wang, Z. Cong, X. Chen, X. Zhang, Z. Qin, G. Tang, N. Li, C. Wang, and Q. Lu, "Terahertz parametric oscillator based on $KTiOPO_4$ crystal," Opt. Lett. **39**, 3706–3709 (2014).

56. W. Wang, Z. Cong, Z. Liu, X. Zhang, Z. Qin, G. Tang, N. Li, Y. Zhang, and Q. Lu, "THz-wave generation via stimulated polariton scattering in $KTiOAsO_4$ crystal," Opt. Express **22**, 17092–17098 (2014).

57. Y. Taira, S. Tripathi, K. Murate, K. Nawata, H. Minamide, and K. Kawase, "A Terahertz Wave Parametric Amplifier With a Gain of 55 dB," IEEE Trans. THz. Sci. Technol. **4**, 753–755 (2014).

58. S. Hayashi, K. Nawata, T. Taira, J. Shikata, K. Kawase, and H. Minamide, "Ultrabright continuously tunable terahertz-wave generation at room temperature," Sci. Rep. **4**, 5045 (2014).

59. T. Edwards, D. Walsh, M. Spurr, C. Rae, M. Dunn, and P. Browne, "Compact source of continuously and widely-tunable terahertz radiation," Opt. Express **14**, 1582–1589 (2006).

60. D. J. M. Stothard, T. J. Edwards, D. Walsh, C. L. Thomson, C. F. Rae, M. H. Dunn, and P. G. Browne, "Line-narrowed, compact, and coherent source of widely tunable terahertz radiation," Appl. Phys. Lett. **92**, 11–14 (2008).

61. D. Walsh, D. J. M. Stothard, T. J. Edwards, P. G. Browne, C. F. Rae, and M. H. Dunn, "Injection-seeded intracavity terahertz optical parametric oscillator," J. Opt. Soc. Am. B **26**, 1196–1202 (2009).

62. Y. Wang, D. Xu, H. Jiang, K. Zhong, and J. Yao, "A high-energy, low-threshold tunable intracavity terahertz-wave parametric oscillator with surface-emitted configuration," Laser Phys. **23**, 55406 (2013).

63. H. M. Pask and J. A. Piper, "Practical 580 nm source based on frequency doubling of an intracavity-Raman-shifted Nd:YAG laser," Opt. Commun. **148**, 285–288 (1998).

64. H. M. Pask and J. A. Piper, "Efficient all-solid-state yellow laser source producing 1.2-W average power," Opt. Lett. **24**, 1490–1492 (1999).

65. R. P. Mildren, M. Convery, H. M. Pask, and J. A. Piper, "Efficient, all-solid-state, Raman laser in the yellow, orange and red," Opt. Express **12**, 785–790 (2004).

66. J. A. Piper and H. M. Pask, "Crystalline Raman Lasers," IEEE J. Sel. Top. Quantum Electron. **13**, 692–704 (2007).

67. H. Pask, P. Dekker, R. Mildren, D. Spence, and J. Piper, "Wavelength-versatile visible and UV sources based on crystalline Raman lasers," Prog. Quantum Electron. **32**, 121–158 (2008).

68. A. Lee, H. Pask, P. Dekker, and J. Piper, "High efficiency, multi-Watt CW yellow emission from an intracavity-doubled self-Raman laser using Nd:$GdVO_4$," Opt. Express **16**, 21958–21963 (2008).

69. J. Lin, H. Pask, D. Spence, C. Hamilton, and G. Malcolm, "Continuous-wave VECSEL Raman laser with tunable lime-yellow-orange output," Opt. Express **20**, 5219–5224 (2012).

70. A. Warrier, J. Lin, H. Pask, R. Mildren, D. Coutts, and D. Spence, "Highly efficient picosecond diamond Raman laser at 1240 and 1485 nm," Opt. Express **22**, 3325–3333 (2014).

71. A. Lee, Y. He, and H. Pask, "Frequency-tunable THz source based on stimulated polariton scattering in Mg:$LiNbO_3$," IEEE J. Quantum Electron. **49**, 357–364 (2013).

2. Materials and Methods

This chapter describes the general materials and methods used in this research work. The concepts of linear and surface-emitted resonator geometries are explained in detail in Section 2.1. In Section 2.2 the optical components and detection equipment specific for use with the THz fields generated in this work are detailed. Section 2.3 covers the general diagnostic equipment utilised in this research (spectrometers, beam profilers, optical power meters, etc.). In Section 2.4 the design and optimization of the fundamental 1064 nm laser resonator, the cornerstone of the various THz polariton lasers developed in this project is evaluated.

2.1. Resonator geometries for an intracavity polariton laser

The angles at which the SPS fields are generated require particular resonator design to enable output coupling of the THz field. Typically the interacting angle θ between the fundamental and Stokes fields ranges from ~0.5 – 5º, resulting in an angle β between the fundamental and THz fields of ~60-65º. The high refractive index in the THz for the various SPS materials (MgO:LN $n \approx 5.2$ around 2 THz; KTP/RTP $n \approx 3.9 - 5.5$~ from 1 – 2.5 THz) [1,2] results in a critical angle for total internal reflection (TIR) below 20º which imposes challenges to the

extraction of the terahertz fields from the SPS material. For a cuboid nonlinear crystal in free space, the THz field would experience TIR in the crystal-air interface, hence being confined to the material as illustrated in Figure 2.1 for the case of magnesium oxide-doped lithium niobate. Therefore, different strategies were implemented to avoid TIR and enable extraction of the THz fields, as detailed in the next section.

$$critical\ angle = \arcsin\left(\frac{n_{air}}{n_{crystal}}\right) \approx 11°$$

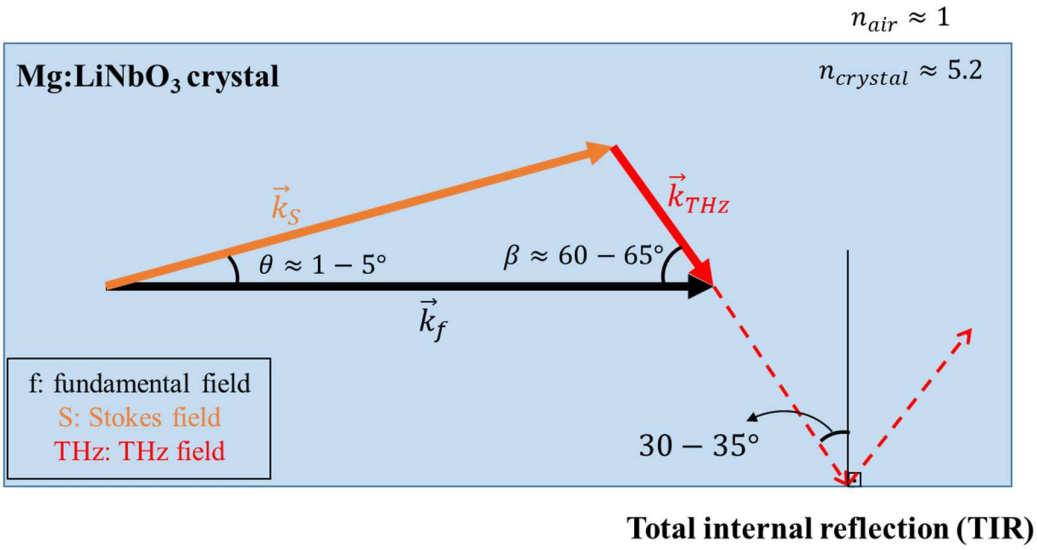

Figure 2.1 – Typical interacting angles between SPS fields in MgO:LN. In a cuboid nonlinear crystal in air, the THz field experiences TIR in the crystal-air interface being confined to the material. Similarly, TIR would also occur in other nonlinear crystals such as KTP and RTP.

2.1.1. Linear resonator geometry

The linear THz polariton laser geometry is shown in Figure 2.2. It is based on linear optical cavities for both fundamental and Stokes fields, and cuboid nonlinear materials. To avoid TIR in the nonlinear crystal-air interface as described in Figure 2.1, high-resistivity (R>10kΩ/cm) silicon prisms are bonded to the crystal's side face [3], as can be seen in Figure 2.2. The high-resistivity silicon has a flat refractive index of $n = 3.4$ in the THz range of interest (1 – 10 THz) [4], which results in a critical angle above 40º, enabling the THz field to be refracted from the crystal into the prisms. The silicon prisms are cut at such angles that the propagating THz field impinges close to normal incidence at the prism-air interface, and is

refracted into the air. The different prisms geometries for the different SPS materials evaluated will be detailed in the next chapter. With the silicon prisms approach, the THz field is emitted along the extension of the prism array, spanning over several millimetres in the resonator axis direction [3]. The Stokes resonator (mirrors M3 and M4 in Figure 2.2) is mounted on a high-precision rotation stage to enable fine angle tuning and consequently fine adjustment of the Stokes wavelength and terahertz output frequency.

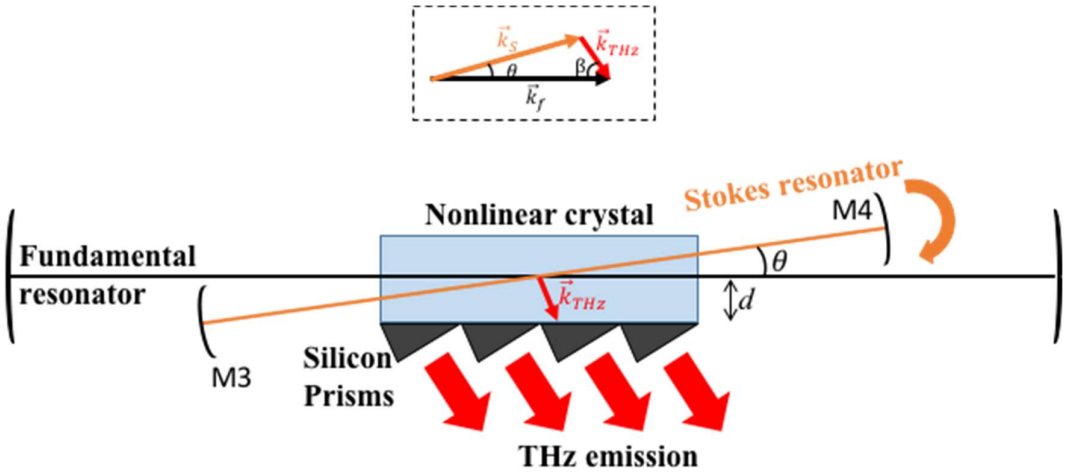

Figure 2.2 – The THz polariton laser with a linear resonator layout. The vectors of the fundamental, Stokes and THz fields are shown inset.

This resonator geometry experiences intrinsic absorption and Fresnel reflection losses imposed to the THz field which can be a limiting factor, as will be discussed in Chapters 3 and 4. To minimise absorption of the THz field during propagation inside the nonlinear crystal, the lateral distance between the SPS interacting region and the material's side face is minimised (distance "*d*" in Figure 2.2). However, the absorption coefficient in the THz range for the SPS crystals can exceed 50 cm^{-1}, and even a 250 μm propagation distance (size comparable to the resonator mode size) would represent more than 70% absorption losses. The difference in refractive index from the Si-prisms ($n = 3.4$) to the air ($n \sim 1$) accounts for additional Fresnel reflection losses of around 30%. To avoid these high intrinsic losses, the surface-emitted configuration was also evaluated.

2.1.2. Surface-emitted resonator geometry

In the surface-emitted (SE) resonator layout the SPS crystal is cut at a trapezoidal geometry, and the fundamental and Stokes fields experiences TIR inside the nonlinear media, as sketched in Figure 2.3. With this layout, the terahertz field is generated close to normal incidence at the TIR surface, and is refracted directly into the air, without the need for the prisms or any other out-coupling element [5].

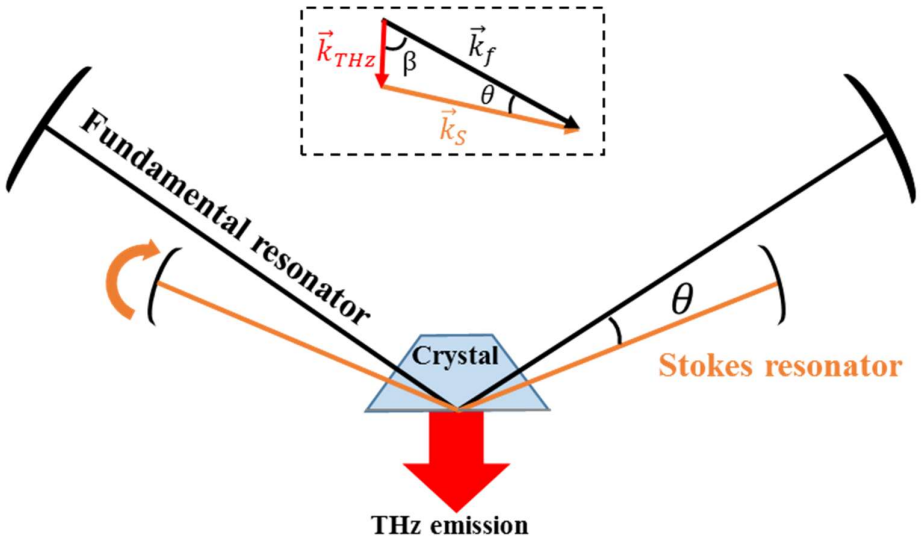

Figure 2.3 – The surface-emitted (SE) configuration layout. The vectors of the fundamental, Stokes and THz fields is shown inset.

The propagation distance of the THz field at the TIR surface is virtually zero, enabling substantial increases in measured THz output power, as will be reported in detail in Chapter 5. The output beam in the SE resonator is smaller than in the linear layout, only limited by the laser mode size inside the resonator at the TIR surface (Figure 2.4); the terahertz field generated away from of the TIR surface is rapidly absorbed inside the material, having negligible contribution to the detected output. The different trapezoidal geometries for different SPS materials will be described in Chapter 5.

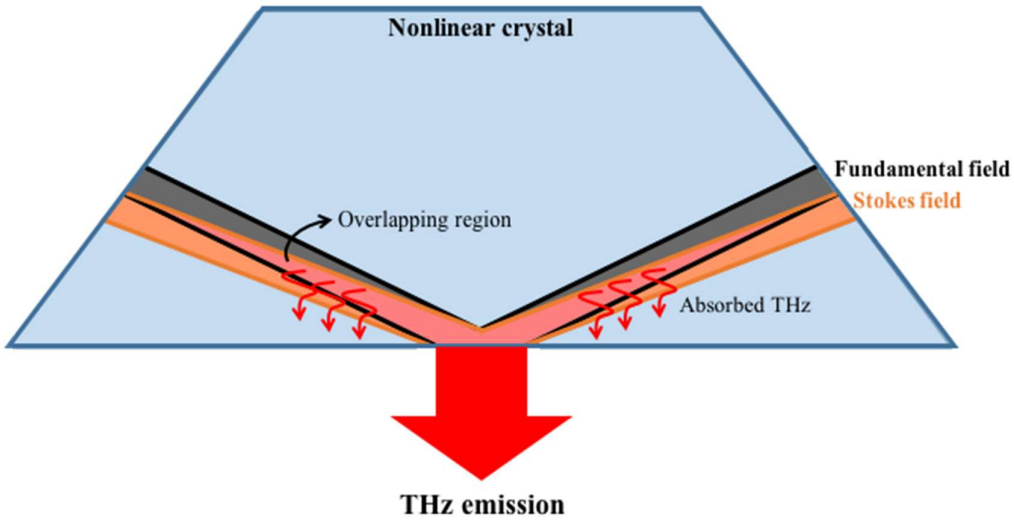

Figure 2.4 – In the surface-emitted configuration the propagation distance at the TIR surface is virtually zero. Terahertz field generated outside that region is strongly absorbed, having negligible contribution to the detected output.

2.2. Terahertz optics and detection equipment

2.2.1. Silicon prisms

High resistivity silicon (ρ>10 kΩ.cm) is a well-documented material for use in THz optics due to its low THz absorption across a broad frequency range and for its uniform refractive index ($n \cong 3.4$) [4]. The silicon prism's exit face was designed to be normal to the propagation direction of the THz fields as sketched in Figure 2.5, and was calculated based on the angles at which the terahertz is refracted into the different materials, which may vary for different crystals. The refracting angle δ into the prisms depends on the incidence angle of the THz field in the crystal's side face (α), which in turns depends on the SPS material refractive indices and interacting angles between fields in SPS process (θ,β). The parameters utilised to design the different prisms are summarised in Table 2.1: refractive indices, the range of interacting angles considered, the range of incidence angles at the crystal's side face and consequent refracted angles inside silicon.

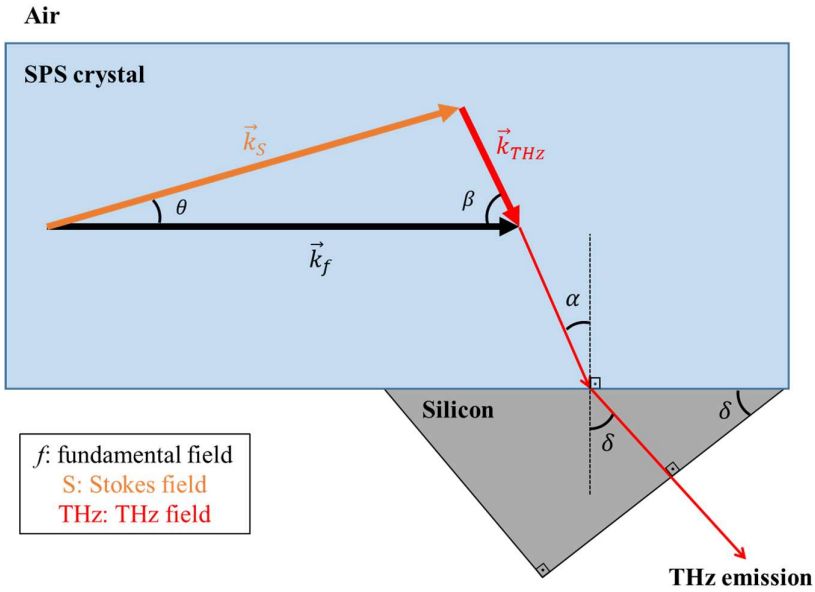

Figure 2.5 – The silicon prism design. The exit face was designed to be normal to the propagation direction of the THz fields.

Table 2.1 – Parameters utilised for calculating silicon prisms geometry for the different SPS crystals evaluated: the refractive indices, range of interacting angles, range of generated angles for the THz field, range of incidence angle in the crystal's side face and respective refraction angle inside silica.

		MgO:LN [1,6,7]	**KTP** [2]	**RTP** [8,9]
SPS Fields	**Fundamental**	1064 nm	1064 nm	
	Stokes	1068 – 1080 nm	1075 – 1093 nm	
	THz	1 – 4 THz	3 – 7.5 THz	
Refractive indices	**Fundamental**	2.232	1.738	1.771
	Stokes	$2.232 - 2.231$	$1.738 - 1.737$	$1.771 - 1.770$
	THz	$5.1 - 6.2$	$3.9 - 6$	
Interacting angles		$\theta \sim 0.5 - 2°$ $\beta \sim 63 - 67°$ $\alpha \sim 27 - 23°$	$\theta \sim 0.8 - 5°$ $\beta \sim 54 - 68°$ $\alpha \sim 36 - 22°$	
Refracting angle into Silicon		$\delta \sim 40 - 42°$	$\delta \sim 30 - 35°$	

The similarities between KTP and RTP optical properties enabled the design of a single set of prims for these two materials, but a second design was necessary for MgO:LN as illustrated in Figure 2.6. These materials were purchased from Crystran Ltd, and their specification can be found in Table 2.2.

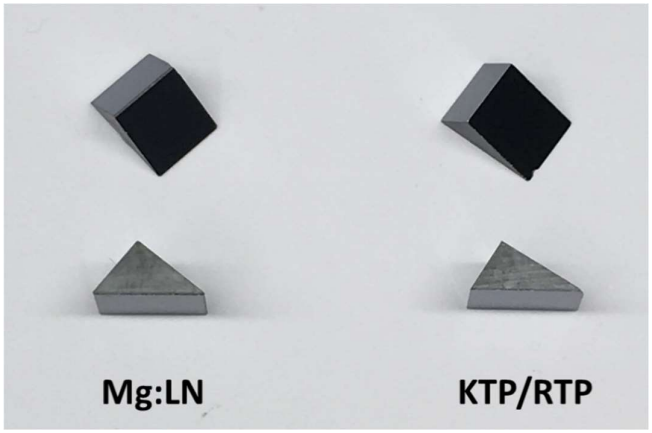

Figure 2.6 – Silicon prisms for (a)MgO:LN and (b)KTP/RTP crystals.

Table 2.2 – Silicon prisms specifications.

	Specification	**Manufacturer**
Si-prisms for MgO:LN	High resistivity silicon (ρ>10 kΩ.cm), FZ grade 7 mm hypotenuse x 5 mm thick 40/50/90° angles	Crystran
Si-prisms for KTP and RTP	High resistivity silicon (ρ>10 kΩ.cm), FZ grade 7 mm hypotenuse x 5 mm thick 32/58/90° angles	Crystran

2.2.2. THz optics and detector

The terahertz field was often manipulated for the measurement of average output power, beam profile, linewidth, polarization, etc., and the elements we had available for the experiments are summarised in Table 2.3. The detection of the THz field output was performed with an optical chopper and a Golay Cell connected to an oscilloscope, also specified in the table below. Due to the absence of a practical THz spectrometer, the THz frequency was calculated from the energy difference between the fundamental and Stokes field wavelengths which were measured with the portable spectrometer.

Table 2.3 – Optical components utilised to manipulate the THz field.

Item	Specification
Gold-coated 90º off-axis parabolic mirror	MPD 508508-90-M01 (Thorlabs)
TPX spherical lenses	25 mm, 50 mm, 75 mm and 100 mm EFL (Tydex)
Tsurupica cylindrical lenses	100 mm EFL (Broadband Inc.)
THz polariser	POL-HDPE-CA25-OD34.9-T7.9 (Tydex)
THz long pass filter	LPF 14.3 (Tydex)
THz window	Si window 50.8 mm x 0.5 mm (Tydex)
Golay cell (THz detector)	GC-1T (Tydex) Optical responsivity: 116.14 kV/W @ 10 Hz
Optical chopper (for Golay cell detection)	Driver: MC2000B (Thorlabs) Blade: MC1F2 (Thorlabs)
Oscilloscope	Tektronix TDS 2014

A Golay cell is a very efficient and simple device to measure THz radiation which was originally conceived by Marcel J. E. Golay [10]. It consists of a container filled with gas, a diaphragm (or membrane) and a light-absorbing material. When incident radiation is absorbed, it heats the gas, which consequently expands, deforming the membrane. This deformation is tracked with the use of a light source and photodetector. The THz signal is thus determined from the change in photodetector output which is in response to the absorbed THz radiation.

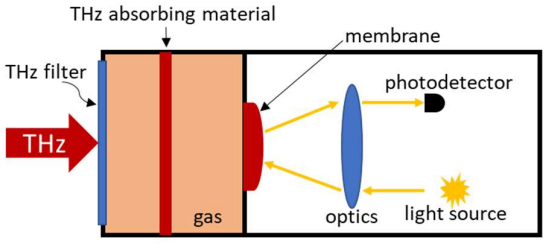

Figure 2. 7 – Working principle of a Golay cell.

The model used in this research is shown in Figure 2.7 (GC-1T, Tydex – Russia) has an optical responsivity of $116.14\,\mathrm{kV/W}$ @ $10\,\mathrm{Hz}$ and a noise equivalent power (NEP) of $1.4 \times 10^{10}\,\mathrm{W/Hz^{1/2}}$ @ $15\,\mathrm{Hz}$, according to the equipment datasheet. The average terahertz output powers (μW) calculated throughout this thesis were calculated converting the signal from the Golay cell (mV), and corrected for the frequency-dependent transmission loss of the LPF 14.3 filter, and the transmission losses in the TPX lens.

Figure 2.8 – Golay cell GC-1T (Tydex). Image reproduced from the manufacturer's website accessed on 16 May 2017, <http://www.tydexoptics.com/pdf/Golay_Detectors.pdf>.

2.2.3. THz camera

A camera sensitive to terahertz radiation was also available and utilised for some THz beam imaging described in Chapter 4 and 5. This equipment was acquired from the Japanese company NEC (Pat number: IRV-T0831), and is illustrated in Figure 2.8. The THz camera is based on an uncooled microbolometer array of 320×240 pixels (23.5 μm pixel pitch). The noise equivalent power of this device is below 100 pW (at 4 THz), and the camera is sensitive from 1 – 7 THz.

Figure 2.9 – Terahertz camera IRV-T0831 (NEC). Image reproduced from the manufacturer's website accessed on 7 April 2017, <http://www.nec.com/en/global/prod/terahertz/>.

2.3. General diagnostic equipment

The general diagnostic equipment utilised throughout the experiment is related in this section. Other specific equipment and materials shall be described whenever appropriate within this thesis.

2.3.1. Laser power meter

The average output power of pump laser diode (808 nm), the 1064 nm fundamental laser, and the near-infrared Stokes fields (~1070 – 1095 nm) were measured with a digital handheld optical power meter (Thorlabs PM100D). The pump diode and fundamental field outputs were measured with a standard thermal sensor (Thorlabs S310C), and the Stokes output was detected with a photodiode power sensor (Thorlabs S130C).

2.3.2. Near-infrared spectrometer

The spectral content of the near-infrared fundamental and Stokes fields were monitored with a portable USB Spectrometer (Ocean Optics HR4000) with a detectable range from 1050 to 1200 nm and 0.09 nm resolution. The wavelength scale of the portable spectrometer was calibrated against a wavemeter (Bristol 771) with a CW 1064 nm laser in order to increase the accuracy in the wavelength measurement. The terahertz frequency tuning was not measured

directly due to an absence of a THz spectrometer. According to the energy conservation law in the SPS process, it was calculated from the energy difference between the fundamental and Stokes photons.

2.3.3. Beam profiler

The spatial profile of the fundamental and Stokes laser outputs were monitored with a Spiricon beam profiler (model SP620U) always positioned perpendicular to the propagation direction.

2.3.4. Photodiodes

The temporal behaviour of the near-infrared fields was monitored to better comprehend the dynamics between the interacting SPS fields. The Q-switched fundamental 1064 nm laser output and the pulsed Stokes laser output were monitored with fast Si photodiodes (Thorlabs DET10A/M) or InGaAs photodiodes (Thorlabs DET10C/M), depending on the availability of these components at the time of the experiment. The specific model utilised in every setup will be indicated in the appropriate sections in Chapter 4 and Chapter 5. Neutral density filters (Thorlabs NEK01 Kit) were in place to attenuate the incident fields and avoid saturation of the sensor.

2.3.5. Oscilloscope

The output signal of the photodiode was connected to a fast oscilloscope (Tektronix 3054; 500 MHz bandwidth) utilised to read and record the temporal behaviour of the different THz polariton laser setups.

2.3.6. Raman spectrometer

The Raman spectra of the three nonlinear crystals evaluated in the experiments (MgO:LN, KTP and RTP) were measured to determine the location and linewidth of the vibrational modes of these crystals, information necessary to calculate the polariton dispersion curve and SPS gain curves. The measurements were made in a confocal Raman spectrometer model inVia™

confocal Raman microscope (Renishaw, UK), from 800 – 100 cm^{-1} with 0.6 cm^{-1} resolution, depicted in Figure 2.9. The excitation wavelength was 532 nm.

Figure 2.10 – Renishaw inVia™ confocal Raman microscope. Reproduced from manufacturer's website, accessed on 11 April 2017, < http://www.renishaw.com/en/invia-confocal-raman-microscope--6260/>.

2.3.7. FTIR Spectrometer

The infrared spectra of the three nonlinear materials (MgO:LN, KTP and RTP) were measured in order to determine the oscillator strength for the vibrational modes in each crystal. The calculated oscillator strengths were also necessary information in the modelling of the dispersion relation and SPS gain curves. The instrument utilised for the infrared spectroscopy was a Bruker Vertex 80v Fourier transform infrared spectrometer (FITR) operating in the far infrared range (680 – 50 cm^{-1}), with 4 cm^{-1} resolution. A picture of the instrument is shown in Figure 2.10.

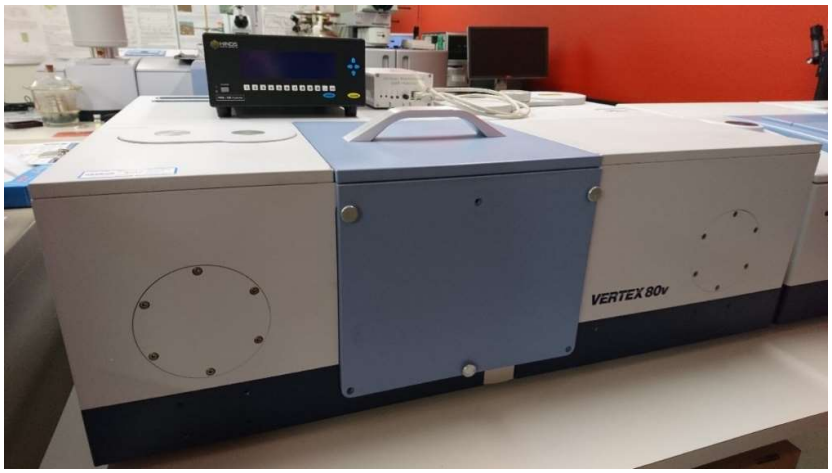

Figure 2.11– Bruker Vertex 80v Fourier transform infrared spectrometer (FITR). Image reproduced from the University of Sydney Vibrational Spectroscopy Facility website, accessed on 11 April 2017, <http://sydney.edu.au/science/chemistry/spectroscopy/instrumentation/vertex.shtml>.

2.4. Fundamental resonator design for an intracavity polariton laser

2.4.1. Fundamental resonator layout

The optical cavities for the fundamental field in the linear and in the surface-emitted configurations were constructed with the same key design parameters (mode volume, resonator length, radius of curvature of laser mirrors, etc.) enabling a more direct comparison between systems. As illustrated in Figure 2.11, in the linear configuration the different cuboid SPS crystals were inserted along the fundamental resonator axis, and in the SE configuration a trapezoidal SPS crystal was responsible for total internal reflection, folding the resonator in a "V-shape".

The fundamental resonator was composed of a diode end-pumped, Q-switched Nd:YAG laser operating at 1064 nm (except in Section 4.4.3, where the coatings were designed to operate at 1340 nm; all details of the 1340 nm resonator will be provided in Section 4.4.3). The total cavity length was designed to be under 250 mm in order to accommodate the various intracavity elements and still maintain compactness.

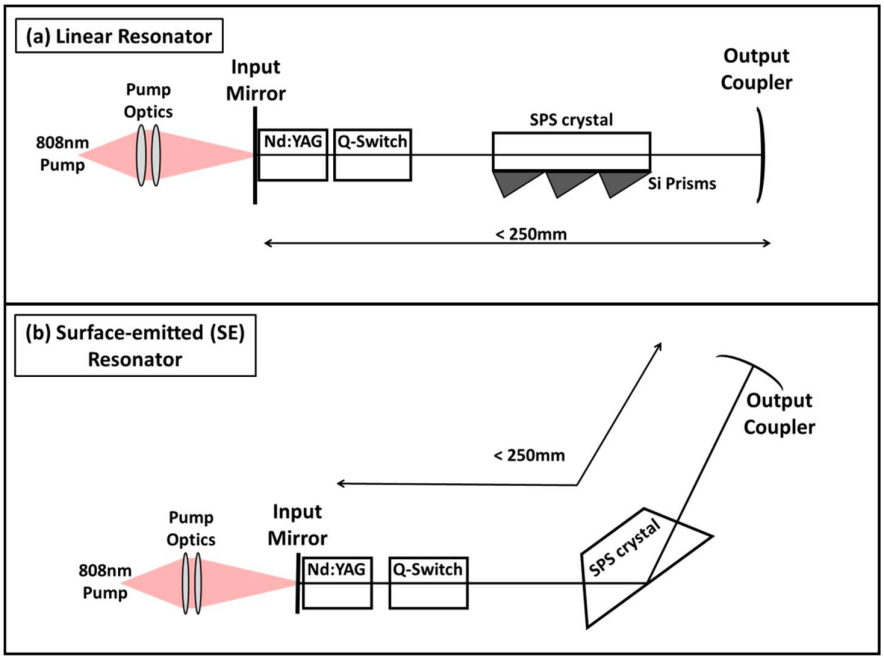

Figure 2.12 – Fundamental resonator layout (a)Linear configuration, SPS crystal on resonator axis. (b)Surface-emitted configuration, SPS crystal responsible for total internal reflection of fundamental field, but maintaining other resonator parameters.

2.4.2. Nd:YAG active media

The laser crystal chosen for the THz polariton laser was the well-established Nd:YAG, and its main properties are listed in Table 2.4. The long upper state lifetime (~230 μm) in Nd:YAG which enables a large population inversion to build-up combined with its excellent thermal properties that reduce the effect of thermal lensing make it an excellent candidate for compact and high-power Q-switched resonators with relatively high resonator Q-factor. This laser material can be conveniently pumped by standard 808 nm diode lasers producing unpolarised 1064 nm output.

The active medium was a 5 mm long, 5 mm diameter 1 at. % Nd:YAG crystal with anti-reflection coating at the pump and fundamental wavelengths (R<0.1%@808 / 1064 nm) provided by Castech Inc (China). The crystal was wrapped in indium foil and mounted in a water-cooled copper mount (water temperature = 25ºC), to minimise thermal lensing, as depicted in Figure 2.12. The 1 at. % Nd:YAG absorption coefficient at 808 nm (11 cm^{-1}) indicates that more than 99% of the incident diode pump laser will be absorbed by the material.

Table 2.4 –1 at. % Nd:YAG crystal material properties.

		Ref.
Density ρ (g/cm^3)	4.56	[11]
Thermal conductivity κ (W/cm.K)	0.14	[11]
Thermal expansion α (10^{-6}/K)	7.5	[11]
Refractive index at 1064 nm	1.82	[11]
$\boldsymbol{dn/dT}$ at 1064 nm (10^{-6}/K)	7.3	[11]
Upper-state lifetime τ (µs)	230	[11]
Absorption coefficient around 808 nm, 1 at. %Nd (cm^{-1})	11	[11]
Stimulated emission cross section σ (10^{-19}cm^2)	2.8	[11]

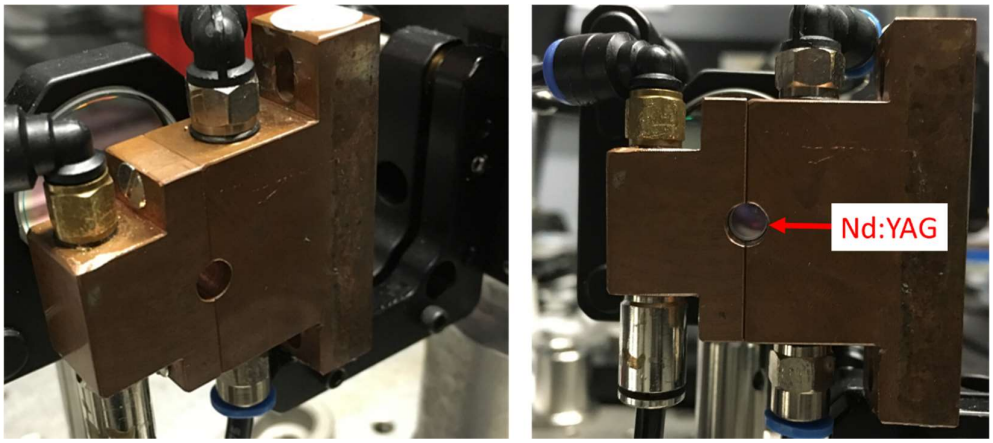

Figure 2.13 – Nd:YAG active media in copper mount with water cooling system.

2.4.3. Acousto-optic Q-switching cell

Stimulated polariton scattering is a third-order nonlinear effect which requires high optical field intensities to manifest (>10 MW/cm^2) [12]. In the intracavity design, the intensity required to exceed SPS threshold can be achieved with an optical Q-switch in the fundamental resonator. The Q-switching process is based on maintaining the resonator Q-factor at a low level for a long period of time, suppressing laser action whilst promoting a population inversion much larger than the steady-state inversion on a conventional laser. Rapidly switching the Q-factor

to a high value will thus entail the rapid build-up of an intense laser pulse, which will be coupled out in a few round-trips, producing pulses typically of dozens of nanoseconds in duration [11].

An acousto-optic Q-switching cell was utilised to achieve the intracavity intensity required to exceed SPS threshold, due to its simplicity of operation and the reduced number of optical interfaces when compared to electro-optical Q-switches. In an acousto-optic Q-switch, the laser Q-factor is switched to a low and high value by respectively turning on and off an acousto-optic modulator (typically quartz) which diffracts radiation out of the cavity (a deeper discussion on the working principles of AOM cells can be found in [11]). In an electro-optical Q-switch (particularly for unpolarised lasers such as Nd:YAG) additional optical elements are required (quarter wave-plates, polarisers), which would increase the intracavity losses impairing laser performance and increasing laser threshold.

The Q-switching cell available for the experiments was manufactured by NEOS (part number 33027-25-2-i). The Q-switch external dimension and picture is shown in Figure 2.13. It was also water-cooled at 25ºC and operated at 3 kHz repetition rate.

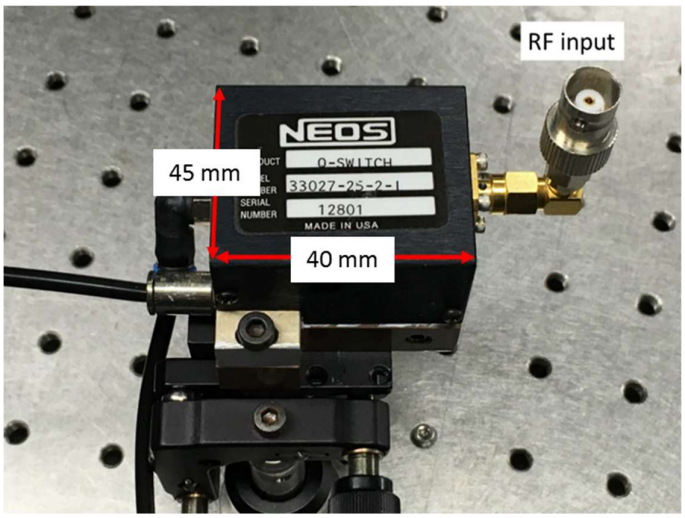

Figure 2.14 – NEOS (part number 33027-25-2-i) acousto-optic Q-switching cell.

2.4.4. Thermal lensing and its influence on resonator design

In solid-state lasers the thermal load in optical crystals promotes non-uniform changes inside the material which have the same refractive effect of a lens. This phenomena is well-known as thermal lensing, and originates from three main mechanisms: refractive index dependence on temperature, refractive index dependence on optical stress (photo-elastic effect), and the bulging of the crystal end faces due to thermal expansion. The effective focal length of the thermal lens (f_{TL}) of a cylindrical crystal can be mathematically expressed as a function of these three mechanisms, respectively as [11]:

$$f_{TL} = \frac{\kappa A}{P_{heat}}\left(\frac{1}{2}\frac{dn}{dT} + \alpha C_{r,\phi} n_0^3 + \frac{\alpha r_0 (n_0 - 1)}{L}\right)^{-1} \tag{2.1}$$

where κ is the thermal conductivity, A is the average mode area in the crystal, P_{heat} is the heat power deposited in the material, dn/dT is the variation of the refractive index with temperature, α the thermal expansion coefficient, $C_{r,\phi}$ the photo-elastic coefficient, n_0 the refractive index without any pump, r_0 the transverse length of the crystal experiencing expansion, and L the crystal length.

In the THz polariton laser the elevated fundamental field intensity required to achieve SPS threshold can be more easily obtained by reducing the mode volume inside the resonator. Consequently, the diode pump beam size also has to be reduced to match the resonator mode. Therefore, strong thermal lensing is expected in the active media, as a result of the high pump absorption confined to a small volume and the quantum defect deficit between the 808 nm pump and the 1064 nm fundamental wavelengths. Hence, thermal lensing is another reason for reducing the total cavity length (and minimise the effects of the thermal lens) as well as the reason for the water-cooling system in the Nd:YAG rod.

In the end-pumping laser the first term is predominant, and the degree of thermal lensing will hence influence the laser resonator design. The thermal lens will be calculated more precisely with the aid of the laser cavity analysis and design software LASCAD® [13] as presented in the next section.

2.4.5. Resonator stability

In paraxial optics, the laser resonator can be expressed as an ABCD matrix, and the TEM_{00} mode wave at any point "*j*" inside the cavity can be written as the complex function q [14]:

$$M = \begin{pmatrix} A & B \\ C & D \end{pmatrix} \tag{2.2}$$

and

$$\frac{1}{q} = \frac{1}{R_j} - i\frac{\lambda}{\pi\omega_j^2} \tag{2.3}$$

where M is the ray-transfer matrix for the laser resonator, R_j and ω_j are the curvature of the wavefront and the mode radius at j, respectively, and λ the wavelength.

For a laser cavity to be stable, the circulating wave at any point inside the resonator repeats itself after one roundtrip. Applying the resonator ray-transfer matrix parameters *ABCD* to the wave function:

$$\frac{1}{q} = \frac{D-A}{2B} - i\frac{\sqrt{4-(A+D)^2}}{2B} \tag{2.4}$$

The stability criteria can be expressed in terms of the matrix M as:

$$(A+D)^2 < 4 \tag{2.5}$$

Comparing (2.4) with the definition of the wave function given in (2.3) the resonator mode size at the position j inside the resonator can be obtained for the TEM_{00} mode:

$$\omega_j^2 = \frac{2B\lambda}{\pi\sqrt{4-(A+D)^2}} \tag{2.6}$$

In the case of a simple resonator composed of two spherical mirrors with radius of curvature R_1 and R_2 separated by a distance d as represented in Figure 2.14, the stability criterion is given by [14]:

$$0 \leq (1 - \frac{d}{R_1})(1 - \frac{d}{R_2}) \leq 1 \qquad (2.7)$$

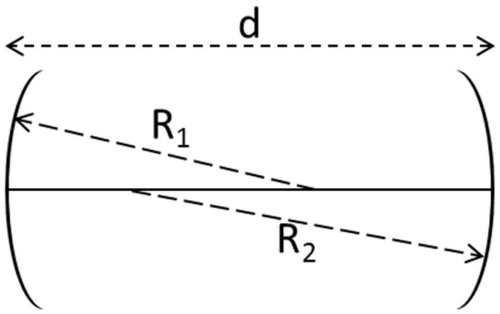

Figure 2.15 – Laser resonator composed of two spherical mirrors of radius R_1 and R_2 separated by a distance d.

And the stability diagram can be can be plotted as in Figure 2.15 (reproduced from [14]):

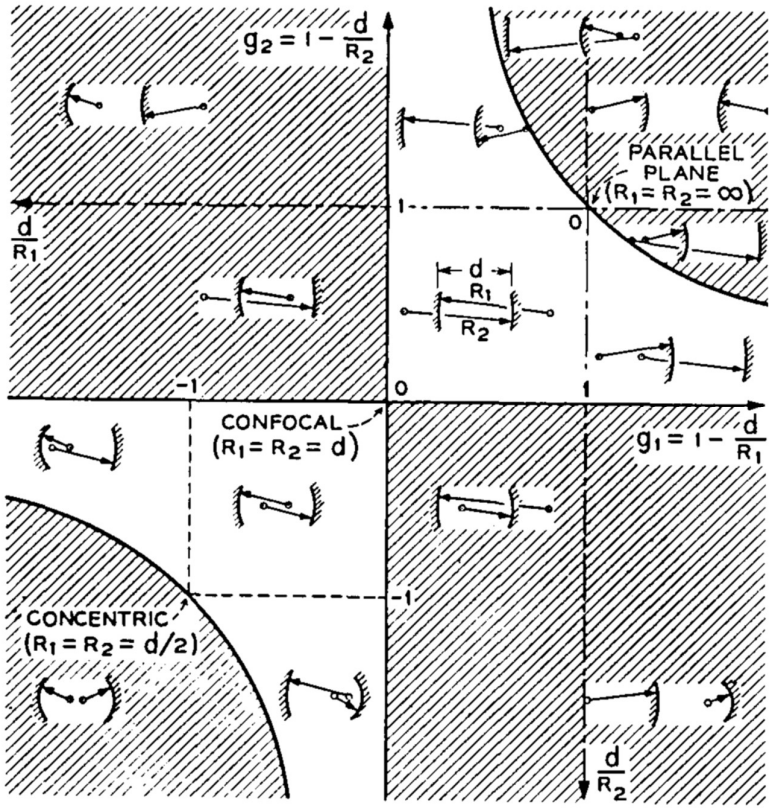

Figure 2.16 – Stability diagram. Unstable resonator systems lie in shaded regions. Reproduced from [14]

The Equation 2.7 can be generalised for a multi-element resonator [15] assuming the following form:

$$0 \leq g_1 g_2 \leq 1 \tag{2.8}$$

where $g_1 = A_1$ and $g_2 = D_2$ are the one-way elements of the *ABCD* resonator matrix.

2.4.6. Fundamental resonator design

The nonlinear crystals available for the experiments ranged from 10 – 20 mm in length along the fundamental resonator axis. With the dimensions and refractive indices of the main components defined (Nd:YAG: $length = 5$ mm, $n = 1.82$; Q-switch - quartz: $length = 40$ mm, $n = 1.45$; SPS crystal: $maximum\ length = 20$ mm, $n{\sim}2.0$), a 230 mm long plane-concave fundamental resonator was designed in the laser cavity analysis and design software LASCAD® [13]. The output coupler radius of curvature (ROC) was set at a relatively high value, 1000 mm concave, to make the alignment less sensitive than a plane-plane resonator but still without forcing the stability too much when added to the expected thermal lensing. In this configuration the resonator mode radius in the Nd:YAG crystal was around 350 μm. A thermal lens of 280 mm is estimated with Equation 2.1 for a 10 W CW diode pump power input at 808 nm. The fundamental optical cavity designed in LASCAD® with the main cavity elements are shown in Figure 2.16. In this resonator, the 280 mm EFL thermal lens was inserted close to the input face of the Nd:YAG crystal.

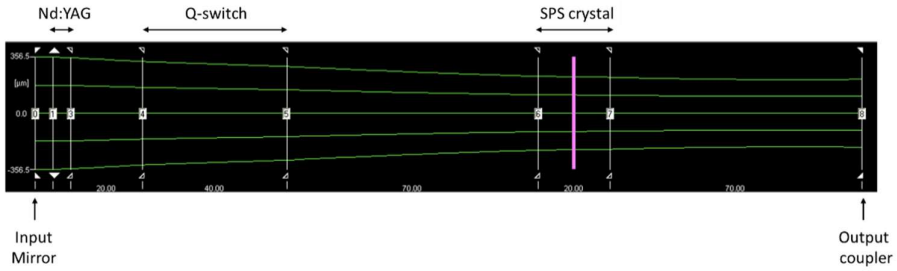

Figure 2.17 – Fundamental resonator designed in LASCAD® software with the main cavity elements highlighted. The calculated thermal lens of 280 mm EFL for a 10 W CW pump laser at 808 nm was included close to the input face of the Nd:YAG crystal.

The insertion of the different SPS crystals in the position indicated in Figure 2.16 in LASCAD® resulted in an overall mode size variation below 2% (<5 μm), and for the purposes of this experiment the intracavity energy density of the fundamental field was calculated considering the mode radius inside the SPS material (measured at the central portion of the material, as indicated by the magenta bar in the figure) to be constant at $w = 230$ μm at maximum 10 W pump.

The stability parameter for this resonator was calculated in LASCAD® and plotted in the stability diagram as shown in Figure 2.17. The calculated $g_1 g_2$ product is represented as a red cross in the plot, and as can be noted the designed resonator is situated in a comfortable position of the stability diagram even at maximum pump power.

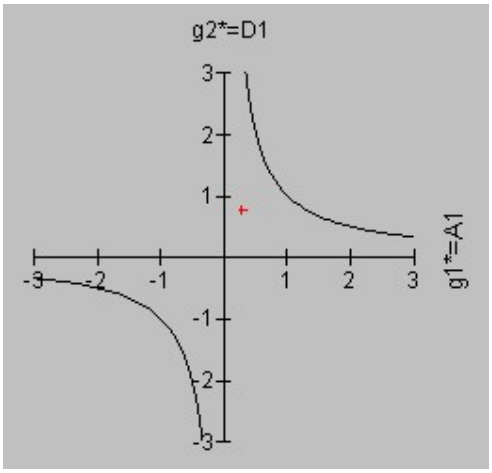

Figure 2.18 – Stability diagram for the fundamental resonator designed in LASCAD® software a calculated thermal lens of 280 mm EFL for a 10 W CW pump laser at 808 nm.

2.4.7. Diode pump scheme

The fundamental resonator was end-pumped by a continuous-wave fibre-coupled diode laser (100 μm core diameter, 0.22 NA) manufactured by LIMO (LIMO Lissotschenko Mikrooptik GmbH, LM B0018), operated at a maximum output power of 10 W. A pair of plano-convex BK-7 lenses (Thorlabs LA1131-B – EFL 50 mm and Thorlabs LA1433-B – EFL 150 mm) was responsible for collimating and re-focusing the fibre output inside the Nd:YAG, and the relative distance of the focusing lens to the active media was adjusted to match the pump spot with the resonator mode size. The measured diode pump power transmitted after the pair of lenses is plotted in Figure 2.18. This value was adopted as the diode pump input in the fundamental cavity.

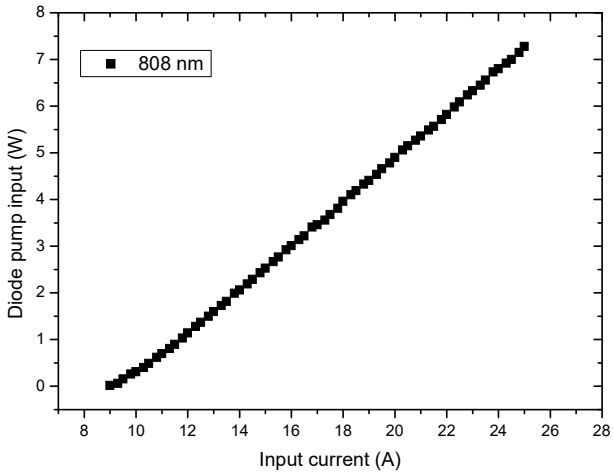

Figure 2.19 – Diode pump power transmitted after the pump lenses. This value was adopted as the diode pump input in the fundamental cavity.

2.4.8. Stokes cavity design

The resonator mode size for the Stokes radiation should match the fundamental mode inside the nonlinear crystal to maximise the SPS efficiency. A mode mismatch would decrease the efficiency for the simple reason that the fields would not be interacting in that particular region of space. An efficient way to address this issue is to build a plane-plane resonator for the Stokes cavity allowing the Stokes field to vary, following the fundamental cavity mode.

2.4.9. Laser mirrors

The laser mirrors for the 1064 nm fundamental resonator and the Stokes cavities are detailed in Table 2.5. For the fundamental cavity, the input mirror (M1) should transmit the diode pump laser at 808 nm and be high-reflective at 1064 nm. The output coupler (OC) should be high reflective at 1064 nm, confining the fundamental field to the resonator and increasing the intracavity intensity. As will be described in Section 4.2, a first OC (OC1) was utilised in the system, and competing SRS lines at 1095 nm were observed in the fundamental cavity; a new OC (OC2) was designed to be lossy at 1095 nm and produce a pure 1064 nm fundamental field. The Stokes cavity mirrors were designed to be highly reflective at the near infrared (1060 – 1100 nm), also to maximise the Stokes field intensity inside the Stokes resonator. The

Stokes mirrors had a geometrical “D-shape” (shown in Figure 2.19) to avoid clipping the fundamental field at small interacting angles. The transmission for the laser mirrors are shown in the Appendix. (The 1.3 μm laser mirrors will be described in Section 4.4.3).

Table 2.5 – Coating specification of the laser mirrors utilised in 1064 nm fundamental and Stokes resonators.

Mirror			Specification	Manufacturer
Fundamental resonator	M1		HR>99.9%@1064 nm HT>98%@808 nm	ATF
	M2	OC1	98.5%<R<99.5%@1064 nm	CVI
		OC2	98.5%<R<99.5%@1064 nm HT>40%@1090-1200 nm	LASEROPTIK
Stokes resonator	M3		HR>99.99%@1064 nm	ATF
	M4		HR>99.9%@1064 nm	VLOC

Figure 2.20 – D-shaped Stokes mirror attached to mechanical mount.

2.4.10. Fundamental resonator performance evaluation

The linear fundamental resonator was assembled without any SPS crystal intracavity and optimised with the objective of validating the initial design and to collect a baseline performance for the next experiments. A picture of the resonator with the main components highlighted is depicted in Figure 2.20 below. The output wavelength was measured at 1064.4 nm using a portable USB spectrometer (Ocean Optics HR4000), but for simplicity it will be referred to in this thesis simply as 1064 nm. The performance of the system was compared for a CW diode pump input and for a 200 Hz, 50% duty-cycle diode pump input to evaluate the effects of thermal lensing. The power transfer curves at 1064 nm for the OC1 output coupler is plotted in Figure 2.21, and the fundamental field spatial profile collected near threshold and at 6 W diode pump power are shown in Figure 2.22. (In plotting the chopped pump diode results, the diode input power value is always the instantaneous power, i.e. the power when the chopper is "open").

The power transfer performance with both pump regimes in the 1064 nm was similar, reaching threshold at 0.5 W diode pump input, and a maximum average output power of 710 mW for the CW-pump and 734 mW when the diode was chopped. However, as can be observed from Figure 2.22, when the resonator is pumped harder the spatial profile of the 1064 nm field degrades considerably, which is anticipated to affect the SPS efficiency. With a chopped diode pump, the thermal load in the system is reduced, and a uniform 1064 nm spatial profile is maintained even at high pump levels. For this reason, the THz polariton laser was always operated in chopped mode, with 200 Hz repetition rate, and 50% duty-cycle. The diode laser chopping was significantly lower than the repetition rate of the Q-switching cell to avoid any influence of the pump duty cycle on the Q-switching operation.

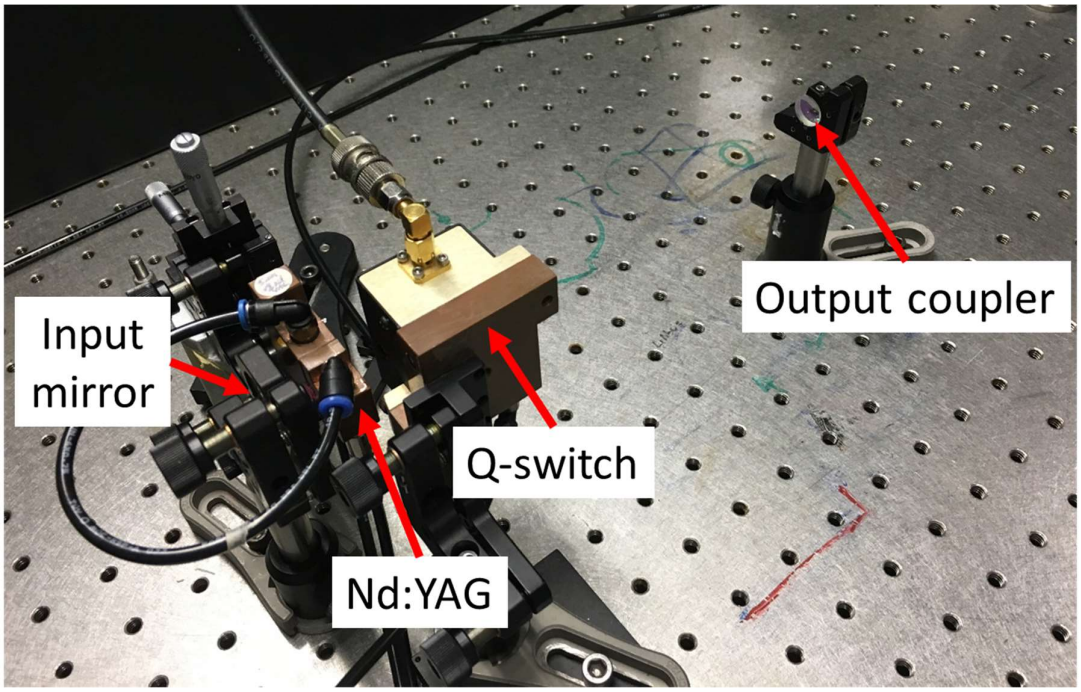

Figure 2.21 – Linear fundamental resonator without SPS crystal with main laser components highlighted.

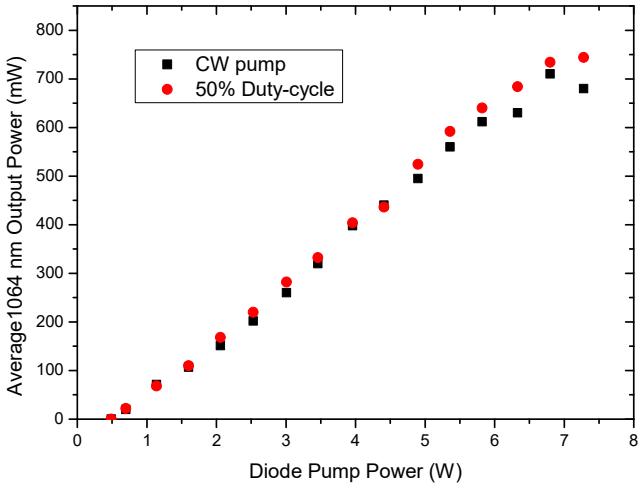

Figure 2.22 – Linear fundamental resonator power transfer without SPS crystal. Average output power at 1064 nm versus diode pump power input.

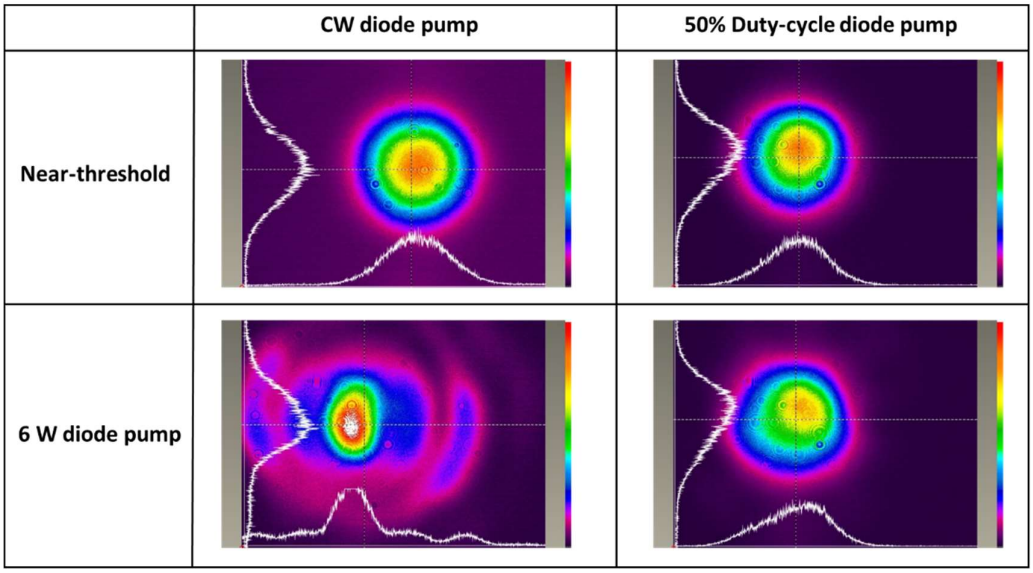

Figure 2.23 – Fundamental 1064 nm spatial beam profile near threshold and at 6 W diode pump input, for different pump regimes; (a) CW diode pump input; (b) 200Hz, 50% duty-cycle. The fundamental field profile degrades at high pump levels when system is CW-pumped. A uniform beam profile is maintained when the pump is chopped.

The maximum average output power measured from the fundamental resonator indicates a pulse energy on the order of $\frac{730\ \text{mW}}{3000\ \text{Hz}} = 243\ \mu\text{J}$ per pulse, and with the output coupling percentage of mirror M2 (0.6%), the measured fundamental pulse width of 60 ns (full-width half maximum, FWHM) and the 230 µm resonator mode radius inside the SPS crystal, a maximum integrated fluence inside the resonator can be estimated:

$$\textit{Estimated maximum integrated fluence inside the fundamental resonator}$$

$$\frac{\textit{Pulse energy} \div \textit{O.C.transmission}}{\textit{Pulse duration} \times \textit{mode area}} = \frac{243\ \mu\text{J} \div 0.6\%}{60\ \text{ns} \times \pi(230\ \mu\text{m})^2} = 400\ \text{MW/cm}^2 \quad (2.9)$$

This estimated figure for the intracavity fundamental field is well in excess of SPS threshold. A similar resonator reported by Lee *et al.* [16] reached SPS threshold at 8.2 MW/cm^2 fundamental field intensity in the MgO:LN crystal. Therefore, the performance of the designed fundamental resonator exceeded the necessary requirements to proceed with the construction of the THz polariton laser.

References

1. X. Wu, C. Zhou, W. R. Huang, F. Ahr, and F. X. Kärtner, "Temperature dependent refractive index and absorption coefficient of congruent lithium niobate crystals in the terahertz range," Opt. Express **23**, 29729–29737 (2015).

2. V. D. Antsygin, A. B. Kaplun, A. A. Mamrashev, N. A. Nikolaev, and O. I. Potaturkin, "Terahertz optical properties of potassium titanyl phosphate crystals," Opt. Express **22**, 25436–25443 (2014).

3. K. Kawase, J. Shikata, H. Minamide, K. Imai, and H. Ito, "Arrayed silicon prism coupler for a terahertz-wave parametric oscillator," Appl. Opt. **40**, 1423–1426 (2001).

4. J. Dai, J. Zhang, W. Zhang, and D. Grischkowsky, "Terahertz time-domain spectroscopy characterization of the far-infrared absorption and index of refraction of high-resistivity, float-zone silicon," J. Opt. Soc. Am. B **21**, 1379 (2004).

5. T. Ikari, X. Zhang, and H. Minamide, "THz-wave parametric oscillator with a surface-emitted configuration," Opt. Express **14**, 1604–1610 (2006).

6. D. E. Zelmon and D. L. Small, "Infrared corrected Sellmeier coefficients for congruently grown lithium niobate and 5 mol. % magnesium oxide–doped lithium niobate," J. Opt. Soc. Am. B **14**, 3319–3322 (1997).

7. E. D. Palik, *Handbook of Optical Constants of Solids Edited*, 2nd ed. (Elsevier US, 1998).

8. M. V Pack, D. J. Armstrong, and A. V Smith, "Measurement of the $\chi^{(2)}$ tensors of $KTiOPO_4$, $KTiOAsO_4$, $RbTiOPO_4$, and $RbTiOAsO_4$ crystals," Appl. Opt. **43**, 3319–3323 (2004).

9. M. Sang, J. Qiu, T. Yang, X. Lu, and W. Zhang, "Optical phonon resonance characteristics comparison of KTP and RTP crystals in terahertz time-domain spectroscopy," Chinese J. Lasers **37**, 389–393 (2010).

10. M. J. E. Golay, "Radiation detecting device," U.S. patent US2557096A (1951).

11. W. Koechner, *Solid-State Laser Engineering - 6th Edition* (Springer US, 2014).

12. T. Edwards, D. Walsh, M. Spurr, C. Rae, M. Dunn, and P. Browne, "Compact source of continuously and widely-tunable terahertz radiation," Opt. Express **14**, 1582–1589 (2006).

13. "Lascad-Software for Laser Cavity Analysis and Design," https://www.las-cad.com/.

14. T. Li and H. Kogelnik, "Laser Beams and Resonators," Appl. Opt. **5**, 1550–1567 (1966).

15. O. Svelto, *Principles of Lasers* (Springer US, 2010).

16. A. Lee, Y. He, and H. Pask, "Frequency-tunable THz source based on stimulated polariton scattering in Mg:$LiNbO_3$," IEEE J. Quantum Electron. **49**, 357–364 (2013).

3. Nonlinear materials for stimulated polariton scattering

In Chapter 1 an overview of the SPS phenomena and how it can be successfully utilised to produce frequency-tunable THz sources was provided. In this chapter a more in-depth analysis of the underlying theory is conducted, and it is applied to investigate the three nonlinear materials utilised in this research: MgO:$LiNbO_3$, KTP and RTP. When designing a THz source based on stimulated polariton scattering it is desirable to have knowledge of the polariton dispersion curve and the SPS gain for the nonlinear material; the first providing predictions about the THz frequency coverage of the source, and the second about the expected relative spectral intensity of the emitted frequencies. The calculation of these two parameters can be performed based principally on information about the SPS modes (frequency, linewidth, and oscillator strength), the dielectric function, and the second and third-order nonlinear coefficients. There is plenty of data reported for $LiNbO_3$, however this information is not completely available in the literature for MgO:$LiNbO_3$, KTP and RTP crystals. Moreover the fundamental data available are not fully satisfactory, with some data missing for some crystals, some experiments limited by instruments available several decades ago, and some lacking information about the conditions under which the data were acquired (e.g. resolution). The

difficulties in compiling all the required data from the literature to perform such calculations for the crystals motivated a specific investigation of the vibrational spectra of the samples to measure these parameters directly.

In Section 3.1 an expression is derived for the SPS gain (Stokes and THz fields) by solving the coupled wave equations for the SPS fields, and a method to calculate the dispersion curve based on Raman and FTIR spectroscopy is presented in Section 3.2. The Raman and FTIR spectra of the three nonlinear materials under investigation are collected and utilised to calculate the dispersion curve, the terahertz absorption coefficient and refractive index, as presented in Sections 3.3 to 3.5; also the Stokes gain for MgO:LN is calculated for different fundamental field intensities. The calculated dispersion relation and absorption coefficient for the terahertz field (and also the SPS gain for MgO:LN) are utilised to make predictions about the THz emission of the sources to be developed.

The value of investigating the material properties to gain insight into the operation of THz lasers based on SPS is clear. However undertaking this study was ambitious, and involves specialised physics and many complexities associated with instrumentation. While this study sheds light on aspects of the THz sources presented in Chapters 4 and 5, there is potential for it to be extended in the future.

3.1. Terahertz gain coefficient

A classical and also quantum mechanical theoretical analysis of stimulated polariton scattering was first developed by Sussman [1] for a terahertz parametric generator, and assuming SPS fields in steady-state. Three decades later the classical approach was revisited by Shikata *et al.* [2], when the classical coupled-wave equations for steady-state SPS fields were solved to obtain analytical expressions for the exponential gains for the THz and Stokes fields. The theory described here is based on these two works.

It is possible to physically interpret the SPS phenomena based on the following classical picture. The intense fundamental field polarised along the appropriate crystal axis interacts with the electron cloud of the polar crystal, displacing the electrons and inducing an electronic dipole moment (second-order nonlinearity). The electronic motion interacts with the crystal lattice, inducing molecular vibrations and an ionic dipole moment (third-order nonlinearity). The ionic-vibration couples with the electronic vibration modulating it back, and giving rise to the parametric scattering process.

3.1.1. The coupled-wave equations

Stimulated polariton scattering is an optical nonlinear process resulting from second and third order optical nonlinearities, and according to the theory in [1], four interacting electromagnetic fields are defined: fundamental $\boldsymbol{E}_f$, Stokes (or idler) $\boldsymbol{E}_S$, terahertz (or signal) $\boldsymbol{E}_T$ and the ionic vibration $\boldsymbol{Q}_0$. Assuming a steady-state and neglecting fundamental field depletion, the following coupled-wave equation can be written:

$$\left[\nabla^2 + \frac{\omega^2}{c^2}\varepsilon_T\right]\boldsymbol{E}_T = -\frac{\omega^2}{c^2}\chi_P \boldsymbol{E}_f \boldsymbol{E}_S^*$$

and (3.1)

$$\left[\nabla^2 + \frac{\omega_S^2}{c^2}\left(\varepsilon_S + \chi_R\left|\boldsymbol{E}_f\right|^2\right)\right]\boldsymbol{E}_S = -\frac{\omega_S^2}{c^2}\chi_P \boldsymbol{E}_f \boldsymbol{E}_T^*$$

where ω, ω_S, ε_T and ε_S respectively denote the terahertz and Stokes frequencies, and the nonlinear material permittivity at the THz and Stokes frequencies. The parameters χ_P and χ_R are the nonlinear susceptibilities for the parametric and Raman-like processes, respectively, and c denote the velocity of light in vacuum. The second and third-order nonlinear susceptibilities can be expressed as a function of the second and third-order nonlinear coefficients (d_E and d_Q, respectively):

$$\chi_P = d_E + \sum_j \frac{S_{0j}\omega_{0j}^2 d_{Qj}}{\omega_{0j}^2 - \omega^2 - i\omega\Gamma_{0j}}$$

and (3.2)

$$\chi_R = \sum_j \frac{S_{0j}\omega_{0j}^2 d_{Qj}^2}{\omega_{0j}^2 - \omega^2 - i\omega\Gamma_{0j}}$$

where ω_{0j} is the frequency, Γ_{0j} the linewidth and S_{0j} the oscillator strength of the j-th SPS mode. Although the nonlinear susceptibility χ_P is referred to as parametric, it also depends on

d_Q, which means it also involves a third-order nonlinearity. The nonlinear coefficient can be written as:

$$d_E = 16\pi d_{33}$$

and

$$d_Q = \left[\frac{8\pi c^4 n_f (S_{33}/L\Delta\Omega)_0}{S_0 \hbar\omega_0 \omega_S^4 n_S(\bar{n}_0 + 1)}\right]^{1/2} \tag{3.3}$$

where n_f and n_S denote the refractive indices at the fundamental and Stokes frequencies, and $\bar{n}_0 = 1/(exp[\hbar\omega_0/kT] - 1)$ is the Bose distribution function ($\hbar$ is the reduced Planck's constant, *k* the Boltzman's constant and *T* the temperature). The spontaneous Raman scattering efficiency $(S_{33}/L\Delta\Omega)_0$ is proportional to the scattering cross section, and is given by the fraction of the incident power S_{33} which is scattered into a solid angle *ΔΩ* in a path length *L* [2].

3.1.2. SPS gain

Solving the coupled equations in (3.1) the following analytical expression for the exponential gains for the terahertz and Stokes fields can be obtained [1,2]:

$$g_T = g_S \cos\beta = \frac{\alpha_T}{2}\left\{\left[1 + 16\cos\beta\left(\frac{g_0}{\alpha_T}\right)^2\right]^{1/2} - 1\right\} \tag{3.4}$$

where β is the angle between the fundamental and THz fields. The gain in the low-loss limit g_0 and the terahertz absorption coefficient α_T can be written as (in cgs units to keep the convention adopted in the source):

$$g_0 = \left(\frac{\pi\omega\omega_S I_f}{2c^3 n_f n_S n_T}\right)^{1/2} \chi_P$$

and

$$\alpha_T = 2|Imk_T| = \frac{2\omega}{c} Im\left[\varepsilon_\infty + \sum_j \frac{S_{0j}\omega_{0j}^2}{\omega_{0j}^2 - \omega^2 - i\omega\Gamma_{0j}}\right]^{1/2} \quad (3.5)$$

where k_T is the terahertz wavevector and $\varepsilon_\infty$the high-frequency component of the dielectric function.

The Stokes wave gain for lithium niobate was calculated by Sussman in [1] according to equation (3.4) for a 694 nm fundamental field having 500 MW/cm^2 intensity, and this is reproduced in Figure 3.1. The data utilised in those calculations are summarised in Table 3.1 [1]. For that particular fundamental wavelength and optical field intensity a peak gain coefficient of the order of 25 cm^{-1} was expected at around 1.5 THz (50 cm^{-1} polariton shift) for the lowest-order A_1 polariton mode in lithium niobate. At higher THz frequencies, the increase in the absorption coefficient α_T results in a decrease in the SPS gain.

Table 3.1 – Material properties of the $LiNbO_3$ A_1 modes utilised in [1] for calculating the Stokes gain coefficient according to equation 3.4.

$\boldsymbol{\omega_0}$ (cm^{-1})	$\boldsymbol{S_0}$	$\boldsymbol{\Gamma_0}$ (cm^{-1})	$\boldsymbol{(\bar{n}_0 + 1)}$	$\boldsymbol{S_{33}/L\Delta\Omega}$ (×10^6 cm^{-1}sr^{-1})	$\boldsymbol{d_Q}$ (×10^6 esu)	$\boldsymbol{\chi_R}$ (×10^{12} esu)
248	16.00	21	1.43	16.0	+1.2	5.3
274	1.00	14	1.34	4.0	-2.3	2.1
307	0.16	25	1.25	0.95	-2.8	0.3
628	2.55	34	1.05	10.2	+1.8	3.1

Other parameters:

$$\boldsymbol{\varepsilon_\infty = 4.6}$$

$$\boldsymbol{d_E = 5.28 \times 10^{-6} esu}$$

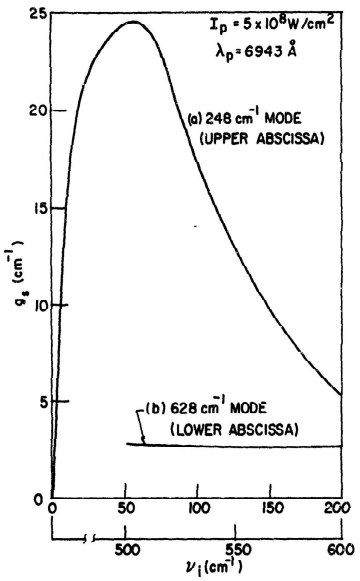

Figure 3.1 – Calculated stimulated gain coefficient g_S as a function of the terahertz frequency for the 248 cm^{-1} mode (curve a) and for the 628 cm^{-1} mode (curve b). Calculations according to equation 3.4 and with data from Table 3.1. Adapted from [1].

This theory has been extensively applied to terahertz parametric oscillators [2–6] and will also be considered valid in this thesis to describe THz polariton laser. It is important to note however that the expression obtained for the SPS gain assumes steady-state electromagnetic fields and an undepleted fundamental field, which might not necessarily be the case in the lasers described this thesis where fundamental field depletion above 50% are observed, and where energy is transferred between the various optical fields on a 1-10 ns scale. This thesis does not propose to develop new theoretical foundations for the interplay between transient SPS fields and for depleted fundamental gain, however this could be an interesting direction for the future and would be essential to make predictions about THz laser performance above threshold. Instead, despite its limitations the existing theory found to be very useful to help guide the design of experimental devices as has been found elsewhere [2,3,7]. In the next section the Stokes gain coefficient will be calculated for MgO:LN with material information extracted from the crystal samples (mode position, linewidth and oscillator strength). The same calculation could not be performed for KTP or RTP because we were unable to find the value for their third order nonlinear coefficients (d_Q) in the literature. To determine this would require calibrated measurements of the scattered Raman intensity per solid angle $(S_{33}/L\Delta\Omega)_0$ in order to obtain the Raman scattering efficiency, requiring not only

a particular infrastructure which was not readily available but also a considerable research effort that was outside the scope of this thesis.

3.2. Method used to calculate the polariton dispersion curve

The polariton dispersion curve of a candidate material for stimulated polariton scattering will dictate the frequency tuning characteristics of the terahertz output, as introduced in Chapter 1. From the dispersion relation combined with the phase matching curves, it is possible to determine the emitted THz (and Stokes) frequencies for every interacting angle between SPS fields. As will be detailed in this section, the polariton dispersion relation can be calculated with knowledge of the dielectric function of the material, which in turn depends on the frequency (ω_{0j}), linewidth (Γ_{0j}) and oscillator strength (S_{0j}) of the polariton modes. For this reason, a thorough search for these parameters in the literature was conducted for the nonlinear crystals utilised in this work (MgO:LN, KTP and RTP).

The frequency and linewidth of the polariton modes in MgO:LN can be found in [2], and the oscillator strengths for lithium niobate were determined in [1]. However, to the best of this author's knowledge, this parameter is not available for the magnesium oxide-doped crystal. For KTP, all the required information about the polariton modes were reported in [8,9], but the infrared spectrum, which is used to determine the oscillator strength, was plotted for measurements taken at 7 K from $100 - 400\ \text{cm}^{-1}$. This frequency range is important to the polariton laser, which will operate at room temperature. Therefore, it would be more appropriate to obtain this data at room temperature. The frequency of the SPS modes for RTP were reported in [10], however this author was unable to find any information about their linewidths and oscillator strengths.

Given these limitations and the lack of material data for an accurate determination of the dispersion relation for each crystal, the material properties of the nonlinear materials utilised in this work were investigated from first principles, and their vibrational spectra (spontaneous Raman and infrared reflection) were measured in order to collect a complete set of results, using the best instrumentation currently available to the experiments (see Chapter 2). With the spectroscopy results, and following a method based on [9], as described in this section, the dispersion curves for the various SPS crystals were calculated. This enabled me to make predictions on the terahertz emission characteristics for each source.

Description of the method

From the Maxwell´s equations the oscillating electric field $\boldsymbol{E}(\omega)$ and the induced polarization $\boldsymbol{P}(\omega)$ in a lossless nonlinear crystal can be written as [1]:

$$\nabla \times [\nabla \times \boldsymbol{E}(\omega)] + \frac{1}{c^2}\varepsilon_\infty \frac{\partial^2 \boldsymbol{E}(\omega)}{\partial t^2} = -\frac{4\pi}{c^2}\frac{\partial^2 \boldsymbol{P}(\omega)}{\partial t^2} \tag{3.6}$$

The induced polarization oscillating at frequency ω arises from mechanical motions in the crystal lattice, and $\boldsymbol{P}(\omega)$ can be written as:

$$\boldsymbol{P}(\omega) = \mathrm{N}e\mathbf{Q}(\omega) \tag{3.7}$$

where N is the number of primitive cells per unit of volume, *e* is the charge associated with the vibration, and $\boldsymbol{Q}(\omega)$ is the displacement from the equilibrium position of the vibrating particles. The force induced by the electric field $\boldsymbol{E}(\omega)$ can be interpreted as a driving force for a harmonic oscillation in the crystal lattice. Assuming a material with a single mode of oscillation at ω_0, this relation is given by:

$$\mu\left[\ddot{\boldsymbol{Q}}(\omega) + \Gamma_0 \dot{\boldsymbol{Q}}(\omega) + \omega_0^2 \mathbf{Q}(\omega)\right] = e\boldsymbol{E}(\omega) \tag{3.8}$$

where the damping coefficient Γ_0 is the mode linewidth, and μ is the reduced mass of the oscillating particles. Considering that the fields $\boldsymbol{E}(\omega)$, $\boldsymbol{P}(\omega)$ and $\boldsymbol{Q}(\omega)$ have an amplitude that varies exponentially as:

$$\begin{aligned} \boldsymbol{E}(\omega) &= E_0 \mathrm{e}^{\mathrm{i}(\mathbf{k}\cdot\mathbf{r}-\omega\mathrm{t})}, \\ \boldsymbol{P}(\omega) &= P_0 \mathrm{e}^{\mathrm{i}(\mathbf{k}\cdot\mathbf{r}-\omega\mathrm{t})} \end{aligned} \tag{3.9}$$

and

$$\boldsymbol{Q}(\omega) = Q_0 \mathrm{e}^{\mathrm{i}(\mathbf{k}\cdot\mathbf{r}-\omega\mathrm{t})}$$

where E_0, P_0, and Q_0 are the amplitudes of the electric field, induced polarization and displacement, respectively, equations 3.6 and 3.8 can thus be re-written respectively as:

$$\left(-k^2 + \frac{\omega^2}{c^2}\varepsilon_\infty\right)\boldsymbol{E}(\omega) = -\frac{4\pi\omega^2}{c^2}\boldsymbol{P}(\omega) \tag{3.10a}$$

and

$$\mu \times (\omega_0^2 - \omega^2 - i\Gamma_0\omega)\boldsymbol{Q}(\omega) = e\boldsymbol{E}(\omega) \tag{3.10b}$$

Replacing equation 3.10b into equation 3.7 leads to:

$$\boldsymbol{P}(\omega) = \frac{\mu \mathrm{N} e^2}{\mu \times (\omega_0^2 - \omega^2 - i\Gamma_0\omega)}\mathbf{E}(\omega) \tag{3.11}$$

Finally, substituting equation 3.11 into equation 3.10a yields an expression for the dispersion curve:

$$k^2 = \frac{\omega^2}{c^2}\left(\varepsilon_\infty + \frac{S_0\omega_0^2}{\omega_0^2 - \omega^2 - i\omega\Gamma_0}\right) = \frac{\omega^2}{c^2}\varepsilon(\omega) \tag{3.12}$$

where $S_0\omega_0^2 = 4\pi N e^2/\mu$ and $\varepsilon(\omega)$ is the dielectric function.

The result in equation 3.12 can be extended for a material with more than one transverse mode, adding one extra term for each mode ω_{0j}, and the second term on the right hand side of equation 3.12 becomes a summation over all modes [1]:

$$k^2 = \frac{\omega^2}{c^2}\left(\varepsilon_\infty + \sum_{\boldsymbol{j}} \frac{S_{0j}\omega_{0j}^2}{\omega_{0j}^2 - \omega^2 - i\omega\Gamma_{0j}}\right) = \frac{\omega^2}{c^2}\varepsilon(\omega) \tag{3.13}$$

where S_{0j} is the oscillator strength and Γ_{0j} is the linewidth of the transverse mode with frequency ω_{0j}.

Hence, to build the dispersion curve for the nonlinear crystal, it is necessary to have knowledge of its dielectric function $\varepsilon(\omega)$, which in turn depends on the position of each mode (ω_{0j}), their respective linewidth (Γ_{0j}) and oscillator strength (S_{0j}). The position and linewidth of the vibrational modes can be determined directly via Raman spectroscopy, and the oscillator strengths can be inferred from the infrared reflection spectra. The dielectric function of the material and the reflectance spectra $R(\omega)$ obtained via infrared reflection spectroscopy are related by the following equation [9]:

$$R(\omega) = \left| \frac{\sqrt{\varepsilon(\omega)} - 1}{\sqrt{\varepsilon(\omega)} + 1} \right|^2 \tag{3.14}$$

Therefore, the procedure adopted in this work to access the dielectric function and enable the construction of the dispersion curve of each nonlinear material utilised for SPS in this thesis is the following:

- Step 1 – Polarised Raman spectroscopy.
  Samples of each material were prepared and the backscattered polarised Raman spectra (configuration $Y(ZZ)\bar{Y}$) were collected, from which the mode position (ω_{0j}), and linewidth (Γ_{0j}) were determined.

- Step 2 – Polarised FTIR spectroscopy.
  The polarised Fourier-transform infrared reflection spectra ($\vec{E}//c-axis\ and\ \vec{E}\ \perp\ c-axis$) for each of the samples were collected, and the oscillator strengths(S_{0j}) for the A_1-symmetry modes were inferred from these results.

- Step 3 – Determination of oscillator strengths (S_{0j})

  With the aid of equation 3.14, and with the expression for the dielectric function $\varepsilon(\omega)$ given in equation 3.13, a Matlab® code using a genetic algorithm was built to model the FTIR spectra.

  For each material, the SPS-active A_1 mode position and linewidths input into the model were those extracted from the Raman spectra (Step 1), and the genetic algorithm adjusted the values for the oscillator strengths(S_{0j}) and the high-frequency component of the dielectric function (ε_∞) to find the best match between the nonlinear curve from the model and the experimental data. Therefore the output of the algorithm was a set of values for the oscillator strengths (S_{0j}) of the A_1-symmetry modes and the coefficient ε_∞ for that material. The Matlab® code is shown in the Appendix.

- Step 4 – The polariton dispersion curve

  In possession of the mode positions, linewidth and oscillator strengths, the polariton dispersion curve for each material was calculated according to equation 3.13.

- Step 5 – Phase-matching curves

  Together with the dispersion curve, the phase matching ("θ-curves") were also plotted on each case. The phase matching curves were calculated from the non-collinear phase matching condition for the SPS phenomena, and details on these calculations are provided in the Appendix. For each crystal, the refractive index in the near-infrared was collected from the literature (MgO:LN from [11]; KTP from [12]; RTP from [13]).

3.3. $MgO:LiNbO_3$ – Magnesium oxide-doped lithium niobate

Lithium niobate and magnesium oxide-doped lithium niobate are the most widely-used nonlinear materials in terahertz sources based on stimulated polariton scattering [2,14–18]. The increase in photorefractive resistance promoted by the MgO-doping and the much superior optical damage resistance of MgO:LN when compared to the undoped material [19] positioned magnesium oxide -doped lithium niobate as an excellent choice for an SPS medium. The advantages of the magnesium oxide doping in crystals for SPS THz sources were first investigated by Shikata *et al.* [2] when a five times increase in the THz output from a MgO:LN TPO was observed in comparison to the undoped crystal. The same research group investigated the effects of different doping percentages and identified the 5 mol% as the optimum concentration; because of an increase in lifetime of the A_1 polariton mode at 250 cm^{-1} and an increase in Raman scattering cross section [4]. Magnesium oxide-doped lithium niobate is a negative uniaxial crystal (ordinary refractive index > extraordinary refractive index; $n_o > n_e$), and belongs to the trigonal crystal system, point group 3m and R3c space group [20]. With four transverse optical A_1 modes, this SPS-active material is well suited to intracavity SPS due to its high optical damage resistance, high nonlinear coefficient and high transparency range. The main optical properties reported in the literature for 5 at.% $MgO:LiNbO_3$ are summarised in Table 3.2.

Table 3.2 - Main optical properties of 5 at.% MgO:$LiNbO_3$ extracted from the literature.

		Reference
Refractive index	2.23@1064 nm 5 – 5.2@0.4 – 1.8 THz	[11,21]
Transparency range	0.4 – 5 μm	[11]
Nonlinear coefficient	$d_{33} = 25$ pm/V@1064 nm	[22]
Laser damage threshold	2.5 J/cm^2	[23]
THz absorption	10 – 70 cm^{-1} from 1 – 2.4 THz	[2]

3.3.1. Raman and FTIR spectra of 5 at.% MgO:$LiNbO_3$

A 5 at.% MgO:$LiNbO_3$ crystal sample was prepared (*x*-cut, 5x5x25 mm^3, with optically polished side faces for THz emission; HC Photonics Corp., Taiwan) and the backscattered Raman and FTIR spectra were measured in the $Y(ZZ)\bar{Y}$ configuration with the electric field polarised parallel to the crystalline *c*-axis ($\vec{E}//c$). The Raman spectra were measured from 100 – 800 cm^{-1} with the Renishaw inVia™ confocal Raman microscope (532 nm excitation wavelength; 0.6 cm^{-1} resolution), and are plotted in Figure 3.2 with the most intense modes highlighted. The vibrational spectra in the orthogonal configuration ($\vec{E} \perp c$) were also collected for the various SPS crystals and are shown in the Appendix. The measurement configuration containing information for the THz polariton laser designed in this research is that of ($\vec{E}//c$). In this Raman spectra four A_1-symmetry modes located at 253, 268, 330 and 632 cm^{-1} can be clearly observed. The linewidth of each mode was estimated using Origin software (OriginLab, Northampton, MA) by fitting a Lorentzian curve for each individual peak, and this data are summarised in Table 3.3.

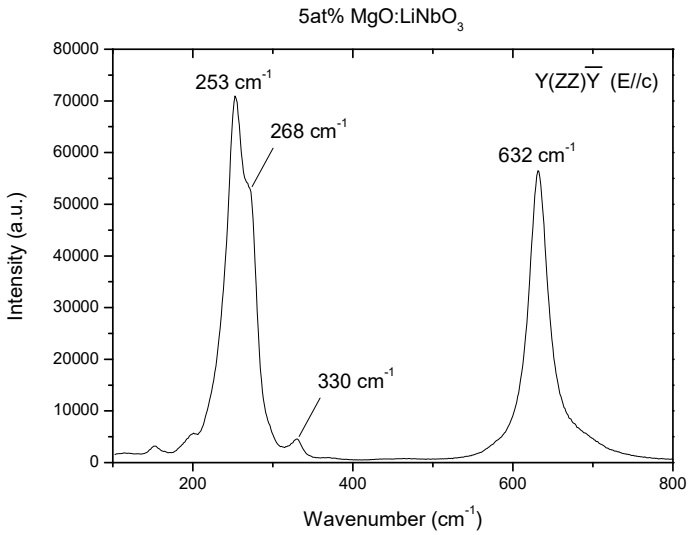

Figure 3.2 – Measured polarised Raman ($\vec{E}//c$) spectra of 5 at.% MgO:$LiNbO_3$ in $Y(ZZ)\bar{Y}$ backscattered configuration with most intense modes highlighted. Four A_1-symmetry modes located at 253, 268, 330 and 632 cm^{-1} can be clearly observed.

The FTIR spectrum of the sample was collected from 100 – 680 cm^{-1} with the Bruker Vertex 80v spectrometer (4 cm^{-1} resolution), and this is plotted in Figure 3.3 for ($\vec{E}//c$). According to the selection rules the E-mode measured at 152 cm^{-1} should not be active in this configuration [24], and it was thought the presence of this mode in the measurements could be due to a slight misalignment between the polariser-crystal axes. However, that mode could not be suppressed even after adjusting the relative angle between them in the spectrometer. A second crystal sample was also evaluated and the same feature was detected at 152 cm^{-1}. The modelling of the curve was conducted using the Matlab® code which considered only the four polariton A_1 modes (i.e. disregarding E-mode measured at 152 cm^{-1}) and is also plotted in Figure 3.3. The modelled curve is in good agreement with the measured data, and it is anticipated that the quality of the fit could be improved without the presence of E-mode at 152 cm^{-1} in the FTIR experimental data. The oscillator strengths for the A_1 modes, and ε_∞, calculated by the model are summarised in Table 3.3 and are reasonably similar to previously reported data for lithium niobate [20]. This author was unable to find corresponding published oscillator strengths for MgO:$LiNbO_3$. The uncertainties for the mode position and linewidth were estimated to be twice the resolution of the Raman spectrometer. The sensitivity of the genetic algorithm output with respect to these uncertainties was used to estimate the uncertainty for the oscillator strength.

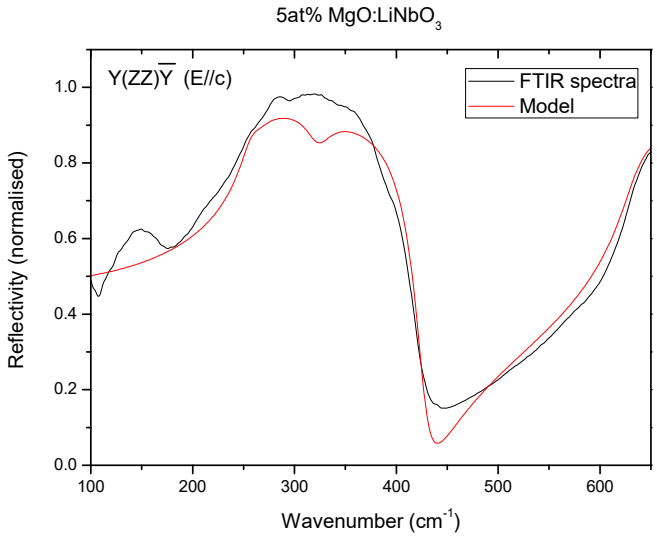

Figure 3.3 – FTIR (Fourier-transform infrared spectra) spectra of 5 at.% $MgO:LiNbO_3$ in backscattered configuration and ($\vec{E}//c$). Black line: measured data; red line: modelled data.

Table 3.3 – Location (ω_{0j}), linewidth (Γ_{0j}) (extracted from polarised Raman spectra) and oscillator strength (S_{0j}) (calculated from FTIR) of detected vibrational modes in 5 at.% $MgO:LiNbO_3$. Calculated $\varepsilon_\infty = 4.20$.

Mode location, ω_{0j} ($\pm$1 cm^{-1})	**Linewidth, Γ_{0j} ($\pm$1 cm^{-1})**	**A_1 modes oscillator strength, S_{0j} ($\pm$0.05)**
253	26	19.89
268	23	1.30
330	18	0.52
632	28	4.42

3.3.2. Polariton dispersion curve

With the data from Table 3.3 the polariton dispersion curve was calculated for MgO:LN, according to equation 3.13, as plotted in Figure 3.4 together with the phase matching "θ-curves" from $\theta = 0°$ *to* $\theta = 5°$. The intersection between the phase matching curves and the dispersion relation define the THz and Stokes frequencies that will be generated via SPS for each interacting angle between the fundamental and Stokes fields. From the dispersion relation it can be observed that for interacting angles between the fundamental and Stokes fields varying

from $\theta \sim 0.5° \; to \; \theta = 5.0°$ the terahertz field frequency would vary continuously from ~30 to 200 cm^{-1} or in Hertz from 1.0 – 6.6 THz (1068 – 1090 nm Stokes). In [2] the dispersion relation was calculated for MgO:LN for polariton frequencies below 150 cm^{-1}, and the reported values agrees with the dispersion curve calculated in this thesis with an error margin below 5%.

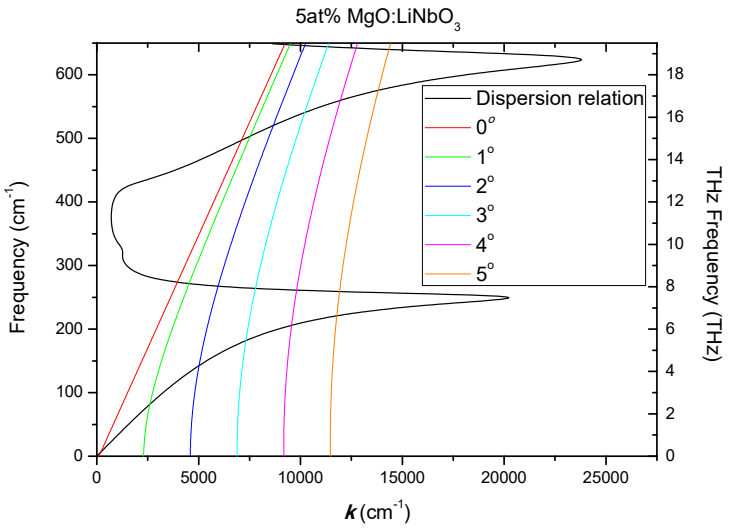

Figure 3.4 – Dispersion relation for 5 at.% MgO:$LiNbO_3$ calculated according to equation 3.13 and with input data from Table 3.3. In the same figure, the phase matching "θ-curves" are plotted for interacting angles ranging from 0º to 5º.

3.3.3. Extraordinary refractive index in the THz frequency range

The relationship between the dielectric function $(\varepsilon(\omega))$and the frequency-dependent refractive index of a material $(n(\omega))$ is given by [25]:

$$n(\omega) = \sqrt{\varepsilon(\omega)} \tag{3.15}$$

The phase matching conditions for SPS in the lasers to be developed require the propagation of extraordinary beams, and for this reason the extraordinary refractive index $(n_e(\omega))$ was calculated for the different SPS material. The extraordinary refractive index for MgO:LN was calculated from 1 – 10 THz and this is plotted in Figure 3.5. For frequencies ranging from ~1 – 4 THz the calculated refractive index increases from ~5.5 – 6.0. The

calculated values are within a 10% margin from those measured in [21] for a 6 at.% MgO:$LiNbO_3$.

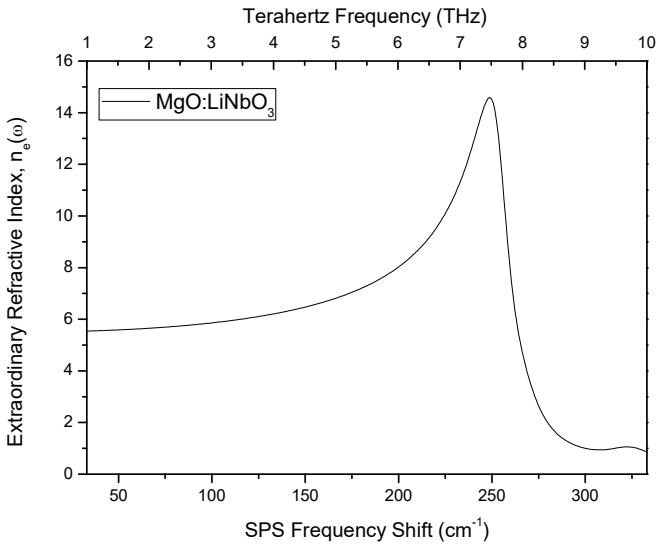

Figure 3.5 – Extraordinary refractive index calculated for 5 at.% MgO:$LiNbO_3$ from 1 – 10 THz.

3.3.4. THz field absorption coefficient (α_T) and limitations to frequency tuning

The ability to produce measurable terahertz signal will depend, among other factors, on the absorption coefficient experienced by the polariton field inside the nonlinear material. Therefore the determination of the absorption coefficient over the frequency range of interest is useful. This is particularly important in the linear configuration, in which the propagation of the THz field inside the nonlinear material is intrinsic prior to its refraction to the Si-prisms. In this work, MgO:LN was not investigated in linear configuration because this was already reported in detail in [26,27], however for completeness the absorption coefficients were calculated. There are plenty of theoretical and experimental data available in the literature for the absorption in MgO:LN below 3.0 THz [2,21,27,28]. These reports indicate calculated absorptions coefficients from ~10 – 60 cm^{-1} from 1.0 – 2.4 THz, and measured values were reported to be as high as 80 cm^{-1}. In [28] an absorption coefficient in excess of 100 cm^{-1} was measured at 3.0 THz. However this information for higher frequencies could not be found. Therefore in this work, the absorption coefficient for MgO:LN was calculated for a broader range of frequencies, from 0.5 – 4.2 THz, covering what is typically generated with intracavity

SPS sources [29,26,27], and this is plotted in Figure 3.6. Such calculations indicate absorption coefficients from ~8 – 60 cm ^{1} in the 1.0 – 2.4 THz range, and this agrees extremely well with the numbers calculated in [2]. The good agreement between the calculations for the dispersion curve, refractive index and absorption coefficient with other work reported in the literature provides confidence to the method adopted in this thesis (and the Matlab® code) to retrieve the dielectric function of the nonlinear crystals.

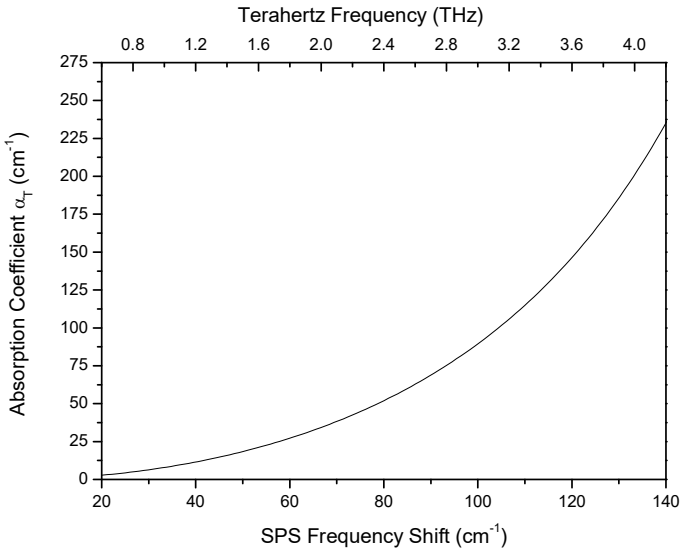

Figure 3.6 – Absorption coefficient calculated for 5 at.% MgO:$LiNbO_3$ from 0.5 – 4.2 THz. Field polarised along crystallographic *z*-axis

The significant increase in the THz absorption coefficient above 3 THz has been pointed to as the main limitation for MgO:LN to generate terahertz fields above this frequency [17], particularly in the linear configuration in which the THz field experiences an intrinsic propagation inside the nonlinear crystal. Recently, an externally pumped TPO based on MgO:LN was reported to generate frequencies as high as 5 THz [30], however not only was the relative power output at higher frequencies much smaller than those below 3 THz, but the system relied on injection-seeding for the Stokes beam, and a special scheme to tune the SPS crystal.

3.3.5. SPS Stokes field gain curve

The gain curve for the Stokes field was calculated according to equation 3.4, and given a 1064 nm fundamental field with intensities ranging from 50 to 600 MW/cm^2 (typical intensities of an experimental device [2,26,27]), and this is plotted in Figure 3.7. For these calculations the polariton mode frequency, linewidth and oscillator strength was obtained from the experimental results in Table 3.3. The second and third-order nonlinear coefficients d_E and d_Q were those presented in Table 3.1 for $LiNbO_3$ because there was no data available for the MgO-doped crystal. The complications of measuring these parameters were already highlighted in Section 3.1, and this is beyond the scope of this thesis. Nevertheless there is future work opportunity in this regard. The calculated curves predict a rapid increase in gain at low frequencies with peak THz emission increasing from ~0.6 to 1.3 THz with increasing intensity, and Stokes gain coefficients of 27 cm^{-1} at 500 MW/cm^2. At higher THz frequencies, the increase in the absorption coefficient α_T dominates and results in a decrease in the SPS gain. The values calculated here are similar to those calculated by Sussman for undoped lithium niobate (25 cm^{-1} for 500 MW/cm^2 pump at 694 nm) [1]. The gain for the THz field has already been calculated for MgO:LN for intensities as high as 300 MW/cm^2, as reported in [2]. The result of those calculations also correlates with the Stokes gain calculated here, and indicated a THz emission peak below 1 THz at room temperature, which decreased considerably towards 3 THz, the gain coefficients were calculated to be above 5 cm^{-1} at peak.

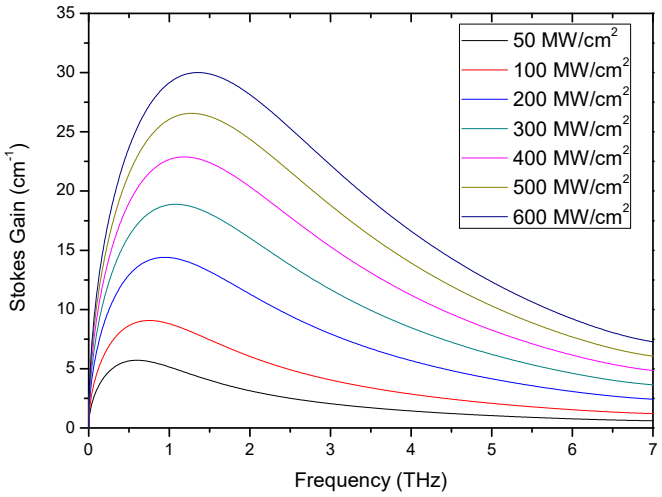

Figure 3.7 – Stimulated polariton scattering gain curve for the THz field in 5 at.% MgO:$LiNbO_3$ calculated from equation 3.4 for different intracavity energy densities.

The Stokes gain curve enables the prediction about the performance of the expected peak emission frequency, in the absence of other sources of loss. In a real device however, there are other factors that influence the SPS output which have not been considered here, such as the overlap volume between the fundamental and Stokes fields in the SPS crystal. The lowest SPS frequency emitted will generally be limited by the minimum interacting angle between the SPS fields that can be produced without clipping the fundamental field beam with the Stokes mirrors. The high-frequency emission will in turn be a compromise between the decrease in Stokes gain and also the decrease in the overlap volume of the fundamental and Stokes fields.

3.4. $KTiOPO_4$ – Potassium titanyl phosphate

Potassium titanyl phosphate is a nonlinear material which has been widely applied to different nonlinear optical processes such as second harmonic generation [31–33], sum and frequency-difference generation [34,35], parametric oscillators [36,37] and stimulated Raman scattering [38,39]. The popularity of KTP arises from the high nonlinear coefficient, high laser damage threshold and transparency range, and these properties are listed in Table 3.4. KTP is a positive biaxial crystal with orthorhombic symmetry and belongs to the point group mm2 and $Pna2_1$ space group, presenting 47 A_1-symmetry modes. This material was first reported as an SPS-active nonlinear crystal shortly before the commencement of this project (July 2014) [40], emitting terahertz radiation in the 3 – 6.5 THz range in an externally-pumped TPO configuration. However, it was never evaluated in an intracavity system which motivated its use in this research. The main optical properties of $KTiOPO_4$ available in the literature are summarised in Table 3.4. The information required to plot the dispersion relation for KTP is well documented for low-temperatures, but this is not the case for room-temperature, the condition under which this crystal will be utilised here. The Stokes gain coefficient could not be calculated due to the lack of information around the third order nonlinear coefficients (d_Q).

Table 3.4 – Main optical properties of $KTiOPO_4$ extracted from the literature.

		Reference
Refractive index	1.74 @1064 nm 3.3 – 4.6@0.3 – 2.4 THz	[12,41]
Transparency range	0.35 – 4.5 μm	[41]
Nonlinear coefficient	$d_{33} = 14.6$ pm/V@1064 nm	[22]
Laser damage threshold	>50 J/cm^2	[42]
THz absorption	<200 cm^{-1} @ 0.3 – 2 THz	[41]

3.4.1. Raman and FTIR spectra of KTP

A $KTiOPO_4$ crystal sample (x-cut, 5x5x20 mm^3, with optically polished side faces; Crystech Inc., China) was also prepared and the backscattered Raman and FTIR spectra were measured in the $Y(ZZ)\bar{Y}$ configuration ($\vec{E}//c$) . The Raman spectra was measured from 100 – 800 cm^{-1} (Renishaw inVia™ confocal Raman microscope; 532 nm excitation wavelength; 0.6 cm^{-1} resolution) and 22 Raman-active A_1 modes could be identified, as plotted in Figure 3.8. The location of these modes and their respective linewidths (determined using Origin software) are summarised in Table 3.5, and are in good agreement with previously reported results [8]. The FTIR spectrum of the sample was collected from 100 – 680 cm^{-1} (Bruker Vertex 80v; 4 cm^{-1} resolution), and is plotted in Figure 3.9 together with the modelled curve (using the same genetic algorithm used to determine the MgO:LN parameters) . The modelled curve is reasonably well-fitted to the experimental data and the calculated oscillator strengths are summarised in Table 3.5. It is important to note that the reflectivity given by equation 3.14, and the number of modes detected at lower frequency (with their respective linewidth) that builds the model, predicts a theoretical reflectivity which is more "spiky" than that measured, this being a limitation of the model at the lower frequency end of KTP. The same phenomenon was encountered in RTP.

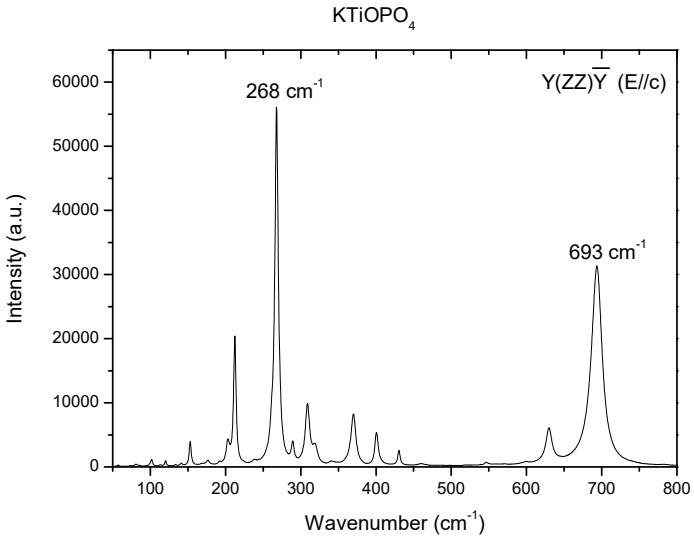

Figure 3.8 – Measured Raman spectra of $KTiOPO_4$ in backscattered configuration $Y(ZZ)\bar{Y}$. The most intense A_1-symmetry modes located at 268 and 693 cm^{-1} are highlighted.

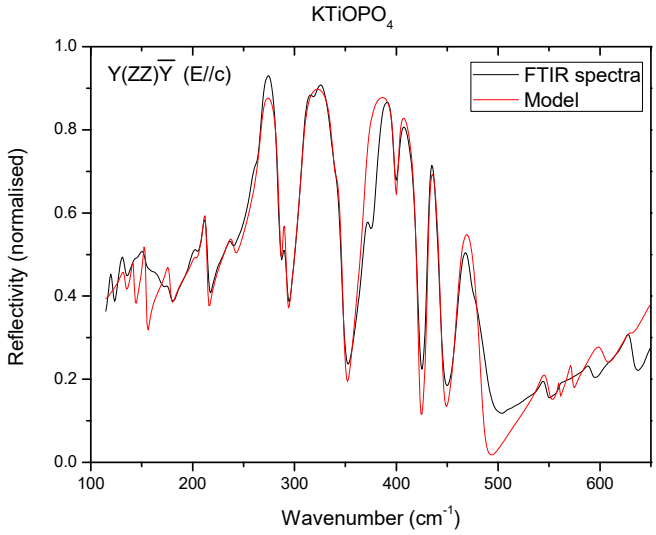

Figure 3.9 – FTIR (Fourier-transform infrared spectra) spectra of $KTiOPO_4$ in backscattered configuration and ($\vec{E}//c$). Black line: measured data; red line: modelled data.

Table 3.5 – Location (ω_{0j}), linewidth (Γ_{0j}) (extracted from polarised Raman spectra) and oscillator strength (S_{0j}) (calculated from FTIR) of detected vibrational modes in $KTiOPO_4$. Calculated $\varepsilon_\infty = 3.28$.

Mode location, ω_{0j} (±1 cm^{-1})	**Linewidth, Γ_{0j} (±1 cm^{-1})**	**A_1 modes oscillator strength, S_{0j} (±0.05)**
113	5	0.13
133	5	0.28
142	3	0.29
153	3	0.45
177	5	0.32
203	6	0.13
212	4	0.69
239	9	0.54
268	6	4.75
289	4	0.17
309	7	2.51
318	11	0.01
340	7	0.03
370	8	1.16
401	5	0.05
431	4	0.11
460	12	0.18
547	11	0.06
572	4	0.02
601	16	0.09
630	10	0.02
693	17	2.25

3.4.2. Polariton dispersion curve

The polariton dispersion curve, and the phase matching "θ-curves" from $\theta = 0° \; to \; \theta = 5°$, were calculated for KTP with data from Table 3.5, and are plotted in Figure 3.10. The modes below 100 cm^{-1} were not considered in the calculation because their oscillator strengths could not be extracted from the FTIR spectra. For the same reason, detailed predictions for terahertz emission below 3 THz could not be made with enough confidence. This represents a limitation of the modelled code for KTP and RTP because they are materials with A_1-active modes at frequencies below what was possible to measure. However, the results reported here will show that the calculated curves demonstrated to be very useful above 3 THz.

In KTP, for interacting angles varying from $\theta = 1.5 - 5.0°$ the terahertz frequency would vary from ~100 to 250 cm^{-1}, corresponding to frequencies ranging from 3.0 – 7.5 THz (1076 – 1094 nm Stokes). The presence of strong infrared absorbing A_1-modes across the angle tuning range in KTP indicate that gaps in the terahertz emission are expected. These gaps can be better comprehended with the aid of Figure 3.11, which represents an expanded view of the dispersion relation around 160 – 200 cm^{-1}. The red line in the figure represents the THz tunable range, which hops from 173 to 186 cm^{-1} around the infrared absorbing A_1-mode at 177 cm^{-1}. This behaviour was reported in externally pumped TPOs using KTP and KTA [40,43]. The terahertz emission gaps will be explored in further detail with the calculations of the absorption coefficient in the following section.

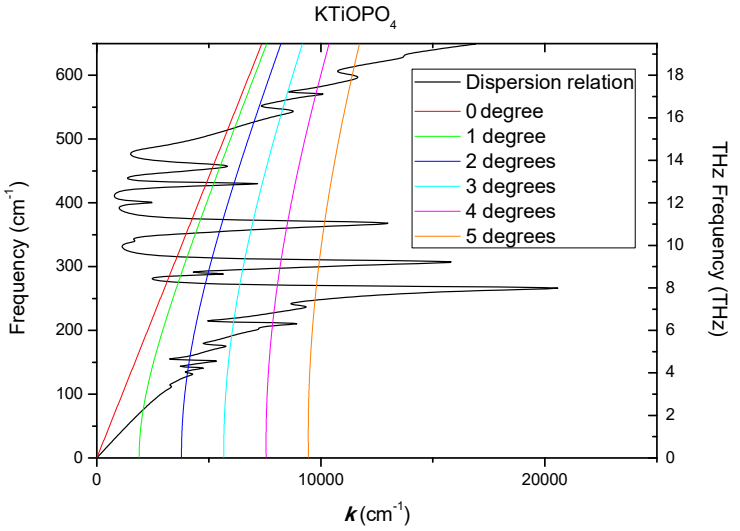

Figure 3.10 – Dispersion relation for $KTiOPO_4$ calculated with input data from Table 3.5. In the same figure, the phase matching "θ-curves" are plotted for interacting angles ranging from 0º to 5º.

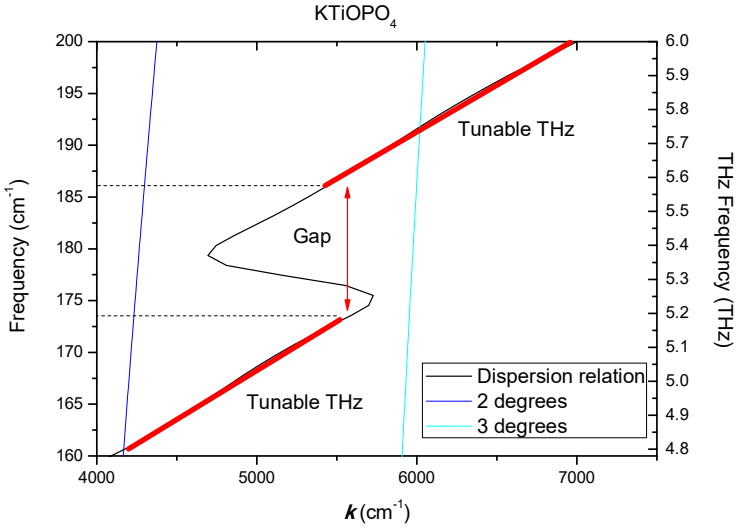

Figure 3.11 – The presence of infrared absorbing A_1-modes in the SPS tuning range leads to gaps in the THz and Stokes wavelength emission. In this example with the dispersion relation expanded around the 177 cm^{-1} mode, it is expected that the tunable THz field hops from ~173 to 186 cm^{-1} corresponding to a 5.15 – 5.55 THz gap.

3.4.3. Extraordinary refractive index in the THz frequency range

The extraordinary refractive index for KTP was calculated from 1 – 10 THz with equation 3.15, and this is plotted in Figure 3.12. Experimental measurements were reported in [41] for frequencies below 2.5 THz, and those values agrees with the calculations within a 10% error margin, even with the limitations of the model below 100 cm^{-1}.

Assuming that terahertz frequencies similar to what was reported for the externally pumped TPO (~3.0 – 6.5 THz [40]) were to be produced, the corresponding refractive indices were calculated to oscillate between 3.3 – 6.7. The non-monotonic behaviour of the refractive index is a consequence of the infrared absorbing modes across the THz tunable range.

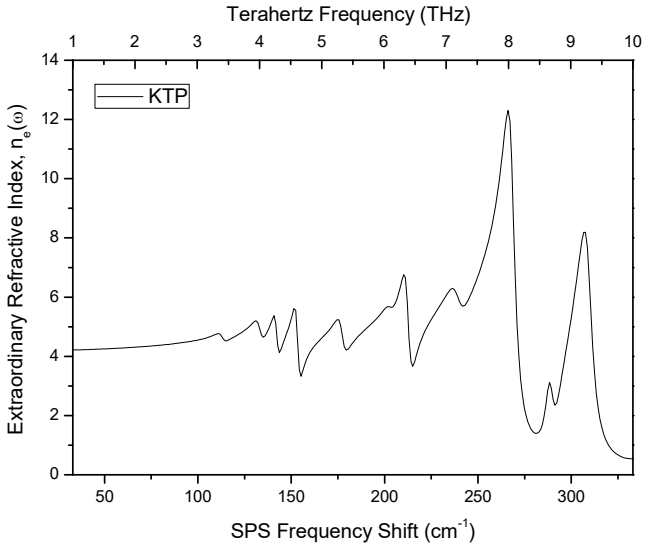

Figure 3.12 – Extraordinary Refractive index calculated for $KTiOPO_4$ from 1 – 10 THz.

3.4.4. THz field absorption coefficient (α_T) and limitations to frequency tuning

The absorption coefficient for the terahertz field (α_T) was calculated for KTP and it is plotted in Figure 3.13 in the frequency range of 1.0 – 7.5 THz. The peaks in absorption are located in the vicinity of the infrared absorbing A_1-modes measured with Raman spectroscopy and also observed in the dispersion curve. The calculated curve predicts absorption coefficients above a thousand per centimetre in most modes, and these high numbers are in accordance to what

was experimentally measured in [41] at an absorbing mode around 2.4 THz (α_T~1000 cm^{-1}). The enormous absorption coefficients across the terahertz tuning range were already reported in [40] and these promote gaps in the THz emission, as already discussed, and this relates to the balance between the THz absorption and the SPS gain described by equation 3.5. Moreover, it is anticipated that such large absorption coefficients may impose serious limitations to the terahertz extraction in the linear configuration, due to the intrinsic propagation of the THz fields inside the nonlinear crystal.

This can be investigated considering the dependence of average propagation distance for the THz field inside the crystal on the interacting angle ($d_{avg}(\theta)$), which can be estimated using simple geometry, as illustrates Figure 3.14. Considering that the fundamental and Stokes cavity modes cross at the intermediate point of the SPS crystal, a mathematical description of $d_{avg}(\theta)$ is given by equation 3.16:

$$d_{avg}(\theta) = d + r_f = \frac{L}{2} * \tan\theta + r_f \tag{3.16}$$

where L is the length of the SPS crystal, and r_f is the fundamental mode field radius.

Using equation 3.16 as an average propagation distance for every interacting angle θ ($L = 10\ mm;\ r_f = 230\ \mu m$) in conjunction with the estimated values for the absorption coefficient, it was determined the range of SPS frequency shifts above 3 THz that would allow at least 0.1% of the generated terahertz to reach the crystal side face within the expected range of interacting angles. This is represented as the shaded areas in the plot of Figure 3.13, and provides a prediction of frequencies with more potential to be detected in the linear configuration with KTP to be from 3.00 – 3.70 THz. Predictions below 3 THz were not attempted due to limitations of the model below 100 cm^{-1}. In the surface emitted configuration, every THz frequency generated via SPS inside the crystal is expected to produce photons that are successfully refracted into the air, hence being potentially detected with the Golay cell.

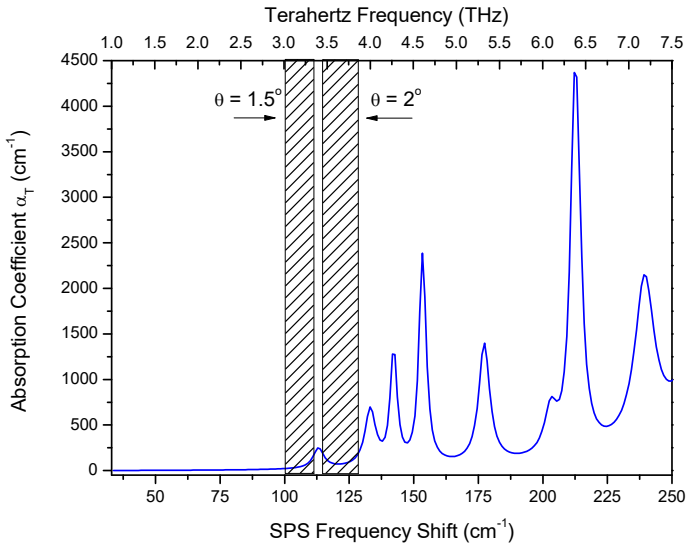

Figure 3.13 – Absorption coefficient calculated for $KTiOPO_4$ from 1.0 – 7.5 THz (field polarised along crystallographic z-axis). Shaded area corresponds to frequencies with more potential to be detected in the linear configuration, from 3.00 – 3.70 THz. In the surface emitted configuration, every THz frequency generated via SPS inside the crystal is expected to produce photons that are successfully refracted into the air, hence being potentially detected with the Golay cell.

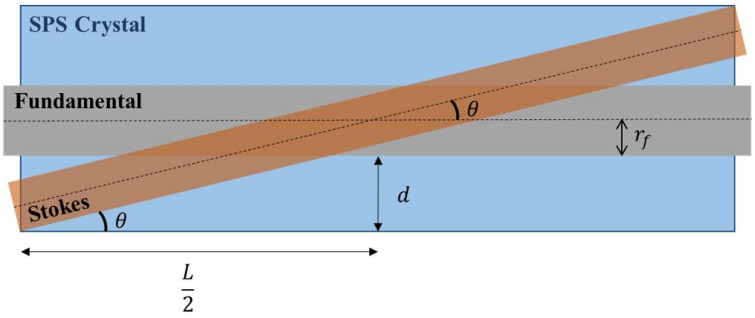

Figure 3.14 – Estimating the average propagation distance for the THz field inside the material $d_{avg}(\theta)$ for an interacting angle θ between the fundamtental and Stokes fields. The beams have been exaggerated for clarity.

It is anticipated that a more accurate prediction of the frequency-limits of each emission gap, and a better description of the system below 3 THz would be obtained with the measurements of the FTIR and Raman spectra at frequencies below 100 and 50 cm^{-1} respectively. Nevertheless, the absorption coefficients calculated here were able to inform the laser design about performance expectations, and to interpret the experimental observations in Chapters 4 and 5.

3.5. $RbTiOPO_4$ – Rubidium titanyl phosphate

Rubidium titanyl phosphate is a nonlinear material largely used in electro-optic devices and switches, due to its low-switching voltage and high laser damage threshold [44]. As an isomorph to KTP, RTP also exhibits a high nonlinear coefficient and high transparency range [45]. The combination of excellent nonlinear properties with high laser damage threshold makes RTP an attractive material for SPS, particularly in intracavity systems. Despite its great potential to generate terahertz output in the 3 – 7 THz range, RTP has not been explored for THz generation via SPS prior to this research work, and it was difficult to find substantial information about this material in the terahertz range. In this Section, the dispersion relation, refractive index and absorption coefficient are reported for RTP above 1.5 THz for the first time to the best of this author's knowledge. As will be reported in Chapter 4 and Chapter 5, this crystal yielded the highest average THz output power detected in this work. The main optical properties of RTP are listed in Table 3.6.

Table 3.6 – Main optical properties of $RbTiOPO_4$ extracted from the literature.

		Reference
Refractive index	1.77 @1064 nm 3.3 – 3.7@0.4 – 1.5 THz	[13,46]
Transparency range	0.35 – 4.5 μm	[44]
Nonlinear coefficient	$d_{33} = 15.5$ pm/V@1064 nm	[47]
Laser damage threshold	>22 J/cm^2	[42]
THz absorption	20 cm^{-1} @ 1.5 THz 150 cm^{-1} @ 1.76 THz	[46]

3.5.1. Raman and FTIR spectra of RTP

A sample of $RbTiOPO_4$ crystal was prepared (x-cut, 5x5x20 mm^3, optically polished side faces; Cristal Laser, France) and the backscattered Raman and FTIR spectra were measured in the

$Y(ZZ)\bar{Y}$ configuration ($\vec{E}//c$). The Raman spectrum was measured from 100 – 800 cm^{-1} with the Renishaw inVia™ confocal Raman microscope (532 nm excitation wavelength; 0.6 cm^{-1} resolution), and 19 Raman-active A_1 modes were identified, as plotted in Figure 3.15. The FTIR spectrum of the sample collected from 100 – 680 cm^{-1} (Bruker Vertex 80v; 4 cm^{-1} resolution) is plotted in Figure 3.16 together with the modelled curve. The modelled curve is again well-fitted to the experimental data. The mode locations, linewidths and calculated oscillator strengths are summarised in Table 3.7. The position and linewidth of the Raman modes correlates well with [10]. The oscillator strength values for RTP could not be in the literature.

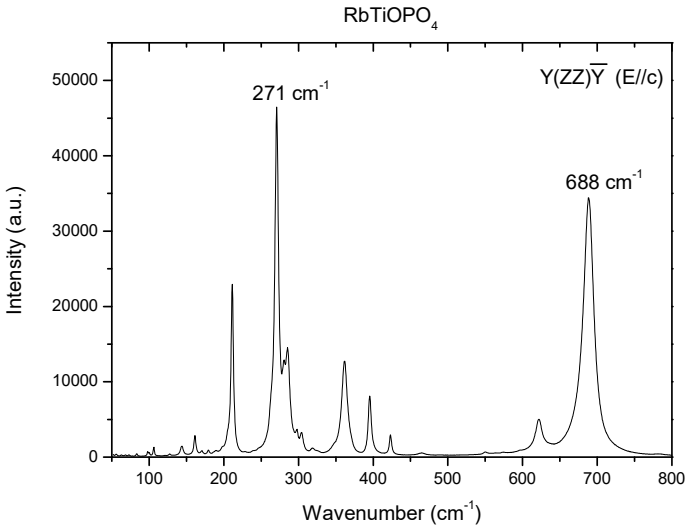

Figure 3.15 – Measured Raman spectra of $RbTiOPO_4$ in backscattered configuration $Y(ZZ)\bar{Y}$. The most intense A_1-symmetry modes located at 271 and 688 cm^{-1} are highlighted.

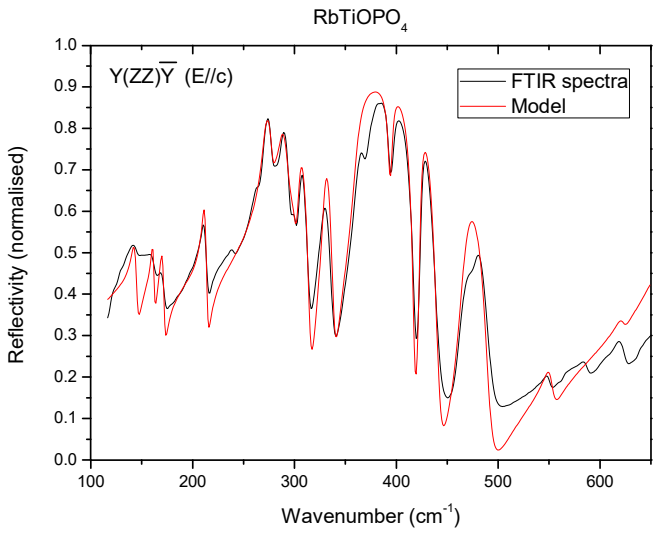

Figure 3.16 – FTIR (Fourier-transform infrared spectra) spectra of $RbTiOPO_4$ in backscattered configuration and ($\vec{E}//c$). Black line: measured data; red line: modelled data.

Table 3.7 – Location (ω_{0j}) and linewidth (Γ_{0j}) (extracted from Raman spectra) and oscillator strength (S_{0j}) (calculated from FTIR) of detected vibrational modes in $RbTiOPO_4$. Calculated $\varepsilon_\infty = 3.30$.

Mode location, ω_{0j} (± 1 cm^{-1})	**Linewidth, Γ_{0j} (± 1 cm^{-1})**	**A_1 modes oscillator strength, S_{0j} (± 0.05)**
107	2	0.11
145	3	0.31
161	3	0.75
170	4	0.43
198	8	0.01
211	4	0.67
271	6	3.71
281	8	0.53
285	8	0.70
297	12	0.30
304	6	0.31
329	6	0.62
361	9	2.06
395	5	0.06
423	4	0.10
465	12	0.27
551	10	0.06
622	9	0.04
688	17	2.35

3.5.2. Polariton dispersion curve

The polariton dispersion relation for RTP was calculated with values from Table 3.7, as plotted in Figure 3.17 together with the phase matching curves from $\theta = 0°\ to\ \theta = 5°$. Adjusting the internal angles from $\theta = 1.3°\ to\ \theta = 5.0°$ in RTP, terahertz frequencies from 3.0 – 7.5 THz (1073 – 1094 nm Stokes) may be generated. Emission gaps are also expected in RTP around the infrared absorbing A_1-modes and this will be further discussed with the calculation of the absorption coefficient in the coming section.

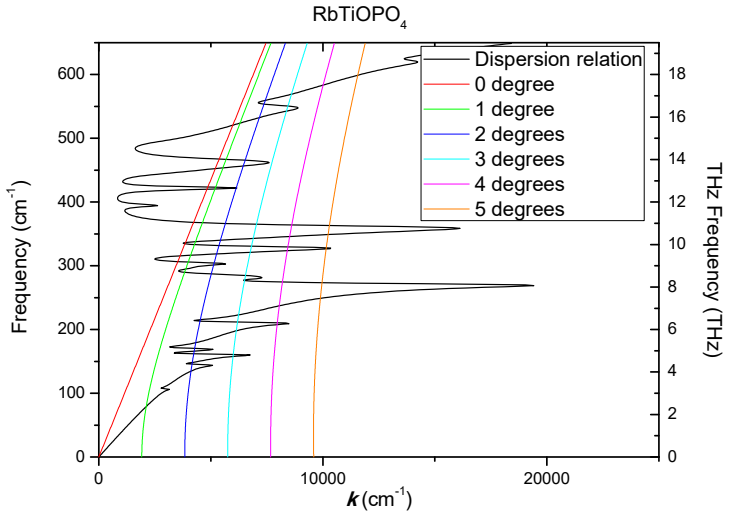

Figure 3.17 – Dispersion relation for $RbTiOPO_4$ calculated with input data from Table 3.7. In the same figure, the phase matching "θ-curves" are plotted for interacting angles ranging from 0º to 5º.

3.5.3. Extraordinary refractive index in the THz frequency range

Using equation 3.15 the extraordinary refractive index for RTP in the THz was calculated from 1 – 10 THz for the first time, and it is plotted in Figure 3.18. Experimental measurements were reported in [46] for frequencies below 1.5 THz, and the validity of a direct comparison is questionable because the values calculated at these frequencies are outside the range of frequencies measured in both FTIR and Raman spectra (<50 cm^{-1}). Nevertheless, the values calculated in this work agree with those experimental results within a 20% error margin.

In RTP considering a range of emitted THz frequencies from ~3.0 – 7.0 THz, the corresponding refractive indices were calculated to oscillate between 2.5 – 6.5. The non-

monotone behaviour of the refractive index in RTP is also a consequence of the infrared absorbing modes across the THz tunable range.

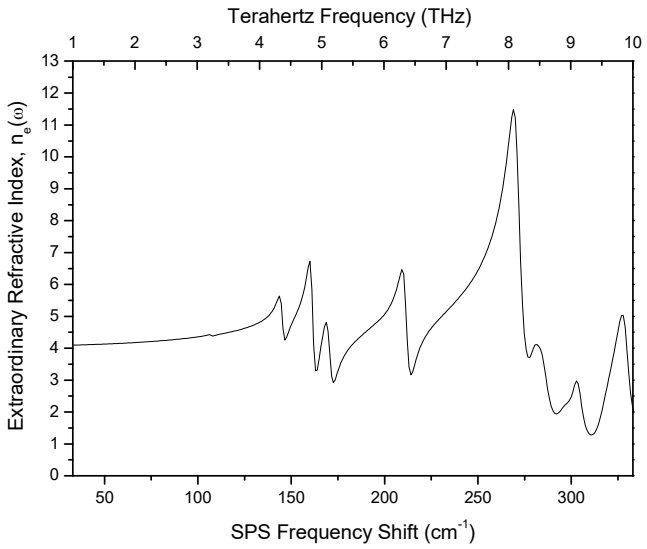

Figure 3.18 – Refractive index calculated for $RbTiOPO_4$ from 1 – 10 THz.

3.5.4. THz field absorption coefficient (α_T) and limitations to frequency tuning

The plot in Figure 3.19 shows the calculated absorption coefficient for the terahertz field (α_T) for RTP in the frequency range of 1.0 – 7.5 THz. As already predicted from the dispersion curve, there are peaks in absorption located in the vicinity of the infrared absorbing A_1-modes measured in the Raman spectroscopy at which the absorption coefficient is very high (>1000 cm^{-1}). The calculated curve predicts peak absorption coefficients even higher than those obtained for KTP, and again the comparison of these results with those reported in [46] is of limited validity due to the limitations of the spectroscopic measurements at lower frequencies. With the same considerations made for KTP, $d_{min}(\theta)$ given by equation 3.16 and frequencies above 3 THz, the plot of Figure 3.19 highlights regions within the SPS interacting region expected to allow at least 0.1% of the THz field generated in linear configuration to reach the RTP crystal's side face. In RTP, the frequencies with more potential to be detected in the linear configuration range from 3.00 to 4.15 THz. This indicates that RTP is more suitable to be used in linear geometry than KTP within the considered frequency range. In the surface emitted configuration, every THz frequency generated inside RTP via SPS is expected

to be produce photons that are successfully refracted into the air, hence being potentially detected with the Golay cell, and this will be a balance between the SPS gain and the terahertz absorption described by equation 3.5.

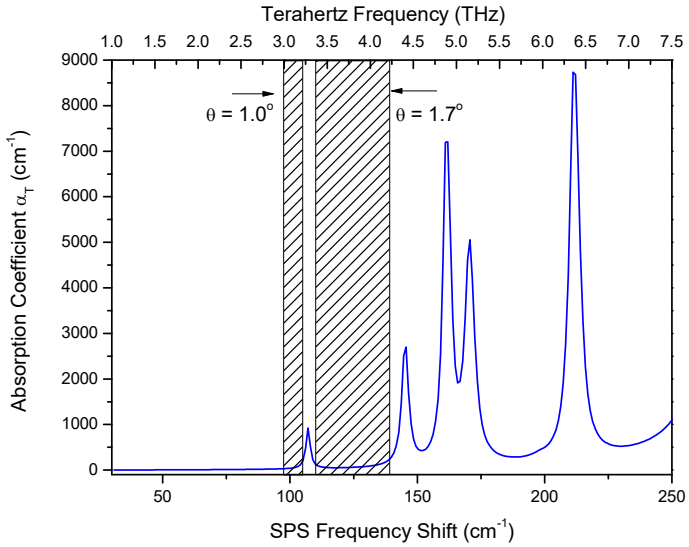

Figure 3.19 – Absorption coefficient calculated for $RbTiOPO_4$ from 1.0 – 7.5 THz (field polarised along crystallographic *z*-axis). Shaded area corresponds to frequencies with more potential to be detected in the linear configuration, from 2.30 – 4.15 THz. In the surface emitted configuration, every THz frequency generated via SPS inside the crystal is expected to produce photons that are successfully refracted into the air, hence being potentially detected with the Golay cell.

Similarly to KTP, it is important to understand a more accurate description of the system below 3 THz and also about the emission gaps in RTP that would be obtained with the measurements of the FTIR and Raman spectra at frequencies below 100 and 50 cm^{-1} respectively. Despite the fact that in this case it was limited by the instruments utilised, the calculated polariton dispersion curve still provided valuable insights to the laser design and expected THz frequency output.

Magnesium oxide-doped lithium niobate has been the material of choice for frequency-tunable THz generation via SPS in both intracavity and externally-pumped systems. The studies conducted in this chapter however revealed that other nonlinear materials such as KTP and RTP exhibit great potential to produce terahertz radiation at higher frequencies, complimentary to those typically obtained from MgO:LN. The presence of infrared absorbing A_1-modes across the SPS range of KTP and RTP are expected to produce gaps in the THz

emission. This investigation also indicated that the high-absorption coefficients resulting from these A_1-modes being across the SPS range will impose serious limitations to their use in the linear configuration. However, as will be revealed in later chapters, with careful resonator design, these crystals can be effectively used to generate THz powers and tuning ranges which eclipse what can be achieved with MgO:LN.

3.6. Chapter summary

In this chapter important material properties relevant to SPS were investigated for the different nonlinear materials utilised in this work; these materials being MgO:LN, KTP and RTP. The polarised Raman and FTIR spectra of each sample were collected in backscattered configuration $Y(ZZ)\bar{Y}$ ($\vec{E}//c$). The vibrational spectra in the orthogonal configuration ($\vec{E} \perp c$) were also collected and are shown in the Appendix. Within the limitations of the collected spectra, and the Matlab® code developed, it was possible to calculate the oscillator strengths for these SPS crystals for the first time to this author's knowledge (in the case of KTP, at room temperature) and these values are summarised in Table 3.3 for MgO:$LiNbO_3$, Table 3.5 for $KTiOPO_4$ and Table 3.7 for $RbTiOPO_4$. The material properties determined for each sample enabled the calculation of the polariton dispersion curve for each material. In the case of RTP, this was the first time the polariton dispersion curve has been calculated. The refractive index and absorption coefficient in the THz (α_T) were also calculated, and the values obtained are in excellent agreement with calculated (and experimental) values reported in the literature for MgO:LN and also experimental measurements previously reported for KTP and RTP, despite the limitations of the modelling at lower frequencies. This strong agreement provides supporting evidence and external validation of the method utilised to calculate the parameters of the A_1 polariton modes, within the context of this research. Moreover, all these material data have been compiled in a single source, which might be very useful for the SPS laser designer.

The dispersion relation for MgO:$LiNbO_3$ predicted THz emission from 1 – 6.6 THz (1068 – 1090 nm Stokes), when varying the interacting angle from $\theta \sim 0.5°$ to $\theta = 5°$, and a peak THz emission around 0.6 – 1.3 THz is expected at 50 – 600 MW/cm^2 fundamental 1064 nm field intensity. In $KTiOPO_4$ and $RTiOPO_4$ for interacting angles ranging from $\theta \sim 1.5$ to $5°$, frequency-tunable THz fields ranging from 3.0 – 7.5 THz were predicted. The existence of infrared absorbing A_1-modes below 100 cm^{-1} in KTP and RTP limited the

theoretical analysis of the systems below 3 THz. The minimum and maximum tuning angle in the real devices are also expected to be influenced, respectively, by the ability to reduce the interacting angle without clipping the fundamental beam, and the maximum angle that would still experience a sufficient overlap between the fundamental and Stokes cavity modes.

In comparison to MgO:LN the polariton dispersion curves of KTP and RTP have considerably more features. The presence of infrared absorbing A_1-modes in the expected SPS tuning range in KTP and RTP is expected to produce gaps across the THz tuning range in the vicinities of those modes (as reported in [40,43]). From the calculated absorption coefficients it was noted that the abrupt increase of the THz absorption towards the absorbing modes might impose serious limitations to the THz field extraction (and consequently the detection) in the linear configuration. Based on the calculated absorption coefficients and the minimum propagation distance inside the SPS crystal, it was estimated that the KTP crystal is likely to produce detectable THz radiation from 3.00 – 3.70 THz in the linear configuration. The same estimate was performed for RTP, which yielded wider frequency range from 3.00 – 4.15 THz, thus being more suitable for operation in linear configuration than KTP. In surface-emitted devices, photons at every terahertz frequency generated inside the material via SPS are expected to be refracted into the air, enabling detection with the Golay cell. The SPS generation will be a balance between the SPS gain and the THz absorption coefficient inside the material.

The lasers described in Chapters 4 and 5 have performance that is a consequence of the terahertz absorption coefficient and dispersion relation uncovered in this chapter.

References

1. S. Sussman, "Tunable Light Scattering from Transverse Optical Modes in Lithium Niobate," Microw. Lab. Rep. No1851, Stanford Univ. (1970).

2. J. I. Shikata, K. Kawase, K. I. Karino, T. Taniuchi, and H. Ito, "Tunable terahertz-wave parametric oscillators using $LiNbO_3$ and $MgO:LiNbO_3$ crystals," IEEE Trans. Microw. Theory Tech. **48**, 653–661 (2000).

3. S. Hayashi, K. Nawata, K. Kawase, and H. Minamide, "Terahertz parametric oscillator sources," Adv. Solid State Lasers, OSA Tech. Dig. Pap. AW2A.1. Opt. Soc. Am. (2014).

4. K. Karino, J. Shikata, K. Kawase, H. Ito, and I. Sahashi, "Terahertz-wave parametric generation characteristics of $MgO:LiNbO_3$," Electron. Commun. Japan, Part II Electron. (English Transl. Denshi Tsushin Gakkai Ronbunshi) **85**, 22–29 (2002).

5. Z. Li, P. Bing, S. Yuan, D. Xu, and J. Yao, "Investigation on terahertz parametric oscillators using GaP crystal with a noncollinear phase-matching scheme," J. Mod. Opt. **62**, 336–340 (2017).

6. M. Wu, Y. Chiu, T. Wang, G. Zhao, A. Zukauskas, F. Laurell, and Y. Huang, "Terahertz parametric generation and amplification from potassium titanyl phosphate in comparison with lithium niobate and lithium tantalate," Opt. Express **24**, 25964–25973 (2016).

7. D. Walsh, "Intracavity Terahertz Optical Parametric Oscillators," (Doctoral dissertation). University of St. Andrews (2010).

8. B. Mohamadou, G. Kugel, F. Brehat, B. Wyncke, G. Marnier, and P. Simon, "High-temperature vibrational spectra, relaxation and ionic conductivity effects in $KTiOPO_4$," J. Phys. Condens. Mattter **3**, 9849–9501 (1991).

9. G. E. Kugel, F. Bréhat, B. Wyncket, M. D. Fontana, G. Marnier, C. Carabatos-Nedelec, and J. Mangin, "The vibrational spectrum of a $KTiOPO_4$ single crystal studied by Raman and infrared reflectivity spectroscopy," J. Phys. C Solid State Phys **21**, 5565–5583 (1988).

10. J. Y. Wang, L. Li, S. Liu, Y. Liu, and J. Wei, "The inelastic light Scattering of $RbTiOPO_4$

single crystal," Ferroelectrics **132**, 197–202 (1992).

11. D. E. Zelmon and D. L. Small, "Infrared corrected Sellmeier coefficients for congruently grown lithium niobate and 5 mol. % magnesium oxide–doped lithium niobate," J. Opt. Soc. Am. B **14**, 3319–3322 (1997).

12. T. Y. Fan, C. E. Huang, B. Q. Hu, R. C. Eckardt, Y. X. Fan, R. L. Byer, and R. S. Feigelson, "Second harmonic generation and accurate index of refraction measurements in flux-grown $KTiOPO_4$," Appl. Opt. **26**, 2390 (1987).

13. J. Carvajal, P. Segonds, A. Pena, J. Zaccaro, B. Boulanger, F. Diaz, and M. Aguilo, "Structural and optical properties of $RbTiOPO_4$:Nb," J. Phys. Condens. Mattter **19**, 116214 (2007).

14. K. Kawase, M. Sato, T. Taniuchi, and H. Ito, "Coherent tunable THz-wave generation from $LiNbO_3$ with monolithic grating coupler," Appl. Phys. Lett. **68**, 2483–2845 (1996).

15. K. Kawase, M. Sato, K. Nakamura, T. Taniuchi, and H. Ito, "Unidirectional radiation of widely tunable THz wave using a prism coupler under noncollinear phase matching condition," Appl. Phys. Lett. **71**, 753–755 (1997).

16. M. Tonouchi, "Cutting-edge terahertz technology," Nat. Photon. **1**, 97–105 (2007).

17. K. Kawase, J. I. Shikata, and I. Hiromasa, "Terahertz wave parametric sources," J. Phys. D Appl. Phys **35**, R1–R14 (2002).

18. K. Kawase, J. Shikata, H. Minamide, K. Imai, and H. Ito, "Arrayed silicon prism coupler for a terahertz-wave parametric oscillator," Appl. Opt. **40**, 1423–1426 (2001).

19. Y. Furukawa, M. Sato, F. Nitanda, and K. Ito, "Growth and characterization of MgO-doped $LiNbO_3$ for electro-optic devices," J. Cryst. Growth **99**, 832–836 (1990).

20. H. E. Puthoff, R. H. Pantell, B. G. Huth, and M. A. Chacon, "Near-forward Raman scattering in $LiNbO_3$," J. Appl. Phys. **39**, 2144–2145 (1968).

21. X. Wu, C. Zhou, W. R. Huang, F. Ahr, and F. X. Kärtner, "Temperature dependent refractive index and absorption coefficient of congruent lithium niobate crystals in the terahertz range," Opt. Express **23**, 29729-29737 (2015).

22. I. Shoji, A. Kitamoto, T. Kondo, and R. Ito, "Absolute scale of the second-order nonlinear optical coefficients," J. Opt. Soc. Am. B **14**, 2268–2294 (1997).

23. Y. Furukawa, A. Yokotani, T. Sasaki, H. Yoshida, K. Yoshida, F. Nitanda, and M. Sato, "Investigation of bulk laser damage threshold of lithium niobate single crystals by Q-switched pulse laser," J. Appl. Phys. **69**, 3372–3374 (1991).

24. A. S. Barker and R. Loudon, "Dielectric Properties and Optical Phonons in $LiNbO_3$," Phys. Rev. **158**, 433–445 (1966).

25. D. Griffiths, *Introduction to Electrodynamics* (Pearson, USA, 2012).

26. T. Edwards, D. Walsh, M. Spurr, C. Rae, M. Dunn, and P. Browne, "Compact source of continuously and widely-tunable terahertz radiation," Opt. Express **14**, 1582–1589 (2006).

27. A. Lee, Y. He, and H. Pask, "Frequency-tunable THz source based on stimulated polariton scattering in Mg:$LiNbO_3$," IEEE J. Quantum Electron. **49**, 357–364 (2013).

28. L. Pálfalvi, J. Heblingj, J. Kuhl, A. Péter, and K. Polgár, "Temperature dependence of the absorption and refraction of Mg-doped congruent and stoichiometric in the THz range Temperature dependence of the absorption and refraction of Mg-doped congruent and stoichiometric $LiNbO_3$ in the THz range," J. Appl. Phys. **123505**, 1–6 (2011).

29. Y. Wang, D. Xu, H. Jiang, K. Zhong, and J. Yao, "A high-energy, low-threshold tunable intracavity terahertz-wave parametric oscillator with surface-emitted configuration," Laser Phys. **23**, 55406 (2013).

30. K. Murate, S. Hayashi, and K. Kawase, "Expansion of the tuning range of injection-seeded terahertz-wave parametric generator up to 5 THz," Appl. Phys. Express **9**, 82401 (2016).

31. T. A. Driscoll, H. J. Hoffman, R. E. Stone, and P. E. Perkins, "Efficient second-harmonic generation in KTP crystals," J. Opt. Soc. Am. B **3**, 683–686 (1986).

32. I. T. McKinnie and A. L. Oien, "Tunable red-yellow laser based on second harmonic generation of Cr:forsterite in KTP," Opt. Commun. **141**, 157–161 (1997).

33. S. V Popov, S. V Chernikov, and J. R. Taylor, "6-W Average power green light generation using seeded high power ytterbium fibre amplifier and periodically poled KTP," Opt. Commun. **174**, 231–234 (2000).

34. K. Kato, "Second-harmonic and sum-frequency generation to 4950 and 4589Å in KTP,"

IEEE J. Quantum Electron. **24**, 3–4 (1988).

35. Z. Haiyong, Z. Ge, H. Chenghui, W. Yong, H. Lingxiong, and C. Zhenqiang, "Multi-watt power blue light generation by intracavity sum- frequency-mixing in $KTiOPO_4$ crystal," Opt. Express **16**, 296–300 (2008).

36. K. Kato, "Parametric Oscillation at 3.2 μm in KTP pumped at 1.064 μm," IEEE J. Quantum Electron. **27**, 3–6 (1991).

37. R. F. Wu, P. B. Phua, K. S. Lai, Y. L. Lim, E. Lau, A. Chng, C. Bonnin, and D. Lupinski, "Compact 21-W 2-μm intracavity optical parametric oscillator," Opt. Lett. **25**, 1460–1462 (2000).

38. V. Pasiskevicius, C. Canalias, and F. Laurell, "Highly Efficient Backward Stimulated Polariton Scattering in Periodically Poled $KTiOPO_4$," Appl. Phys. Lett. **88**, 41110 (2006).

39. Z. Cong, X. Zhang, Q. Wang, Z. Liu, X. Chen, S. Fan, X. Zhang, H. Zhang, X. Tao, and S. Li, "Theoretical and experimental study on the Nd:YAG/$BaWO_4$/KTP yellow laser generating 8.3 W output power," Opt. Express **18**, 3335–3337 (2010).

40. W. Wang, Z. Cong, X. Chen, X. Zhang, Z. Qin, G. Tang, N. Li, C. Wang, and Q. Lu, "Terahertz parametric oscillator based on $KTiOPO_4$ crystal," Opt. Lett. **39**, 3706–3709 (2014).

41. V. D. Antsygin, A. B. Kaplun, A. A. Mamrashev, N. A. Nikolaev, and O. I. Potaturkin, "Terahertz optical properties of potassium titanyl phosphate crystals," Opt. Express **22**, 25436–25443 (2014).

42. F. Wagner, A. Hildenbrand, J. Y. Natoli, M. Commandré, F. Théodore, and H. Albrecht, "Laser damage investigation in $KTiOPO_4$ (KTP) and $RbTiOPO_4$ (RTP) crystals: Threshold anisotropy and the influence of SHG," Laser-Induced Damage in Opt. Mater. **6720**, 672015 (2007).

43. W. Wang, Z. Cong, Z. Liu, X. Zhang, Z. Qin, G. Tang, N. Li, Y. Zhang, and Q. Lu, "THz-wave generation via stimulated polariton scattering in $KTiOAsO_4$ crystal," Opt. Express **22**, 17092–17098 (2014).

44. A. Hildenbrand, F. Wagner, J. Y. Natoli, M. Commandré, H. Albrecht, and F. Théodore, "Laser damage investigation in $RbTiOPO_4$ crystals: A study on the anisotropy of the

laser induced damage threshold," Laser-Induced Damage in Opt. Mater. **6403**, 64031W (2006).

45. H. Albrecht, C. Bonnin, Y. Gromfeld, and M. A. Herrmann, "Characterization of $RbTiOPO_4$ crystal for non-linear and electro-optic applications," Photonics West 2006 Solid state lasers XV **6100**, 1–12 (2006).

46. M. Sang, J. Qiu, T. Yang, X. Lu, and W. Zhang, "Optical phonon resonance characteristics comparison of KTP and RTP crystals in terahertz time-domain spectroscopy," Chinese J. Lasers **37**, 389–393 (2010).

47. M. V Pack, D. J. Armstrong, and A. V Smith, "Measurement of the $\chi^{(2)}$ tensors of $KTiOPO_4$, $KTiOAsO_4$, $RbTiOPO_4$, and $RbTiOAsO_4$ crystals," Appl. Opt. **43**, 3319–3323 (2004).

4. Linear resonator polariton lasers

This chapter describes the linear resonators assembled with KTP and RTP crystals and utilising Si-prisms to out-couple the THz field. MgO:$LiNbO_3$ as an intracavity SPS crystal, having previously been studied in considerable details in the linear configuration by others at Macquarie University [1] is not described in this chapter. However it forms a basis for some of the experiments reported in this chapter and for this reason the paper by A. Lee, Y. He and H. Pask [1] is included in the Appendix. Prior to the work reported in this thesis, I reproduced those results in the laboratories to gain experience with the subtleties of the alignment and operation of these lasers.

Section 4.1 describes the assembly of the linear resonator polariton laser, so-called because each of the fundamental and Stokes resonators are in a linear layout. Section 4.2 explores competition effects between stimulated polariton scattering (SPS) and stimulated Raman scattering (SRS) which were both observed in the linear resonator. This undesired competition was investigated, and a spectral selection strategy was successfully implemented to avoid the undesired Raman scattering. The linear resonators with spectrally pure fundamental and SPS-Stokes fields are reported in Section 4.3. Wavelength-tunable Stokes radiation was measured from a resonator using KTP, indicating that strong SPS fields were being generated inside the material, however no THz field could be detected. On the other

hand, frequency-tunable THz radiation was measured from a resonator using RTP. It was the first time RTP was used for generate THz radiation and these results have been published [2]. However the range of terahertz frequencies detected from RTP was limited compared to the range of Stokes wavelengths generated inside the material via SPS. Considerable effort was devoted to understand the difficulties in measuring terahertz signal from the nonlinear materials, including a deeper analysis of the terahertz absorption coefficient around the emitted frequencies, drawing on the information in Chapter 3. Further, I constructed a fundamental resonator lasing on the 1342 nm line in Nd:YVO_4 to investigate the possibility of THz absorption in the Si-prisms (absorption by free-carriers induced by scattered near-infrared radiation).

4.1. The linear THz polariton laser

The fundamental resonator described in Chapter 2 was used as the foundation for the linear THz polariton laser. It was modified by the insertion of the nonlinear crystal and the inclusion of an additional pair of mirrors to form a separate cavity for the Stokes field. The linear THz polariton laser layout with the main cavity elements highlighted is shown in Figure 4.1. The diode end-pumped, Q-switched (3 kHz) Nd:YAG fundamental cavity has already been described in detail in Chapter 2 (see section 2.1). In the geometries assembled in this work the polarization of the 1064 nm photons must be parallel to the *z*–axis of the SPS crystal, in this respect, the Q-switch preferentially polarized the fundamental field. To minimise the intracavity losses and the cavity length, no additional polarising elements were inserted into resonator.

The Stokes cavity is formed by a pair of flat mirrors M3 (HR>99.99%@1064 nm) and M4 (HR>99%@1064 nm) separated by 85 mm, forming an external angle (θ_{ext}) with respect to the fundamental cavity axis. To avoid obstruction of the fundamental beam at small interacting angles, the Stokes mirrors were both cut with a geometrical D-shape. The external angle θ_{ext} and the interacting angle θ between the fundamental and Stokes fields inside the nonlinear crystal are related by the Snell's law of refraction:

$$\sin(\theta_{ext})n_{air} = \sin(\theta)n_{crystal} \tag{4.1}$$

where n_{air} and $n_{crystal}$ are the refractive indices of air and the nonlinear crystal, respectively.

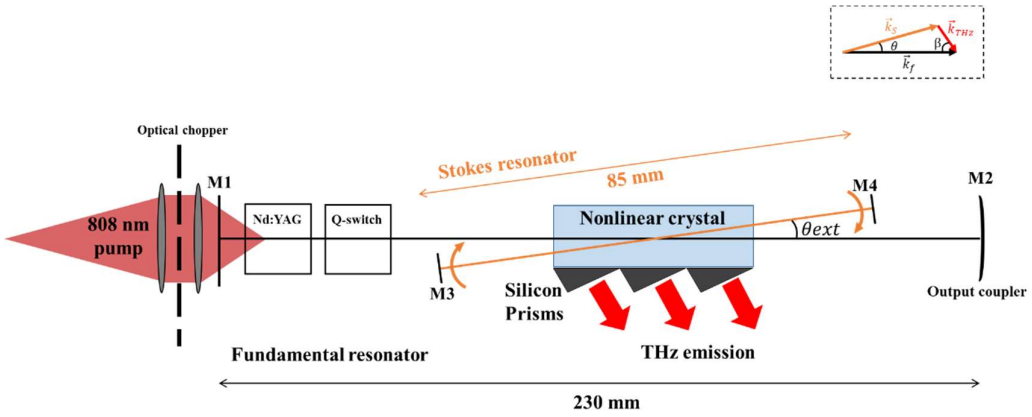

Figure 4.1 – Linear THz polariton laser resonator layout.

The Stokes cavity mirrors were mounted on a precision rotation stage (Thorlabs PR01; 5 arcmin resolution) which enabled a fine adjustment of the angle θ_{ext} between Stokes and fundamental cavities, and consequently enabled a fine tuning in the THz frequency output (Figure 4.2). The measured output powers from the fundamental and Stokes cavities are those leaking from mirrors M2 and M4, respectively.

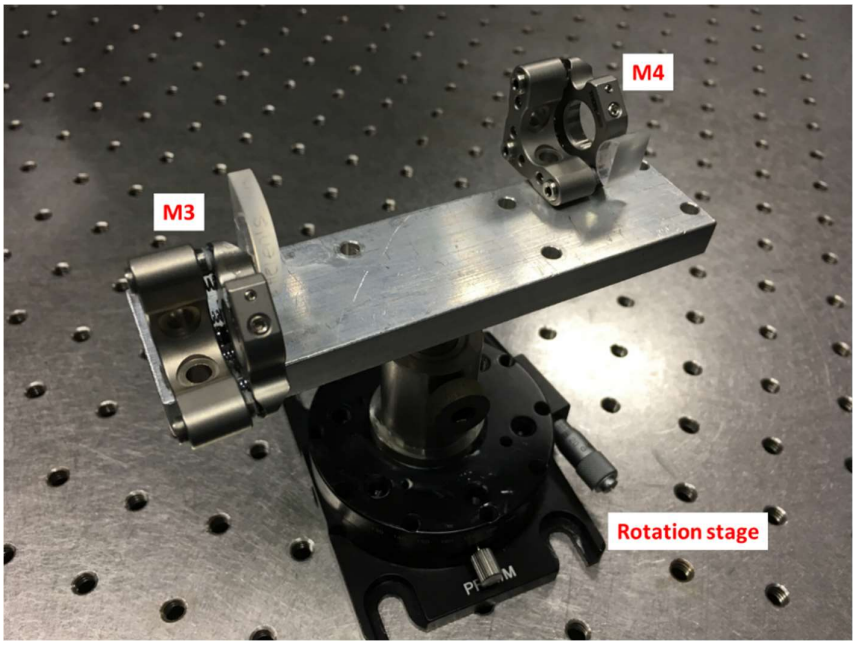

Figure 4.2 – Stokes field resonator for the linear THz polariton laser configuration. Stokes mirrors (M3 and M4) were mounted on a precision rotation stage (Thorlabs PR01) to enable fine adjustment of the interacting angle between SPS fields and, consequently, fine tuning of the THz field output frequency.

4.2. Competition effects between stimulated polariton scattering (SPS) and stimulated Raman scattering (SRS) in $KTiOPO_4$

The 1064.4 nm laser characterised in Chapter 2 (wavelength herein referred to as 1064 nm for simplicity) was developed as a platform for the linear resonators to produce the desired frequency-tunable THz radiation. However, when inserting the KTP crystal inside the fundamental field resonator, extra infrared lines at wavelengths of 1095.5 nm and 1128.6 nm were detected leaking from mirror M2 at high pump levels, as a consequence of stimulated Raman scattering (SRS) of the intense 1064 nm field. Moreover, when the Stokes cavity was aligned for SPS, additional spectral lines were measured in both fundamental and Stokes cavities, with each spectral line having a different diode pump threshold. These were identified as combinations of different SPS and SRS processes. These lines were investigated as detailed in the following subsections. The presence of such lines is detrimental to the SPS process efficiency and a new output coupler with a different optical coating was designed and used to avoid the competing Raman lines arising from the SRS process.

4.2.1. $KTiOPO_4$ crystal

As a continuation of the ongoing research at Macquarie University which started with linear resonators based on intracavity MgO:LN [1,3] operating in the 1 – 3 THz range, the first material evaluated in this research for intracavity SPS was potassium titanyl phosphate, with the main objective of extending the frequency coverage of these compact THz sources. The KTP crystal utilised in the linear resonator was an *x*-cut cuboid with dimensions of $5\times5\times20$ mm^3, and end faces anti-reflection (AR) coated from 1064 – 1100 nm (R<0.1%). The material was provided by Crystech Inc., China [4]. The side faces perpendicular to the *y*-axis were optically polished in-house to enable the attachment of silicon prisms to enable the out-coupling of the THz field. Three high-resistivity Si-prisms (geometrical dimensions: 7 mm hypotenuse x 5 mm-thick, 32/58/90º angles; as per the calculation described in Chapter 2) were attached to the KTP's side face via liquid-mediated Van der Waals bonding [5]. The image in Figure 4.3 shows the complete assembly for the SPS laser resonator in a linear configuration utilising KTP.

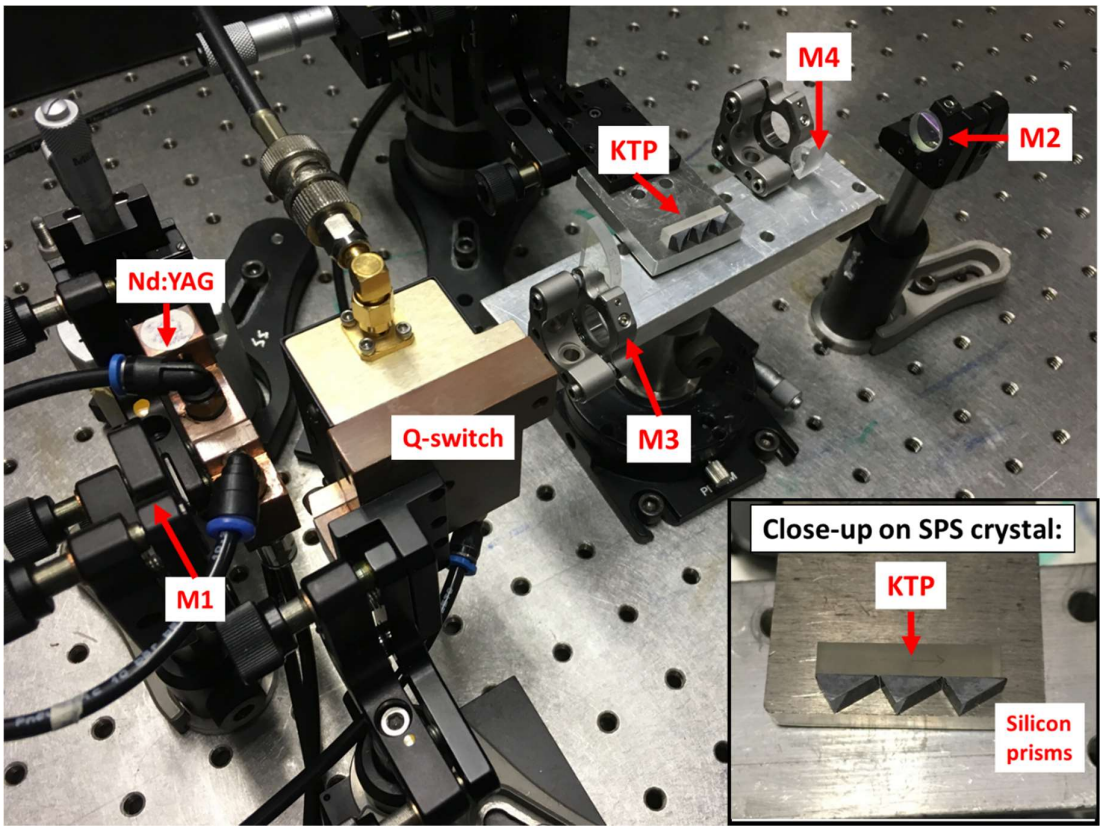

Figure 4.3 – SPS laser resonator in a linear configuration utilising intracavity $KTiOPO_4$ crystal. The inset in the lower-right shows a close-up on the crystal and the Si-prisms.

4.2.2. Evaluation of the fundamental resonator with the $KTiOPO_4$ crystal

With the Stokes mirrors misaligned, so that no SPS would occur (i.e. no SPS fields resonating), the performance of the fundamental laser with the intracavity KTP crystal was evaluated. The threshold for the 1064 nm field was reached at 0.6 W incident diode pump power (200 Hz; 50% duty-cycle); this is compared to the 0.5 W without the KTP crystal (refer to section 2.4.10). The slight increase in threshold for the fundamental field can be attributed to the additional intracavity losses introduced by the KTP crystal. At higher diode pump levels, additional spectral lines were measured in the fundamental cavity direction leaking from M2 as a consequence of stimulated Raman scattering (SRS) of the intense fundamental 1064 nm field. For diode pump powers above 2.8 W the laser output from the fundamental cavity was composed of two spectral lines, the 1064 nm radiation and a second wavelength measured at 1095.5 nm. Above 4.3 W of diode pump a second Raman shift was detected, and the spectral output of the fundamental laser was composed of a total of three lines emitted simultaneously:

1064 nm, 1095.5 nm and 1128.6 nm as shown in Figure 4.4. These lines correspond to the first-Stokes (1095.5 nm) and second-Stokes (1128.6 nm) Raman shifts of the 268 cm^{-1} mode in KTP as summarised in Table 4.1.

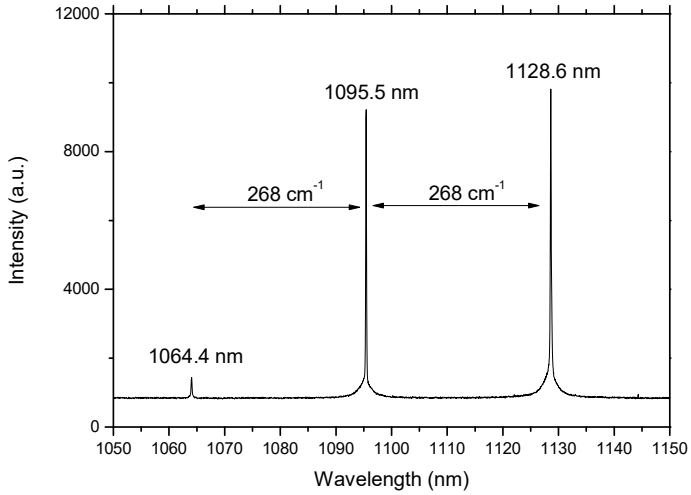

Figure 4.4 – Spectral output from the fundamental field resonator measured at 4.5 W diode pump power without SPS (i.e. Stokes mirrors misaligned). Three spectral lines were emitted simultaneously: the fundamental 1064.4 nm field, and the first and second-Stokes at 1095.5 nm and 1128.6 nm, respectively. These lines arose from the Raman shift of the 1064 nm wavelength on the 268 cm^{-1} mode. Note that the spectrum is not spectrally calibrated and in fact the 1064 nm field was significantly more intense than the other lines and had to be strongly attenuated to prevent saturation of the spectrometer.

Table 4.1 – Spectral content of fundamental resonator without SPS (i.e. Stokes mirrors misaligned). The lines at 1095.5 nm and 1128.6 nm correspond to the first and second-Stokes shift of the 1064 nm wavelength on the 268 cm^{-1} mode in KTP.

Wavelength (nm)	**Threshold (W)**	**Origin of field**
1064.4	0.6	Fundamental Nd:YAG line
1095.5	2.8	First-order Raman shift (268 cm^{-1})
1128.6	4.3	Second-order Raman shift (268 cm^{-1})

In order to better understand the energy loss from the 1064 nm field to the Raman-shifted lines, the fundamental laser was power transferred, and the spectral content was separated with the aid of a dispersive element (NIR transmission diffraction grating, 300grooves/mm; GTI25-03A, Thorlabs Inc., USA). The average output power of each line was corrected for the losses introduced by the grating, and is plotted in Figure 4.5. As can be noted from the figure, the 1064 nm laser output scales linearly with diode pump input from laser threshold to the threshold for SRS. As the system reaches threshold for SRS (2.8 W diode pump input), the 1064 nm average output power plateaus as the field is depleted by the Raman process, and the 1095 nm field scales in power. A similar process repeats when the second-Stokes shift reaches threshold at 4.3 W, with the 1095 nm field also plateauing and the energy being transferred to the 1128 nm field. The undesired SRS lines presents a strong loss for the fundamental 1064 nm field. Prior to the onset of SRS, the resonator performs similarly to what was reported in Chapter 2 (without the intracavity SPS crystal), being considered satisfactory. With the Raman effect depleting the fundamental field, however, the maximum average output power obtained from this resonator at 1064 nm decreases to less than 50% of that obtained previously in Chapter 2 at maximum diode pump power.

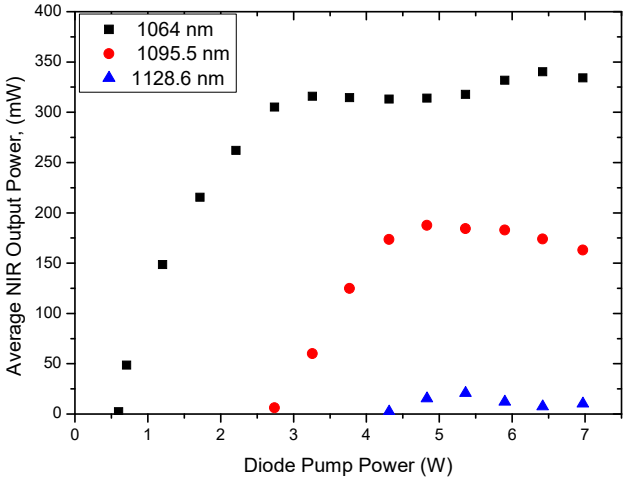

Figure 4.5 – Power transfer curve for the fundamental resonator without SPS (i.e. Stokes mirrors misaligned). The fundamental 1064 nm field saturates above 2.8 W of diode pump as a consequence of energy being transferred to the Raman process (Raman-shifted lines at 1095 and 1128.6 nm). Similarly the 1095.5 nm line saturates at ~4.5 W diode pump as it cascades to the 1128.6 nm field.

Next, the spectral content of the output from the fundamental and Stokes resonators were investigated with the Stokes resonator aligned for SPS.

4.2.3. The competing SPS and SRS fields in the $KTiOPO_4$ crystal

With the Stokes mirrors aligned, the lowest SPS threshold was reached for a 3.0 W diode pump input. In that configuration a 1086 nm Stokes field ($\theta = 3.0°$) was detected from the Stokes cavity as a result of stimulated polariton scattering. At this pump level 300 mW average power at 1064 nm were detected from mirror M2, indicating a pulse energy on the order of $\frac{300\ \text{mW}}{3000\ \text{Hz}} =$ 100 µJ per pulse. The full-width half maximum (FWHM) 1064 nm pulse width was measured to be 60 ns at SPS threshold. At the 0.6% output coupling, and considering the 230 µm resonator mode radius inside the SPS crystal (from the resonator design detailed in Chapter 2) the SPS threshold intensity can be estimated:

$$SPS\ threshold\ intensity = \frac{100\ \mu\text{J} \div 0.6\%}{60\ \text{ns} \times \pi(230\ \mu\text{m})^2} = 167\ \text{MW/cm}^2$$

It is likely that the undesired losses to the 1095.5 nm Raman shift in the fundamental resonator may influence this figure, i.e. this system may operate at lower threshold if the undesired SRS process in the fundamental resonator is suppressed. The effects of the competition between SPS and SRS could be clearly observed at higher pump levels. When the laser diode was running above 7.4 W diode pump the spectral content emanating from the Stokes cavity was composed of three laser lines, the 1086 nm SPS field and two other lines located at 1118.3 and 1153.0 nm (Figure 4.6). These extra lines in the Stokes cavity are also SPS lines, but arising from the polariton scattering of the first-Stokes (1095.5 nm) and second-Stokes fields (1128.6 nm) resonating in the fundamental cavity. The 1086 nm SPS Stokes field emitted at this particular interacting angle represents a 187 cm^{-1} shift from the 1064 nm fundamental laser, and the same frequency separation exists between 1095.5 and 1118.3 nm and between 1128.6 and 1153.0 nm.

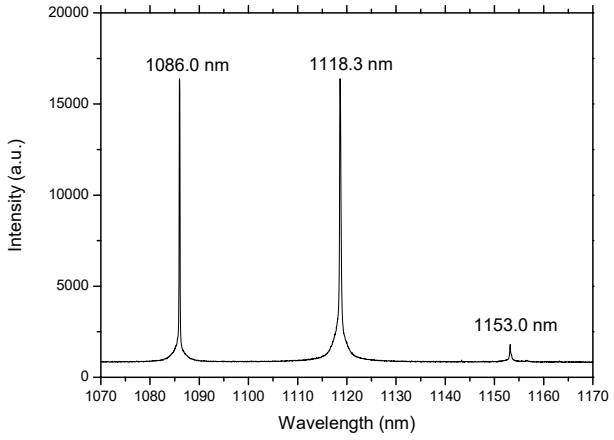

Figure 4.6 – Stokes cavity spectral content at 7.5 W diode pump input. Three Stokes lines are measured at 1086.0 nm, 1118.3 nm and 1153.0 nm corresponding respectively to SPS of the 1064.4 nm, 1095.5 nm and 1128.6 nm fields oscillating in the fundamental resonator

The SPS nature of these fields was confirmed by adjusting the Stokes cavity angle and observing the three SPS Stokes lines moving in wavelength simultaneously and always representing equivalent shifts from the 1064 nm, 1095.5 nm and 1128.6 nm lines. This behaviour can be noted from Figure 4.7. Adjusting the interacting angle from $\theta \sim 2 - 3.5°$, SPS

from the 1064 nm line produced tunable Stokes output from around 1081 – 1087 nm, and the 1095.5 nm line produced simultaneous SPS Stokes output with wavelength tunability from 1112 – 1120 nm. This corresponds to predicted THz frequencies from ~4.1 – 6.0 THz being generated inside the KTP crystal. The amount of radiation produced at the third SPS stokes line (~1153 nm) was very weak and was not present at many interacting angles, which is why it was left out of the plot. A small amount 1064 nm and 1095.5 nm radiation from the fundamental cavity was scattered and collected by the spectrometer at some angles. (To confirm that the 1064 nm and 1095 nm radiation were resonating only in the fundamental cavity, the Stokes cavity was blocked and only the SPS lines were suppressed).

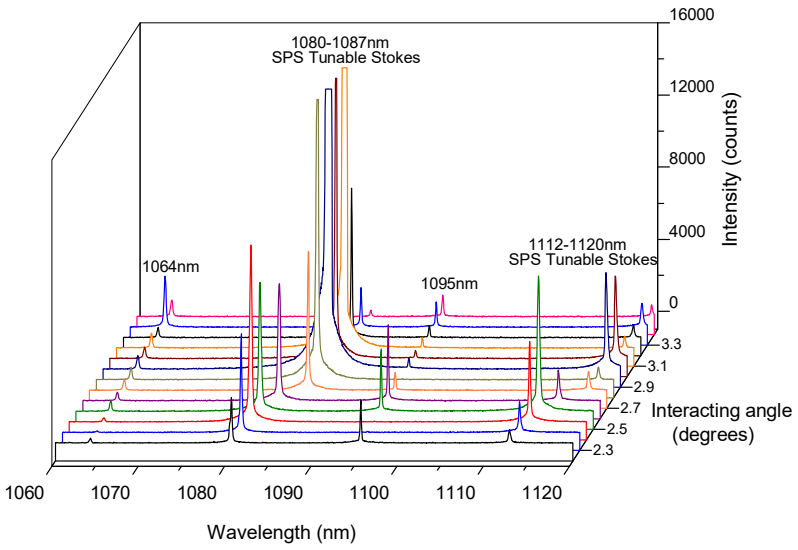

Figure 4.7 – Tuning of the SPS Stokes fields in KTP. Adjusting the interacting angle from $\theta \sim 2 - 3.5°$, SPS from the 1064 nm and the 1095.5 nm lines produced, respectively, wavelength-tunable Stokes output from 1081– 1087 nm and 1112.0 – 1120 nm, corresponding to predicted THz frequencies from ~4.2 – 6.0 THz being generated inside the KTP crystal. A small portion of scattered 1064 nm and 1095.5 nm fields from the fundamental resonator can also be noted at some particular angles.

The energy interplay between SPS and SRS fields could be more clearly comprehended with the power transfer of this system, plotted in Figure 4.8 for the fundamental and Stokes cavity fields. From this plot there is evidence of competition between the two nonlinear phenomena (SPS and SRS). The SRS represents a loss for the fundamental 1064 nm field, as already discussed. Similarly the stimulated polariton scattering phenomena can also be interpreted as a loss for the 1064 nm, but in this case it is also depleting the other fields

oscillating in the fundamental resonator giving rise to an undesired competition between these two phenomena for the 1064 nm fundamental energy. Observing the power transfer for the 1064 nm field it can be noted that the depletion is so strong that it experiences a drop in power above SPS threshold (instead of simply saturating). The 1095.5 nm field does not vanish with the onset of SPS, indicating that both phenomena coexist and SRS has sufficient gain to induce undesired losses to the 1064 nm field. From the power transfer for the polariton fields it can be noted that the 1086 nm SPS power scales linearly from SPS threshold and saturates with the appearance of the 1118.3 nm field. The 1118.3 nm field also power scales linearly and saturates when the 1153.0 nm field develops. At higher pump levels, when all three SPS fields saturate, the fundamental 1064 nm and the Raman shifted 1095.5 nm fields return to increase, indicating stronger losses to SRS. The signal at 1128.6 nm transmitted after the diffraction grating in this configuration was weak (below the noise level of the power meter) and could not be measured with confidence. The threshold for each field observed in both fundamental and Stokes cavities and their respective origin (SRS or SPS) is summarised in Table 4.2. It is worth noting that the undesired SRS competing with SPS for the 1064 nm energy caused instabilities in both laser resonators and fluctuations in power of the fundamental, SRS and SPS fields. Clearly this competition is both complex and undesired.

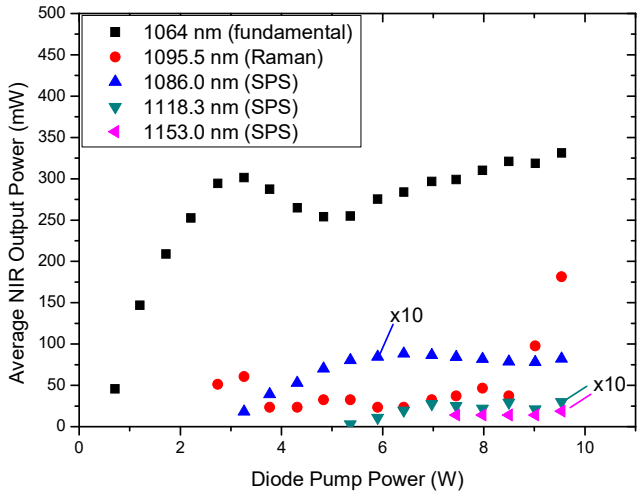

Figure 4.8 – Power transfer curve for fields oscillating in the fundamental and Stokes cavities. Fundamental cavity fields: 1064 nm (fundamental) and 1095.5 nm (first-order Raman). Stokes cavity fields magnified 10 times (polariton fields): 1086 nm, 1118.3 nm and 1153.0 nm.

Table 4.2 – Spectral content of fundamental and Stokes resonators with respective oscillation threshold when angle between the resonators was $\theta = 3.0°$ in KTP. At this interacting angle the predicted SPS shift in KTP is 187 cm^{-1}. The Raman shift is at 268 cm^{-1}.

	Wavelength (nm)	Threshold (W)	Origin of field
Fundamental cavity fields	1064.4	0.6	Fundamental Nd:YAG line
	1095.5	2.8	First-order Raman shift (268 cm^{-1})
	1128.6	4.8	Second-order Raman shift (268 cm^{-1})
Stokes cavity fields	1086.0	3.0	SPS of 1064 nm (187 cm^{-1})
	1118.3	5.3	SPS of 1095.5 nm (187 cm^{-1})
	1153.0	7.5	SPS of 1128.6 nm (187 cm^{-1})

4.2.4. Suppression of the undesired SRS fields with an intracavity etalon

The competition between SPS and SRS is detrimental to the laser performance with regards to the THz generation from the SPS process. The presence of undesired Raman shifts represents substantial losses for the fundamental field and instabilities in the SPS Stokes field output, and hence the stimulated Raman scattering phenomena should be suppressed. SRS in this system is enabled by the high reflectivity of the fundamental resonator mirrors at wavelengths corresponding to the first and second Stokes SRS shifts (R>99% at 1095 and 1128 nm) that would resonate both 1095 nm and 1128 nm fields.

To suppress the SRS process, it is essential to introduce loss at the first and second Stokes wavelengths. For this reason an etalon was inserted in the fundamental resonator to suppress the Raman fields and evaluate the expected benefits to the polariton scattering. The etalon is an optical element containing two plane-parallel interfaces that acts as a Fabry-Pérot cavity, and the spectral transmission of this cavity will depend primarily on the etalon's thickness, refractive index, and transmission spectra [6]. Therefore with an intracavity etalon it is possible to induce losses to the Raman fields yet maintain a good transmission at 1064 nm inside the fundamental resonator. The etalon utilised in this experiment was selected among a limited collection available in the laboratory, and was a 250 μm-thick fused silica substrate with 30%

reflectivity (410 GHz free spectral range; 167 GHz bandwidth; Finesse = 2.5). The etalon transmission curve versus the tilt angle with respect to the cavity axis (ϕ) can be calculated with the following equation [7]:

$$T = \frac{(1-R)^2}{1 + R^2 - 2Rcos\left[\left(\frac{2\pi}{\lambda}\right) * 2nt * cos\phi\right]} \tag{4.2}$$

where R is the reflectivity of the etalon, n is the refractive index of the etalon substrate, t the etalon thickness and λ the wavelength.

This is plotted in Figure 4.9 for the 1064 nm fundamental laser and the undesired Raman lines, and it shows that it is possible to selectively introduce losses to the Raman lines whilst maintaining high transmission at 1064 nm. The etalon was inserted in the fundamental resonator mounted on an opto-mechanical stage with angle adjustment (fine tuning in the transmission spectra of the etalon can be obtained with angle-tuning). The resonator was optimised with the intracavity etalon, and the etalon angle was adjusted to suppress any undesired Raman fields (tilt angle <5º to minimise walk-off losses). The power transfer curve for both fundamental and Stokes cavities was collected as plotted in Figure 4.10. With the intracavity etalon in the fundamental resonator the system produced a pure 1064 nm field. As a consequence, when the Stokes cavity was unblocked a pure SPS field at 1086 nm was detected from that resonator. In this configuration, the SPS phenomena is the only nonlinear phenomena responsible for depleting the 1064 nm field [1,8] generating a single Stokes radiation wavelength, with no competing SRS or SPS lines being generated.

The power transfer was first conducted with the Stokes cavity blocked (i.e. no SPS), and is labelled as undepleted 1064 nm. The depleted 1064 nm field is the output power at 1064 nm with the Stokes cavity unblocked, and consequently the SPS process active. In this case, the 1064 nm is depleted because part of its energy is being lost to the SPS process, decreasing the fundamental output power.

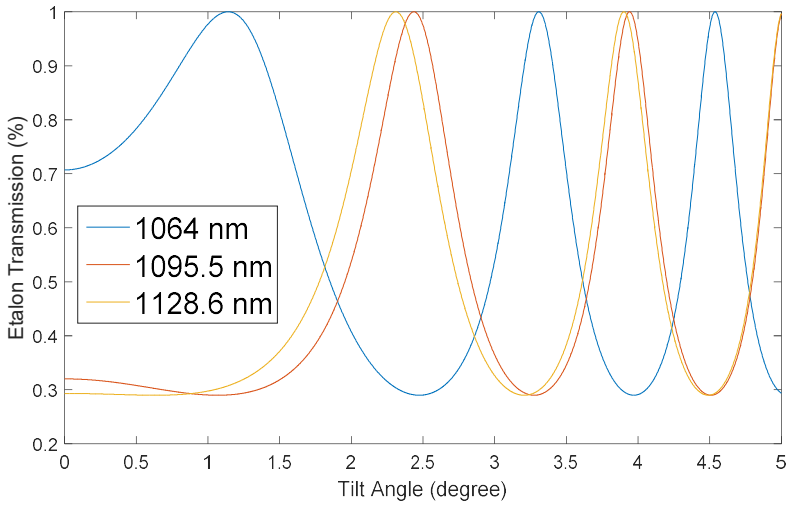

Figure 4.9 – Etalon transmission curve (250 µm-thick fused silica substrate with 30% reflectivity) versus tilt angle for 1064 nm, 1095.5 nm and 1128.6 nm. The transmission curve shows that it is possible to adjust the etalon angle to introduce selective losses to the undesired Raman lines whilst maintaining a high transmission for the 1064 nm fundamental field.

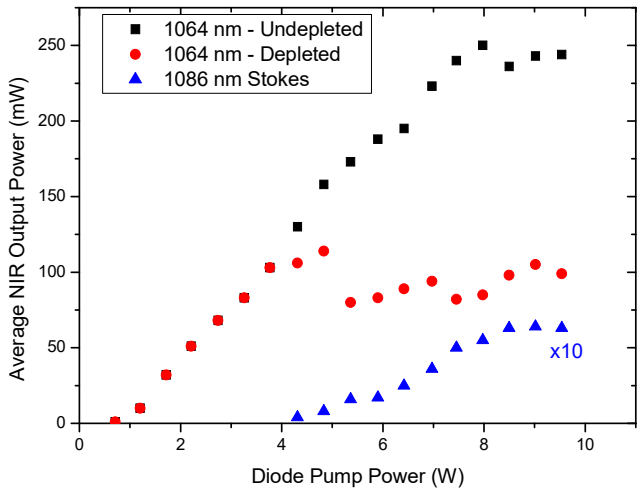

Figure 4.10 – Power transfer curve for fields oscillating in the fundamental and Stokes cavities with the intracavity etalon inserted into fundamental resonator. A pure 1064 nm field resonates in the fundamental cavity and a pure SPS field at 1086 nm (magnified 10x) resonates in the Stokes cavity. Increase in fundamental and SPS thresholds are attributed to increase in intracavity losses from the etalon.

The system reached 1064 nm threshold at 0.71 W diode pump power and SPS threshold at 4.2 W, and this increase in thresholds to the previous 3.0 W is due to the additional intracavity losses introduced by the etalon. These include walk-off losses and other factors such

as etalon flatness, coating quality and cleanliness. However, despite the higher diode pump power there was a decrease in the intracavity intensity required to achieve SPS threshold. Considering the measured fundamental output power (~125 mW) and pulse width (60 ns FWHM) at SPS threshold, the estimated intracavity intensity with the intracavity etalon is 69 MW/cm^2, less than half the value required when the competing SRS was present.

As anticipated, the suppression of the undesired wavelengths with the use of an etalon is an effective technique to produce pure fundamental and SPS fields. The intracavity etalon was useful to validate the concept, however the increase in intracavity losses introduced by this additional element is not desirable for the intracavity THz polariton laser. To this end, it was explored the use of a custom designed mirror which maintained reflectivity at the fundamental wavelength and was lossy at the undesired SRS Stokes wavelength.

4.2.5. Suppression of the undesired SRS fields with an optimised end mirror

A pure fundamental laser at 1064 nm is expected with a narrower-band coating on at least one of the fundamental cavity mirrors M1 or M2, having the specification for high reflectivity at 1064 nm but sufficient transmission at 1095 and 1128 nm. Therefore a new coating for the output coupler (mirror M2) was specified to be high reflective at 1064 nm (98.5%<R<99.5%) and transmissive for the Raman fields (T>40% from 1090 – 1200 nm) and supplied by Laseroptik GmbH, Germany. The new M2 mirror (1000 mm ROC; R = 99.4%@1064 nm; T>40% from 1090 – 1200 nm) was inserted in the fundamental laser cavity. The fundamental resonator was power transferred with the Stokes cavity blocked (i.e. no SPS fields), as plotted in Figure 4.11. Threshold for the 1064 nm field was obtained at 0.6 W, and a maximum average output power in excess of 550 mW was detected. The slight increase in threshold and the small decrease in maximum output power when compared to the resonator without the KTP crystal (Chapter 2) can be attributed to the reflection and absorption losses introduced by the nonlinear material. At this maximum output power, the measured laser pulse width (60 ns FWHM at maximum pump), and the output coupling percentage (0.6%) indicate intracavity intensities in the order of 300 MW/cm^2 are being generated, which are well in excess of SPS threshold.

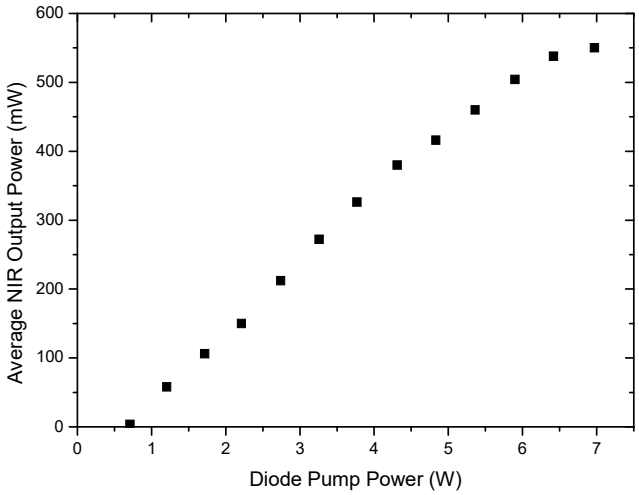

Figure 4.11 – Power transfer curve for the pure 1064 nm fundamental cavity field with the new output coupler with high transmission from 1090-1200 nm.

The spectral output confirmed that a pure 1064 nm field was being generated across the entire power transfer curve, as can be noted from the spectral output from the fundamental cavity at 7 W diode pump shown in Figure 4.12.

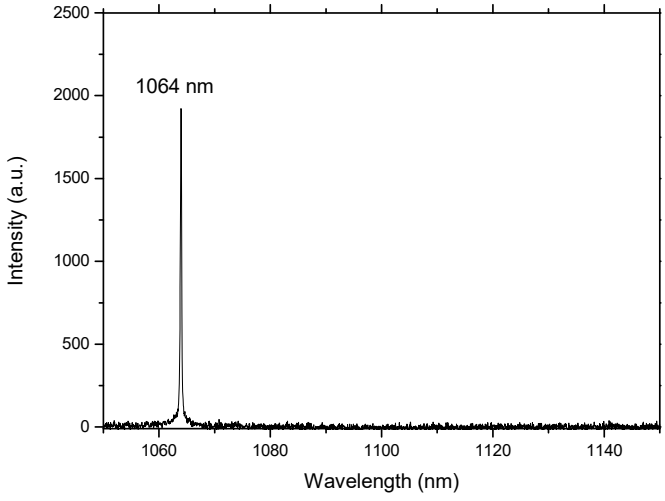

Figure 4.12 – Spectral content of the fundamental cavity at 7 W diode pump exhibiting a pure 1064 nm field.

With a pure spectral output at 1064 nm in the fundamental cavity the Stokes resonator was unblocked and realigned with the objective of producing a pure and stable SPS field and enable THz measurements.

4.3. Optimised linear THz polariton laser based on intracavity $KTiOPO_4$ crystal

With the optimised end mirror for the fundamental resonator, the linear THz polariton laser with the KTP crystal was re-constructed. The lateral position of the KTP crystal inside the resonator was adjusted so the distance travelled by the THz field from the SPS interacting region inside the material to the Si-prisms was minimal. As explained in Chapter 2 and from the absorption coefficients calculated in Chapter 3, this is to minimise the effects of strong THz absorption inside the material [9]. The lowest SPS threshold was obtained with the Stokes resonator angled to generate a Stokes wavelength of 1086 nm ($\theta \cong 3.1°$), for a 3.2 W diode pump input. The measured fundamental output power (~125 mW) and pulse width (60 ns FWHM) at SPS threshold lead to a similar figure for the estimated intracavity intensity (69 MW/cm^2), which was expected given that the only modification in the resonator was a replacement of the output coupler, which maintained the same output coupling percentage (0.6%) at 1064 nm.

4.3.1. Power transfer and wavelength-tunability of the Stokes field

With a stable 1064 nm fundamental field practically the same wavelength-tunable range was achieved for the SPS fields, but now the spectral content was composed of a single SPS line, and the power output was clearly more stable, varying within less than 10%, as opposed to variations as high as 50% with the previous mirror and without the etalon. Adjusting the interacting angle from $\theta \sim 2.0 - 3.5°$, tunable Stokes output from 1080.8 – 1087.7 nm was produced, corresponding to polariton frequencies from 4.29 – 5.91 THz being generated inside the nonlinear crystal. The measured Stokes wavelength versus interacting angle, and the corresponding SPS tuning range overlapped with the calculated dispersion curve are plotted in Figure 4.13. As predicted in Chapter 3 from the calculated dispersion relation (see Figure 3.10

and Figure 3.11), gaps in the Stokes emission were observed. They were located around 1082 nm and 1084 nm and correspond respectively to the 153 cm^{-1} and 177 cm^{-1} infrared absorbing modes detected in the Raman spectra for KTP. In the experimental device, when adjusting the interacting angle between the fundamental and Stokes resonators towards an A_1-mode, the absorption losses for the SPS fields inside the nonlinear crystal increase significantly, and as a consequence, it was observed that the measured Stokes wavelength would abruptly change, leaping over the mode frequency. This hop signifies that the SPS fields are thus generated at frequencies adjacent to the mode, which experiences lower absorption loss. The lower-end of the SPS tunable range in this device is limited by the 142 cm^{-1} infrared absorbing mode, and the upper limit is a consequence a mode mismatch between the fundamental and Stokes cavity modes at higher interacting angles.

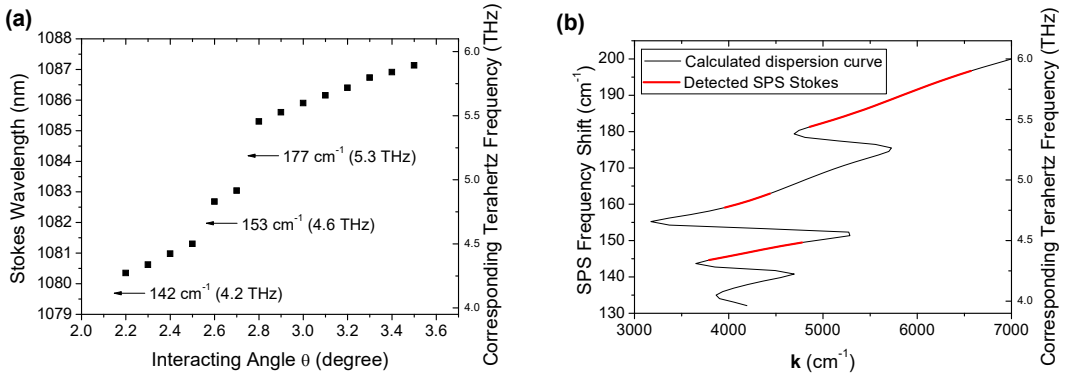

Figure 4.13 – SPS tuning range in the linear KTP resonator. (a)Stokes wavelength output versus interacting angle θ. (b)SPS tuning range overlapped with calculated dispersion curve (from Figure 3.10). Discontinuities in the Stokes emission are due to infrared absorbing A_1 modes in the crystal measured at 153 cm^{-1} and 177 cm^{-1}.

The system was power transferred for a 1086 nm Stokes field ($\theta = 3.0°$) and the output power of the undepleted fundamental (Stokes cavity blocked), depleted fundamental (Stokes cavity unblocked, SPS process active) and Stokes fields is plotted in Figure 4.14. In intracavity SPS systems the output power of the depleted 1064 nm is lower than that of the undepleted field. This is because with the onset of SPS, part of the fundamental field energy is channelled to the generated Stokes and THz fields. The percentage of this decrease in power from the undepleted to the depleted 1064 nm field is an indicator of the SPS conversion efficiency. The higher the percentage of depletion, the more energy is being converted from the fundamental to the SPS fields, and consequently the higher the expected THz (and Stokes) output [8,1]. For

this reason, the percentage of depletion is a useful metric when analysing the efficiency of intracavity THz lasers. The intracavity systems reported in [1] and [8] exhibited fundamental field depletions that exceeded 50% when pumping more than twice above threshold.

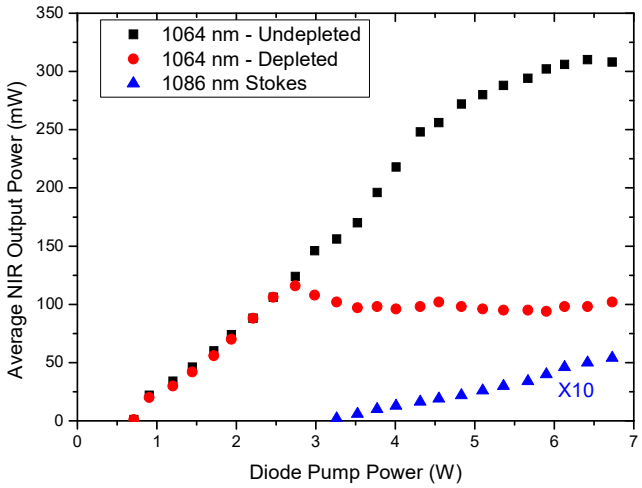

Figure 4.14 – Power transfer curve for the 1064 nm fundamental field (depleted and undepleted) and 1086 nm Stokes field (magnified 10 times).

The percentage of depletion achieved by using KTP in a linear configuration approached 70% at high diode pump levels. This is a high value, indicating that 1086 nm Stokes (and 5.6 THz) fields are being efficiently generated inside the nonlinear material. The natural following step was to detect the 5.6 THz fields being generated inside the KTP and out-coupled by the Si-prisms. To detect the THz radiation from the various THz polariton lasers assembled in this thesis the same set up was always utilised, and was composed of the Golay cell (with input 50 mm EFL TPX lens and LPF 14.3 filter) connected to the oscilloscope and the optical chopper at 10 Hz. As an additional check to ensure any detected THz signal was not contaminated with scattered near-infrared light, it was always verified that a BK7 window would completely suppress the signal being measured, validating it as purely THz radiation (the BK7 window blocks the THz but not the near-infrared).

4.3.2. Attempts to detect THz signal

It was not possible to detect any signal at 5.6 THz with the Golay cell. The Stokes cavity angle was tuned across the entire SPS tuning range and yet no THz fields could be detected being emitted from the Si-prisms. The interacting fundamental and Stokes fields were resonating as close to the KTP's edge as possible to maintain SPS emission, meaning that the distance travelled by the THz field inside the crystal was the minimum achievable with this laser. In real devices, the minimum travelled distance is not only given by equation 3.15. In fact, it is a compromise of the geometrical constrains that lead to equation 3.15 along with the effect of "sweet spots" inside the SPS crystal which allows efficient nonlinear conversion. These spots are due to crystal inhomogeneity and possibly also end coating irregularities leading to regions of the crystal which performed better than others. Any attempt to laterally translate the KTP crystal inserted into the resonator to reduce the THz propagation distance would sometimes result in an abrupt reduction of the Stokes field output measured from M4 as a result of either clipping the Stokes resonator mode by the edge of the crystal or the interaction of the fundamental field with a region of the crystal that is non-optimal for SPS generation.

The absence of THz detection across the entire SPS tuning range had never been observed in the intracavity systems based on MgO:LN previously assembled at Macquarie University. Clearly there was a difference associated with the different nonlinear material and/or the silicon prisms designed for this crystal, and there were no linear systems based on KTP with Si-prisms in the literature to be compared with. Terahertz emission using a surface-emitting KTP had however been reported, continuously tunable from 3.17 – 3.44 THz, 4.19 – 5.19 THz and 5.55 – 6.13 THz [10]. It was proposed that the inability to detect THz signal at any frequency from this particular system was being caused by one or more of three possible factors:

Terahertz absorption inside KTP

In Chapter 3 it was calculated that terahertz frequencies from 3.0 to 3.7 THz would be more likely to be detected from KTP in linear configuration, and this would correspond to interacting angles below 2º. The minimum interacting angle was limited by clipping of the fundamental beam in the resonator and mechanical damage (chipping) near the edges of the end-face closest to the emitting surface of the crystal as a consequence of in-house polishing of the THz-emitting surface of the crystal, and unfortunately, the minimum interacting angle achieved in the experimental system was around 2º, and frequencies below 3.7 THz were not being

produced inside the crystal to validate those predictions. The calculated absorption coefficients in the THz at SPS frequency shifts produced in the linear KTP are highlighted in the plot of Figure 4.15, together with a representation of the limits for the interacting angles. For small interacting angles the absorption coefficients are the largest, exceeding 1000 cm^{-1}, indicating that the THz fields below 4.5 THz were probably being completely absorbed through propagation inside KTP. From the shape of the absorption coefficient curve, it would still be valid to consider those terahertz fields generated with frequencies around 4.9 THz and 5.6 THz. However, with the calculated absorption coefficients (~200-250 cm^{-1}) and the minimum propagation distance ($d_{min}(\theta)$; equation 3.15) it was inferred that less than 10^{-5}% of the generated THz field would have a chance to reach the side face of KTP. This indicated that absorption inside the material was very likely to be the limiting factor in the THz detection from KTP. It is noted, however, that the calculated absorption coefficients are very sensitive to the parameters of the measured A_1-modes (position, linewidth and oscillator strength), and as noted in Chapter 3 there is some degree of uncertainty associated with the calculated absorption coefficients.

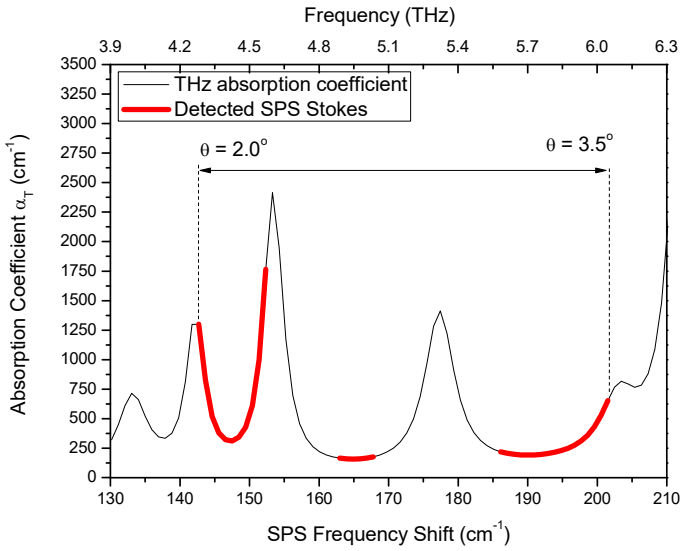

Figure 4.15 – Calculated absorption coefficient in KTP for terahertz frequencies generated via SPS in the linear geometry.

Terahertz detection efficiency at higher frequencies

The losses in the detection system (Golay cell, TPX lenses, LPF filter) increase considerably above 4 THz, as will be further investigated later in this chapter. This could be causing an

increase in the minimum detectable THz signal which could have been above the average output power emitted by the silicon prisms. However, similar setups were utilised to successfully detect terahertz output at frequencies as high as 6.5 THz in externally pumped systems [10,11]. For the same reasons that in MgO:LN similar detection setups could be utilised in intracavity and externally-pumped systems, it was reasonable to expect that for KTP this would also be the case. Moreover, this was the only detection apparatus available in the laboratory.

Terahertz absorption by free-carriers in the silicon prisms

It could be possible that the THz photons transmitted through the crystal were being absorbed inside the Si-prisms by free-carriers. Scattered near-infrared radiation (808 nm, 1064 nm or 1080-1087 nm) impinging on the prisms can induce free carriers (electrons) which will absorb the terahertz radiation. Energy densities as low as 10 μJ/cm^2 were reported in [9] to be sufficient to generate free carriers in silicon, and a common practice to avoid this issue is the insertion of physical barriers around the Si prisms to minimise the chance that scattered infrared light will impinge on them. In the linear MgO:LN systems previous to this work, the strategy of introducing mechanical blockers to prevent these scattered light of reaching the prisms was implemented with success. In KTP however, such a strategy did not assist with detecting THz.

To completely avoid the induction of free carriers by the fundamental and Stokes fields, a system was built with a fundamental resonator lasing at the 1.3 μm line of Nd^{3+} ions. The strategy of operating the fundamental laser at a longer wavelength (and hence lower photon energy) to avoid the induction of free-carrier in the Si-prisms was successfully demonstrated in a THz polariton laser based on MgO:LN [12], and was also investigated here for the system using KTP.

4.3.3. 1342 nm fundamental laser

The high resistivity silicon prisms are very convenient to extract THz radiation from nonlinear crystals generated via SPS because of the material's low absorption coefficient, and 'flat' refractive index in the THz range ($n = 3.41$) [13]. However, it is known that scattered near infrared fields (808 nm diode pump lasers, 1064 nm fundamental, or 1070-1090 nm Stokes) impinging on the Si-prisms may induce free-carriers (electrons) in the silicon, that strongly

absorb THz radiation [14]. In the presence of free carriers, any THz signal emanating from the nonlinear material and transmitted into the silicon prisms will thus be absorbed within the Si-prisms due to the induced free electrons.

In the linear intracavity THz polariton laser where Si-prisms are used to extract the terahertz radiation, both fundamental and Stokes fields oscillate closely to the crystal/prism interface (in order to minimise the propagating distance of the THz fields inside the material) and any scattered 1064 nm fundamental, or the corresponding Stokes, would induce the free carriers in silicon. The induction of free carriers occurs if the photon energy of the incident field is above the band gap energy in silicon which corresponds to 1120 nm at room temperature (1.12 eV at 300 K [15]). Hence this issue could be avoided utilising the 1342 nm line in Nd:YVO_4 for the fundamental laser. This research group recently demonstrated great improvements in THz emission from MgO:LN via this technique, with 62.3 μW being detected at 1.33 THz [12] (as opposed to the previous 6.45 μW at 1.82 THz [1]), and this increase being largely attributed to the absence of free carriers.

The experimental setup for the 1342 nm SPS laser with intracavity KTP is very similar to the 1064 nm system, as illustrated in Figure 4.16. This is the same resonator reported in [12] into which a KTP crystal was inserted. The fundamental resonator was 230 mm long and composed of two flat mirrors M5 and M6, and the Stokes resonators was ~100 mm long (with two D-shaped flat mirrors M7 and M8 mounted on a rotation stage). The mirror coatings are summarised in Table 4. 3; the input mirror M5 was highly transmissive for the 880 nm diode pump and also 1064 nm fundamental wavelengths; the output coupler M6 and both Stokes cavity mirrors were highly reflective in the 1.3 μm range (HR>99%@1280 – 1520 nm).

The laser crystal of choice was a Nd:YVO_4 because it exhibits a significantly higher laser emission cross-section than Nd:YAG at the 1.3 μm line [16]; the crystal was a 4×4×10 mm *a*-cut 0.3 at.% Nd:YVO_4, with anti-reflection coated end-faces (R<0.5%@808/880 nm; R<0.2%@1342 nm). The pump laser was a fibre-coupled diode laser (200 μm core; 0.22NA) delivering 60 W output at 808 nm, and focused to a 570 μm diameter inside the laser crystal. A similar acousto-optic Q-switch cell was utilised, operating at 5 kHz, and with AR coatings for 1342 nm. The KTP crystal had the same geometrical specifications as used in the previous experiments in section 4.2 (*x*-cut, 5×5×20 mm^3) the only difference being the end-face coating (R<0.2%@1320-1380 nm). Three silicon prisms were attached to the crystal's (optically polished) side faces to out-couple the terahertz fields.

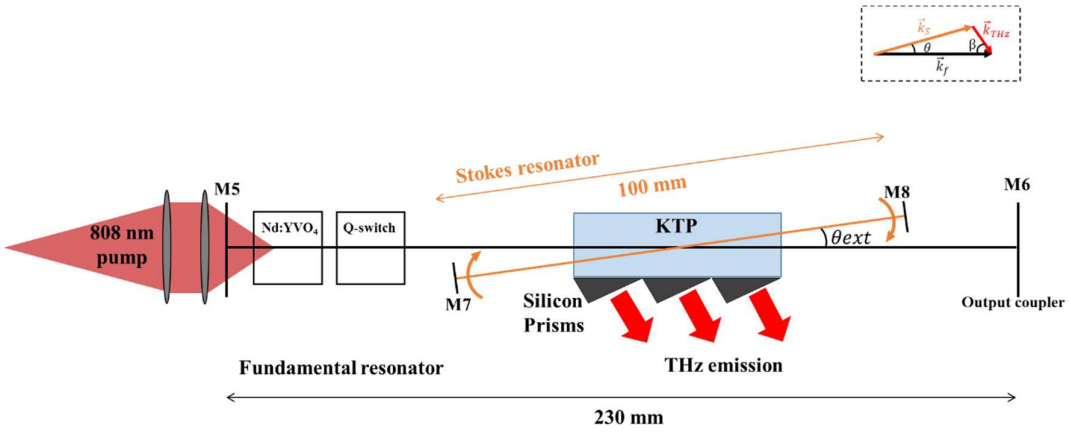

Figure 4.16 – Resonator layout for the THz polariton laser with 1342 nm fundamental resonator and intracavity KTP.

Table 4. 3 – Optical coatings for the 1342 nm fundamental field.

Mirror		Specification	Manufacturer
Fundamental resonator	M5	HR>99.9%@1342 nm HT>95%@1064 nm HT>99%@808 nm	Layertec
	M6	HR>99%@1280 – 1520 nm	
Stokes resonator	M7, M8	HR>99%@1280 – 1520 nm	

With this system, wavelength tunable Stokes radiation from 1367.2 – 1378.5 nm was detected with a calibrated spectrometer (NIRQuest512), corresponding to frequencies from 4.1 – 5.92 THz being generated inside the material, as shown in Figure 4.17. The power transfer curve for the most efficient SPS generation (1370.5 nm) is presented in Figure 4.18. From the plot it can be noted that the fundamental 1342 nm field reached threshold at 3.25 W diode input, and SPS threshold was achieved for 9.2 W diode pump power. From the measured fundamental pulse width (~125 ns FWHM), the output coupling percentage (1%), and the 285 μm mode radius the calculated intracavity intensity at SPS threshold was as low as 20 MW/cm^2, a value 3 times that obtained at 1064 nm, and similar to that obtained for MgO:LN in [12]. In this resonator no signs of SRS competition were observed.

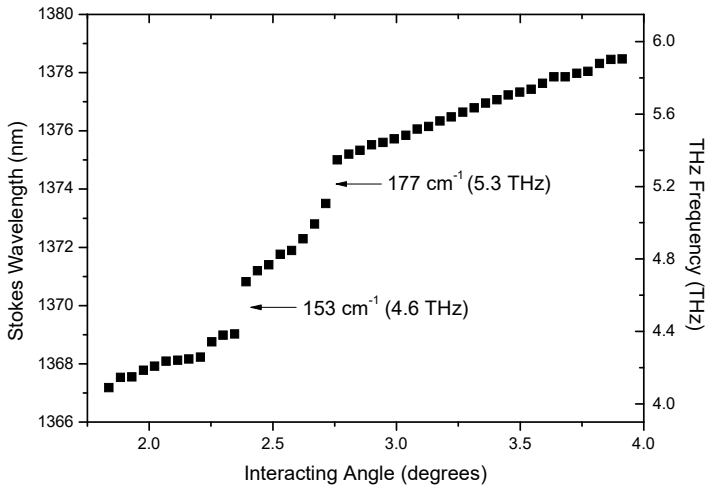

Figure 4.17 – Detected Stokes wavelength and corresponding THz frequency versus interacting angle in KTP for a 1342 nm fundamental wavelength.

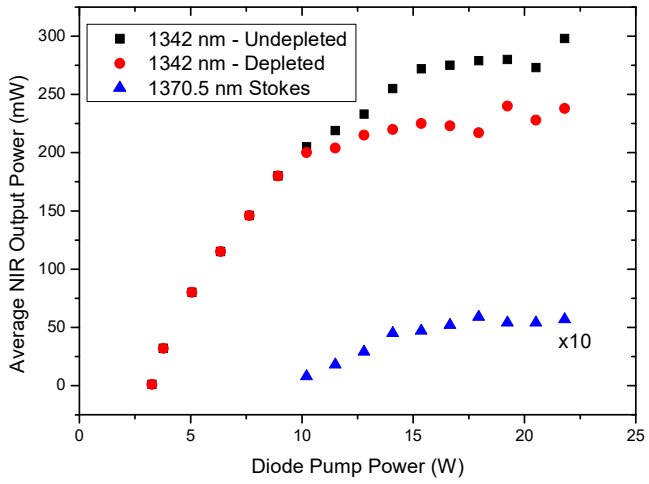

Figure 4.18 – Power transfer curves for the 1342 nm fundamental (depleted and undepleted) and 1370.5 nm Stokes (magnified 10 times).

The 1342 nm fundamental field produced a strong SPS Stokes field with pump depletions in excess of 20%, and this level of depletion being similar to those observed in [12], in which

a substantial increase in THz output was observed in MgO:$LiNbO_3$. Despite the low SPS thresholds, reasonable pump depletion and high average Stokes output power, no THz signal could be detected from the system for any frequency across the tunable range. This result suggests that the induction of free carriers in silicon was not the limiting factor for detection of terahertz radiation from the linear THz polariton laser based on KTP.

4.3.4. KTP summary

The results in Section 4.3 suggest that once the issues of competition between SPS and SRS were overcome, the KTP polariton laser was effective in generating THz radiation in 3 tunable bands, from 4.29 – 4.50 THz, 4.80 – 4.95 THz and 5.45 – 5.91 THz. The low threshold and high fundamental depletion suggest that this generation was efficient yet no THz could be detected. The exact cause for the lack of detectability was not determined, although a number of insights into the possible factors which may have heavily affected the THz detection from this crystal were offered. The investigation of the 1342 nm resonator indicated that the possible presence of free carriers in silicon was not the limiting factor for THz detection. The fact that an externally-pumped KTP system [10] generated measurable THz output using similar detection apparatus indicated that the detection system should also be able to measure THz radiation emanating from the prisms. On these grounds absorption of the terahertz fields by KTP before it exits the crystal is the most likely reason for the absence of detectable THz signal.

It was anticipated in Chapter 3 that KTP would be likely to produce the highest extractable THz fields in the 3.0 – 3.7 THz range, based on the calculated absorption coefficients and the average minimum propagation distance inside the crystal. These frequencies would have been achieved with interacting angles below $\theta = 2°$, however they could not be achieved in the experimental setup, which did not allow the validation of such predictions. The region of interacting angles below $\theta = 2°$ is important in the linear configuration either with KTP or RTP because it combines lower THz absorption coefficients with smaller $d_{min}(\theta)$. With the results obtained for KTP there was no indications that the RTP crystal would produce SPS emission below $\theta = 2°$, given the similarities between the crystals and the fact that the same resonator would be used.

As will be seen in the next section, the evaluation of RTP, which did produce detectable THz output, provides further insight into this KTP issue.

4.4. THz polariton laser based on intracavity $RTiOPO_4$ crystal

A rubidium titanyl phosphate crystal was also evaluated as a nonlinear material in the linear THz polariton laser, and in contrast to KTP, produced detectable, frequency-tunable THz output thereby shedding some light on the issues noted in the previous section. The RTP crystal utilised in the linear resonator was an *x*-cut cuboid with dimensions of 4×4×20 mm^3, and end faces anti-reflection (AR) coated from 1064 – 1100 nm (R<0.1%). The material was provided by Crystal Laser, France. The side faces perpendicular to the *y*-axis were optically polished in-house to enable the attachment of the silicon prisms responsible for the out-coupling of the THz field. The three high-resistivity Si-prisms (geometrical dimensions: 7 mm hypotenuse x 5 mm-thick, 32/58/90º angles; as per calculation described in Chapter 2) were attached to the RTP's side face with the same technique utilised previously and the material was inserted into the fundamental resonator.

4.4.1. Frequency tunability of the terahertz and Stokes fields

The same laser mirrors optimised for KTP (i.e. those which suppressed SRS competition) were utilised with the intracavity RTP crystal, and 1064 nm threshold was achieved at 0.7 W diode pump input, indicating that the RTP crystal utilised is introducing higher intracavity losses than the previous KTP. In the RTP crystal it was possible to produce SPS activity at interacting angles below 2°, maybe due to a more careful resonator setup and an end-face with a sharper edge as a consequence of better in-house polishing (through refinement of the polishing technique I used) of the emitting side face. This indicates, according to calculations from Chapter 3, that frequencies as low as 3.1 THz are being generated at a closer distance to the crystal's side face, with corresponding absorption coefficient below 300 cm^{-1} for frequencies as high as 4.2 THz.

The lowest SPS threshold was obtained with the Stokes resonator aligned to generate a Stokes wavelength of 1078.5 nm ($\theta \cong 1.3°$) for a 3.4 W diode input, slightly higher than that obtained in KTP. Wavelength-tunable Stokes output was detected from 1076.2 to 1091.7 nm when the interacting angle was adjusted from $\theta = 1 - 3.6°$, as plotted in Figure 4.19. Also in Figure 4.19 the SPS tuning range (red curve) is overlaid with the dispersion relation calculated

in Chapter 3. This shows that THz frequencies from 3.10 to 7.05 THz were being generated inside the material. The discontinuities in the Stokes output correspond to the infrared absorbing A_1 modes in RTP measured at 106, 143, 161, 170 and 211 cm^{-1}. The maximum average Stokes power was sustained at a reasonably similar level across the different Stokes wavelengths produced as shown in Figure 4.20, indicating a comparable SPS efficiency across the SPS tuning range.

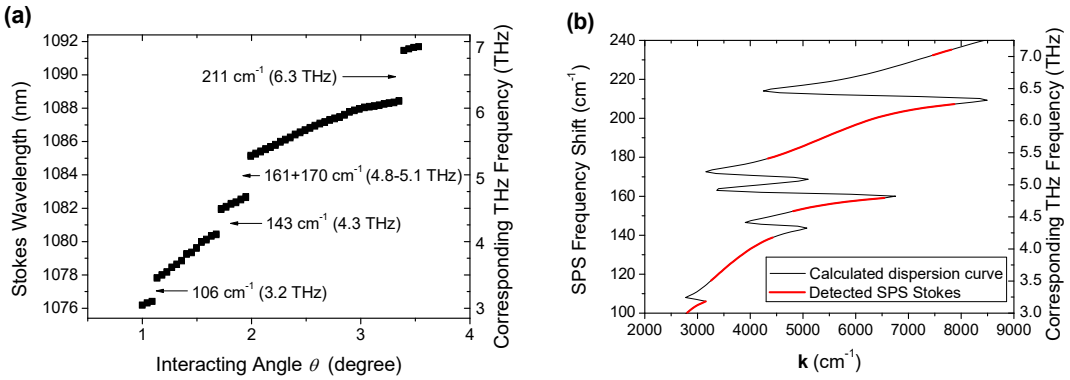

Figure 4.19 – SPS tuning range in the linear RTP resonator. (a)Stokes wavelength output versus interacting angle θ. (b)SPS tuning range overlapped with calculated dispersion curve. Discontinuities in the Stokes emission are due to infrared absorbing A_1 modes in the crystal measured at 106, 143, 161, 170 and 211 cm^{-1}.

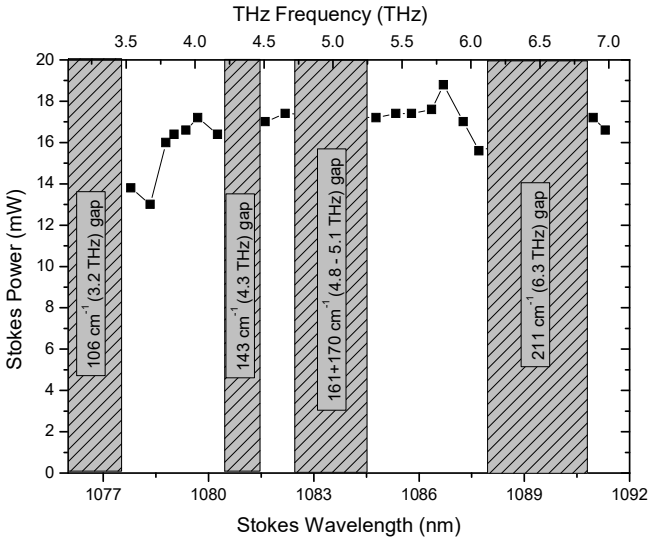

Figure 4.20 – Maximum average Stokes power versus wavelength. Discontinuities in the Stokes emission are due to infrared absorbing A_1 modes in the crystal measured at 106, 143, 161, 170 and 211 cm^{-1}.

Using the same detection setup as used when trying to detect THz output from the KTP laser, it was possible to detect frequency-tunable output from this system. Terahertz radiation was detected for Stokes wavelengths from 1076.3 – 1080.3 nm, corresponding to frequencies ranging from 3.10 – 4.15 THz. The range of detected frequencies for RTP in the linear geometry correlated extremely well with those frequencies predicted in Chapter 3 (3.00 – 4.15 THz). The terahertz output power versus THz frequency for 5.5 W diode pump input is plotted in Figure 4.21 together with the calculated absorption coefficients. Because the Golay signal is corrected for the losses in the detection system, the plotted average output power corresponds to the power of the free-space propagating THz field after exiting the Si-prisms.

The detected terahertz field from RTP was continuously tunable from 3.10 to 3.17 THz, and from 3.50 to 4.15 THz. The emission gap from 3.17- 3.50 THz is a consequence of the A_1 infrared absorbing mode at 106 cm^{-1}, and the upper limit at 4.15 THz approaches the 143 cm^{-1} mode. The dips in THz power observed at 3.68, 3.84 and 4.01 THz correspond to water vapour absorption [17] present in the laboratory environment. No THz field was measured above 4.15 THz, and from the plot in Figure 4.21 it can be noted that the calculated terahertz absorption coefficient substantially increases immediately after the 143 cm^{-1} gap, which indicates that the terahertz fields above 4.5 THz could be being completely absorbed inside the material. An experimental analysis was conducted with the system with RTP to directly investigate the absorption coefficient and also other experimental parameters with the objective of clarify further and bring substantial experimental evidences to the understanding of the limits in THz detection from linear resonators, as will be discussed in subsection 4.4.4.

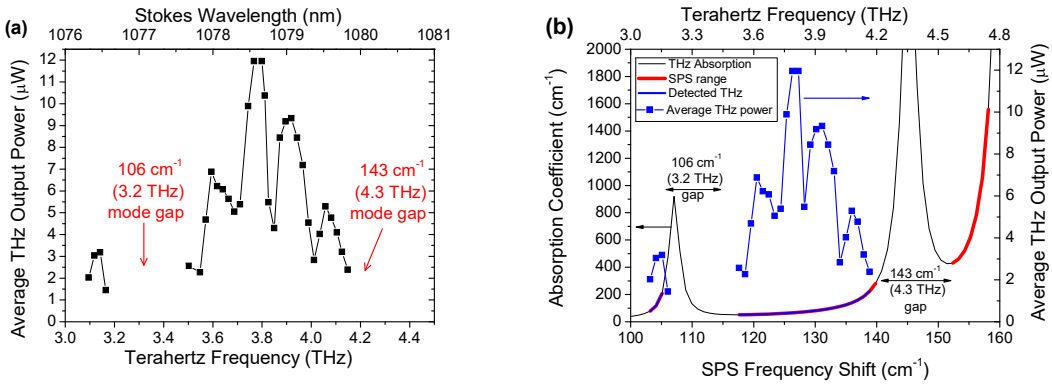

Figure 4.21 – Average THz output power versus THz frequency in RTP. (a) Plot against Stokes wavelength. (b) Plot overlapped with absorption coefficient. Discontinuities in the Stokes emission are due to infrared absorbing A_1 modes in the crystal.

4.4.2. Power transfer characteristics

The highest average THz output power was obtained at around 3.80 THz (1078.5 nm Stokes). The power transfer curves for the depleted 1064 nm, the 1078.5 nm Stokes and the 3.80 THz fields are plotted in Figure 4.22. At SPS threshold the 1064 nm output power was ~115 mW, indicating pulse energies around 38 μJ. The measured fundamental pulse duration at SPS threshold was 70 ns (FWHM), leading to an estimated SPS threshold intensity of 54 MW/cm^2, a value comparable to that obtained for KTP in the previous section (60 MW/cm^2)

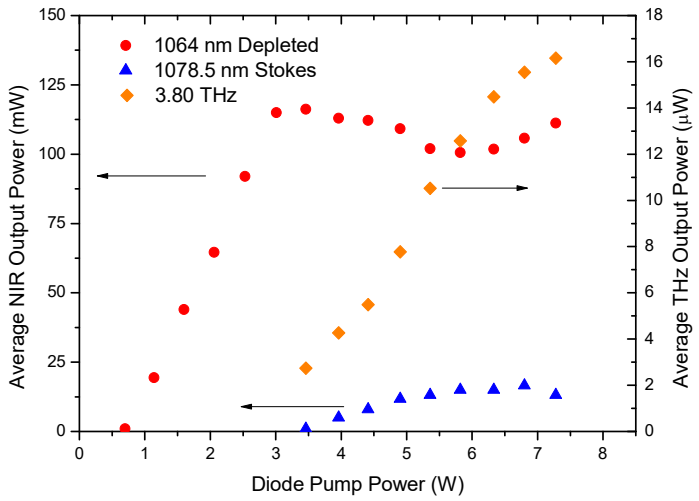

Figure 4.22 – Average output powers measured versus incident diode pump power for the depleted 1064 nm fundamental, 1078.5 nm Stokes and 3.80 THz fields.

A maximum average output power of 16.2 μW was detected at 3.80 THz, for a 7.3 W diode pump input (5.4 nJ per pulse). To the best of this author's knowledge, this was the highest THz average output power ever reported for an intracavity SPS laser at the time these experiments were conducted (Dec. 2015), and the results were published in [2].

The pump depletion of the linear RTP THz polariton laser at 3.80 THz versus diode pump input is plotted in Figure 4.23. The percentage of depletion exceeds 60% when above 5 W of diode pump, suggesting a very good mode matching between the interacting fields, and good

SPS conversion efficiency. The Stokes output power versus pump depletion is plotted in Figure 4.24, showing a near-linear relation between the percentage of depletion and the Stokes power output within the data range. This is an important experimental observation because it indicates that the more effectively the fundamental field is depleted the more Stokes and THz photons will be generated, suggesting this parameter should be maximised during laser design.

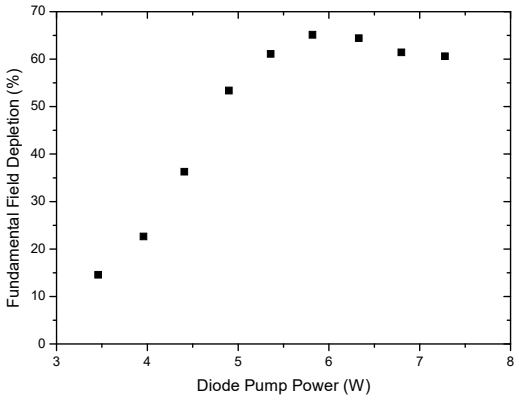

Figure 4.23 – Fundamental field depletion of the RTP THz polariton laser versus diode pump power at 3.80 THz.

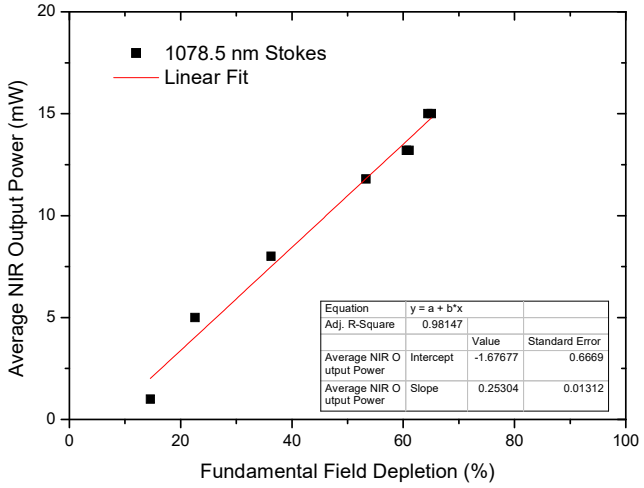

Figure 4.24 – Average output power at 1078.5 nm Stokes versus fundamental field depletion. A near-linear relation between these two parameters can be inferred.

4.4.3. Temporal profile

The temporal profiles of the fundamental field (depleted and undepleted), and 1078.5 nm Stokes pulses are plotted in Figure 4.25 for a 6.0 W diode pump input. The characteristics of these pulses are typical from intracavity SPS lasers [1,8]. The fundamental field pulse width decreased from 50 ns to 21 ns (FWHM) as a consequence of the SPS process. This reduction in pulse width is associated with the transfer of energy to the SPS fields, and can be interpreted as the pump depletion observed in a temporal scale [8]. The Stokes pulse builds up with a 32 ns delay, at the peak of the depleted 1064 nm pulse (and the fundamental field pulse decays), to a FWHM pulse width of 17 ns. With the Stokes pulse width the maximum peak power for the THz radiation can be estimated to be 317 mW.

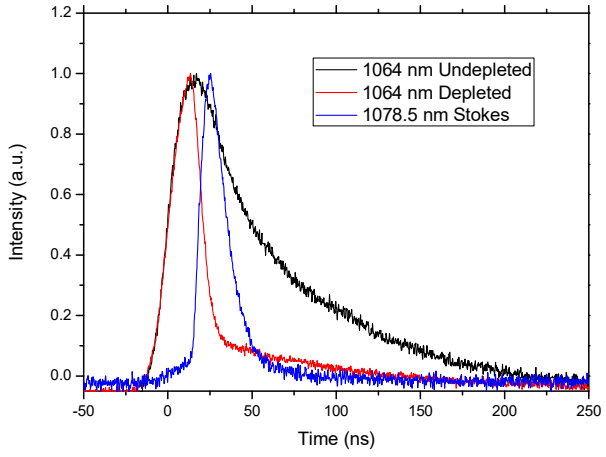

Figure 4.25 – Temporal profiles of the fundamental (depleted and undepleted) and 1078.5 nm Stokes at 6.0 W diode pump power.

4.4.4. Limiting factors on terahertz detection above 4.15 THz

The measured wavelength-tuning range for the SPS Stokes fields in RTP indicated that frequencies from 3.10 – 7.05 THz were being generated inside the material. However, no terahertz fields could be detected above 4.15 THz. This can be considered in the context of the calculated absorption coefficient as shown in the plot of Figure 4.26. The black line indicates the calculated absorption coefficient, the red line represents the SPS tuning range, and the thick

blue line highlights the THz frequencies that were detected. The range of detected frequencies in RTP agrees very well with the calculations made in Chapter 3 (Figure 3.18), where it was predicted that frequencies from 3.05 – 4.15 THz were more likely to be detected from RTP in a linear configuration.

The range of THz frequencies detected from the intracavity polariton lasers is different from what was observed in the externally-pumped, surface-emitted TPO's based on KTP and KTA (similar nonlinear materials) reported in the literature, from which the terahertz fields were detected across the entire Stokes tuning range [10,11], and the reported upper limits were at 6.12 and 6.43 THz, respectively. These results give a strong indication that the absorption inside the nonlinear material was the limiting factor for the linear configuration utilising Si-prisms to out-couple the THz fields. Nevertheless, not to rely solely on the calculated absorption coefficients and to produce additional experimental information, other factors influencing on the terahertz detection above 4.15 THz in RTP were explored, including the THz generation efficiency, the THz extraction efficiency from the crystal, and the transmission losses through propagation in air and through the detection system. Exploring these factors will also help to explain the inability to detect THz emission from the system utilising KTP, from which THz frequencies in the 4 – 6 THz range were generated inside the material.

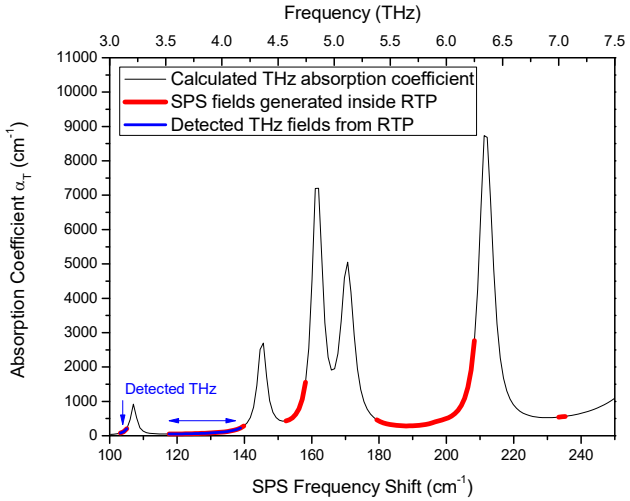

Figure 4.26 – Analysis of the terahertz detection limits from the calculated absorption coefficient limits. Black line represents the calculated absorption coefficient, red line represents the SPS frequencies generated inside RTP, and the blue line highlights the THz frequencies detected from the Si-prisms.

Terahertz generation efficiency

For every interacting angle in SPS, a sufficient amount of THz photons has to be generated inside the material to account for all the losses in the system and still enable detection at that particular frequency. Hence it is important to compare the number of terahertz photons generated inside the nonlinear crystal at frequencies within the THz detectable range with those generated at higher frequencies, outside the detection limits. If the efficiency of the SPS process in RTP decreases considerably in the 5.2 – 6.0 THz range for example, it would be expected that no THz detection could be possible despite the lower in absorption coefficient (Figure 4.26).

A comparison of the number of THz photons generated internally for every different frequency can be made by monitoring the Stokes output power across the SPS tuning range. Assuming that for each 1064 nm photon experiencing stimulated polariton scattering one pair of THz and Stokes photons must be generated, the Stokes laser output power is, in theory, linearly proportional to the number of Stokes and THz photons pairs generated internally, in the absence of other optical processes. For this reason, the Stokes laser output power and the percentage of fundamental depletion at 7 W diode pump input were measured across the Stokes wavelength-tuning range, as plotted in Figure 4.27. The horizontal line in the figure represents the Stokes power measured at 1078.5 nm, wavelength corresponding to the terahertz emission peak at 3.80 THz. From this plot we note that the measured Stokes output power for wavelengths as high as 1088 nm is greater than that measured at 1078.5 nm (THz detection peak), suggesting that the number of photons generated in the 3.90 – 6.10 THz range should be similar to or exceed that at 3.80 THz. The fundamental field depletion is high over the same range, with values between 50 and 55% for frequencies as high as 5.70 THz. As described above, it was expected that the THz power should scale similarly to the Stokes power, yet this is clearly not what was detected from the system. This analysis suggested that the efficiency of the SPS process (and consequently the THz generation) was maintained across a much wider range than what was possible to realise THz detection, and therefore other factors were affecting the THz detection above 4.15 THz.

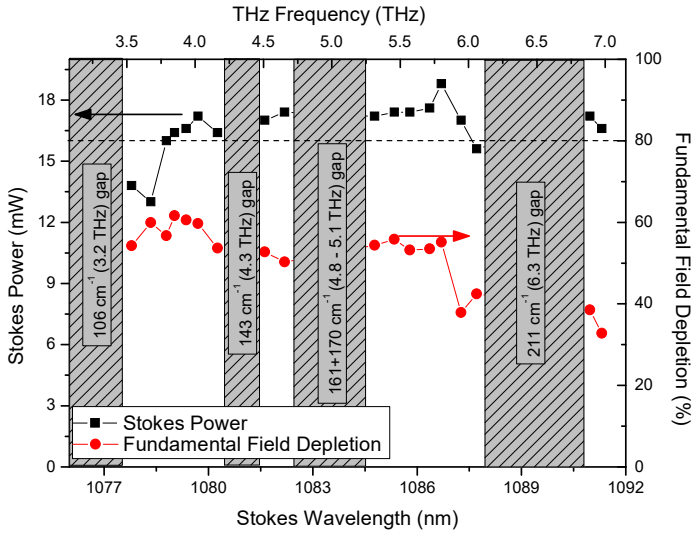

Figure 4.27 – Average output powers measured versus incident diode pump power for the depleted 1064 nm fundamental, 1079 nm Stokes and 3.8 THz fields.

Terahertz extraction and detection efficiency

The THz field generated inside the SPS crystal travels through multiple materials and interfaces before being successfully detected by the Golay cell to produce a measurable signal. The absorption and Fresnel reflection losses at each material and interface in the optical path are relevant and shall be analysed individually, from the THz propagation through RTP and silicon prisms (extraction efficiency), propagation through free space, and transmission losses though the detection optics in front of the Golay cell.

The extraction of the THz photons from the material begins with the propagation from the SPS interacting region within the RTP to the crystal's edge to which the Si-prisms were bonded. High absorption coefficients were calculated in Chapter 3 for this process, and this was quantified by directly measuring the absorption coefficient in RTP at different THz frequencies. For these measurements the RTP crystal was mounted on a translation stage having micron-scale resolution (Thorlabs PT1/M; 10 μm resolution), and the distance travelled by the THz beam inside RTP was varied by translating the crystal across the fundamental cavity axis (Figure 4.28). The THz output power was monitored versus the increment in propagating distance, and was found to follow an exponential dependence, as shown in Figure 4.29. From the exponential decay the absorption coefficients at 3.80 THz, 3.98 THz and 4.10 THz were obtained according to Beer's law. The measured absorption coefficients are related in Table 4.4 together with those coefficients calculated in Chapter 3. The values measured at 3.80 THz

and 3.98 THz agree reasonably well with the coefficients calculated in Chapter 3. At 4.10 THz an increase in absorption was expected as the 143 cm^{-1} mode was approached. This was predicted by the calculations, however it was not reflected in the experimental measurement. The measured absorption coefficients are very high, as expected, which justifies minimising the propagation distance inside the material. However, the real dimension of the fundamental and Stokes mode volumes, and the RTP crystal size limits the minimum lateral distance achievable, and the system was already optimised in this regard.

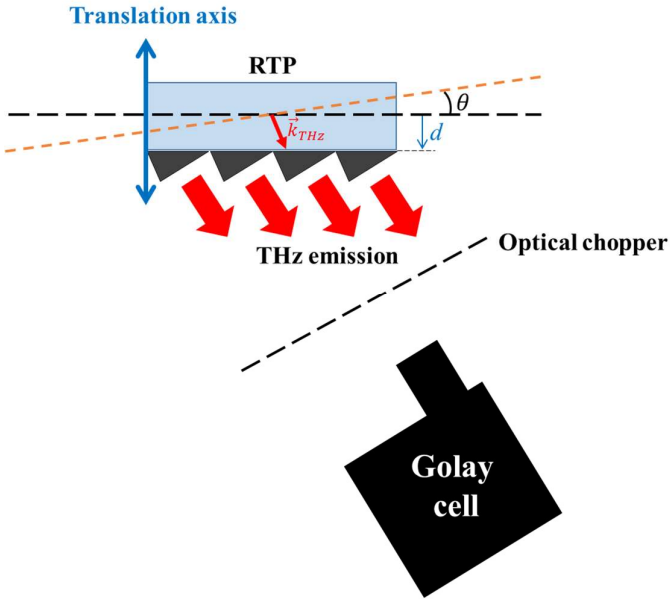

Figure 4.28 – THz absorption measurements setup. The RTP crystal is mounted on a translation stage and the THz output power is monitored versus the increment in propagation distance for the THz field. The absorption coefficient is obtained according to Beer's Law.

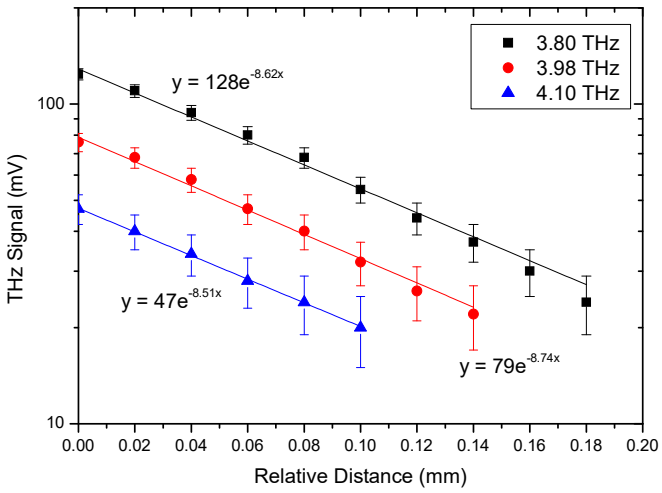

Figure 4.29 – Terahertz output power versus increment in propagation distance inside RTP at 3.8, 3.98 and 4.1 THz. The corresponding absorption coefficient at each frequency was determined with a best-fit for the exponential decay.

Table 4.4 – Calculated and experimentally measured THz absorption coefficient at 3.80 THz, 3.98 THz and 4.10 THz.

	Absorption Coefficient α_T (cm^{-1})	
	Measured (± 10 cm^{-1})	Calculated (Chapter 3)
3.80 THz	86	73
3.98 THz	87	94
4.10 THz	85	139

The high values measured for absorption coefficients supported the conclusion that absorption of the THz field was the limiting factor for THz field detection in the linear resonator. However, for the completeness of the analysis, the other losses were also estimated. The losses for the THz field continue as the transmitted THz photons that reach the RTP-prism interface suffer a refraction and a partial reflection (Fresnel loss), followed by a propagation through the prism, and a second refraction in the prism-air interface. The absorption in silicon is known to increase at higher THz frequencies, and absorption losses ranging from 10% at

4 THz to 25% at 7 THz [18]. The combined Fresnel reflection losses in the RTP-prism and in the prism-air interfaces are estimated to be around 30% from ~3 – 7 THz, using the extraordinary refractive index calculated in Chapter 3, and assuming the refractive index of silicon to be $n = 3.41$.

The THz photons that successfully refract out from the prisms propagate in free-space, which in this case is the atmospheric air in the laboratory environment. The absorption in air has to be accounted for, particularly due to the presence of water vapour. However it is expected that water vapour absorption would cause dips and fine structure in the THz spectra similar to what is observed in Figure 4.21 (e.g. at 3.65 THz and 3.85 THz), but not supress a wide THz emission band.

Finally, the transmitted THz field is accessible for detection, and to be detected these photons have to be transmitted through the LPF 14.3 filter, the 50 mm EFL TPX lens, and the Golay cell TPX window. While the losses appear relatively uniform across the frequency range on account of the Fresnel reflection and Si absorption losses, this is certainly not the case for the other elements in the detection path. In particular the LPF 14.3 filter, the TPX lens and the TPX window in front of the Golay detector. Each of these materials exhibit transmission losses that substantially increase with THz frequencies, as can be noted from their transmission spectra (Appendix). The estimated transmission losses through each component are listed in Table 4.5 for different THz frequencies. The total transmission at 2 THz is around 46%, and this value decreases to 31% at 4 THz and to only 3% at 7 THz. The 10-fold decrease in transmission from ~4 – 7 THz implies that the minimum detectable signal at 7 THz needs to be 10 times stronger than that at 4 THz. Considering that the minimum signal at 3.8 THz was ~2 μW, a minimum of ~20 μW at 7 THz should impinge on the detection system to be measurable. This value is above the maximum value detected at 3.80 THz.

Table 4.5 – THz transmission in detection optics calculated with material transmission data sheet.

	Transmission		
	2 THz	4 THz	7 THz
Long pass filter	80%	61%	17%
TPX 50mm EFL Lens	68%	65%	30%
Golay cell TPX window	82%	78%	58%
Total transmission	46%	31%	3%

With this investigation it was concluded that the absence of a detectable signal above 4.15 THz in the linear THz polariton laser based on RTP, and the complete absence of detectable THz when KTP was used, is due to the increase in THz absorption inside the SPS crystals at higher frequencies (due to tuning towards the strong 271 cm^{-1} mode in RTP and 268 cm^{-1} mode in KTP). The high absorption losses, associated with the increasing losses in the out-coupling prisms and detection optics, attenuate the THz field to a level which is below the minimum detectable signal, being a strong limitation for RTP and KTP crystals in this configuration

The linear configuration has been a standard for systems utilising MgO:LN, especially in the intracavity configuration, and initially it was thought that it would work just as effectively for KTP and RTP. However, the strong absorption coefficients calculated in Chapter 3, and the other undesired effects reported in this chapter indicated otherwise. The competition between SPS and SRS observed when first investigating KTP, was examined thoroughly and successfully avoided with the design of a new end mirror for the fundamental cavity. The high absorption coefficient, however, could not be circumvented due to the intrinsic propagation of the THz fields inside the nonlinear crystal in the linear THz polariton laser.

There was an excellent agreement between the theoretical predictions from Chapter 3 and the experimental results reported in this chapter. The gaps in THz emission correlates with those predicted by the calculated dispersion curve. The limitations around terahertz detection above 4.2 THz in KTP or RTP agree well with the predictions from the calculated absorption coefficients. Furthermore, the useful terahertz signal detected from RTP enabled an

experimental analysis of the limitations in the extraction and detection of the THz field at higher frequencies.

This all strongly suggests that the linear configuration is far from ideal for generating THz radiation using KTP or RTP. As it will be revealed in the next chapter, there is a significantly better resonator design which fully exploits the wide tunability of the KTP and RTP crystals, and which maximises the extraction of the THz radiation generated inside these crystals.

4.5. Chapter summary

In this chapter undesired competition effects between stimulated Raman scattering and stimulated polariton scattering were identified in the KTP crystal, which resulted in undesired depletion of the fundamental 1064 nm by the 1095 nm and 1128 nm Raman lines. This required the design of a new output coupler with sufficient losses at the undesired Raman wavelengths, which successfully produced a pure 1064 nm field in the fundamental resonator, and a corresponding SPS field which was also spectrally pure in KTP and in RTP. With the new output coupler, frequency-tunable THz radiation was detected in RTP ranging from 3.10 to 3.17 THz, and from 3.50 to 4.15 THz, and a maximum average output power of 16.2 μW was detected at 3.80 THz. To the best of the author's knowledge this was the highest average output power in the THz ever detected in an intracavity SPS laser at the time, and the first time a crystal different from lithium niobate was investigated in the intracavity design. Those excellent results were published in [2].

There was evidence of frequencies as high as 7 THz being generated internally in RTP; and in KTP, wavelength-tunable Stokes radiation indicated that frequencies from 4.29 – 5.91 THz were being generated internally, however no THz detection could be realised with that material. This is consistent with the findings in Chapter 3 that strong absorption within the nonlinear crystals would be likely to limit the extraction of THz radiation above 4.15 THz. In this chapter the losses in the detection system were also estimated to be alarmingly high towards 7 THz.

The KTP and KTA TPOs reported in the literature with successful THz detection at frequencies above this level [10,11] utilised similar detection mechanisms, but the most significant difference between them and the linear THz polariton laser is that those systems

make use of the surface-emitted configuration, which virtually eliminates the absorption losses inside the nonlinear material, refracting the THz beam directly to the air. More importantly, in those reported systems utilising the surface-emitted configuration, the THz emission follows the SPS tuning range

References

1. A. Lee, Y. He, and H. Pask, "Frequency-tunable THz source based on stimulated polariton scattering in Mg:$LiNbO_3$," IEEE J. Quantum Electron. **49**, 357–364 (2013).

2. T. A. Ortega, H. M. Pask, D. J. Spence, and A. J. Lee, "Stimulated polariton scattering in an intracavity $RbTiOPO_4$ crystal generating frequency-tunable THz output," Opt. Express **24**, 10254–10264 (2016).

3. A. J. Lee and H. M. Pask, "Continuous wave, frequency-tunable terahertz laser radiation generated via stimulated polariton scattering," Opt. Lett. **39**, 442–445 (2014).

4. "Crystech Inc.," www.crystech.com.

5. E. Yablonovitch, D. M. Hwang, T. J. Gmitter, L. T. Florez, and J. P. Harbison, "Van der Waals bonding of GaAs epitaxial liftoff films onto arbitrary substrates," Appl. Phys. Lett. **56**, 2419–2421 (1990).

6. W. Smith, "Mode Selection in Lasers," Proc. IEEE **6**, 422 (1972).

7. W. Koechner, *Solid-State Laser Engineering - 6th Edition* (Springer US, 2014).

8. T. Edwards, D. Walsh, M. Spurr, C. Rae, M. Dunn, and P. Browne, "Compact source of continuously and widely-tunable terahertz radiation," Opt. Express **14**, 1582–1589 (2006).

9. K. Kawase, J. Shikata, and H. Ito, "Terahertz wave parametric source," J. Phys. D. Appl. Phys. **35**, R1–R14 (2002).

10. W. Wang, Z. Cong, X. Chen, X. Zhang, Z. Qin, G. Tang, N. Li, C. Wang, and Q. Lu, "Terahertz parametric oscillator based on $KTiOPO_4$ crystal," Opt. Lett. **39**, 3706–3709 (2014).

11. W. Wang, Z. Cong, Z. Liu, X. Zhang, Z. Qin, G. Tang, N. Li, Y. Zhang, and Q. Lu, "THz-wave generation via stimulated polariton scattering in $KTiOAsO_4$ crystal," Opt. Express **22**, 17092–17098 (2014).

12. A. Lee, D. Spence, and H. Pask, "Tunable THz polariton laser based on 1342 nm wavelength for enhanced terahertz wave extraction," Opt. Lett. **42**, 2691–2694 (2017).

13. J. Dai, J. Zhang, W. Zhang, and D. Grischkowsky, "Terahertz time-domain spectroscopy characterization of the far-infrared absorption and index of refraction of high-resistivity, float-zone silicon," J. Opt. Soc. Am. B **21**, 1379 (2004).

14. K. Kawase, J. Shikata, H. Minamide, K. Imai, and H. Ito, "Arrayed silicon prism coupler for a terahertz-wave parametric oscillator," Appl. Opt. **40**, 1423–1426 (2001).

15. S. Sze and K. Ng, *Physics of Semiconductor Devices* (Wiley, 2007).

16. H. Ogilvy, M. Withford, P. Dekker, and J. Piper, "Efficient diode double-end-pumped Nd:YVO_4 laser operating at 1342 nm," Opt. Express **11**, 2411–2415 (2003).

17. I. Hosako, N. Sekine, M. Patrashin, S. Saito, K. Fukunaga, Y. Kasai, P. Baron, T. Seta, J. Mendrok, S. Ochiai, and H. Yasuda, "At the dawn of a new era in terahertz technology," Proc. IEEE **95**, 1611–1623 (2007).

18. E. Bründermann, H. W. Hübers, and M. F. G. Kimmitt, *Terahertz Techniques* (Springer, USA, 2012).

5. Surface-emitted resonator polariton lasers

The terahertz absorption coefficients calculated in Chapter 3 predicted strong limitations to the detection of THz fields above 4.2 THz in the linear configuration, which was experimentally confirmed in Chapter 4 for KTP and RTP crystals. The transmission losses in the detection system were also identified to be high, however the detection equipment utilised in this research, particularly the Golay cell and the long pass filter LPF14.3 (to prevent scattered near-infrared light from impinging on the Golay cell) was similar to that utilised in other experiments which had successfully detected terahertz radiation from KTP and KTA at frequencies as high as 6.43 THz [1,2]. The main difference between the linear system described in Chapter 4 and those externally pumped TPOs reported in [1] and [2] is that the TPOs were configured in the surface-emitted (SE) layout, instead of a linear layout with Si-prisms to out-couple the THz field.

In the surface-emitted configuration the THz field generated at the surface of the nonlinear crystal is refracted directly into the air, as explained in Chapter 2, which virtually eliminates the absorption losses inside the material and also eliminates the need for Si-prisms. The possibility of better extracting the THz field from the SPS crystal thus motivated the

investigation of the surface-emitted layout in the intracavity design. The strategy was highly successful, and this chapter reports the results obtained with the THz polariton laser in surface-emitted configuration for three different nonlinear materials. First, substantial improvements in the performance of a system based on magnesium oxide-doped lithium niobate are described in Section 5.1, as a result of the deposition of a protective Teflon coating on the crystal. These great results have been published in Optics Express [3] and this publication is reproduced in the Appendix. Secondly, terahertz output could be extracted from KTP, and the first intracavity THz polariton laser based on KTP is reported in Section 5.2. The surface-emitted configuration was also investigated in RTP for the first time, and as detailed in Section 5.3, it exhibited wide frequency-tunability and delivered the highest average THz output power of all investigated configurations.

5.1. MgO:$LiNbO_3$ crystal

Magnesium oxide-doped lithium niobate has been extensively investigated in surface-emitted configuration in externally pumped systems [4–7] but little work has been reported in the intracavity layout. Indeed, a single report was found in the literature of an intracavity MgO:LN in SE configuration [8], in which a maximum pulse energy of 283 nJ was detected at 1.54 THz, and the system was continuously tunable from 0.75 – 2.75 THz. This was obtained with a side-pumped arrangement, a 350º stack of quasi-CW diode arrays delivering 595 mJ pump pulses; the MgO:LN crystal utilised was also relatively large compared to the systems reported here, measuring $70 \times 46 \times 5\ \mathrm{mm}^3$ in the *x*, *y* and *z* crystallographic direction respectively. As a stepping stone for developing Macquarie University's expertise on the surface-emitted layout, the first THz polariton laser assembled in surface-emitted configuration was based on an intracavity MgO:LN crystal. Valuable improvements were achieved with this investigation, and the results detailed in this section were reported in the literature [3].

5.1.1. Laser design

In the surface-emitted configuration the SPS crystal is designed in such a geometry that both fundamental and Stokes resonator fields experience total internal reflection (TIR) inside the nonlinear crystal, and the phase matching angles result in a THz field being generated at

approximately normal incidence on the TIR surface, and so the terahertz output is refracted directed into the air, as already explained in the first two chapters of this thesis. The layout of the THz polariton laser in SE configuration is shown in Figure 5.1. The nonlinear crystals under investigation were cut at with a trapezoidal geometry, and the TIR surface was the longer base of the trapezoid. The length of the resonators and all the other optical components for the fundamental and Stokes cavities were the same as those utilised in the linear design. The external angle between the fundamental and the Stokes resonators was adjusted by rotating the Stokes cavity mirrors, which were mounted on independent rotation stages (Thorlabs PR01; 5 arcmin resolution) enabling fine tuning of the interacting angle.

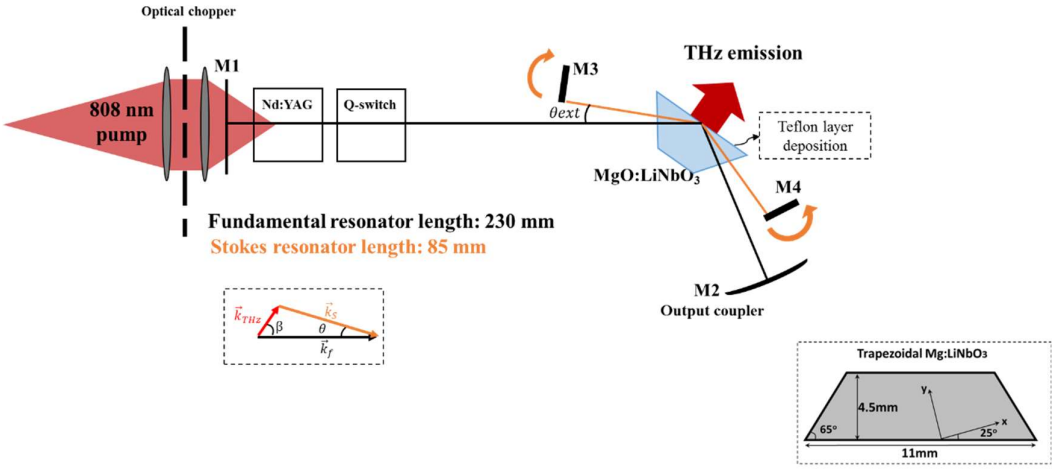

Figure 5.1 – Layout of the THz polariton laser in surface-emitted configuration. The same fundamental and Stokes resonator were utilised for the three different nonlinear crystals evaluated (MgO:LN, KTP and RTP).

The nonlinear material utilised in this assembly to satisfy the geometrical and phase-matching condition for the surface-emitted configuration was a trapezoidal 5 at.% MgO:$LiNbO_3$ crystal with base angle of 65˚, longer base of 11 mm, 4.5 mm height and 8 mm thickness in the crystallographic *z*-axis direction (Castech Inc., China). The crystallographic *xy* plane orientation with respect to the crystal geometry is represented in Figure 5.2. The end faces of the material were polished to a high standard (10/5 scratch/dig) and anti-reflection coated for the fundamental and Stokes wavelengths (R<0.2%@1060 - 1090 nm) and the TIR surface was initially optically polished by the

manufacturer to a standard quality (80/50 scratch/dig). In the first experiments, presented in Section 5.2.2, the crystal was used as provided. For reasons which will be clarified later in this chapter, a protective Teflon layer (AF Amorphous Fluoroplastic Solutions; AF 2400; The Chemours Company, USA; Material data sheet in the Appendix) was applied to the TIR surface, and a comparative evaluation of the crystal with and without this coating was performed as detailed in Section 5.2.5. The complete assembly of the THz polariton laser with the MgO:LN in SE configuration is shown in Figure 5.3

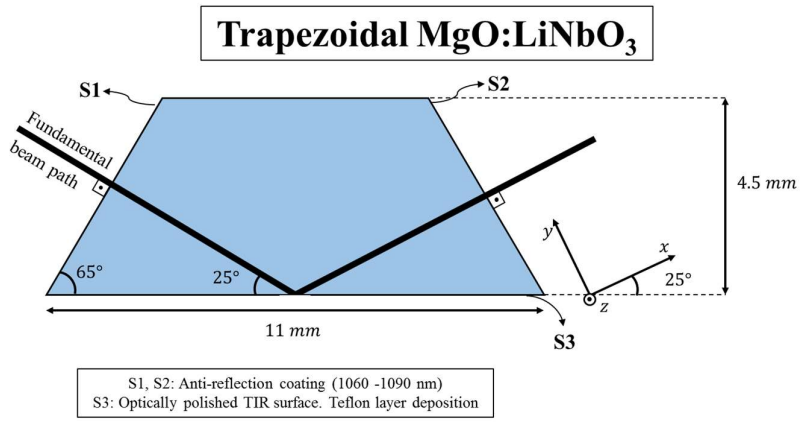

Figure 5.2 – The trapezoidal 5 at.% MgO:$LiNbO_3$.

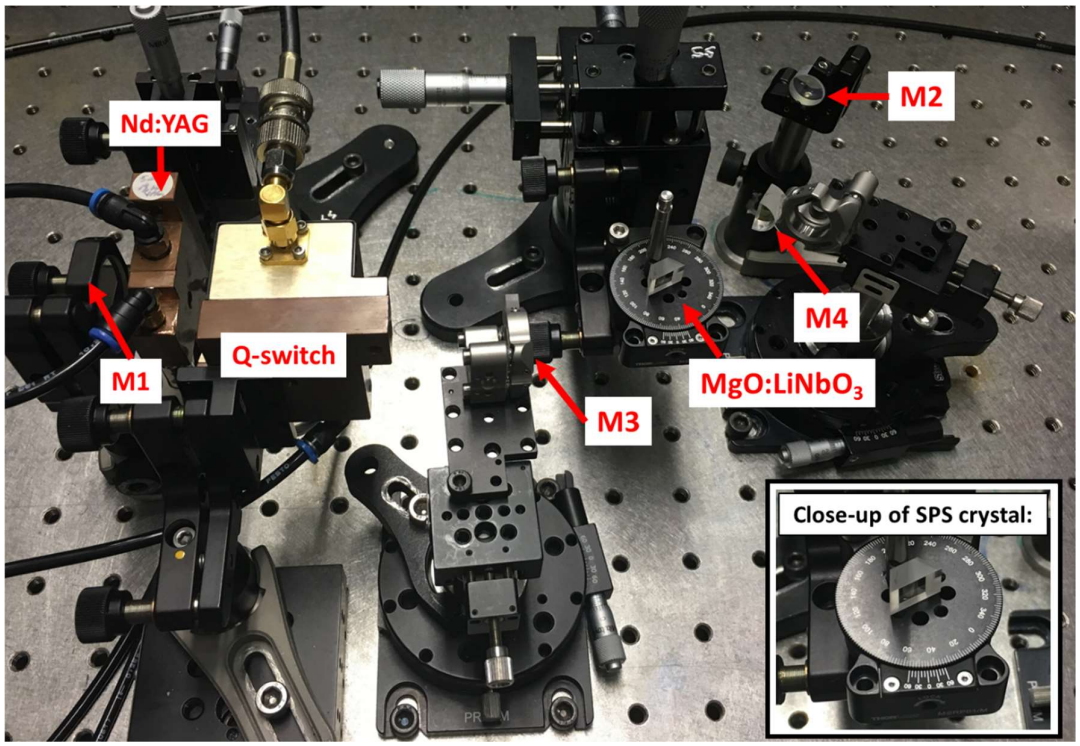

Figure 5.3 – THz polariton laser with 5 at.% $MgO:LiNbO_3$ in surface-emitted configuration.

5.1.2. Performance with unprotected TIR surface

The system power transfer for the fundamental and SPS fields is plotted in Figure 5.4 for the most efficient SPS generation at 1071.0 nm Stokes (1.76 THz). Fundamental field threshold was achieved at 0.6 W diode input (determined by extrapolating the experimental data) and the lowest SPS threshold was reached at 2.8 W. With the 1064 nm output power at this pump level (150 mW), the output coupling percentage (0.6%), the cavity mode inside the crystal (230 μm radius) and the measured pulse width (125 ns FWHM) the calculated SPS threshold intensity is around 40 MW/cm^2. This value is higher than what was reported for other linear intracavity systems (12 MW/cm^2 reported in [9] and 8.2 MW/cm^2 reported in [10]), but is smaller than the 90 MW/cm^2 reported in [8] for another intracavity MgO:LN in SE configuration. The power transfer of the system with the unprotected MgO:LN crystal was limited to 4 W diode pump input, above which laser damage to the TIR surface was observed (appeared to be damage to the external surface). At the limit of laser damage an average output power of 20.1 μW was detected at 1.76 THz with fundamental field depletion in excess of 44%. The interacting angle was adjusted from $\theta = 0.7 - 1.4°$ for a 3 W diode pump (to avoid laser

damage) and wavelength-tunable Stokes radiation from 1070.1 to 1075.1 was detected, with corresponding frequency-tunable terahertz fields from 1.50 – 2.81 THz being detected with the Golay cell.

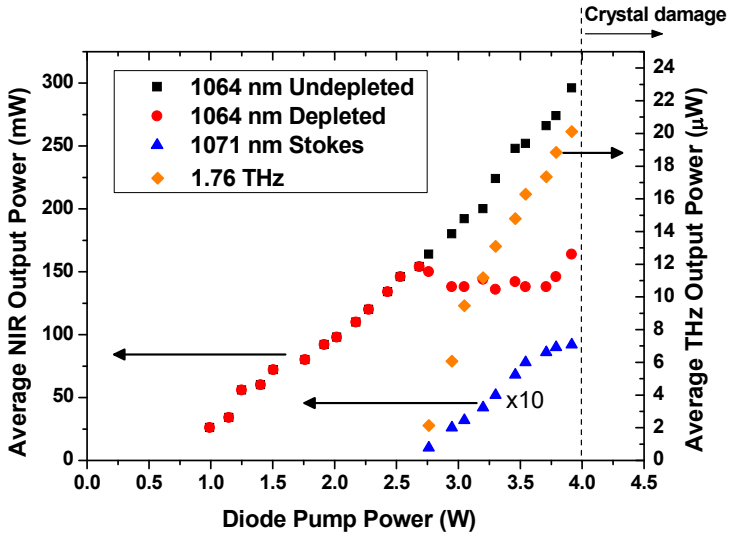

Figure 5.4 – Power transfer for the fundamental 1064 nm (depleted and undepleted), 1071.0 nm Stokes (magnified 10 times) and 1.76 THz fields without the protective Teflon coating on the MgO:$LiNbO_3$.

The horizontal beam profile for the THz radiation propagating in free space was measured with a knife-edge mounted on a precision translation stage (Thorlabs PT1/M; 10 μm resolution). In the knife-edge technique, a blocking element (knife) is translated across the beam cross-section and optical power is measured (Figure 5.5). The terahertz radiation is expected to be produced in a close to Gaussian profile [11], and in this case the Gaussian best-fit of the derivative of the knife-edge intensity profile yields the spatial beam profile [12]. The knife was manually translated (50 μm step size) and the transmitted THz signal monitored, and the profile typical from a knife-edge is plotted in Figure 5.5 together with the smoothed curve. The derivative of the smoothed knife-edge curve provides a Gaussian beam with 2.0 mm ($1/e^2$) horizontal beam diameter at 1 mm from the TIR surface, and this is also plotted in Figure 5.5. This value is slightly higher than the ~1.1 mm horizontal mode size of the interacting fields at the TIR surface (460 μm diameter ÷ cos(65º)). The minimum distance for the knife-edge measurements (1 mm) was limited by the mechanical mounts of the crystal and the knife edge.

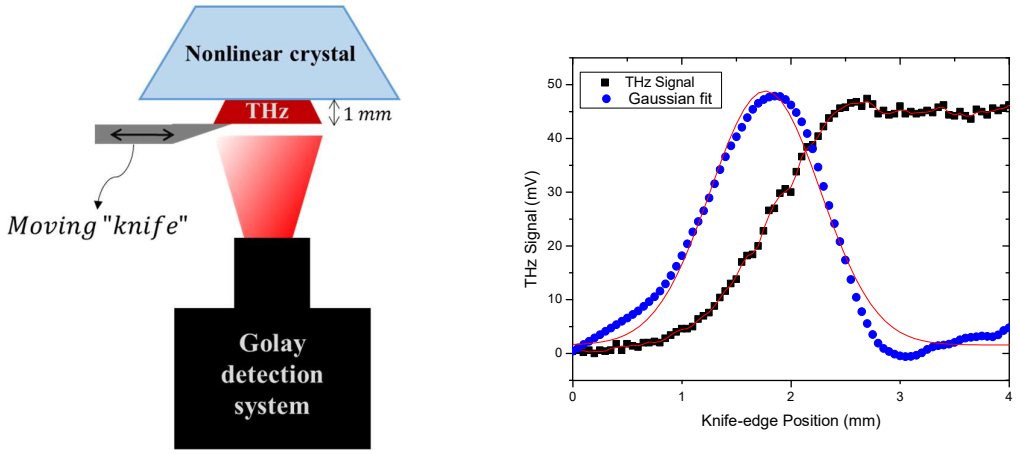

Figure 5.5 – Knife-edge measurements layout, and experimental results of the horizontal beam profile after 1 mm propagation in free space from the TIR surface. The Gaussian best-fit of the derivative of the knife-edge measurements indicates a 2.0 mm horizontal beam diameter.

These preliminary results were very promising, with a 3-fold increase in the output power obtained over the linear configuration [10], despite the limitations to the diode pump power. It was evident that the terahertz output power was limited by laser damage to the MgO:LN crystal bounce surface, and this issue was investigated.

5.1.3. Laser damage threshold of MgO:$LiNbO_3$ crystal

The literature concerning laser-induced damage of lithium niobate is somewhat complex, and there are three main categories of damage, being laser-induced surface and bulk damage, and photorefractive damage. The laser-induced damage of lithium niobate is affected by the occurrence of photorefractive damage (mainly in the bulk). Dopants such as MgO which are added to reduce photorefractive damage are found to actually reduce the laser induced damage threshold [13]. For a 5% MgO doping concentration, a bulk damage threshold of 2.5 J/cm^2 was reported in [13] (1053 nm, 25 ns pulses). It is common for the surface damage threshold to exceed the bulk damage threshold in $LiNbO_3$, and these were respectively reported to be 22 J/cm^2 and 12 J/cm^2 in [14] for a 1064 nm, 10 ns/pulse laser. I was unable to find corresponding data for MgO:$LiNbO_3$ in the literature.

Considering the 300 mW average output power at 1064 nm for a 4 W diode pump, the fundamental mode size inside at the TIR surface (570×230 µm ellipse) and the transmission of the output coupler (M2), the fluence of the fundamental field at the TIR surface can be

estimated to be around 3 J/cm^2 at 4 W diode pump, and this is significantly lower to what was reported for the undoped lithium niobate. It was noted that the laser damage to the TIR surface occurred more frequently during alignment of the Stokes cavity mirrors, during the onset of the SPS process. When the SPS fields are stable, the fluence is lower (~2 J/cm^2) due to depletion of the fundamental field. These observations are consistent with the 2.6 J/cm^2 surface damage threshold reported in [15]. The surface damage threshold is also influenced by surface roughness [16,17], and it is noted that the crystal's input faces which were polished to a higher quality figure (10/5 in comparison to the 80/50 for the TIR surface) were not damaged during power transfer. In consultation with the manufacturer, however, we were informed that it would not be possible to increase the surface quality of the TIR surface of the crystal. To remove the damaged spots the TIR surface was re-polished to the same standard (80/50) by the crystal manufacturer.

5.1.4. Protective Teflon coating

The application of a protective Teflon coating to the TIR surface of the MgO:$LiNbO_3$ crystal was investigated as an alternative to improve the laser damage resistance. The premise here is that the Teflon coating will to prevent the interaction of the evanescent wave field of the totally internally reflected field with imperfections and impurities on the crystal surface; this is an approach which has successfully been used in other solid state lasers [18,19]. When the incident angle θ_i of an electromagnetic field at an optical interface between two media is above the critical angle (θ_c), the field experiences total internal reflection (TIR), and the refraction angle θ_t assumes a complex value giving rise to a transmitted plane wave ($\boldsymbol{E_t}$) which exponentially decays, and can be described by [20]:

$$\boldsymbol{E_t} = \boldsymbol{E_0} e^{jk_x h} = \boldsymbol{E_0} e^{-hx} \tag{5.1}$$

and

$$k_x = \left(\frac{2\pi}{\lambda}\right) n_t \cos\theta_t \tag{5.2}$$

where k_x is the component of the wave-vector normal to the TIR surface, λ is the radiation wavelength, h is the evanescent wave decay coefficient defined by $k_x = jh \quad \left(j \equiv \sqrt{-1}\right)$, and

n_t is the refractive index of the media to which the radiation is transmitted. The evanescent wave decay coefficient can be rewritten as:

$$h = \frac{2\pi}{\lambda} n_t \left[\left(\frac{\sin \theta_i}{\sin \theta_c} \right)^2 - 1 \right]^{1/2} \tag{5.3}$$

For a protective Teflon coating ($n_t = 1.3$ at 1064 nm) at an incident angle of 65˚ at an MgO:LN-Teflon interface, the attenuation of the evanescent wave amplitude was calculated and plotted versus the Teflon thickness as shown in Figure 5.6. According to the plot a ~120 nm-thick Teflon layer would be sufficient to lead to a 1/*e* attenuation of the evanescent wave field amplitude to its value at the MgO:LN/Teflon interface, and this thickness was considered as a minimum thickness that should result in a substantial reduction of the evanescent wave intensity at the air interface. This level of attenuation should be sufficient to prevent any laser-induced damage at power levels encountered in the systems under investigation.

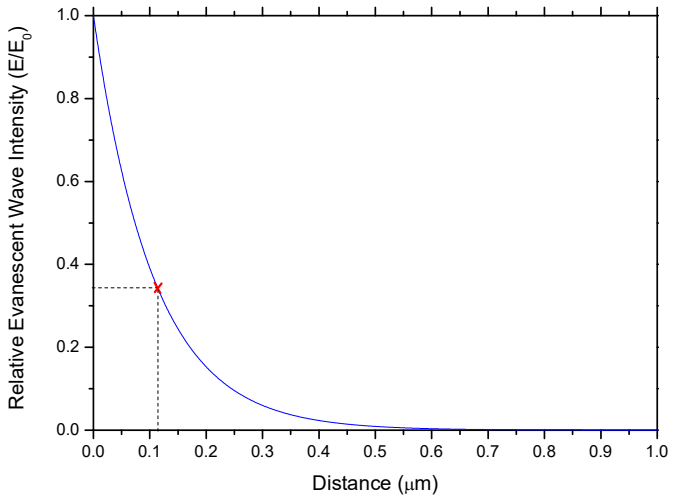

Figure 5.6 – Evanescent wave amplitude attenuation versus Teflon layer thickness. A 120 nm-thick Teflon layer is sufficient to attenuate the amplitude to 1/e of its initial value (red cross).

A solution of Teflon (AF Amorphous Fluoroplastic Solutions; AF 2400; The Chemous Company, USA) was deposited on the TIR surface using spin-coating, and the material was

solidified by heating the coated crystal to evaporate the solvent present in the applied layer [21]. Prior to the deposition on the crystal, microscope slide samples were spin-coated in house (WS-400BZ-6NPP, Laurell Technologies Inc., USA) with the AF 2400 solution at three different rotation speeds (1000, 2000 and 3000 rpm for 60 s; and heated for 5 minutes at 112˚C), to evaluate the effect of the rotation speed on the layer thickness [21]. The thickness of the Teflon layer deposited on the samples spin-coated at different rpm's was measured with a surface profiler (Tencor Alphastep 500) and the results are plotted in Figure 5.7. From the plot it can be noted that a 2000 rpm spin rate was sufficient to produce a ~150 nm-thick layer. The surface profiler has a depth-sensitive needle, and to measure the coating thickness deposited on the samples I scratched the deposited layers with a blade, producing a physical gap in the coating material, and the depth of from the top of the Teflon layer to the microscope slide substrate was measured with the needle. This destructive measurement technique should not be applied to the laser crystal. For this reason the value measured for the microscope slide samples was considered to be equivalent to the layer thickness to be deposited on the crystal. A single layer of Teflon was then deposited on the TIR surface of the MgO:LN crystal at 2000 rpm for 60 s and heated for 5 minutes at 112˚C and the resulting thickness of the layer (~150 nm) was considered sufficient to neglect the effects of the evanescent wave field. The absorption coefficient of Teflon is below 4 cm^{-1} in the terahertz frequency range of interest [22], indicating that less than 0.01% of the THz radiation would be absorbed during a 150 nm propagation.

The potential use of the Teflon layer as an anti-reflection coating for the THz field was also investigated as a means to reduce the Fresnel losses associated with extraction of the THz field. With the refractive index data calculated in Chapter 3 for the THz fields ($n \sim 5.5 - 6$), Fresnel losses in the order of 50% are expected in the MgO:LN for angles close to normal incidence. However it is anticipated that the single layer of Teflon was not expected to act as a thin-film interference coating for the THz radiation because its thickness was around three orders of magnitude lower than the wavelength of the THz fields (75 – 200 μm).

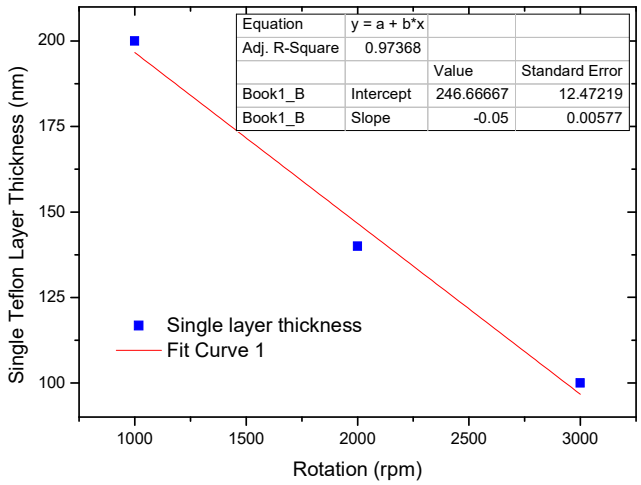

Figure 5.7 – Single Teflon-layer thickness versus spin-coating machine rotation speed for microscope slide samples. Samples were spun for 60 s, followed by 5 minutes heating at 112ºC. A 2000 rpm rotation speed was found to be sufficient to produce a Teflon-layer with thickness greater than 120 nm (a thickness that results in a 1/*e* attenuation of the evanescent wave at 1064 nm).

5.1.5. Performance with Teflon-coated TIR surface

The magnesium oxide-doped lithium niobate crystal with the protective Teflon layer on the TIR surface was inserted in the resonator, and the laser was realigned. No laser-induced damage was observed, even when pumping with powers of 4 W and higher. However, at 6 W diode pump the undepleted 1064 nm field rolled over due to the strong thermal lensing in the fundamental resonator (despite the chopped pump diode), which limited the diode pump level. The laser damage threshold for the Teflon coated crystal could not be determined in this experiment, yet it could be inferred that an increase in damage threshold of at least 50% over the unprotected material was obtained, by considering the maximum output power at the fundamental wavelength which could be tolerated in both cases (450 mW maximum 1064 nm output with the coated material versus 300 mW with the unprotected crystal).

The system was power transferred and plots of the fundamental (depleted and undepleted), 1071.0 nm Stokes and 1.76 THz fields are shown in Figure 5.8. The threshold for the fundamental field was not affected by the re-polishing and Teflon deposition coating. The SPS threshold however showed a small increase (17%) to 3.3 W, and this may originate from the interaction of the fundamental field with slightly different regions in the crystal bulk and

there may be corresponding local variation in the SPS gain (due to impurities, local defects, etc.). This also impacted on the SPS threshold intensity, increasing it to about 66 MW/cm^2 (considering 240 mW average 1064 nm output power and the measured 121 ns pulse width at SPS threshold). The possibility of pumping the system harder enabled an increase in the detected THz signal, as expected. A maximum average output power of 58.6 µW was detected at 1.76 THz for a 6.5 W diode pump power input, with fundamental field depletion exceeding 55%. This represents an 8-times increase in maximum THz power that could be detected, in comparison to the linear resonator reported in [10], and a diode-to-THz conversion efficiency of 8.7×10^{-4}%, double the value obtained in [23] and one order of magnitude over [8]. Worth noting that this THz frequency also does not correspond to where we expect the highest THz power to be achieved (see Stokes gain curve, Figure 3.7), suggesting that the efficiency of the system could be increased further.

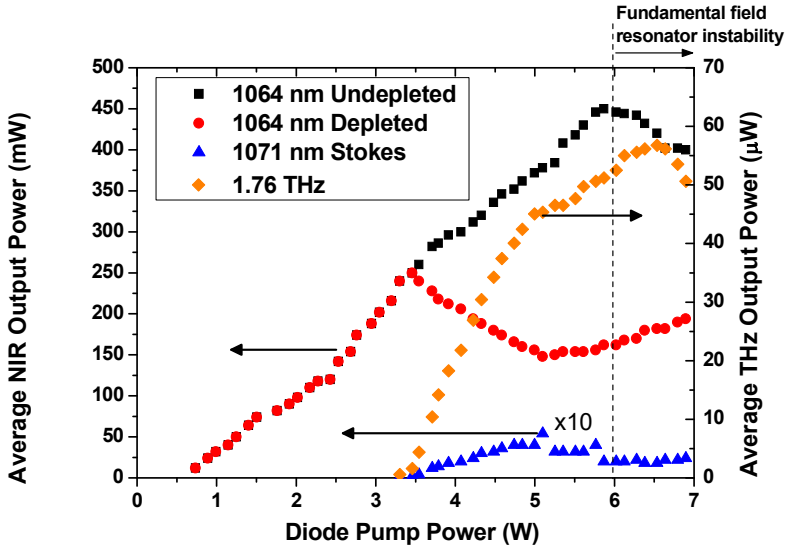

Figure 5.8 – Power transfer for the fundamental 1064 nm (depleted and undepleted), 1071.0 nm Stokes (magnified 10 times) and 1.76 THz fields with the protective Teflon layer on the MgO:$LiNbO_3$ TIR surface.

The temporal behaviour of the fundamental (depleted and undepleted) and 1071.0 nm Stokes fields measured at maximum THz emission (6.5 W pump), is shown in Figure 5.9. The fundamental pulse width decreased from 126 ns to 53 ns (FWHM) as a consequence of depletion, and the 1071.0 nm Stokes pulse was measured to build up with a 77 ns delay from the fundamental pulse, with a measured width of 18 ns (FWHM). The ratio between the areas

of the depleted and undepleted 1064 nm pulses indicates a fundamental field depletion of 59%, correlating well with that estimated from the power transfer curves.

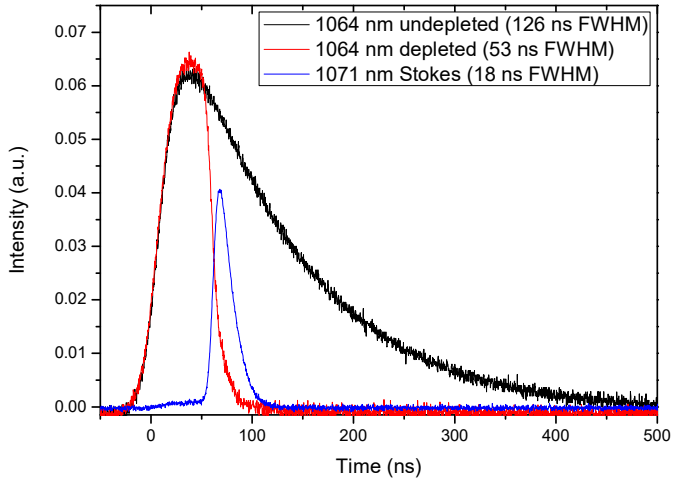

Figure 5.9 – Temporal profiles of the 1064 nm fundamental (depleted and undepleted) and 1071.0 nm Stokes fields at maximum THz output (6.5 W diode pump power).

Improvements in the frequency-tuning range of the SPS laser with the protective Teflon layer on the nonlinear crystal were also observed. When the interacting angle was adjusted from $\theta = 0.7 - 1.8°$, wavelength-tunable Stokes radiation was detected from 1070.0 to 1079.2 nm, and corresponding terahertz frequencies continuously tunable from 1.46 – 3.84 THz were detected. The plot in Figure 5.10 shows the frequency coverage of the terahertz field for the unprotected and the Teflon-coated MgO:$LiNbO_3$ with the diode pump at each point optimised for the maximum THz signal from the Golay cell. The pump powers at which maximum THz power was achieved at each frequency varied between 3 and 4 W for the unprotected crystal and between 5 and 7 W for the Teflon-coated material. The substantial 83% increase in frequency coverage with the protective Teflon coating is attributed to the increase in laser damage resistance that enabled a higher diode pump power to be utilised, and consequently enabled SPS threshold to be reached at higher THz frequencies. The THz beam profile was not measured in this case but it is expected to remain similar to the 2.0 mm previously measured.

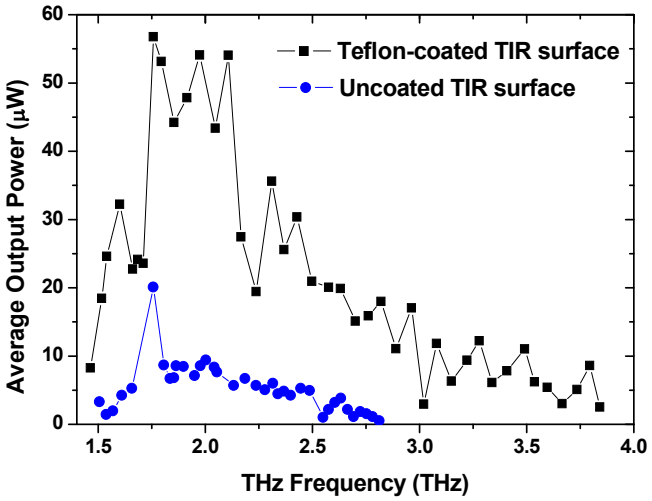

Figure 5.10 – Comparative plot of terahertz frequency-coverage of the system with the unprotected nonlinear crystal and after the deposition of a Teflon layer on the TIR surface. In each case, the diode pump power was adjusted to obtain a maximum average THz output power.

Magnesium oxide-doped lithium niobate is probably the most important nonlinear material for frequency-tunable THz generation via stimulated polariton scattering, and laser damage to the crystal has been often reported as a liming factor in performance [8,24,25]. With the application of a single Teflon-layer to the crystal's TIR surface utilising the simple spin-coating technique it was possible to augment the system tolerance to the intracavity field intensity and higher diode pump powers were enabled. As a consequence, the system delivered higher average terahertz output power and also a significantly wider frequency-tunability. It is of particular importance to note that with the surface-emitted geometry and with the deposition of the Teflon coating, frequencies approaching 4 THz were detected from MgO:LN, and this is substantially higher than the ~3 THz maximum frequency typically detected from this crystal. Terahertz signal at such high frequencies were recently reported from an externally-pumped MgO:LN, however it relied on injection-seeded system of notably greater complexity [26].

This enhancement in performance offered by the Teflon coating could be readily translated to other intracavity systems and also externally pumped THz parametric oscillators. The experimental knowledge acquired with the assembly of the MgO:LN in surface-emitted configuration was utilised to extend the investigation to KTP and RTP crystals, with the

objective of producing terahertz sources with frequency-tunable THz output at higher frequencies (~4 – 6 THz), expanding the frequency coverage of the available sources.

5.2. $KTiOPO_4$ crystal

In Chapter 4 a linear terahertz polariton laser based on an intracavity KTP crystal was assembled and wavelength-tunable Stokes radiation was successfully produced via SPS, corresponding to frequencies from 4.29 – 6.02 THz being generated inside the material. The high absorption coefficients calculated in Chapter 3 indicated that the THz fields at such frequencies would be strongly absorbed inside KTP, imposing serious limitations to the detection of terahertz signal, and in fact no THz wave could be detected from the system. In the surface-emitted configuration, the propagation losses are avoided for the THz fields generated at the TIR surface of the crystal, and terahertz fields are expected to be refracted into the air across the entire SPS range, facilitating detection. Thus, following from the work on the surface-emitted MgO:LN crystal, a KTP crystal in surface-emitted configuration was examined.

The nonlinear material utilised in this assembly was a trapezoidal $KTiOPO_4$ crystal with base angle of 60˚, longer base of 12 mm, 5 mm height and 8 mm thickness in the crystallographic *z*-axis direction (Crystech Inc., China). The crystallographic *xy* plane orientation with respect to the crystal geometry is represented in Figure 5.11. The material was supplied with the end faces polished to high quality (10/5 scratch/dig), and anti-reflection coated for the fundamental and Stokes wavelengths (R<0.3%@1060 - 1090 nm). The TIR surface was polished to a standard quality (80/50 scratch/dig). The trapezoidal KTP crystal was inserted in the surface emitted resonator described in the previous section (replacing the MgO:LN) and the performance of the system was evaluated.

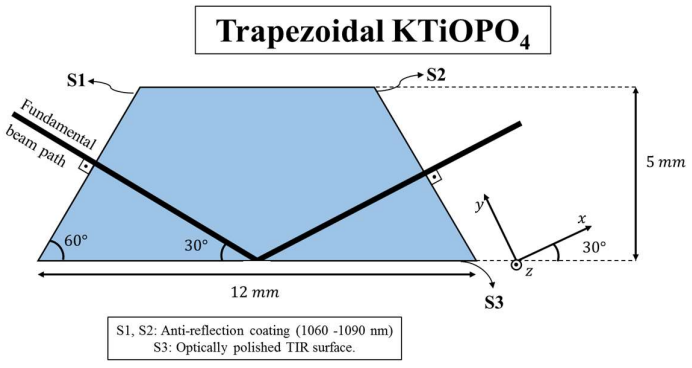

Figure 5.11 – The trapezoidal $KTiOPO_4$.

5.2.1. Performance without an intracavity etalon

The resonators were realigned with the intracavity KTP crystal in surface-emitted configuration. As a result of SPS, wavelength-tunable Stokes radiation from 1080.9 to 1083.4 nm was detected from the Stokes mirror M4 when the interacting angle was adjusted from $\theta \sim 2.0 - 2.8°$, corresponding to polariton frequencies from 4.29 – 4.94 THz. This is a smaller range than that obtained in Chapter 4 for the linear resonator, in which frequencies from 4.29 – 5.91 THz were generated inside KTP when the interacting angle was adjusted from $\theta \sim 2.0 - 3.5°$. This is because for higher interacting angles ($\theta \sim 2.8 - 3.5°$) the spectral output of the Stokes resonator used in the surface-emitted configuration cavity contained additional infrared radiation at a fixed wavelength of 1095.5 nm, and this is attributed to backscattered stimulated Raman scattering at 268 cm^{-1}. The output coupler mirror (M2) prevented this wavelength from lasing in the fundamental resonator, as detailed in Chapter 4. However the broadband coating on the Stokes mirrors were not designed to this end. This SRS line at 1095.5 nm was suppressed with the insertion of an intracavity etalon in the Stokes resonator, as will be discussed in the next section.

Despite the smaller SPS tuning range when compared to the linear layout, the performance of the surface-emitted resonator without the etalon was evaluated first, and frequency-tunable terahertz radiation was successfully detected. This is the first time KTP has been used in an intracavity surface-emitted design. The system was power transferred for the most efficient SPS generation at an interacting angle of $\theta = 2.5°$, and the 1064 nm fundamental (depleted and undepleted), 1081.5 nm Stokes and 4.46 THz field outputs are plotted in Figure 5.12. Fundamental threshold was achieved for 0.6 W diode pump power, and SPS threshold was reached at 4.1 W. With the 1064 nm output power at this pump level (400 mW), the output coupling percentage (0.6%), the cavity mode inside the crystal (230 μm radius) and the measured pulse width (115 ns FWHM), the calculated SPS threshold intensity is around 116 MW/cm^2. The calculated SPS intensity at threshold was substantially higher than that obtained in the linear configuration (69 MW/cm^2) and yet is comparable to that obtained for the externally pumped KTP TPO using a surface-emitted configuration, reported in [2]. This suggests that different thresholds might be expected in linear or SE configurations. A maximum average output power of 59.0 μW was detected at 4.46 THz, for a 6.7 W diode pump, with depletion in excess of 58%. Above this pump level, the THz and near-infrared fields decreased in power due to strong thermal lensing. No laser damage to the TIR surface was observed in

KTP within the context of this experiment suggesting that KTP has a significantly higher laser damage threshold than MgO:LN. The application of Teflon was therefore not pursued in these experiments.

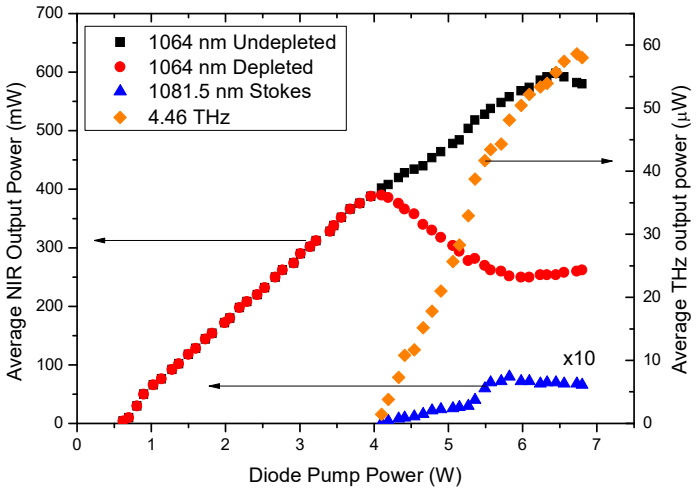

Figure 5.12 – Power transfer for the fundamental 1064 nm (depleted and undepleted), 1081.5 nm Stokes (magnified 10 times) and 4.46 THz fields in the $KTiOPO_4$ crystal in surface-emitted configuration without the intracavity etalon.

This was the first time that THz was detected from an intracavity SPS system based on KTP crystal. The power levels detected were superior to what is typically obtained in linear resonators (Chapter 4, and [9,10]) and were comparable to those reported for the surface-emitted MgO:LN in the previous section. With the KTP in surface-emitted configuration, it was possible to detect terahertz radiation across the entire SPS tuning range, from 4.29 to 4.51 THz, and from 4.92 to 4.94 THz as plotted in Figure 5.13 for a 5.5 W diode pump input. In the same figure, the measured Stokes output power is displayed. The gap in THz emission from 4.52 to 4.91 THz corresponds to the infrared A_1 absorbing mode measured at 153 cm^{-1}.

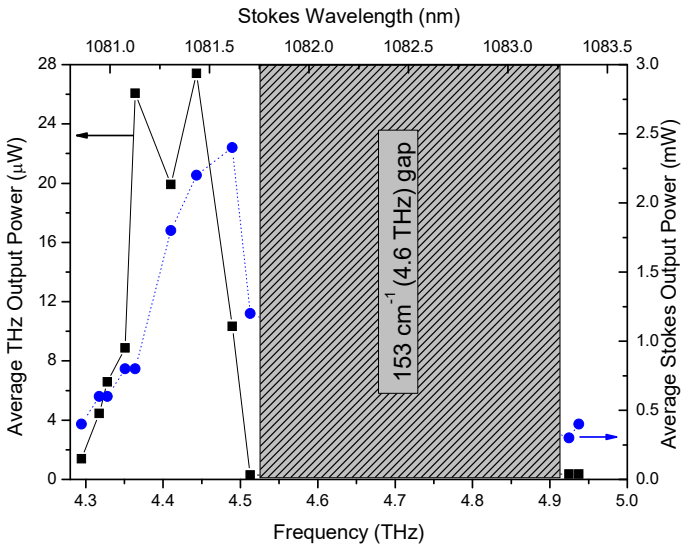

Figure 5.13 – Measured average THz and Stokes output power versus terahertz frequency in the intracavity KTP in surface-emitted configuration without the intracavity etalon in the Stokes resonator at 5.5 W diode pump.

The assembly of the surface-emitted resonator with the intracavity KTP crystal overcame the factors that limited terahertz detection in the linear configuration. These results complement the prediction from Chapter 3 and the experimental results from Chapter 4, strongly indicating that absorption of the THz fields inside the SPS crystals was indeed the limiting factor for THz detection above 4.2 THz in the linear configuration.

However, the presence of the SRS line at 1095.5 nm in the Stokes resonator for interacting angles above $\theta = 2.8°$ was supressing the generation of SPS fields at higher frequencies, limiting the polariton field to a maximum 4.94 THz frequency, as opposed to the 5.91 THz observed in the linear resonator (Chapter 4). This undesired line, attributed to a 268 cm^{-1} backscattered Raman shift in KTP, indicates that in the SE resonator assembly, the Raman gain is somehow more significant with respect to the SPS gain, when compared to what was produced in the linear resonator (Chapter 4). A higher Raman gain relative to the SPS gain would give rise to a competing stimulated Raman scattering in the Stokes cavity. The smaller dimension of the SPS crystal along the fundamental and Stokes cavity axes for the trapezoidal material in comparison to the linear cuboid was investigated as the potential origin for this different behaviour. In the linear resonator, the maximum effective interacting length for the SPS fields inside the cuboid KTP is the proper crystal length along the resonator axis, which

was 20 mm (Chapter 4). This value is smaller in the surface-emitted geometry, and is limited to a maximum of 10.4 mm for the trapezoidal KTP (Figure 5.14).

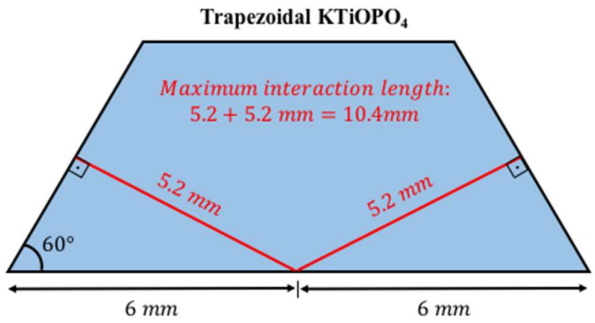

Figure 5.14 – Maximum interaction length in the surface-emitted KTP trapezoid with 12 mm base length.

Considering both fundamental and Stokes fields to have a constant beam radius inside the SPS crystal given respectively by w_1 and w_2, the interacting length for the SPS fields for a given interacting angle ($L(\theta)$) can be estimated (to an upper limit) with the following expression:

$$L(\theta) = L_1 + L_2 = \left(\frac{w_1}{\tan\theta}\right) + \left(\frac{w_2}{\sin\theta}\right) \tag{5.4}$$

where the distances L_1 and L_2 are represented in Figure 5.15.

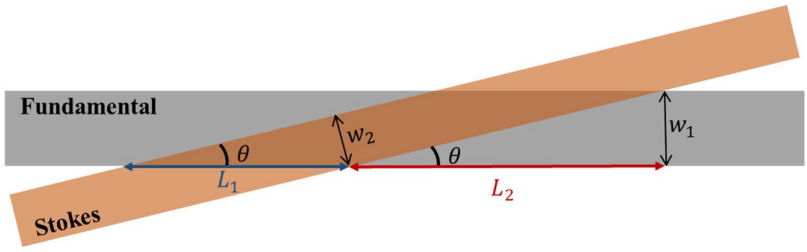

Figure 5.15 – Estimate of the interacting length for a fundamental field (mode radius w_1) and a Stokes field (mode radius w_1) interacting at an angle θ. To facilitate for the reader, the diagram is sketched for a linear geometry,

however, the same is valid for a surface-emitted layout because the mirror reflection does not alter the interacting length.

For a fundamental and Stokes resonator mode radius of $w_1 = w_2 = 230$ µm inside the nonlinear crystal, the interacting length given by equation 5.4 can be calculated as a function of the interaction angle, as plotted in Figure 5.16. From the figure it can be noted that for angles above 2.5º the interaction length $\left(L(\theta)\right)$ decreases below 10.4 mm. This indicates that for interaction angles above $\theta = 2.5°$ the physical dimension of the trapezoid does not impose any geometrical limitation to the interacting SPS fields. Therefore, with regards to the interacting volume of the fundamental and Stokes resonator modes inside the KTP crystal, the trapezoidal geometry was not a limiting factor for the SPS gain from $\theta \sim 2.8 - 3.5°$.

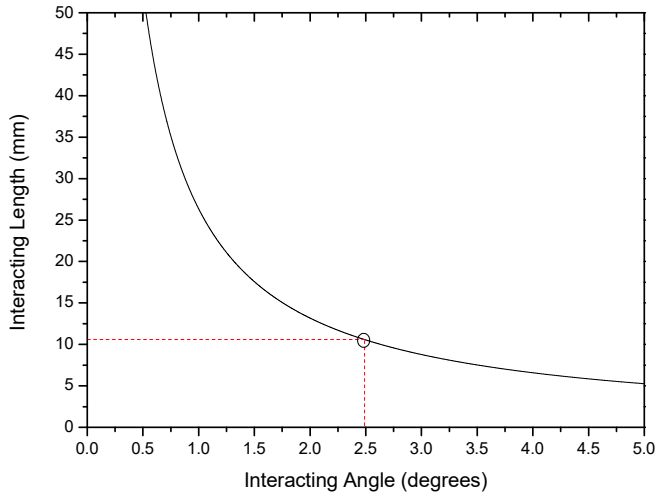

Figure 5.16 – Interaction length versus interacting angle between SPS fields for a 230 µm mode radius for the fundamental and Stokes fields.

Another difference that can be noted from the linear to the surface-emitted resonator is the higher slope efficiency of the 1064 nm field (depleted and undepleted) in the SE resonator. The higher fundamental field power out-coupled from the surface-emitted resonator indicates that higher intracavity fields were being generated inside the resonator, however it would not be straightforward to relate it to the Raman competition observed here. It is also not completely clear why the SPS threshold increased in the SE configuration when compared to the linear resonator from Chapter 4, keeping in mind that the optical components were kept the same,

and the KTP crystals were provided by the same manufacturer. This suggests that the SPS gain equations obtained in Chapter 2, with the assumptions of steady-state SPS fields are likely to be inaccurate to describe the complex dynamics of the intracavity nonlinear SPS phenomena.

Nevertheless, the Raman-shifted line in the Stokes cavity was undesired, and an etalon was inserted in the Stokes cavity with the objective of introducing loss to the 1095.5 nm field, and produce pure SPS emission, as described next.

5.2.2. Performance with intracavity etalon in the Stokes resonator

Frequency-tunable terahertz detection

The presence of the 1095.5 nm Raman line in the Stokes resonator for interacting angles in the $\theta \sim 2.8 - 3.5°$ range was undesired, and the same etalon utilised previously was inserted in the Stokes resonator (250 μm-thick, reflectivity R=30%, fused silica substrate, finesse = 2.5) with the objective of inducing losses to the 1095.5 nm field. The etalon was inserted at near-normal incidence in the Stokes cavity, and at every interacting angle θ the tilt angle of the etalon was optimised for maximum SPS power. With the etalon inside the Stokes resonator the range of interacting angles producing frequency tunable THz radiation was similar to that produced in the linear resonator (Section 4.3.1). For interacting angles from $\theta \sim 2.3 - 3.5°$ wavelength-tunable Stokes radiation was detected from 1080.9 to 1087.2 nm, and the corresponding terahertz frequencies could be detected across the entire SPS tunable range, as plotted in Figure 5.17 for a 5.5 W diode pump power. Also in the same figure, the detected Stokes output is shown. Terahertz radiation continuously tunable from 4.29 – 4.53 THz, 4.88 – 5.03 THz and from 5.47 – 5.89 THz was detected. The gaps in SPS emission corresponding to frequencies from 4.54 – 4.87 THz and from 5.04 – 5.46 THz are located respectively in the vicinity of the 153 and 177 cm^{-1} A_1 modes measured in KTP. The presence of the etalon inside the Stokes cavity limited the minimum interacting angle to $\theta = 2.3°$, and any attempt to reduce the interacting angle below this value would result in clipping of the fundamental beam by the edge of the etalon substrate. The upper limit on the frequency tunable range is attributed to a poor overlap between the fundamental and Stokes beams at higher interacting angles.

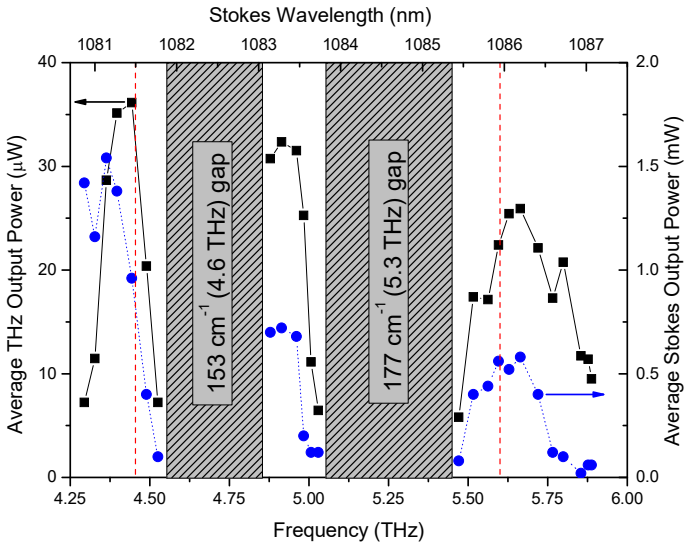

Figure 5.17 – Measured average THz output power and Stokes output power versus terahertz frequency in the intracavity KTP in surface-emitted configuration with the intracavity etalon (250 μm-thick, R=30%, fused silica substrate) in the Stokes resonator. Diode pump power was set at 5.5 W. Vertical dashed lines represents frequencies at which the system was power transferred (4.46 and 5.58 THz).

Power transfer at 4.46 THz and 5.58 THz

The system was power transferred at the same SPS frequency as that before the insertion of the etalon, at 4.46 THz ($\theta = 2.5°$; 1081.5 nm Stokes), and also around the emission peak at a higher frequency, at 5.58 THz ($\theta = 3.0°$; 1085.9 nm Stokes), as plotted in Figure 5.18. The fundamental threshold was again reached at 0.6 W diode pump. For the polariton frequency at 4.46 THz the presence of the etalon did not promote an increase in the SPS threshold, which was measured as 4.1 W diode pump (the estimated intensity at SPS threshold was also similar, 116 MW/cm^2). The maximum average terahertz output power detected at 4.46 THz was 67.4 μW for a diode pump power of 7.3 W, representing a 14% increase over the value measured without the etalon; the pump depletion in this case exceeded 61%.

The SPS threshold for the 5.58 THz generation was reached at 4.9 W diode pump. With the 1064 nm output power at this pump level (440 mW), the output coupling percentage (0.6%), the cavity mode radius inside the crystal (230 μm) and the measured pulse width (115 ns FWHM), the calculated SPS threshold intensity is around 128 MW/cm^2. A maximum average output power of 70.9 μW at 5.58 THz was measured at 7.3 W diode pump (fundamental depletion of 59%), the highest output detected across the entire SPS range for this material, and also a value superior to that detected from MgO:LN.

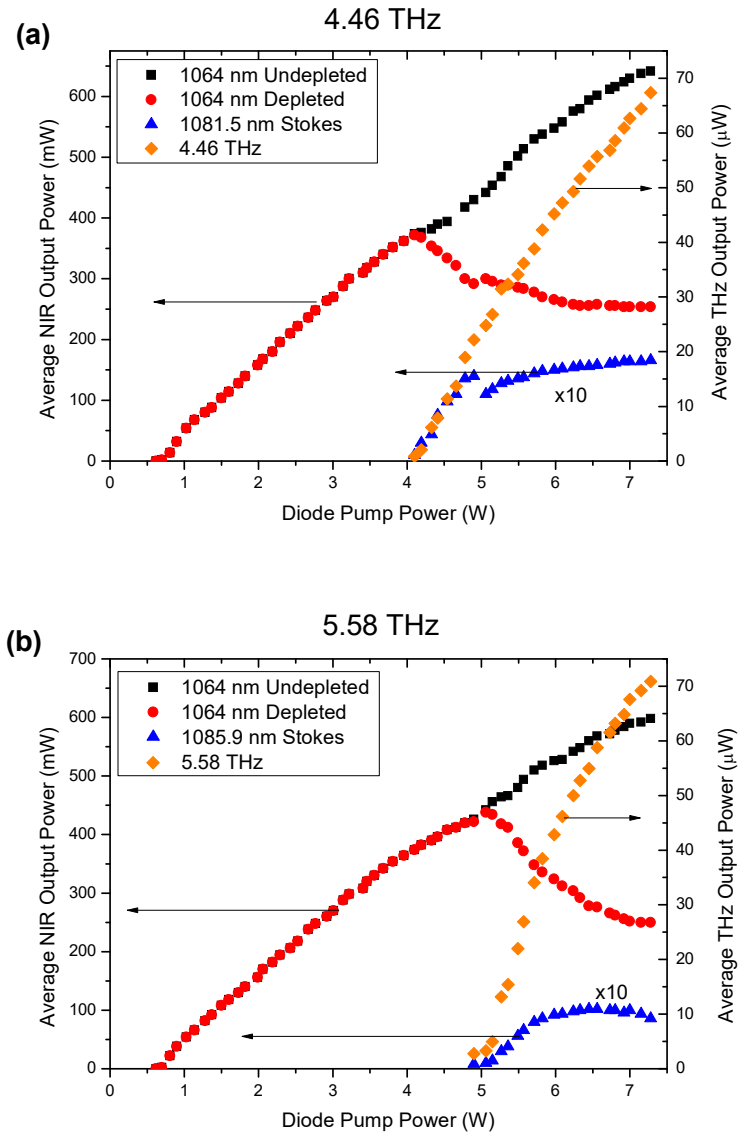

Figure 5.18 – Power transfer for the fundamental 1064 nm (depleted and undepleted) and SPS fields in the $KTiOPO_4$ crystal in surface-emitted configuration with the intracavity etalon (250 μm-thick, R=30%, fused silica substrate). (a) 1081.5 nm Stokes (magnified 10 times) and 4.46 THz fields. (b) 1085.9 nm Stokes (magnified 10 times) and 5.57 THz fields.

The intracavity etalon demonstrated the possibility of reproducing the same SPS tunable range in the surface-emitted configuration as to what was achieved in the linear approach (Chapter 4). However, the fine angle tuning of the etalon at every interacting angle to suppress the 1095.5 nm was required and introduced an inconvenient complexity to the process. Ideally, a solution similar to what was implemented in Chapter 4 to eliminate the competition between SPS and SRS in the fundamental resonator is desired, and a new Stokes mirror was considered,

having sufficient transmission losses at 1095.5 nm but high reflectivity at the Stokes wavelengths. Although, we were informed by different laser mirrors suppliers that the production of such mirror coatings was unfeasible due to the proximity between the Stokes wavelengths (1080-1087 nm) and the 1095.5 nm Raman shift. For this reason, the frequency-tunability of the surface-emitted THz polariton laser based on KTP could not be improved further. It is also important to note that the etalon utilised was not optimised for this experiment, but selected among a limited collection available in the laboratory.

Temporal profile

The temporal characteristics of the fundamental (depleted and undepleted) and 1081.5 nm Stokes output were measured at 6.8 W diode pump, as plotted in Figure 5.19. The fundamental pulse width decreased from 104 ns to 44 ns (FWHM) as a consequence of depletion, and the 1081.5 nm Stokes pulse builds up with a 52 ns delay from the fundamental pulse, with a measured width of 42 ns (FWHM). The ratio between the areas of the depleted and undepleted 1064 nm pulses indicates a fundamental field depletion of 53%, correlating reasonably well with that estimated from the power transfer curves. It is not entirely clear the reason for such a long Stokes field pulse width when compared to the ~20 ns typically observed from these intracavity systems.

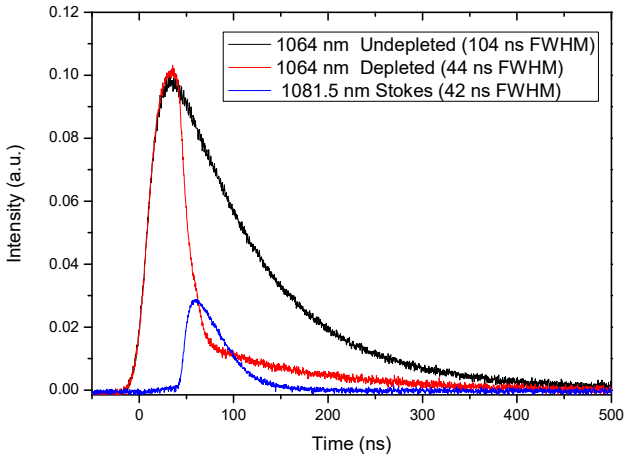

Figure 5.19 – Temporal profiles of the fundamental (depleted and undepleted) and 1081.5 nm Stokes at 6.8 W diode pump power.

Terahertz field polarization

The nature of the SPS process in the system dictates that the fundamental and Stokes fields would be vertically polarised (polarization along the *z*-axis), and the THz signal is also expected to exhibit the same polarization. The polarization state of the terahertz output was inferred with a linear polariser (POL-HDPE-CA25-OD34.9-T7.9, Tydex, Russia) oriented perpendicular to the THz propagation direction (parallel to the TIR surface of KTP), and mounted on a rotation stage (Thorlabs PRM1/M; 5 arcmin resolution). The plot in Figure 5.20 shows the transmitted power at 4.46 THz after the polariser with the transmission axis of the polariser rotated from $0-90°$ with respect to the vertical axis. From the plot it is clear that maximum transmission is obtained with the transmission axis of the polariser is vertically aligned, and hence the terahertz output was confirmed to be vertical (parallel to the crystal's *z*-axis and consistent with the polarization of the Stokes field). From the maximum detected THz signal (32.0 μW) and minimum measurable THz system during these measurements (0.2 μW) a polarization ratio of 160:1 (vertical:horizontal) is calculated.

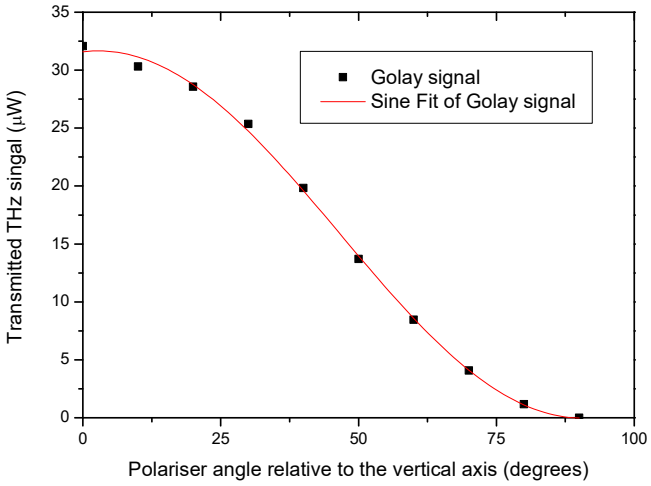

Figure 5.20 – Measurement of the polarization state of the terahertz radiation generated by the KTP crystal in surface-emitted configuration with a linear polariser. The measurements indicate a vertically polarised THz output from the laser.

Terahertz field linewidth

The linewidth of the terahertz field was calculated based on the coherence length of the 4.46 THz radiation. The coherence length (L_{coh}) of electromagnetic radiation propagating in air (propagation velocity c), is related to the linewidth ($\Delta\upsilon$) of the field by the following relation [12]:

$$L_{coh} = \frac{c}{\pi\Delta\upsilon} \tag{5.5}$$

The coherence length of the THz field was measured with a manually adjusted scanning Fabry-Pérot interferometer constructed using two plane-parallel silicon windows (50.8 mm diameter, 0.5 mm thick; Tydex) [27]. One silicon window was fixed in place, and the second was mounted on a precision translation stage (Thorlabs PT1/M; 10 µm resolution). The interferometer was placed with the windows perpendicular to the THz propagation direction, as shown in Figure 5.21. The terahertz signal transmitted by the interferometer versus the separation between the silicon windows (50 µm steps) was monitored with and without the etalon in the Stokes cavity, as plotted in Figure 5.22. For separation distances below the

coherence length, the power transmitted after the interferometer will be a result of the interference in the Fabry-Pérot cavity, and thus will present maximum and minimum intensity depending on constructive and destructive interference [27]. Above the coherence length, the interference pattern vanishes and the transmitted intensity is simply the incident intensity minus the transmission losses of the interferometer (basically Fresnel reflection losses in this case). From the measurements, a coherence length of around 3.3 mm (±0.1 mm, considering a ±1 step uncertainty) was measured in both cases, leading to an estimated linewidth of 29 GHz (±1 GHz). This is comparable to the free-running linewidth observed in other intracavity and externally pumped SPS systems (50 – 100 GHz) [28,29]. The etalon inserted in the Stokes cavity did not promote any linewidth narrowing in the THz field because this is primarily determined by the linewidth of the fundamental field. It is anticipated that the measured linewidth of the terahertz output could be reduced with the insertion of a high finesse etalon in the fundamental and/or Stokes resonators as was reported in [29]. Further investigation of the linewidth was however beyond the scope of this thesis.

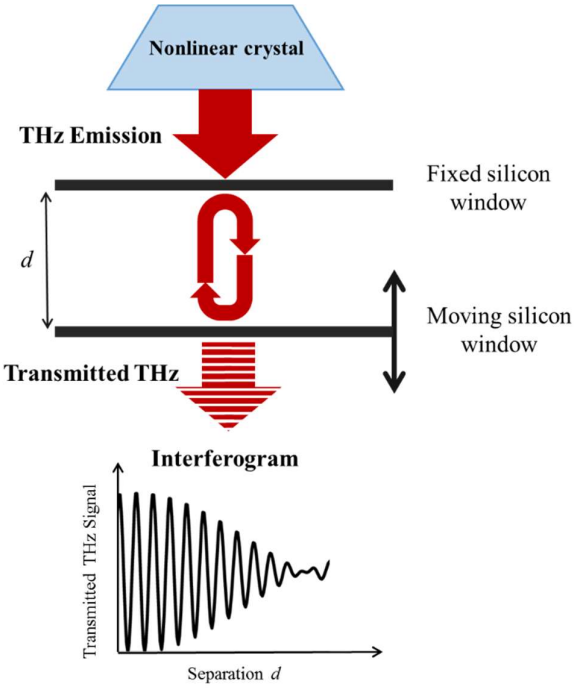

Figure 5.21 – Schematic for linewidth measurements. A Farby-Pérot interferometer composed of two silicon windows is placed on the THz beam path. Power transmitted by the interferometer is monitored versus window separation "*d*".

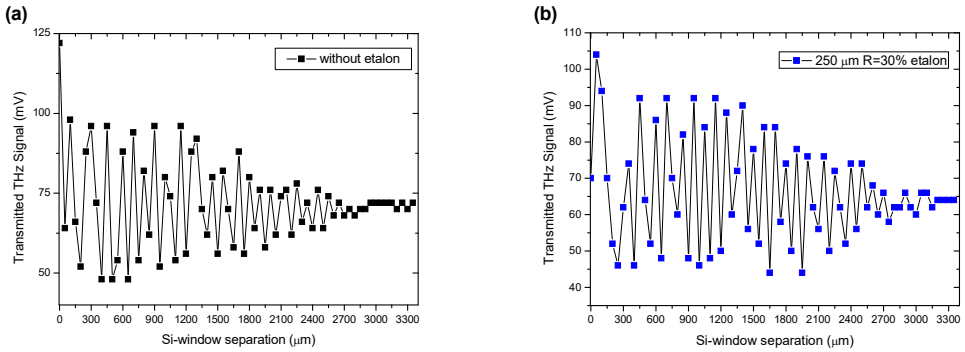

Figure 5.22 – Terahertz signal transmitted by the Fabry-Pérot interferometer versus separation distance between Si-windows. (a) free-running laser, without etalon in Stokes cavity. (b) with 250 μm-thick, R=30% etalon in Stokes cavity. Measured coherence length is 3.3 mm (±0.1 mm) and calculated linewidth 29 GHz (±1 GHz) in both cases.

Terahertz beam spatial profile

The THz output power delivered by the surface-emitted configuration enabled reliable measurements of the terahertz beam with the THz camera (IRV-T0831, NEC Corporation, Japan). The terahertz radiation was focused with a spherical lens (50 mm EFL, Tydex, Russia) into the camera as represented in Figure 5.23. The lens was placed at ~100 mm from the TIR surface, and the position of the THz camera was optimised to be at the focal spot of the lens. The image in Figure 5.24 shows that the terahertz beam at 4.46 THz was tightly focused to a 1080×830 μm spot (horizontal×vertical; $1/e^2$, ±50 μm) on the terahertz camera. The small asymmetry on the image is a consequence of the ellipsoid nature of the generated THz beam. The relatively small and uniform spot size obtained is comparable to what was measured in other intracavity devices [30] and is considered suitable for THz spectroscopy applications.

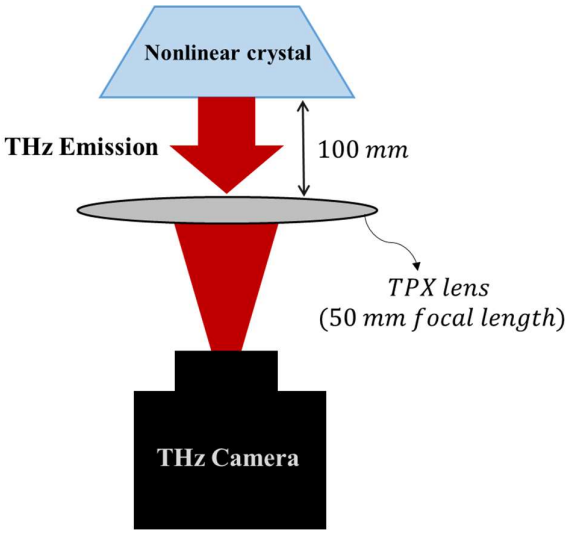

Figure 5.23 – Experimental layout for the THz beam imaging with 50 mm EFL spherical lens and THz camera (IRV-T0831, NEC Corporation, Japan).

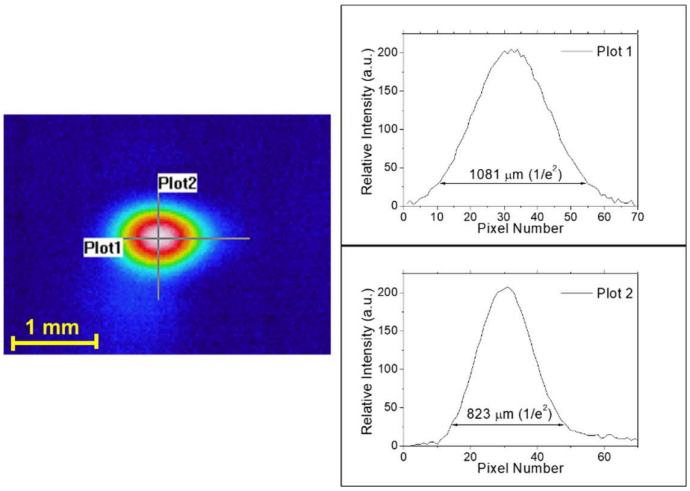

Figure 5.24 – Terahertz beam at 4.46 THz focused to a 1080×830 μm spot ($1/e^2$) with a 50 mm EFL spherical lens into the THz camera.

In summary, the surface-emitted THz polariton laser based on intracavity KTP was successfully constructed and yielded high average output power in the THz, wide THz-frequency-tunable range, considerably narrow free-running linewidth (29 GHz), and could be focused to a tight spot size (1080×830 μm $1/e^2$; with a 50 mm EFL focusing lens). These performance parameters indicate that this system is an extremely good source for investigating real-world applications with THz sources in the ~4.3-5.9 THz range, providing complimentary information to what could be achieved with MgO:LN systems. However, the need for the etalon

in the Stokes cavity is somewhat inconvenient for the operation of the laser. For this reason, the RTP crystal was also explored as an alternative material to generate higher THz frequencies in SE configuration.

5.3. $RbTiOPO_4$ crystal

The RTP crystal was investigated in surface-emitted configuration with the objective of producing frequency-tunable THz output at frequencies above 3 THz, complementing what is typically obtained from MgO:LN (~1 – 3 THz) and without the inconvenience of the SRS competition in the Stokes cavity, as was observed when using KTP. It was found that the RTP crystal in surface-emitted configuration exhibited the highest average THz output power of all experimental setups, and a broad spectral coverage, and for this reason was the configuration with the most thorough investigation.

For this experiment a trapezoidal $RbTiOPO_4$ crystal with base angle of 60˚, longer base of 12 mm, 5 mm height and 8 mm thickness in the crystallographic *z*-axis direction (Crystech Inc., China) was used. The crystallographic *xy* plane orientation with respect to the crystal geometry is represented in Figure 5.25. The material was supplied with the end faces polished to a high quality (10/5 scratch/dig) and anti-reflection coated for the fundamental and Stokes wavelengths (R<0.3%@1060 - 1090 nm), and the TIR surface was polished to a standard quality (80/50 scratch/dig). The trapezoidal RTP crystal was inserted in the surface emitted resonator (replacing the KTP) and the performance of the system was evaluated.

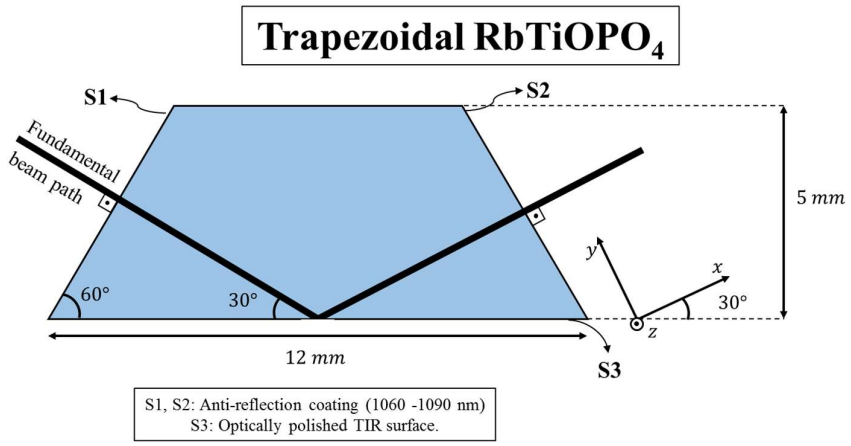

Figure 5.25 – The trapezoidal $RbTiOPO_4$.

5.3.1. Frequency-tunable terahertz detection

The fundamental and Stokes resonators were realigned and pure SPS emission was detected in the Stokes cavity across the entire Stokes wavelength tuning range. Adjusting the interacting angles from $\theta = 1 - 2.8°$,wavelength-tunable Stokes radiation was detected from 1076.1 to 1087.5 nm leaking from mirror M4, corresponding to frequencies from 3.05 to 5.98 THz being generated inside the material. This SPS range is smaller than what was observed in the linear resonator based on RTP (described in Chapter 4, Section 4.3.4), in which SPS fields corresponding to frequencies as high as 7.05 THz were generated internally (1091.7 nm Stokes; interacting angle $\theta = 3.5°$). For interacting angles above $\theta = 2.8°$ the SPS process disappeared in the SE polariton laser, and no optical fields were resonated in the Stokes cavity. This is the same interacting angle above which 1095.5 nm SRS competition was observed in KTP, and indicates that the SPS process efficiency was poor above this interacting angle for the surface-emitted resonator. As it was the case for KTP, this cannot be simply explained with the reduction in the crystal length from 20 mm (linear cuboid RTP from Section 4.3.4) to 10.4 mm (trapezoidal RTP, similar calculation as in Figure 5.14) because according to Equation 5.4 (and the plot in Figure 5.15) the estimated interacting length above $\theta = 2.8°$ is below 10 mm, which means that the dimension of the trapezoidal is not a limiting factor for the SPS gain. However, this observation can be understood as an additional experimental indicator that the dynamics underlying the intracavity SPS fields are more complex than that presented in Chapter 3, assuming steady-state SPS fields. It was mentioned in Chapter 3 that there is scope for developing the SPS theory for intracavity resonators, considering transient interacting fields and depleted fundamental field, yet this is outside the scope of this thesis.

The frequency coverage of the system based on surface-emitted RTP is shown in Figure 5.26, where the maximum average THz and Stokes output power is plotted versus terahertz frequency for a 5.5 W diode pump and interacting angles from $\theta = 1 - 2.8°$. Continuously tunable terahertz emission was detected in four regions, from 3.05 to 3.16 THz, from 3.50 to 4.25 THz, from 4.57 to 4.75 THz and from 5.40 to 5.98 THz. The emission gaps from 3.17 to 3.49 THz, 4.26 to 4.56 THz and from 4.76 to 5.39 THz correspond, respectively, to the infrared absorbing A_1 modes measured at 106, 143 and 161 cm^{-1}. The diode pump power required to reach SPS threshold for each frequency is shown in Figure 5.27, and it indicates an overall decrease in SPS threshold with increasing frequency. The decrease in threshold does

not necessarily translate to higher THz detection. The maximum THz emission at 4.10 THz is indeed located in a local minimum for the SPS threshold, but the lowest diode pump power required to reach SPS threshold occurred around 5.80 THz, frequency at which a dip in terahertz emission was detected as can be noted from Figure 5.26. This fact highlights once again the complexities of detecting the THz signal, and could be attributed, as well as the other dips in the terahertz emission, to water vapour absorption in the laboratory environment [31].

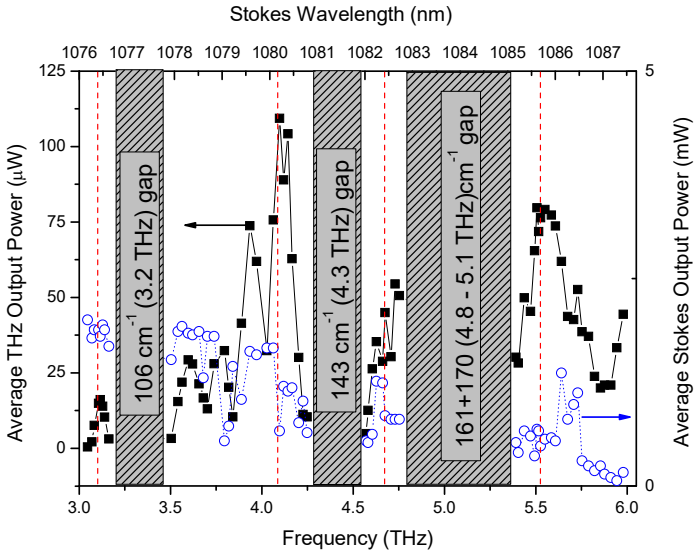

Figure 5.26 – Measured average THz output power and Stokes output power versus terahertz frequency in the intracavity RTP in surface-emitted configuration at 5.5 W diode pump. Vertical dashed lines represent frequencies at which the system was power transferred: 3.12 THz, 4.10 THz, 4.69 THz and 5.53 THz

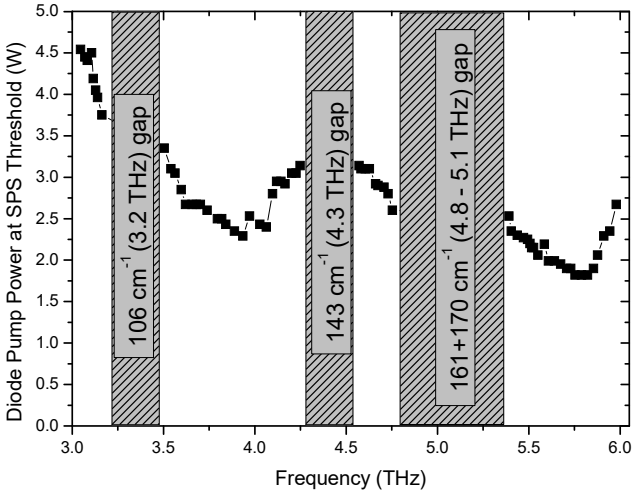

Figure 5.27 – Diode pump power required to reach SPS threshold versus THz frequency.

For all crystals assembled in surface-emitted configuration (RTP, KTP and MgO:LN), terahertz radiation could be detected for every interacting angle generating SPS. That is, in the surface-emitted layout, terahertz radiation was detected at every interacting angle at which wavelength-tunable Stokes field could be measured. The power transfer curves at different terahertz frequencies were analysed to provide a clearer understanding about the behaviour of the source across the SPS tuning range.

5.3.2. Power transfer at 3.12 THz, 4.10 THz, 4.69 THz and 5.53 THz

The system was power transferred at four different terahertz frequencies (four different interacting angles θ between the fundamental and Stokes fields), corresponding to local THz emission peaks, with the objective of further investigating the power characteristics of the source across the frequency-tunable range. These frequencies are located at 3.12 THz ($\theta = 1.1°$; 1076.3 nm Stokes), 4.10 THz ($\theta = 1.6°$; 1080.1 nm Stokes), 4.69 THz ($\theta = 1.9°$; 1082.4 nm Stokes) and 5.53 THz ($\theta = 2.2°$; 1085.7 nm Stokes). The power transfer curves are plotted in Figure 5.28 for the fundamental (depleted and undepleted), Stokes and THz fields. Fundamental field threshold was obtained at 0.6 W, similar to the surface-emitted resonators with KTP and MgO:LN. The threshold for SPS at every frequency required different diode

pump power, and different average 1064 nm output power and pulse width, as summarised in Table 5.1.

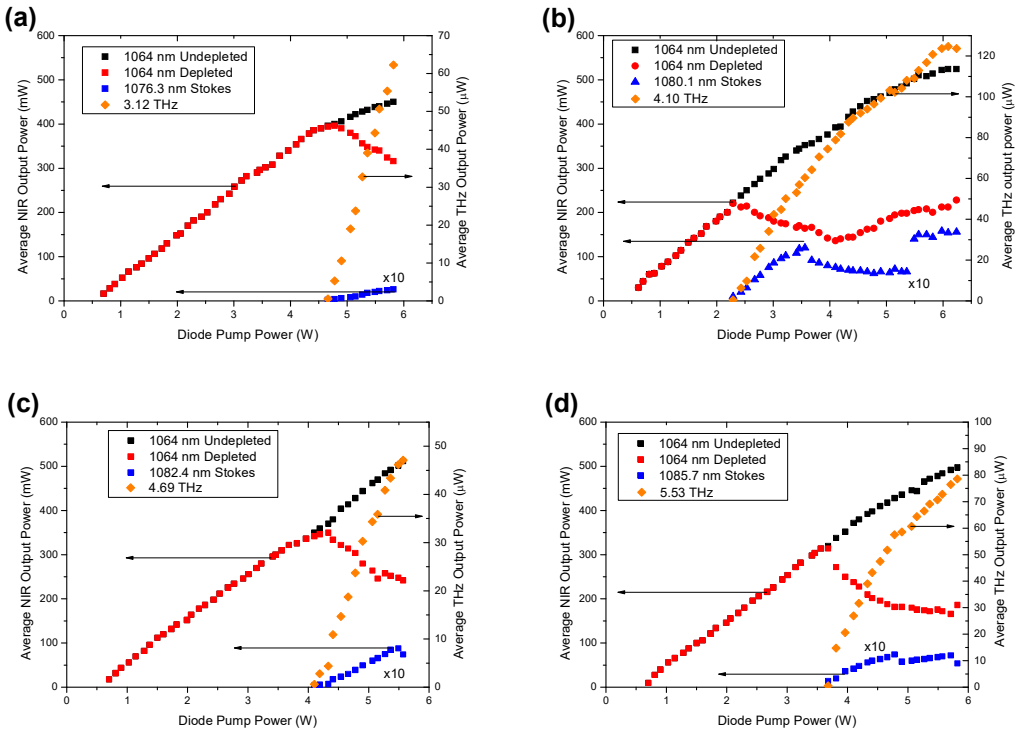

Figure 5.28 – Power transfer for the fundamental 1064 nm (depleted and undepleted) and SPS fields in the $RbTiOPO_4$ crystal in surface-emitted configuration at four different SPS frequencies. (a) 1076.3 nm Stokes (magnified 10 times) and 3.12 THz fields. (b) 1080.1 nm Stokes (magnified 10 times) and 4.10 THz fields. (c) 1082.4 nm Stokes (magnified 10 times) and 4.69 THz fields. (d) 1085.7 nm Stokes (magnified 10 times) and 5.53 THz fields.

The intensity required to reach SPS intensity for each terahertz frequency was calculated with data from Table 5.1, and considering the output coupling percentage (0.6%) and the 230 μm mode radius inside the crystal. The calculated values for the SPS threshold and the maximum average output power measured in the THz are summarised in Table 5.2 at the four frequencies investigated. The minimum SPS threshold intensity occurred at 4.10 THz, where a value of 27 MW/cm^2 was calculated, and at 3.12 THz the calculated SPS threshold intensity was the highest, 63 MW/cm^2. These values are comparable to those obtained for the linear resonator in Chapter 4 (54 MW/cm^2) and reported in [9,10] for MgO:LN. A maximum average output power of 124.7 μW was measured at 4.10 THz (6 W diode pump; 60% fundamental field depletion), and this was the highest THz output detected across all investigated

configurations. In fact, this is a very significant milestone for intracavity SPS lasers, since it was the first time an intracavity THz laser source crossed the hundred-microwatt average power level. Indeed, it represents more than 10-time increase in any other intracavity SPS THz system reported before this project [8–10], and pushes the technology towards the microwatt range.

Table 5.1 – Diode pump power, fundamental output power and pulse width at SPS threshold at 3.12 THz, 4.10 THz, 4.69 THz and 5.53 THz.

Value at SPS threshold	**3.12 THz**	**4.10 THz**	**4.69 THz**	**5.53 THz**
Diode pump power (W)	4.7	2.3	4.1	3.7
Average 1064 nm output power (mW)	395	220	345	315
1064 nm pulse width (FWHM, ns)	210	270	230	240

No laser-induced damage to the TIR surface of the RTP crystal was observed within the context of this experiment. Although, the maximum average output power measured at 3.12, 4.69 and 5.53 THz was limited by laser damage to the Stokes mirror M4. After full characterization of the system at 4.10 THz (power transfer, temporal and spatial profile, and linewidth measurements) the terahertz frequency was adjusted to 4.69 THz for power transfer at this frequency, and laser damage to the mirror M4 was subsequently observed at 5.5 W diode pump power. The mirror was cleaned in place, so as not to lose alignment, and was translated in order to remove the damage spot from the Stokes beam path, but damage was observed again between 5.5 and 6 W diode pump. The process of cleaning and laterally translating the mirror was repeated a few times but the system could not be pumped at powers above 6 W anymore without damage to mirror M4. It was decided to proceed with the power transfer at the other two frequencies and extract as much terahertz power as possible until laser damage occurred. It became clear that after the first incidence of damage, the mirror coating degraded, and the adjacent portions of the coating became less resistant to laser-induced damage. These mirrors have been used extensively for a long period of time, and particularly were used throughout all this research thesis. Some fatigue effect, or even debris from the environment may have deposited on the mirror surface, and could have played a role in the first damage, incident which might have spread further debris to the surrounding areas as well. Cleaning the mirror with isopropyl alcohol or even acetone was not sufficient to prevent this damage from

reoccurring. Replacing the mirror could also be an option, but at this stage of the project it could have compromised the comparison of this systems with the previous work. Positively, the emission at the most efficient frequency of 4.10 THz could be fully characterised without any laser damage issues, and it is anticipated that with new laser mirrors with more robust coatings the maximum THz output at the other frequencies would increase.

Despite the laser damage to the Stokes mirror at final power transfer measurements, the surface-emitted resonator with the intracavity RTP yielded an amount of THz signal across the tunable range (related in Table 5.2) substantially higher than the maximum 16.2 μW detected in the linear approach (Chapter 4, Section 4.4), showing a clear benefit of this layout. With regards to frequency-tunability, the surface-emitted configuration performance was also superior to the linear design, with frequencies as high as 5.98 THz being detected (as opposed to 4.15 THz in the linear resonator) as a consequence of the terahertz field generation at the crystal surface which avoids propagation losses.

Table 5.2 –SPS threshold intensity and maximum average output power measured at 3.12 THz, 4.10 THz, 4.69 THz and 5.53 THz. For each frequency the SPS threshold intensity was calculated considering the output coupling percentage (0.6%) and the 230 μm mode radius inside the crystal.

	3.12 THz	**4.10 THz**	**4.69 THz**	**5.53 THz**
SPS Threshold intensity (MW/cm^2)	63	27	50	44
Maximum average THz output power (μW)	62.3	124.7	47.1	78.6

5.3.3. Temporal profile

With the interacting angle adjusted for 4.10 THz emission ($\theta = 1.6°$) the fundamental 1064 nm (depleted and undepleted) and the 1080.1 nm Stokes temporal profile were measured as plotted in Figure 5.29 for a 6.0 W diode pump. The fundamental pulse width decreased from 104 ns to 44 ns (FWHM) as a consequence of depletion, and the 1081.5 nm Stokes pulse builds up with a 39 ns delay from the fundamental pulse, with a measured width of 12 ns (FWHM). The strong

degree of depletion can be clearly observed from the plot, and the early decay of the depleted fundamental pulse (when compared to the undepleted field) is a consequence of pumping the system far above threshold. The ratio between the pulse area of the depleted and undepleted fields indicates fundamental field depletions in excess of 65%, a value comparable to that measured with the power transfer curves.

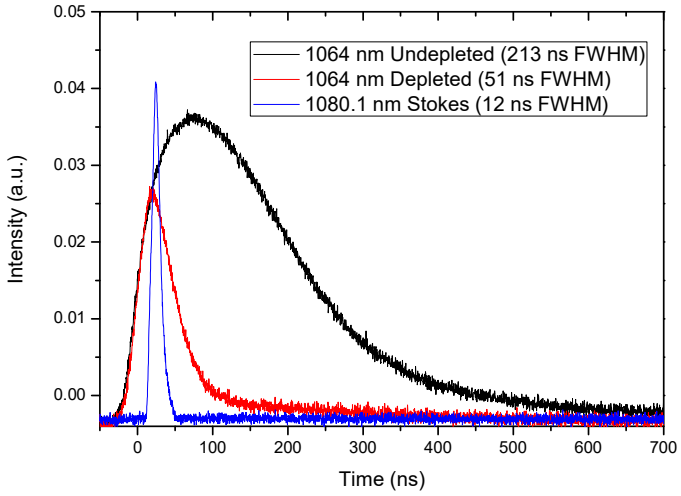

Figure 5.29 – Temporal profiles of the fundamental (depleted and undepleted) and 1080.1 nm Stokes at 6.0 W diode pump power.

5.3.4. Terahertz field polarization

The polarization state of the terahertz output from the RTP crystal was inferred with the same method adopted in KTP. The linear polariser (POL-HDPE-CA25-OD34.9-T7.9, Tydex, Russia) was placed perpendicular to the THz propagation direction (parallel to the TIR surface of RTP), and mounted on a rotation stage (Thorlabs PRM1/M; 5 arcmin resolution). The plot in Figure 5.30 shows the transmitted power at 4.10 THz after the polariser with the transmission axis of the polariser rotated from $0-90°$ with respect to the vertical axis. The maximum terahertz signal measured with the transmission axis of the polariser aligned with the vertical axis, indicates that the terahertz field emanating from the RTP crystal is vertically polarised. From the maximum detected THz signal (34.0 μW) and minimum measurable THz system during these measurements (0.2 μW) a polarization ratio of 170:1 (vertical:horizontal) is

calculated, similar to that of KTP. This was already expected given the similarities of this system with the previous resonator.

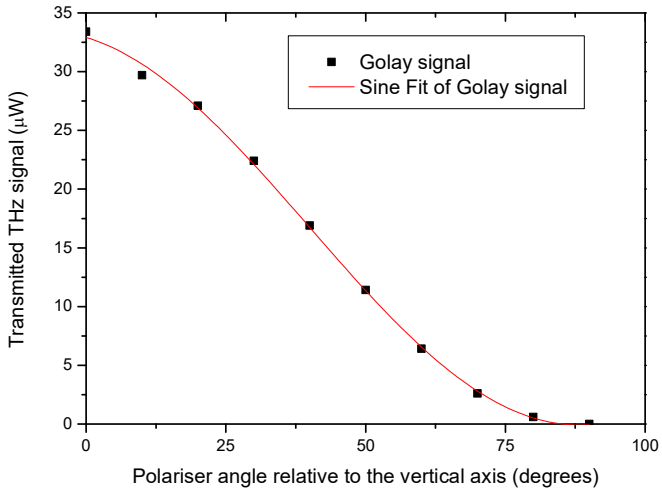

Figure 5.30 – Measurement of the polarization state of the terahertz radiation generated by the RTP crystal in surface-emitted configuration. The measurements indicate vertically polarised THz output from the laser.

5.3.5. Terahertz field linewidth

The linewidth of the terahertz field was calculated from the measurement of the coherence length of the terahertz radiation at 4.10 THz with the Fabry-Pérot interferometer composed of two silicon windows described in the previous section. The terahertz signal transmitted by the interferometer versus the separation between the silicon windows (10 μm steps) was monitored as plotted in Figure 5.31. The coherence length for the terahertz field generated from RTP was around 3.4 mm (±0.1 mm, considering a ±5 step uncertainty) leading to a calculated linewidth of 28 GHz (±1 GHz). The linewidth calculated for RTP from the interferometric measurements is very similar to that obtained for KTP, and this was also expected given the similarities between both resonators. The smaller step size utilised for these measurements did not bring any benefit to the measured linewidth, but increased the amount of time required to collect the data. It is anticipated that the insertion of intracavity etalons in the system would promote further reduction in the emitted linewidth [29].

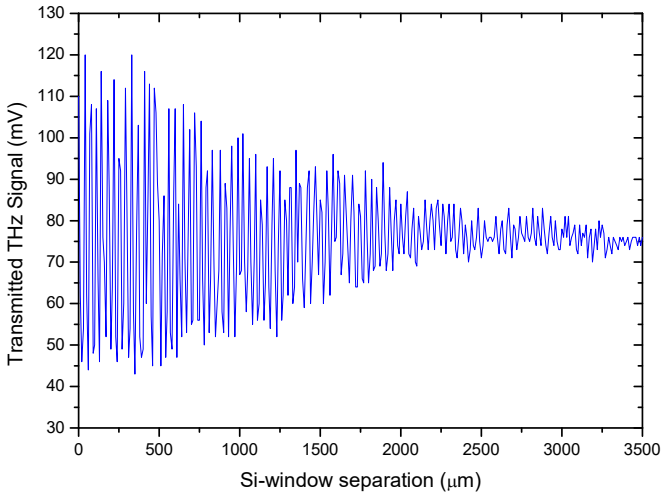

Figure 5.31 – Terahertz signal transmitted by the Fabry-Pérot interferometer versus separation distance between Si-windows for a 4.10 THz signal from RTP. Measured coherence length is 3.4 mm (±0.1 mm) and calculated linewidth 28 GHz (±1 GHz).

5.3.6. Terahertz field spatial profile

The THz radiation generated by RTP in surface-emitted configuration was collected with a spherical lens element (50 mm EFL, Tydex, Russia) and focused to the THz camera (IRV-T0831, NEC Corporation, Japan) to demonstrate the ability to produce uniform and tightly-focused beam spots. The lens element was placed at ~100 mm from the TIR surface, and the position of the THz camera was adjusted to be at the focal spot of the lens. The image in Figure 5.32 shows that the terahertz beam at 4.10 THz was focused to a beam below 1 mm in diameter, with a 920×680 μm^2 spot (horizontal×vertical; $1/e^2$, ±50 μm) on the terahertz camera. The small asymmetry on the image is a consequence of the ellipsoid nature of the generated THz beam, and the shoulders observed in the vertical direction are attributed to terahertz radiation scattered in the imaging optics. It is important to note that the imaging optics are not anti-reflection coated for the THz, and with the increase in terahertz optical power, it is expected that scattered light would appear in the detector.

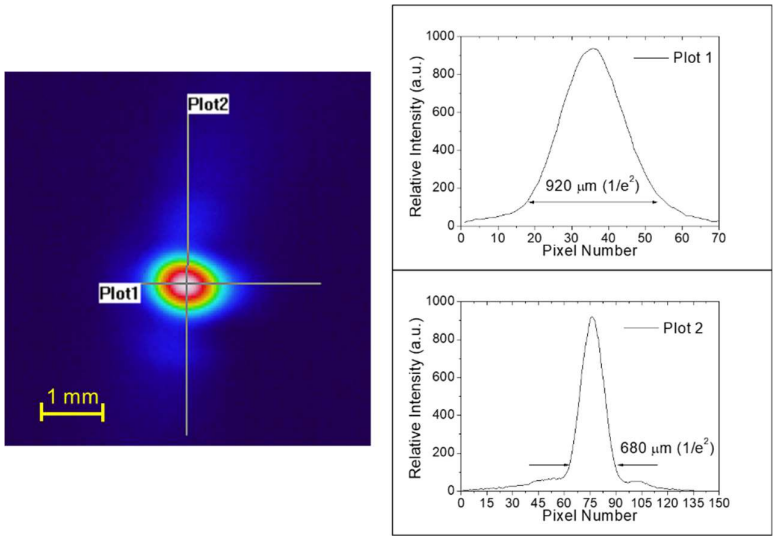

Figure 5.32 – Terahertz beam at 4.10 THz focused to a 920×680 µm^2 spot (1/e^2) with a 50 mm EFL spherical lens into the THz camera.

The characteristics of the 4.10 THz field propagating in free space were investigated with the calculation of the horizontal and vertical beam quality factor (M^2). The M^2 of a laser contains information about the beam divergence, and it can be measured by monitoring the beam waist over propagation distance. For a Gaussian beam of wavelength λ, with a minimum beam waist W_0 at $z = 0$, the beam waist diverges with propagating distance "z" according to the relation [32]:

$$W(z) = W_0 \left[1 + \left(\frac{z}{z_R}\right)^2\right]^{1/2} \tag{5.6}$$

where the Rayleigh range z_R relates to the M^2 by:

$$z_R = \frac{\pi W_0^2}{M^2 \lambda} \tag{5.7}$$

The horizontal and vertical beam waists of the THz beam were measured versus propagation distance from the TIR surface, and the horizontal and vertical M^2 values were calculated considering that the minimum beam waist for the terahertz beam was that at the TIR surface of the crystal, and the terahertz field propagated in free space following equation 5.6. The beam waists were measured with the knife-edge technique, at distances varying from

1 to 16 mm from the TIR surface, with 50 µm step size across the beam waist. The horizontal and vertical knife-edge profiles (together with the smoothed curves) are plotted in Figure 5.33. The knife-edge profiles indicate a stronger divergence in the vertical axis, and this is a consequence of the ellipsoid nature of the THz beam at the TIR surface, which has the smaller axis in the vertical plane. The horizontal and vertical beam waists were calculated from the knife-edge measurements with the same procedure performed for KTP and are plotted in Figure 5.34. The values measured at 1 mm from the crystal indicate a horizontal and vertical beam diameter of 1240 and 480 µm, respectively. These values are in good approximation with the mode size at the TIR surface extracted from resonator *ABCD* modelling (1140×460 µm^2). The horizontal beam diameter exhibited an unexpected minimum beam waist at ~5 mm away from the crystal, and this could be a result of a small misalignment between the terahertz fields generated from the two propagation directions inside the resonator, as illustrated in Figure 5.35.

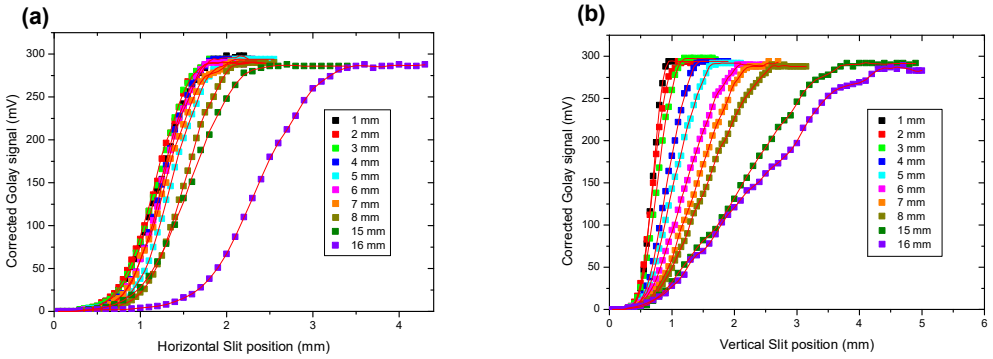

Figure 5.33 – Knife-edge measurements of the (a) horizontal and (b) vertical beam profile from 1 mm to 17 mm propagation in free space from the TIR surface of RTP.

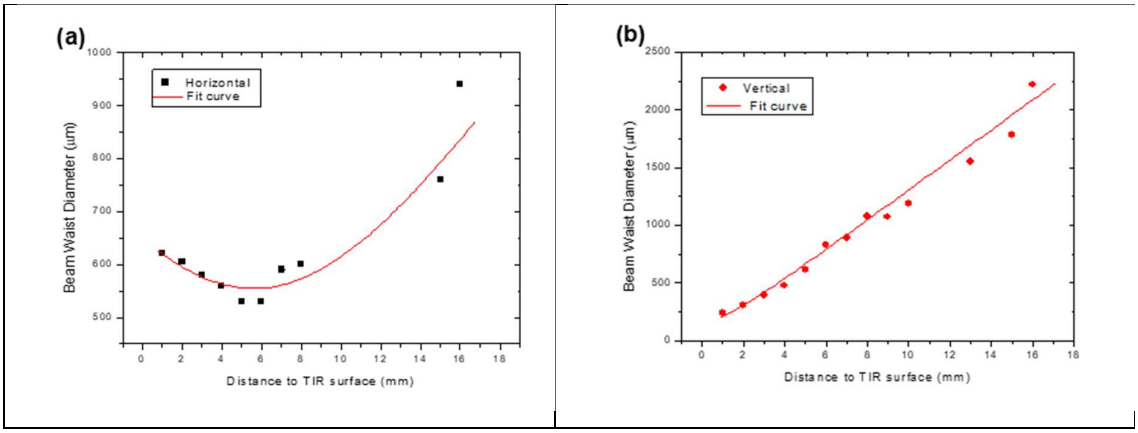

Figure 5.34 –Horizontal and vertical beam waist diameter for the 4.10 THz calculated from the knife-edge measurements. Profiles measured from 1 to 17 mm from the TIR surface of the RTP crystal.

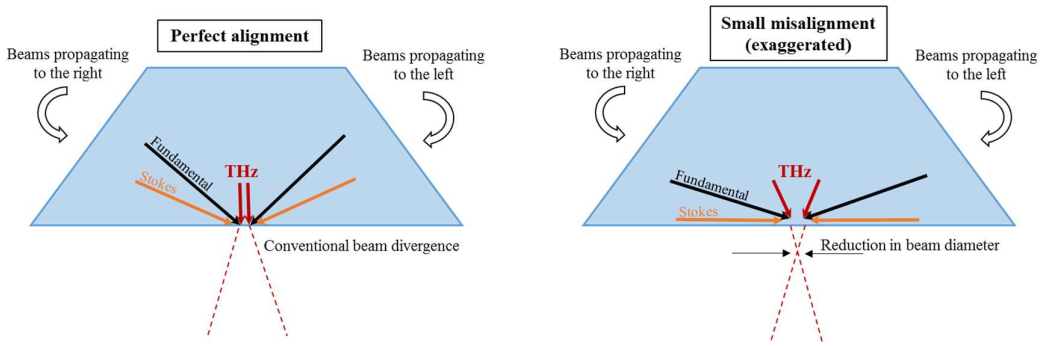

Figure 5.35 – Exaggerated representation of a small misalignment between THz fields generated in counter propagating directions. This could result in an effective beam waist outside the nonlinear crystal.

With the beam diameters from Figure 5.34 the horizontal and vertical beam quality parameters were calculated respectively to be $M_H^2 \sim 1.57$ and $M_V^2 \sim 1$. This indicates that the vertical component of the terahertz beam is nearly diffraction-limited. The beam quality parameter for the horizontal component is slightly poorer as a consequence of the bounce on the TIR surface. The beam quality factor for the surface-emitted resonator is substantially lower than the values reported in [30] for the linear configuration, where a horizontal and vertical M^2 values of 6.7 and 2.3 were respectively reported. The brightness of a Gaussian laser beam is inversely proportional to the square of the M^2 parameter [12], indicating that the brightness of the THz output from the surface-emitted configuration is considerably greater than that for the linear configuration, which will have a positive impact in every potential application in THz spectroscopy or imaging. Moreover, the smaller beam divergence also enables the use of more compact optics and apertures, potentially reducing the size of the instrumentation required to manipulate the output beam.

5.4. Discussion

The experimental results obtained with the different intracavity SPS crystals in surface-emitted configuration reported in this chapter, demonstrated the superiority of this layout over the linear configuration with Si-prisms reported in Chapter 4. As predicted in Chapter 3, the high absorption experienced by the THz field during the intrinsic propagation inside the nonlinear material experienced in the linear design is a strong disadvantage of the linear layout, particularly at frequencies above 4 THz, where high absorption coefficient (which can easily

exceed 100 cm^{-1}) is combined with the increase in propagating distance inside the material. The surface-emitted configuration enables the terahertz field generated at the crystal TIR surface to be refracted directly into the air, virtually eliminating the absorption losses for the photons generated at the crystal/air interface. The avoidance of this important source of losses for the THz field culminated in far superior performance of the surface-emitted resonators.

5.4.1. Notes on SPS threshold

First and foremost it is important to note that the laser resonators reported in this research were not optimised to minimise SPS threshold, but to maximise terahertz output power and extend the frequency coverage. This was clearly achieved as per the results presented in Chapters 4 and 5, and as it will be further discussed in the next section. Although it is of great value to compare the SPS threshold intensity for the different crystals in linear or surface-emitted configuration, as well as to make connections between these values with figures reported in the literature for similar resonators. The SPS threshold intensity (and crystal manufacturer) for all resonators reported in this thesis are summarised in Table 5.3, together with other values available in the literature for intracavity MgO:LN in linear [9,10] and surface-emitted [8] configurations, and for the externally-pumped KTP TPO [2]. The investigation of THz sources based on intracavity KTP and RTP crystals were original contributions of this thesis, and hence there were no intracavity values available for comparison.

The four SPS threshold intensities compiled in the table for MgO:LN are for intracavity systems, and it can be noted that there was an increase in SPS threshold from the linear to the surface-emitted configuration (from ~8-12 MW/cm^2 to 40-90 MW/cm^2), which might be due to the increase in losses for adding an extra surface in the optical resonator (TIR surface). It is also worth noting that the THz resonators developed at Macquarie University (the linear resonator reported in [10] and the surface-emitted resonators reported in this chapter) exhibit output coupling percentages for the fundamental and Stokes fields that are lower than what is typically utilised in Q-switched lasers, thus the fundamental output power and pulse width are very sensitive to small changes in intracavity losses. Changes to these parameters influence the SPS threshold calculation. Such influence was observed in KTP, with the calculated SPS threshold intensity for the intracavity linear resonator (69 MW/cm^2) being substantially smaller than that obtained for the intracavity surface-emitted resonator (116 MW/cm^2). Moreover, the

116 MW/cm^2 calculated for KTP is similar to what was measured in [2] with a similar SE KTP crystal in externally-pumped geometry. In RTP the behaviour observed was the opposite, with the SPS threshold decreasing from 54 MW/cm^2 in the linear resonator to 27 MW/cm^2 in the surface-emitted resonator. In fact, this was the lowest SPS threshold intensity calculated among all resonators reported in this thesis. However, as can be noted from the table, the RTP crystals utilised in the linear and SE resonators were supplied by different manufacturers, and small differences in crystal quality (purity, optical quality, thin-film coatings, scattering) would alter the intracavity losses strongly impacting in the calculated SPS threshold. In summary, the comparison between the lowest SPS threshold for each laser assembly, even when utilising the same SPS material, is limited by different crystal manufacturers, thin-film coatings, crystal quality, etc. Nevertheless, it can be noted from the table that for KTP the intracavity approach exhibited reduced SPS threshold intensity when compared to externally pumped systems. Similar comparisons were made for MgO:LN in [9,10] showing similar conclusions, this being one of the great benefits of the intracavity design.

Table 5.3 – SPS threshold intensity for intracavity MgO:LN, KTP and RTP crystals in the different resonators reported in this thesis, and values reported in the literature for intracavity (when available) and also externally-pumped TPOs. The manufacturer for the different crystals investigated at Macquarie University are indicated in parenthesis.

	Lower SPS threshold intensity (MW/cm^2)			
Material	**Linear layout**		**Surface-emitted layout**	
MgO:LiNbO$_3$	Edwards et. at. [9]	**12**	Wang *et al*. [8]	**90**
	Lee *et al.* [10] (HC Photonics)	**8**	This thesis (Castech)	**40-66**
KTiOPO$_4$	This thesis (Crystech Inc.)	**69**	Wang *et al.* [2]*	**121**
			This thesis (Crystech Inc.)	**116**
RbTiOPO$_4$	This thesis (Cristal Laser)	**54**	This thesis (Crystech)	**27**

*the system reported in [2] is an externally-pumped TPO

5.4.2. Notes on THz frequency coverage and output power

An overview of the global achievements regarding the terahertz frequency coverage and THz output power resulting from this research, with a general comparison with the state-of-the-art sources prior to the commencement of this PhD candidature will be provided in Chapter 6. This section, however, provides a more specific comparison between the various systems making use of the same SPS material in different layout.

For MgO:$LiNbO_3$ the laser damage to the TIR surface of the nonlinear crystal observed in the initial stage of the research was overcome with the deposition of a protective Teflon coating on the material. For MgO:LN systems generating SPS from 1064 nm fundamental fields, the maximum average output power reported in [10] for a linear resonator was 6.45 μW (5 W diode pump), and the surface-emitted layout reported here delivered 58.6 μW output for only 6.5 W diode pump, an increase of practically one order of magnitude in power. The frequency coverage of the source was also substantially improved, increasing in 80%, from 1.53 – 2.82 THz in [10] to 1.46 – 3.84 THz in the SE resonator. The surface-emitted layout reported in this chapter can also be compared with other intracavity systems, such as the early work on linear resonators developed at the University of St. Andrews [9], and the first intracavity surface-emitted resonator developed at the University of Tianjin [8], bearing in mind the following differences between systems. Those resonators operated at much lower repetition rates (10 – 15 Hz), and hence instead of average power it is reasonable to compare pulse energies. The pulse energies reported in [9] were 5 nJ/pulse, and in the surface-emitted resonator reported in this chapter they were above 19 nJ/pulse. The frequency-coverage of that linear system was from 1.2 – 3.05 THz, a shorter range when compared to what was reported here. The maximum energy per pulse obtained in [8] was 283 nJ, however it required much higher diode pumping, which results in a lower overall efficiency. The diode-to-THz efficiency in [8] was $\frac{283\ \text{nJ @ THz}}{595\ \text{mJ @ 808 nm}} = 4.7 \times 10^{-7}$ whilst this figure for the surface-emitted resonator reported in this thesis was $\frac{58.6\ \mu\text{W @ THz}}{6.5\ \text{W @808 nm}} = 9.0 \times 10^{-6}$, one order of magnitude higher even at a much higher repetition rate.

The limitations imposed to the linear configuration at frequencies above 4.2 THz for KTP and RTP crystals make the benefits of the surface-emitted configuration for these crystals absolutely evident. In the linear configuration reported in Chapter 4 both crystals exhibited

wavelength-tunable Stokes radiation corresponding to a wide range of THz frequencies being generated inside the materials, 4.07 – 5.91 THz in KTP and 3.10 – 7.05 THz in RTP. However no terahertz output could be detected from KTP, and the detection in RTP was limited to 3.10 – 4.15 THz. In the surface-emitted geometry both crystals exhibited a wide range of wavelength-tunable Stokes radiation, and terahertz fields were successfully detected across the entire SPS range.

In KTP an undesired 1095.5 nm Raman line was detected in the Stokes cavity for interacting angles above $\theta = 2.8°$, which was limiting the SPS performance. This line was suppressed with the insertion of an etalon in the Stokes resonator, and terahertz radiation continuously tunable from 4.29 – 4.53 THz, 4.88 – 5.03 THz and from 5.47 – 5.89 THz was detected, and the gaps from 4.54 – 4.87 THz and from 5.04 – 5.46 THz were identified to be located in the vicinity of the 153 and 177 cm^{-1} A_1 modes measured in KTP. This was the first time a crystal different from magnesium oxide-doped lithium niobate was reported in an intracavity surface-emitted layout, and the frequency-coverage was comparable to that reported for an externally-pumped TPO [2]. The maximum average output power measured from KTP was 70.9 μW at 5.58 THz for a diode pump power of 7.3 W.

The RTP crystal produced terahertz output continuously tunable in four regions, from 3.05 to 3.16 THz, from 3.50 to 4.25 THz, from 4.57 to 4.75 THz and from 5.40 to 5.98 THz. The emission gaps from 3.17 to 3.49 THz, 4.26 to 4.56 THz and from 4.76 to 5.39 THz corresponded to the infrared absorbing A_1 modes measured at 106, 143 and 161 cm^{-1}. This crystal yielded the maximum average output power among all resonators assembled, and delivered 124.7 μW at 4.10 THz for a modest 6 W diode pump. This represents a substantial increase on the 16.2 μW average output power detected at 3.80 THz in Chapter 4, and it was the first time an intracavity THz laser exceeded the very important milestone of the hundred-microwatt level.

The linewidth of the terahertz emission was measured to be below 30 GHz for KTP and RTP crystals. The linewidth of the THz was not measured for MgO:LN but it is expected to be similar, given the terahertz linewidth is governed by the fundamental field linewidth, which was virtually the same in all cases. This linewidth is sufficiently narrow to enable the use of these sources in real-world spectroscopic applications that involve the investigation of molecules of more complex structure such as illicit drugs etc [33]. It is also anticipated that the insertion of high-finesse etalons in the fundamental and Stokes resonators would further reduce

the terahertz linewidth [29], and this is within the scope of future developments. With a narrower linewidth, the investigation of fine structures such as greenhouse gases could be performed [9,31]. The ability to tightly focus the terahertz output below 1 mm was also demonstrated with the images collected with the THz camera, further supporting the use of these sources in THz spectroscopy and spectral imaging applications. The spatial profile measured with the knife-edge technique enabled the calculation of the beam quality parameter of the terahertz output from the RTP crystal, to be $M_H^2 \sim 1.57$ and $M_V^2 \sim 1$ in the horizontal and vertical dimensions, respectively. The comparison of these figures with the beam quality of linear resonators [11,30] (typically $M_H^2 \sim 6$ and $M_V^2 \sim 2$) shows that the surface-emitted resonator has the capacity to produce much brighter THz sources.

5.5. Chapter Summary

The surface-emitted geometry was investigated in this chapter for intracavity MgO:LN, KTP and RTP crystals, and the reported results from the experiments demonstrate the superiority of this layout in comparison with the linear approach (with Si-prisms) for all three materials, with regards to output power and frequency coverage. The strong absorption coefficients calculated in Chapter 3, which limited the THz detection above 4.2 THz in the linear configuration (Chapter 4) for KTP and RTP, were not an issue for the surface-emitted geometry, as anticipated. In the surface-emitted layout it was possible to detect terahertz output for every interacting angle generating wavelength-tunable Stokes radiation, for all nonlinear material investigated.

In MgO:LN, laser damage to the TIR surface of the crystal was observed and was overcome with the deposition of a Teflon coating onto it. The Teflon-coated crystal delivered 58.6 μW output at 1.76 THz for only 6.5 W diode pump, and showed continuous tunability from 1.46 – 3.84 THz. This research enabled the first successful frequency-tunable THz detection from an intracavity SPS source based on KTP. The KTP crystal produced 70.9 μW at 5.58 THz for 7.3 W diode pump, and was continuously tunable from 4.29 – 4.53 THz, 4.88 – 5.03 THz and from 5.47 – 5.89 THz. The RTP crystal yielded the maximum terahertz power detected among all resonator assemblies, 124.7 μW were measured at 4.10 THz for a modest 6 W diode pump. The system produced terahertz output continuously tunable in four regions, from 3.05 to 3.16 THz, from 3.50 to 4.25 THz, from 4.57 to 4.75 THz and from

5.40 to 5.98 THz. The beam quality of the terahertz field produced was also superior to those typically obtained in linear resonators, indicating the capacity of the surface-emitted configuration in producing much brighter THz fields.

The experimental results reported in this chapter represent a significant original contribution to the field of intracavity SPS sources. The most important nonlinear materials for intracavity SPS were explored, and the power and frequency characteristics of the sources indicate that the surface-emitted geometry has the greatest potential to produce high-power, narrow-linewidth and high brightness frequency-tunable THz sources.

References

1. W. Wang, Z. Cong, Z. Liu, X. Zhang, Z. Qin, G. Tang, N. Li, Y. Zhang, and Q. Lu, "THz-wave generation via stimulated polariton scattering in $KTiOAsO_4$ crystal," Opt. Express **22**, 17092–17098 (2014).

2. W. Wang, Z. Cong, X. Chen, X. Zhang, Z. Qin, G. Tang, N. Li, C. Wang, and Q. Lu, "Terahertz parametric oscillator based on $KTiOPO_4$ crystal," Opt. Lett. **39**, 3706–3709 (2014).

3. T. Ortega, H. Pask, D. Spence, and A. Lee, "THz polariton laser using an intracavity Mg:$LiNbO_3$ crystal with protective Teflon coating," Opt. Express **25**, 1604–1610 (2017).

4. Y. Wang, Z. Li, J. Li, C. Yan, T. Chen, D. Xu, W. Shi, H. Feng, and J. Q. Yao, "Energy scaling of a tunable terahertz parametric oscillator with a surface emitted configuration," Laser Phys. **24**, 125402 (2014).

5. W. Wang, X. Zhang, Q. Wang, Z. Cong, X. Chen, Z. Liu, Z. Qin, P. Li, G. Tang, N. Li, C. Wang, Y. Li, and W. Cheng, "Multiple-beam output of a surface-emitted terahertz-wave parametric oscillator by using a slab MgO:$LiNbO_3$ crystal," Opt. Lett. **39**, 754–757 (2014).

6. G. Tang, Z. Cong, Z. Qin, X. Zhang, W. Wang, N. Li, Q. Fu, Q. Lu, and S. Zhang, "Energy scaling of terahertz-wave parametric sources," Opt. Express **23**, 4144–4152 (2015).

7. Z. Yang, Y. Wang, D. Xu, W. Wentao, P. Duan, C. Yan, L. Tang, and J. Yao, "High-energy terahertz wave parametric oscillator with a surface-emitted ring-cavity configuration," Opt. Lett. **41**, 2262–2265 (2016).

8. Y. Wang, D. Xu, H. Jiang, K. Zhong, and J. Yao, "A high-energy, low-threshold tunable intracavity terahertz-wave parametric oscillator with surface-emitted configuration," Laser Phys. **23**, 55406 (2013).

9. T. Edwards, D. Walsh, M. Spurr, C. Rae, M. Dunn, and P. Browne, "Compact source of continuously and widely-tunable terahertz radiation," Opt. Express **14**, 1582–1589 (2006).

10. A. Lee, Y. He, and H. Pask, "Frequency-tunable THz source based on stimulated polariton scattering in Mg:$LiNbO_3$," IEEE J. Quantum Electron. **49**, 357–364 (2013).

11. K. Kawase, J. Shikata, H. Minamide, K. Imai, and H. Ito, "Arrayed silicon prism coupler for a terahertz-wave parametric oscillator," Appl. Opt. **40**, 1423–1426 (2001).

12. T. Ross, *Laser Beam Quality Metrics* (SPIE Press, 2013).

13. Y. Furukawa, A. Yokotani, T. Sasaki, H. Yoshida, K. Yoshida, F. Nitanda, and M. Sato, "Investigation of bulk laser damage threshold of lithium niobate single crystals by Q-switched pulse laser," J. Appl. Phys. **69**, 3372–3374 (1991).

14. Y. Sun, C. F. Li, Z. Y. Li, and F. Gan, "Investigation of nonlinear absorption and laser damage on lithium niobate single crystals," Proc. SPIE **1848**, 594–598 (1993).

15. T. Ikari, R. Guo, H. Minamide, and H. Ito, "Energy scalable terahertz-wave parametric oscillator using surface-emitted configuration," J. Eur. Opt. Soc. **5**, 1–4 (2010).

16. R. H. and J. B. and A. Guenther, "Surface roughness and laser damage threshold," IEEE J. Quantum Electron. **13**, 361–363 (1977).

17. D. W. Camp, M. R. Kozlowski, L. M. Sheehan, M. A. Nichols, M. Dovik, R. G. Raether, and I. M. Thomas, "Subsurface damage and polishing compound affect the 355-nm laser damage threshold of fused silica surfaces," Proc. SPIE **3244**, 356–364 (1998).

18. R. J. Shine, A. J. Alfrey, and R. L. Byer, "40-W cw, TEM00-mode, diode-laser-pumped, Nd:YAG miniature-slab laser," Opt. Lett. **20**, 459–461 (1995).

19. M. Ostermeyer, D. Mudge, P. J. Veitch, and J. Munch, "Thermally induced birefringence in Nd:YAG slab lasers," Appl. Opt. **45**, 5368–5376 (2006).

20. J. Reitz, F. Milford, and R. Christy, *Foundations of Electromagnetic Theory* (Addison-Wesley, USA, 2008).

21. N. J. Bazin, J. E. Andrew, and H. A. McInnes, "Formation of Teflon AF Polymer Thin Films as Optical Coatings in the High Peak Power Laser Field," Proc. SPIE 3492, Third Int. Conf. Solid State Lasers Appl. to Inert. Confin. Fusion **3492**, 964–969 (1999).

22. E. Bründermann, H. W. Hübers, and M. F. G. Kimmitt, *Terahertz Techniques* (Springer, USA, 2012).

23. A. Lee, D. Spence, and H. Pask, "Tunable THz polariton laser based on 1342 nm

wavelength for enhanced terahertz wave extraction," Opt. Lett. **42**, 2691–2694 (2017).

24. M. Wu, Y. Chiu, T. Wang, G. Zhao, A. Zukauskas, F. Laurell, and Y. Huang, "Terahertz parametric generation and amplification from potassium titanyl phosphate in comparison with lithium niobate and lithium tantalate," Opt. Express **24**, 25964–25973 (2016).

25. Q. Meng, B. Zhang, S. Zhong, and L. Zhu, "Damage threshold of lithium niobate crystal under single and multiple femtosecond laser pulses: theoretical and experimental study," Appl. Phys. A **122**, 582 (2016).

26. K. Murate, S. Hayashi, and K. Kawase, "Expansion of the tuning range of injection-seeded terahertz-wave parametric generator up to 5 THz," Appl. Phys. Express **9**, 82401 (2016).

27. A. Siegman, *Lasers* (University Science Books, 1986).

28. K. Kawase, M. Sato, T. Taniuchi, and H. Ito, "Coherent tunable THz-wave generation from $LiNbO_3$ with monolithic grating coupler," Appl. Phys. Lett. **68**, 2483–2845 (1996).

29. D. J. M. Stothard, T. J. Edwards, D. Walsh, C. L. Thomson, C. F. Rae, M. H. Dunn, and P. G. Browne, "Line-narrowed, compact, and coherent source of widely tunable terahertz radiation," Appl. Phys. Lett. **92**, 11–14 (2008).

30. D. Walsh, "Intracavity Terahertz Optical Parametric Oscillators," (Doctoral dissertation). University of St. Andrews (2010).

31. I. Hosako, N. Sekine, M. Patrashin, S. Saito, K. Fukunaga, Y. Kasai, P. Baron, T. Seta, J. Mendrok, S. Ochiai, and H. Yasuda, "At the dawn of a new era in terahertz technology," Proc. IEEE **95**, 1611–1623 (2007).

32. W. Koechner, *Solid-State Laser Engineering - 6th Edition* (Springer US, 2014).

33. K. Kawase, Y. Ogawa, and Y. Watanabe, "Non-destructive terahertz imaging of illicit drugs using spectral fingerprints," Opt. Express **11**, 2549–2554 (2003).

6. Conclusion and future work

6.1. Summary of original contributions of this research

The first demonstration of terahertz sources with frequency-tunable output based on intracavity SPS in the last decade opened a completely new perspective for the development of compact, robust, cost-effective and highly efficient THz sources for real-world applications. Since these first developments conducted at the University of St. Andrew's (UK) from 2006-2010, little work has been reported in the field despite its great potential. For this reason, when writing this thesis the author found it difficult to draw comparisons between the lasers reported here with other systems in the literature. The relatively small amount of work reported in the field of intracavity SPS lasers is because the research and development of such devices requires a very particular laser engineering expertise, which can be found only in selected research groups. There is a synergy between intracavity Raman lasers and intracavity lasers based on SPS, or as described by the St. Andrew's group, intracavity THz OPO's. Macquarie University's longstanding expertise in the area of intracavity Raman lasers made them well positioned to tackle the challenges of polariton lasers and they have been responsible for the majority of the

progresses reported in the field of intracavity polariton lasers since 2013, and the work reported in this thesis represents an important segment of this research effort.

The work conducted during this PhD candidature, and reported in this thesis, had the primary objective of extending the frequency coverage and output power of such devices, with the investigation of different SPS materials such as KTP and RTP, and application of novel resonator designs. In reality, the achievements documented in this thesis have a much broader reach and relate to three fronts: the basic investigation of the SPS material properties, the substantial extension of the frequency coverage, and significant increase in output power level and diode-to-THz efficiency. These achievements were obtained due to a careful laser design, with innovative approaches and with the understanding of the underlying physics behind the intracavity SPS process.

In Chapter 3, spectroscopic techniques were utilised to determine core properties of the SPS materials that dictate the performance of SPS sources. As a result, the dispersion curve for RTP was calculated for the first time (to the best of this author's knowledge), which enabled predictions around the THz emission of SPS sources based on that crystal. More importantly, the thorough investigation reported in Chapter 3 indicated serious limitations of the linear geometry using KTP and RTP crystals with regards to the production of measurable THz signal above 4.20 THz, due to the strong absorption coefficients for the THz fields. This was confirmed experimentally as reported in Chapter 4, where wavelength-tunable Stokes radiation was detected from KTP with corresponding terahertz frequencies from 4.29 – 5.91 THz being generated, but no THz fields could be measured. In RTP, frequency-tunable THz radiation was detected for the first time, ranging from 3.10 to 3.17 THz, and from 3.50 to 4.15 THz, and a maximum average output power of 16.2 μW was detected at 3.80 THz (7.3 W diode pump; the gap in THz emission is due to the infrared absorbing mode measured at 106 cm^{-1}). At that time, this was the highest average output power in the THz ever detected from an intracavity SPS laser, this despite the limitations of RTP in linear geometry. It was also the first time a crystal different from lithium niobate was investigated in an intracavity design.

The surface-emitted layout was investigated in Chapter 5 for intracavity MgO:LN, KTP and RTP crystals, as a technique to avoid the intrinsic limitations of the linear geometry. For all materials investigated, the reported results demonstrated the superiority of the surface-emitted layout in comparison with the linear approach, when concerning output power and frequency coverage. In the surface-emitted geometry, terahertz radiation was detected for every

interacting angle producing wavelength-tunable Stokes radiation. Moreover, the measured output power levels were also higher in every case. In MgO:LN laser damage to the crystal was identified and avoided with the deposition of a Teflon coating on the TIR surface of the material. The Teflon-coated crystal delivered 58.6 μW output at 1.76 THz for only 6.5 W diode pump (9.0×10^{-6} diode-to-THz efficiency), and was continuously tunable from 1.46 – 3.84 THz. This represented a new record-high for output power, frequency-coverage and diode-to-THz efficiency for an intracavity SPS source.

The first successful frequency-tunable THz detection from an intracavity SPS source based on KTP was also reported. The KTP crystal produced 70.9 μW at 5.58 THz for 7.3 W diode pump (9.7×10^{-6} diode-to-THz efficiency), and was continuously tunable from 4.29 – 4.53 THz, 4.88 – 5.03 THz and from 5.47 – 5.89 THz. The gaps in the THz emission from KTP are located in the vicinity of the 153 and 177 cm^{-1} A_1 modes.

The RTP crystal yielded the maximum terahertz power detected among all resonator assemblies, and 124.7 μW was measured at 4.10 THz for a modest 6 W diode pump (1.3×10^{-5} diode-to-THz efficiency). The system produced terahertz output continuously tunable in four regions, from 3.05 to 3.16 THz, from 3.50 to 4.25 THz, from 4.57 to 4.75 THz and from 5.40 to 5.98 THz, and the gaps in THz emission corresponds to the infrared absorbing A_1 modes measured at 106, 143 and 161 cm^{-1}. Those results represented an important milestone, since it was the first time an intracavity SPS source exceeded the 0.1 mW average output power level and exhibited a diode-to-THz efficiency in the 10^{-5}-level. The beam quality parameter of the terahertz output from the RTP crystal was also measured to be excellent in comparison to a previously reported intracavity system in linear geometry, being $M_H^2 \sim 1.57$ and $M_V^2 \sim 1$ in the horizontal and vertical dimensions respectively. The power and frequency characteristics of the sources indicate that the surface-emitted geometry has the greatest potential to produce high-power, narrow-linewidth and high brightness, frequency-tunable THz sources, with exceptionally low pump powers.

The significant extension of the frequency coverage of intracavity SPS sources resulting from this PhD research can be more clearly observed with the aid of Figure 6.1. The figure shows the frequency coverage of intracavity SPS sources prior to this PhD candidature in red (also related in Chapter 1), and the contributions from this research work in blue. The pioneering use of KTP and RTP in an intracavity configuration enabled the extension of the frequency coverage from the previous 3.05 THz upper limit to a current 5.98 THz with RTP.

Moreover, the maximum average output power measured during this PhD research is more than 10 times higher than what was achievable previously (St. Andrew's 2008, Figure 6.1). The diode-to-THz conversion efficiency increased one order of magnitude over the previous best result, reaching 2.1×10^{-5} (compared to 1.3×10^{-6}; Macquarie University 2013, Figure 6.1).

The significant improvements obtained in this research can be attributed in great extent to the use of the surface-emitted configuration which avoids the absorption losses for the THz field generated at the TIR surface of the SPS crystal. There is also merit associated with the fundamental resonator having a higher Q-factor (<1% output coupling percentage) than what is typically used in Q-switched laser, which resulted in very high intracavity intensity, easily exceeding SPS threshold and producing pump depletion up to 80%.

From the results reported in this thesis it can be concluded that the surface-emitted configuration is a much superior layout for the construction of frequency-tunable THz sources based on intracavity SPS, when compared to the linear configuration based on Si-prisms, yielding higher average output power and wider frequency-coverage in comparison to linear resonator designs. The technology investigated here is versatile, and with a simple exchange of SPS crystal it is possible to switch the frequency coverage of the device. Furthermore, this device can be easily applied to real-world devices, which is one of the natural evolutions of this research.

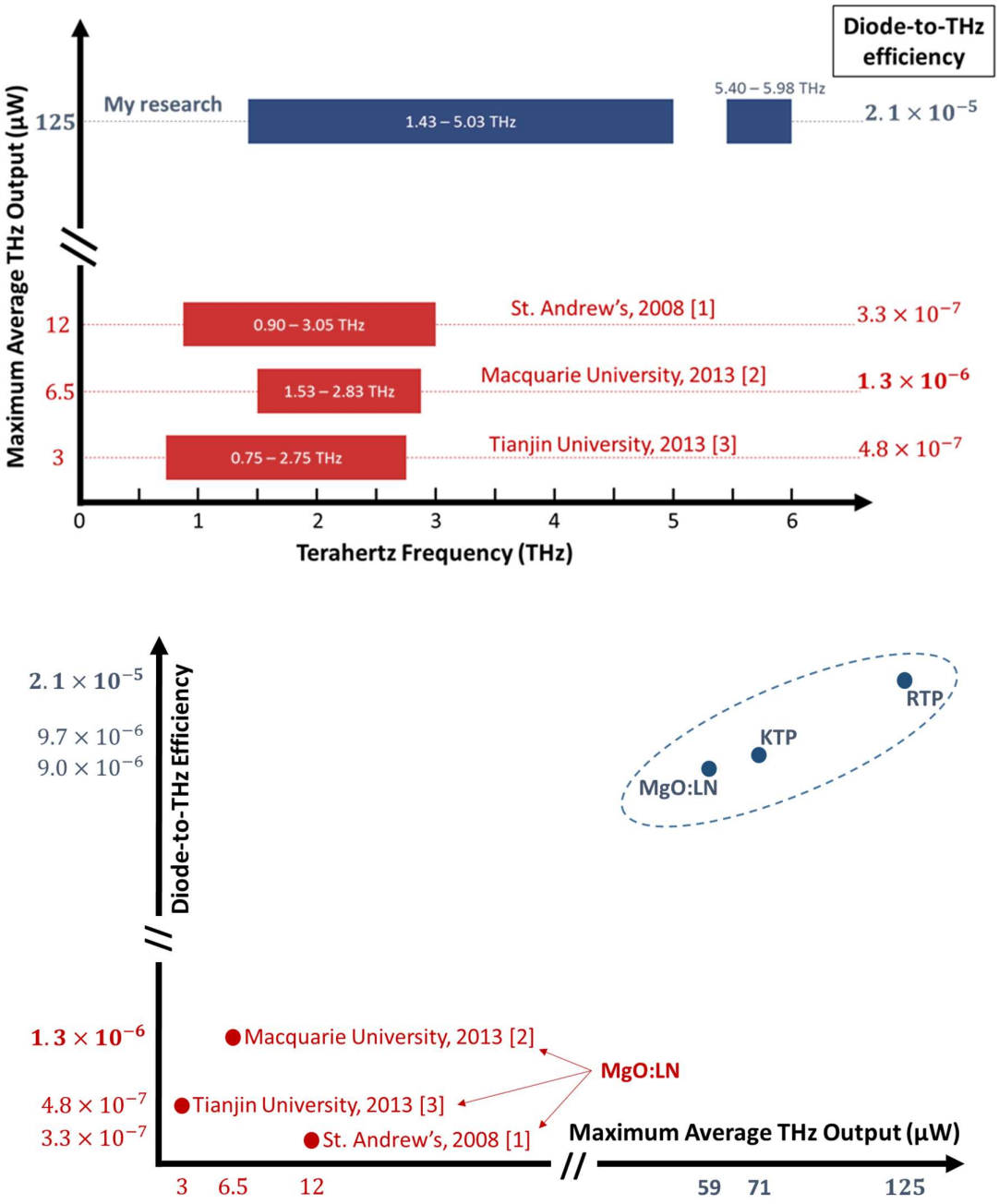

Figure 6.1 – Intracavity SPS sources performance. Top chart: average output power versus terahertz frequency coverage; bottom chart diode-to-THz efficiency versus maximum average THz output. Data for intracavity SPS sources prior to this PhD candidature are presented in red and the contributions from this research work reported in this thesis is presented in blue. [1] D. Stothard, *et al.* Appl. Phys. Letter 92, 141105 (2008). [2] A. Lee, *et al.*, IEEE J. of Quant. Electron. 49, 357-364 (2013). [3] Y. Wang, *et al.*, Laser Phys. 23, 055406 (2013).

6.2. Future developments

The work presented in this thesis reports significant and original contributions to the field of THz sources based on intracavity SPS with respect to the understanding of material properties, frequency coverage, output power and diode-to-THz efficiency. However, there is scope for further improvements in the engineering of these sources.

With the investigation of KTP and RTP, it was not possible to cover the gap from ~5.0 to 5.4 THz, which represents an inconvenience. It would be pertinent to investigate other nonlinear materials with the objective of generating SPS fields covering this frequency range, such possible materials include potassium titanyl arsenate crystal or semiconductors such as gallium phosphide.

The lower THz frequency emitted by the different sources investigated in this research is limited by the minimum angle which could be achieved between the Stokes and fundamental resonators, without clipping the fundamental field. Instead of using a two-mirror Stokes cavity, a four-mirror "U-shaped" Stokes resonator could be used. Other researchers reported an improvement in the minimum interacting angle achievable with this design (D. Walsh 2011, "Intracavity Optical Parametric Oscillators", doctoral thesis, University of St. Andrews, St. Andrews, UK).

There is also scope for revisiting the theory of SPS gain and developing equations for intracavity systems, considering transient fields instead of the current steady-state theory. This investigation could be complemented experimentally, investigating the influence of the resonator mode sizes on the SPS process efficiency, which can be easily achieved by modifying the radius of curvature of the output coupler.

With the appropriate infrastructure, the material properties can also be further explored, investigating the vibrational spectra of the SPS materials at frequencies below 100 cm^{-1}. This would enable refining the calculations of the polariton dispersion curve, extraordinary-wave refractive index and absorption coefficient. Also, with calibrated Raman spectra measurements, the third-order nonlinear coefficient d_Q could also be measured, enabling the calculation of the Stokes and THz gain curves.

The linewidth of the THz emission is considered satisfactory for many real-world applications, however if there is the need to reduce it further, high-finesse etalons could be

inserted in the fundamental and Stokes resonators to this end (similarly to what is reported by D. Stothard, *et al.* in Appl. Phys. Letter 92, 141105, (2008)).

All the above improvements are likely to be conducted in parallel with different experimental setups. The systems developed and reported in this thesis however, shall be prepared to be utilised in real-world applications, as a complementary tool to the ongoing research being conducted at Macquarie Univeristy . In this research the hydration level of biological material via transmission and reflection THz spectroscopy is under investigation.

The first step towards this objective is to introduce electronically controlled rotation stages in the Stokes cavity mirrors, to automate the frequency scan. This will be followed by the insertion of an automated translation stage for the samples, and a data logger to monitor the signal output from the Golay cell. We are also interested in utilising these sources to explore materials of interest to homeland security and border control, such as toxic and illicit substances.

6.3. Final words

The outcomes of the research conducted during this PhD candidature, and reported in this thesis, has brought new perspective to THz lasers based on intracavity SPS technology. With the use of different nonlinear materials in the surface-emitted configuration, significant improvements to the frequency-coverage of these systems were demonstrated, and also substantial increase in terahertz output power and diode-to-THz conversion efficiency was reported. These sources are sufficiently advanced and technology-ready, and will offer exceptional value to the field of THz spectroscopy and spectral imaging, with potential to address a wide variety of emerging real-world applications.

Appendix

A.1. Early work on THz lasers based on intracavity SPS by this research group at Macquarie University. Paper by: Andrew Lee, Yabai He and Helen Pask, " Frequency-Tunable THz Source Based on Stimulated Polariton Scattering in Mg:$LiNbO_3$," IEEE J. Quantum Electron. 49, 357-364 (2013)

The work reported in this paper was conducted at Macquarie University prior to the commencement of this PhD research, however it is considered a stepping stone for the work developed during this research and for this reason is related in this thesis.

Frequency-Tunable THz Source Based on Stimulated Polariton Scattering in Mg:$LiNbO_3$

Andrew Lee, Yabai He, and Helen Pask

***Abstract*— We report a very compact, laser diode end-pumped THz laser source, which utilizes two resonators to generate frequency-tunable radiation across the range 1.53–2.82 THz via stimulated polariton scattering (SPS) in a Mg:$LiNbO_3$ crystal. To the best of our knowledge, this THz system operates with the lowest pump power threshold (2.4 W), and highest conversion efficiency (6.45 μW average output power at 1.82 THz for 5 W input diode pump power) ever reported for a THz source based on SPS.**

***Index Terms*— Nonlinear frequency conversion, Raman, solid-state laser, stimulated polariton scattering (SPS), terahertz.**

I. Introduction

ELECTROMAGNETIC radiation in the terahertz frequency range (0.1 – 10 THz) has been historically considered one of the most difficult to generate and detect [1]–[4]. While the potential for THz radiation to be used in medicine, biology, security and other applications has been abundantly documented [5]–[9], the uptake of THz technologies has been hampered by a lack of practical, low-cost sources. In particular, narrow band, tunable sources in the 1–3 THz frequency range are particularly important for spectral fingerprinting and imaging applications involving many organic and inorganic compounds [5], [9]. In the past decade, considerable progress has been made towards the generation of THz radiation using a variety of optical approaches. Of particular note are sources based on optical frequency mixing, which include: difference frequency generation (DFG) between two laser beams [10], [11]; and terahertz parametric generation (TPG)—a process where a fundamental laser interacts with an optically-active vibrational mode of a crystal by stimulated polariton scattering (SPS) to generate a Stokes shifted beam and tunable THz radiation [12]–[15].

THz generation via optical frequency mixing is particularly versatile as it is compatible with established, robust, solid-state laser platforms such as Nd lasers and vertical-external-cavity surface-emitting-lasers (VECSEL), and can in principle be operated in continuous-wave (CW), Q-switched or mode-locked regimes. A clear benefit of SPS is that only one pump laser is required, but to date this has not yet translated to superior output powers or performance. Recently a CW THz source was demonstrated using a dual-wavelength VECSEL pump source, constituting a particularly effective and practical THz source [16]. In this paper, we are concerned with the SPS approach, and we have investigated the potential for reducing the pump power requirements, and the factors limiting optical efficiency.

It is important, and sometimes overlooked, that as early as the 1960s, scientists reported tunable far-infrared lasers, tunable Raman lasers and submillimetre wave lasers, typically operating in the 1–3 THz spectral region [17]–[20]. The first observation of tunable stimulated Raman emission was reported by Gelbwachs *et al.* [18], using a Q-switched ruby laser to excite the A_1 symmetry 248 cm^{-1} polariton mode in a lithium niobate ($LiNbO_3$) crystal. Tunability was achieved by varying the angle between the excitation laser beam and the resonator in which the $LiNbO_3$ crystal was placed. Further work ensued, leading to the description in 1975 [20] of a continuously tunable submillimetre wave source based on the 248 cm^{-1} polariton mode in $LiNbO_3$, to cover most of the 100–1000 cm^{-1} range. There followed several decades of relatively little activity in this area, however during this time there were significant developments in crystal growth, optical coating and solid-state laser technologies. When terahertz technology became a popular area of research in the late 1990s, this class of $LiNbO_3$–based laser sources that were pioneered ~4 decades earlier, re-emerged under the banner of Terahertz Parametric Generators and Oscillators.

$LiNbO_3$ has several transverse-optical (TO) modes that are both Raman and infrared active, and the frequency of these modes are dependent on their wavevector. The energy of these modes is partly mechanical and partly electromagnetic, and the corresponding quanta are known as polaritons. An excellent review of polaritons can be found in [21], and studies of the polariton modes of $LiNbO_3$ can be found for example in [13], [17], [22], and [23]. The polariton mode in $LiNbO_3$ at ~248 cm^{-1} is the one of particular interest for THz generation around 1–3 THz due to the high nonlinear gain and lowest absorption [13]. The dual "mechanical/electromagnetic" character of the polariton mode, gives rise to complex nonlinearities. Stimulated polariton scattering (SPS) is a third-order nonlinear process in which stimulated "Stokes" radiation (υ_S) results from an interaction between fundamental field photons (υ_f) of sufficient intensity and the polariton mode (υ_P) in the crystal.

$$\upsilon_S = \upsilon_f - \upsilon_P. \tag{1}$$

The polariton frequency υ_P must lie on the materials dispersion curve (w-k diagram), which has been well-studied in [24], and therefore there are a unique combination of frequencies

Manuscript received September 26, 2012; revised January 7, 2013; accepted January 27, 2013. Date of publication February 6, 2013; date of current version February 26, 2013. This work was supported by Australian Research Council's Discovery Projects funding scheme under Project DP110103748.

The authors are with the MQ Photonics Research Centre, Department of Physics and Astronomy, Macquarie University, Sydney NSW 2109, Australia (e-mail: andrew.lee@mq.edu.au; yabai.he@mq.edu.au; helen.pask@mq.edu.au).

Color versions of one or more of the figures in this paper are available online at http://ieeexplore.ieee.org.

Digital Object Identifier 10.1109/JQE.2013.2244850

and wavevectors allowed for the scattering process. In the case of a fundamental field at 1064 nm, and the 248 cm^{-1} mode of $LiNbO_3$, Stokes radiation is typically in the near-infrared wavelength range of 1068–1081 nm, while the polariton frequency is in the range ~1.0–4.4 THz. Significantly, there is strong absorption of the polariton radiation by $LiNbO_3$ in this range, which has a strong influence on the way this process operates [13].

Early studies of such tunable submillimetre sources used pulsed ruby lasers for excitation in generator [17] or oscillator configurations [18], [20]. More recently, there have been several studies in which a Nd laser has been used [12]–[15], [25]–[27]. An alternative to using high peak power lasers is to instead use an intracavity configuration whereby the high intensity fundamental field inside a laser cavity can achieve threshold for the SPS process more easily. Furthermore, by utilising an intracavity configuration, the pump field also undergoes multiple passes through the SPS crystal. Such an approach has been investigated by Edwards *et al.* who have demonstrated promising results from a resonator formed around a 50 mm long, Mg:$LiNbO_3$ crystal, placed within the cavity of an end-pumped, Q-switched, Nd:YAG laser [28]. From this system, they achieved THz emission, tunable from 1.2–3.05 THz, with maximum energy of ~5 nJ. While they showed excellent tuning range and output power, the system still operated with a high pump diode power threshold of 20 W (quasi-CW with 500 μs pulses), and was fairly large, with a resonator length of 37 cm. They note that the intracavity power required to reach threshold for the SPS process is lower than that required for extra-cavity SPS systems (~12 MW/cm^2 c.f. >30 MW/cm^2 [14]) and that the most significant factor limiting power scaling of their system is absorption of the THz field as it propagates towards the exit surface of the Mg:$LiNbO_3$ crystal which is used for SPS.

While long (≥50 mm) Mg:$LiNbO_3$ crystals are ideal in generator configurations as they offer more single-pass gain, they are not necessarily optimal for oscillator configurations in which multiple passes of the SPS gain crystal can be achieved. This is especially true of intracavity configurations where the resonating mode size can also be very small, provided that the damage threshold of the Mg:$LiNbO_3$ crystal (~100 MW/cm^2 [29]) is not exceeded. In this work we demonstrate that there are significant merits to using shorter SPS crystals in intracavity oscillator configurations, in conjunction with small resonator mode sizes, and high-Q cavities, to achieve a broad THz frequency tuning range, reduce THz attenuation, and reduce THz generation threshold. Here, we demonstrate a significant step towards the realisation of a practical, frequency-tunable THz radiation source which is compact and robust, and importantly has very low operating power requirements. All these traits are desirable for a THz source which may be applied to applications outside the laboratory environment.

II. Experimental Arrangement

The terahertz radiation source reported here comprised an end-pumped, Q-switched 1064 nm Nd:YAG laser with an intracavity Mg:$LiNbO_3$ crystal for generation of THz radiation. A second cavity was formed around the Mg:$LiNbO_3$ crystal to oscillate the near-infrared Stokes field generated through the SPS process. The angle between the axes of the two cavities could be varied and determined the exact Stokes wavelength and THz frequency. Details of the system setup are shown in Fig. 1. The Nd:YAG crystal was end-pumped by a fibre-coupled (400 μm diameter, 0.22 NA) 808 nm continuous-wave diode laser at power levels up to 10 W. The diode output pump radiation was focused to a 400 μm diameter pump spot inside a 7 mm long, 5 mm diameter, 1 a.t. % Nd:YAG crystal, that was anti-reflection (AR) coated for both 808 nm and 1064 nm wavelengths. The fundamental (1064 nm) resonator was formed by a flat mirror M1 coated high transmission at 808 nm (T = 99.4%) and high reflecting at 1064 nm (R > 99.9%), and a concave mirror M2 (100 cm radius of curvature (ROC)), which was also coated high transmission at 808 nm (T = 83.5%) and high reflecting at 1064 nm (R = 99.4%). The two mirrors were separated by 124 mm. An intracavity acousto-optic Q-switch (NEOS, part number 33027-25-2-i) was used to achieve pulsed operation and so deliver the high peak powers required to reach threshold for SPS. The repetition rate was 3 kHz.

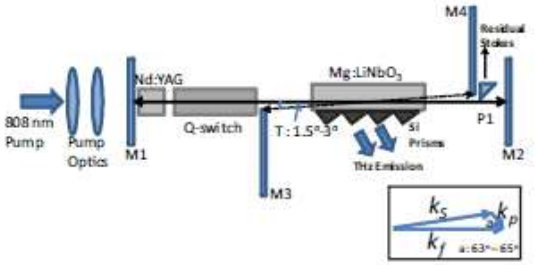

Fig. 1. Layout of the experimental system for the generation of frequency-tunable THz radiation using SPS in an intracavity arrangement. The angle between the fundamental field generated between mirrors M1 and M2, and the Stokes field generated between mirrors M3 and M4 is exaggerated for clarity (external angle (θ) ranges from 1.5°–3.0°).

SPS was achieved in a congruent, x-cut, 5 a.t.% Mg:$LiNbO_3$ crystal (sourced from HC Photonics Corp.), having dimensions of 5 mm × 5 mm × 25 mm, and end-faces AR coated for 1064–1090 nm (R < 0.1%). The Stokes resonator with length 64 mm was formed around the Mg:$LiNbO_3$ crystal using two flat mirrors M3 and M4 which were D-shaped to avoid clipping of the fundamental beam. Both mirrors were coated for high reflectivity across the range 1064–1080 nm, with M3 and M4 having manufacturer specified reflectivity of >99.99% and 99.9% respectively. These two mirrors were mounted on a common platform on a rotation stage, which enabled their rotation relative to the fundamental cavity, centred about the Mg:$LiNbO_3$ crystal. SPS was achieved for angles of ~1.5–3.0 degrees (external angle) between the two resonator axes. The wave-vector diagram showing the interaction of the fundamental (k_f), Stokes (k_S) and polariton (k_P) fields is shown in the inset of Fig. 1. The generated polariton field (THz radiation)

propagates at ~63–65 degrees to the resonator axis. The high refractive index of Mg:$LiNbO_3$ at THz frequencies [30] means the THz wave suffers total internal reflection (TIR) at a crystal-air interface. Therefore, as per the work of Kawase *et al.* [14], [31], high-resistivity ($R > 10\,k\Omega\,cm^{-1}$) silicon (Si) prisms were used to overcome TIR and enable extraction of the generated THz radiation. They were contacted via liquid-mediated Van der Waals bonding [32] onto one of the two optically-polished side faces of the crystal (those perpendicular to the x-axis).

ABCD resonator modelling [33] was carried out to estimate the resonator mode size in the Mg:$LiNbO_3$ crystal. We estimated the thermal lens in the Nd:YAG crystal had a focal length of ~150 mm at maximum pump power (10 W). Accordingly we determined the TEM_{00} mode diameter of the fundamental field in the Mg:$LiNbO_3$ to range between 550 μm for the passive cavity and 450 μm for the cavity pumped with 10 W diode power. These relatively small fundamental field spot sizes are ideal as these lead to high fundamental field power densities within the Mg:$LiNbO_3$ crystal, reducing the diode pump powers required to reach threshold for SPS [19]. The corresponding diameters of the Stokes field are also small as these are dictated by the mode size of the fundamental field within the Mg:$LiNbO_3$ crystal. Small mode sizes are preferable as they are not clipped as readily by the edges of the Mg:$LiNbO_3$ crystal and the oscillator mirrors. This in turn enables a wider angle/THz frequency tuning range, and THz generation to take place closer to the Mg:$LiNbO_3$ crystal/Si prism interface, reducing the THz propagation distance and therefore attenuation.

The power-scaling characteristic of the fundamental and Stokes fields were monitored by examining their leakage through mirrors M2 and M4 respectively. A 90° prism was used to reflect the Stokes beam transmitted through mirror M4 for detection purposes. Depletion of the fundamental field via SPS was determined by measuring the change in fundamental field power when the Stokes cavity was blocked and un-blocked. The spectral content of these beams was examined using a high-resolution fibre-coupled grating spectrometer (Ocean Optics, HR4000), and the temporal characteristics of the Stokes and fundamental fields were measured using a fast photo diode. The frequency of the THz output was inferred from the difference in corresponding optical frequencies between the measured fundamental and Stokes wavelengths as per equation 1. The THz radiation transmitted through the Si prisms was measured using a calibrated Golay cell (68 kV/W @ 20 Hz) and a mechanical chopper with a 50% duty cycle at a frequency of 20 Hz. A 200 μm thick layer of polytetrafluoroethylene (PTFE) and 100 μm thick layer of black polyethylene were used to block undesired IR and visible radiation from being detected by the Golay cell.

III. Results

Threshold for the fundamental (1064 nm) field was achieved at an incident diode pump power of 0.55 W, and the lowest threshold for SPS was achieved at 2.4 W incident diode pump power, as determined from the onset of Stokes field oscillation.

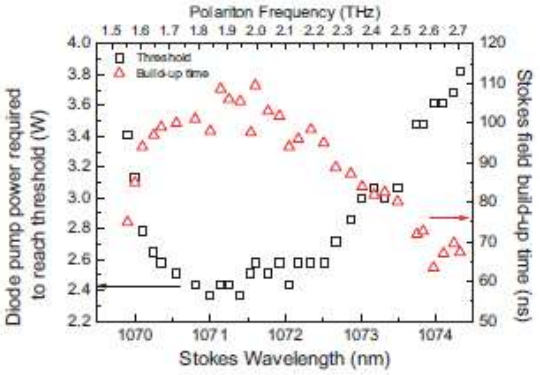

Fig. 2. Plot of diode pump power required to reach SPS threshold and the corresponding Stokes field build-up time as a function of Stokes wavelength/polariton frequency.

From measurements of the fundamental field leaking through mirror M2, we estimated that the corresponding average intracavity fundamental power was ~9.6 W. In this case, the angle between the Stokes and fundamental resonators was set to deliver the lowest possible threshold, which in this case corresponded to a Stokes field wavelength of 1071 nm and a polariton frequency of 1.84 THz. Just below SPS threshold, the fundamental field had a full width at half maximum (FWHM) pulse duration of ~200 ns, thus yielding a fundamental field power density of 8.2 MW/cm^2 required to reach SPS threshold.

The dependence of diode pump power required to achieve SPS threshold, and the corresponding build-up time of the Stokes field as a function of the Stokes field wavelength/polariton frequency have been measured and are plotted in Fig. 2. The build-up time was measured as the difference in time between the leading edges (at half maximum) of the fundamental and Stokes field pulse shapes. Continuous tuning of the Stokes wavelength/polariton frequency was achieved by rotating the Stokes resonator with respect to the fundamental resonator. The external angle between the two resonators was ~1.5° at a Stokes wavelength of 1070 nm, and this increased to ~3° at a Stokes wavelength of 1074 nm.

There are a number of interesting features to note in Fig. 2. There is a significant dip in the diode pump power required to achieve threshold for Stokes and polariton generation for frequencies in the range 1.8–2.2 THz, and there is a corresponding increase in the Stokes field build-up time. These features can be attributed to a number of factors, as follows. Clipping of the fundamental field by the Stokes resonator mirrors (M3 and M4) occurs for low Stokes wavelengths/polariton frequencies due to the small angle between the Stokes and fundamental fields (this ultimately limits the lowest polariton frequency that may be generated in the system). There is also a change in SPS gain within the Mg:$LiNbO_3$ crystal as a function of THz frequency, which is considered in detail in [14] and [19]; the SPS gain rapidly increases from 0 THz to ~1.9 THz, and

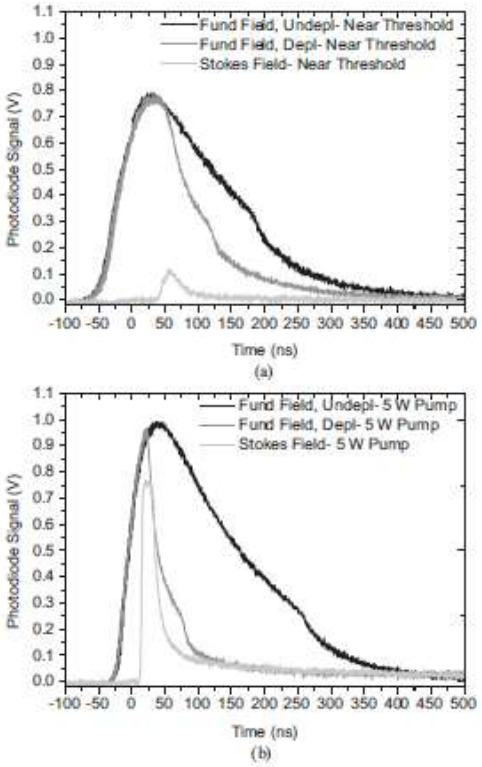

Fig. 3. Temporal profiles of the Stokes field and the fundamental field when depleted and undepleted when operating (a) near threshold and (b) at 5-W incident diode pump power. The system was tuned to generate emission at 1.8 THz.

then gradually decreases as the polariton frequency increases towards 3 THz. It is a monotonically decreasing function of the polariton absorption coefficient, which as described later in this paper, we have measured to increase significantly by $\sim$11 cm^{-1} for just a small change in THz frequency from 1.9 to 2.3 THz. Finally, as the angle between the fundamental and Stokes fields increases, the interaction region between the two fields decreases, and this further contributes to higher thresholds at the higher THz frequencies.

The Stokes field build-up times are relatively long, corresponding to between around 200 and 350 transits through the Mg:$LiNbO_3$ crystal. The build-up times are inversely proportional to the diode pump powers at threshold. This is simply due to the fact that at lower powers, more round trips are required to reach threshold for a given value of SPS gain. The low cavity losses for the fundamental and Stokes field are particularly important in allowing such long build-up times. As noted in [34] for extracavity OPOs, the measured build-up time can also be influenced by the pump-dependent rate of growth of the fundamental field.

The SPS threshold at a diode pump power of 2.3 W, achieved in this work is very low. A much higher diode pump

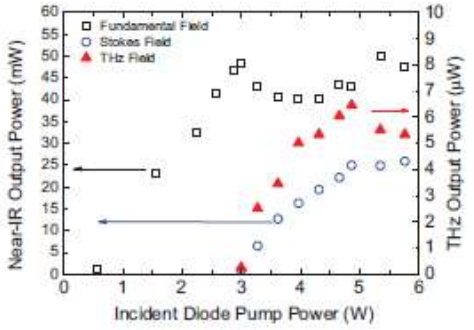

Fig. 4. Measured output of the fundamental, Stokes, and polariton fields as a function of incident diode pump power. The Stokes wavelength and polariton frequency are 1070.92 nm and 1.82 THz, respectively.

power of 20 W (quasi-cw with 500 μs pulses) was required to achieve SPS threshold in [28], and their fundamental field cavity had a high output coupling of 10 %, leading to shorter fundamental field pulses and reduced accumulation of fundamental photons in the cavity while the Stokes field was building up. In this work, we have low output coupling of $\sim$1 % for the fundamental field and this has undoubtedly contributed to the relatively-low diode powers required to reach SPS threshold, as was predicted in [28]. There are however several other contributing features of our laser design including: smaller mode size in the Mg:$LiNbO_3$ crystal which increases power density within the SPS crystal, shorter Stokes resonator which results in reduced round-trip and build-up times [35], and higher-Q resonator for the Stokes field. Other design differences such as the shorter Raman crystal (25 mm c.f. 50 mm) and unpolarised fundamental field would, in isolation, tend to favour higher thresholds, but these are outweighed by the effects of shorter resonator length and smaller mode-size in our system.

The pulse profiles of both the fundamental field (with and without depletion), and the Stokes field are shown in Fig. 3, for the two cases of the system operating near threshold and at a maximum diode pump power of 5 W. The plots show that the build-up time and pulse duration of the Stokes pulse both decrease, while pump depletion increases as the incident diode pump power increases. The build-up time decreases from $\sim$70 ns slightly above threshold to $\sim$20 ns at maximum pump power. This implies that the Stokes field builds up over $\sim$111 round trips near threshold and this decreases to $\sim$32 round trips at maximum pump power. In comparison to the work of Edwards *et al.* [28], who only quotes build-up time at maximum pump power, the Stokes field in our compact resonator undergoes more round-trips ($\sim$32 vs 17) as it builds in intensity. This contributes to the lower threshold observed in our system.

Fig. 4 shows the power scaling characteristics of the laser for the case of the Stokes resonator generating output at 1070.92 nm, and THz radiation at $\sim$1.82 THz. This is also the frequency at which maximum measured THz output power was obtained. Above the threshold for SPS (3 W diode pump

power in this case), the fundamental field is strongly depleted, indicating efficient conversion to the Stokes and polariton fields. A slower increase in the Stokes field power is observed and it appears to saturate for incident pump powers above 5 W; note that the Stokes field powers measured outside the resonator are relatively low, owing to the high reflectivity of mirrors M3 and M4 which are chosen to resonate the Stokes field for low threshold. The measured THz power grows steadily until the incident diode power is 5 W, and then starts to decrease slightly. The fundamental field displays a corresponding increase in power. Such behaviour is consistent with back conversion of Stokes and THz fields to the fundamental through the reciprocal process of sum frequency generation (SFG). Back conversion is a well-known process that limits the power-scaling of optical parametric oscillators (OPOs) in the regime of strong pump field depletion [36], [37]. Based on the measured Stokes field power leaking through mirror M4, we estimate that at a ~5 W incident diode pump power, 52 W of Stokes power (average) is being resonated. Depletion of the fundamental field was found to be ~57% for the case of 5 W incident diode pump power.

The maximum average THz output power measured from the system was 6.45 μW. Given the pulse repetition frequency was 3 kHz, this corresponded to a pulse energy of >2 nJ per pulse. Since the THz beam was not resonated, its pulse duration is expected to be shorter than the 14 ns measured for the Stokes pulse. Accordingly we estimate the peak power of the THz output to be well in excess of 150 mW.

The overall (diode to THz) conversion efficiency of the system is extremely low, due to the large difference in diode and THz photon energies. An upper limit to the efficiency is set by the photon quantum efficiency which is ~0.49% (ratio of 1.8 THz photon energy to diode pump photon energy). Using the data in Fig. 4, the measured THz efficiency (diode input to THz) was in fact 1.3×10^{-4}%, approximately 3 orders of magnitude lower than the quantum efficiency. Using our measurement of the fundamental field leaking through mirror M2 and a depletion of 57%, combined with a fundamental to THz photon quantum deficit of 0.64%, we estimate that up to 35 mW of average THz power is generated internally within the Mg:$LiNbO_3$ crystal. Accordingly we estimate that the efficiency with which the THz radiation is extracted from the Mg:$LiNbO_3$ crystal is ~0.04%. Some of the factors that contribute to this low extraction efficiency are as follows. The THz radiation is generated in two directions depending on the transit direction of the fundamental and Stokes fields, and we only collect the THz radiation propagating towards the silicon prisms. Other factors include significant absorption of the THz field within the Mg:$LiNbO_3$ crystal (absorption coefficients in excess of 64 cm^{-1} at 2.34 THz have been measured in this work), absorption of the THz field in the silicon prisms [38], and Fresnel reflections at the Mg:$LiNbO_3$/Si prism and Si Prism/air interfaces which we calculate to be 6% and 29% respectively. Clearly, improvements to the extraction efficiency of the THz radiation are an important part of optimising the performance of THz lasers.

The fundamental, Stokes and THz field output powers as a function of frequency-tuning are shown in Fig. 5. As the angle between the Stokes and fundamental field resonators was increased, the Stokes wavelength changed from 1069.8 up to 1074.7 nm, corresponding to a THz frequency tuning range of 1.53–2.82 THz.

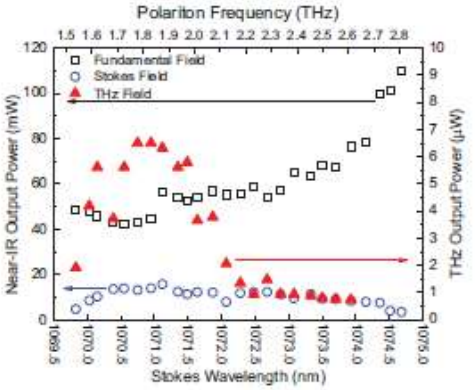

Fig. 5. Fundamental, Stokes, and THz field output powers as a function of Stokes wavelength/polariton frequency at an incident diode pump power of 4 W.

The powers for the fundamental, Stokes and THz fields were measured for an incident diode pump power of 4 W. It is the detected THz power that depends most strongly on angle. As the angle between the resonators is increased, the detected THz radiation increases rapidly for frequencies from ~1.53–1.80 THz, and this is consistent with the increase in gain due to the SPS process [14] and reduced clipping of the fundamental field beam that occurs at low frequencies/small angles. As the angle between the resonators increases further, there is a significant decrease in the detected THz radiation, this being due to a reduction in the SPS gain, and most significantly due to a rapid increase in absorption of the THz radiation within the Mg:$LiNbO_3$ crystal, which increases with THz frequency [13]. The dip in detected THz power at ~1.68 THz was very repeatable and corresponds to an absorption feature due to water vapour in the ambient environment [39]. The Stokes field shows little change as a function of tuning as it does not suffer absorption within the Mg:$LiNbO_3$ crystal like the THz field. There is however, a reduction in the Stokes field output at each end of the tuning range and this is consistent with the increase in the diode pump power required to reach SPS threshold. The increase in fundamental field output power for frequencies beyond ~2.3 THz is indicative of reduced SPS gain and hence reduced conversion efficiency to the Stokes and THz fields.

IV. Improving THz Output Power: Conversion and Extraction Efficiency

There are two factors limiting the maximum detectable THz radiation from this system, the efficiency of THz generation and the efficiency of THz radiation extraction. Based on our results, the generation efficiency is largely limited by back-conversion of the Stokes and THz fields to the fundamental field, brought about by strong depletion.

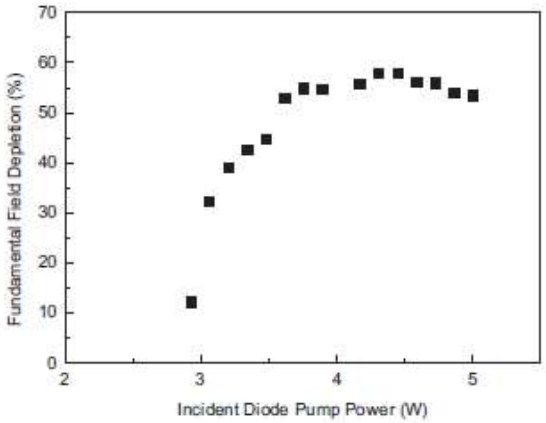

Fig. 6. Fundamental field depletion as a function of incident diode pump power for a system set to generate emission at 1.82 THz.

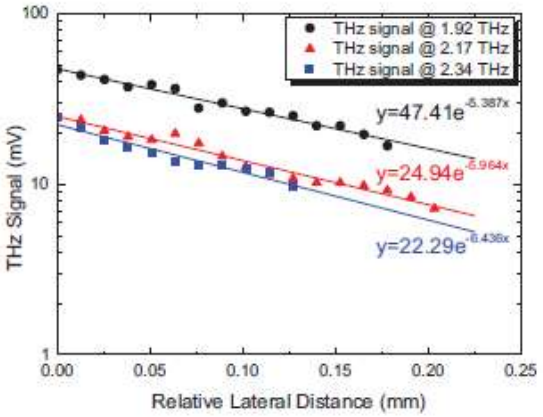

Fig. 7. Measured THz radiation as a function of relative lateral distance travelled by the THz field through the Mg:$LiNbO_3$ crystal taken at frequencies of 1.92, 2.17, and 2.34 THz. Lines of best-fit and their corresponding equation are shown.

A plot of the fundamental field depletion as a function of incident diode pump power, with the Stokes resonator angled to generate emission at 1.82 THz (frequency at which maximum THz power was detected) is shown in Fig. 6. The plot shows that depletion of the fundamental field increases rapidly above threshold and saturates at ~1.3 times above threshold. The rapid increase in depletion is suitable for strong THz generation at relatively low diode pump powers, however, for higher pump powers, the strongly depleted fundamental field makes the system highly susceptible to back-conversion. This is because the fundamental field intensity is effectively pinned once above SPS threshold [34], and increasing diode pump energy is transferred to the Stokes and THz fields.

It is clear from Fig. 5 that the detected THz radiation decreases considerably as the THz frequency increases. This change is largely driven by absorption of the THz radiation within the Mg:$LiNbO_3$ crystal. We have examined the absorption properties of the Mg:$LiNbO_3$ crystal used in our work, by measuring the THz power as the Mg:$LiNbO_3$ crystal was translated laterally across the fundamental beam, such that the distance travelled by the THz beam before exiting the crystal could be varied. Fine translation was accomplished by Vernier control of a translation stage. The measured THz signal detected on the Golay cell, as a function of distance (measured with respect to the position where the THz generation region was as close to the side of the crystal as possible without clipping) are shown in Fig. 7 for a range of THz frequencies. As expected, the change in THz signal power follows a Beer's Law dependence. By fitting the slopes of each set of measurements, the absorption coefficients were determined to be 54 ± 15 cm^{-1} at 1.92 THz, 60 ± 12 cm^{-1} at 2.17 THz and 64 ± 26 cm^{-1} at 2.34 THz.

These measurements are consistent with those observed in [13] and show clearly how even small shifts in THz frequency can result in a significant change in absorption and therefore THz output power. These measurements also highlight the importance of minimising the propagation distance of the THz radiation. Reducing this distance by as little as 180 μm (less than half the fundamental field mode diameter) can lead to a doubling of the detected THz power. Ikari *et al.* [40] demonstrated a novel solution to the problem of THz absorption in an external resonator THz parametric oscillator by using a so-called "surface emitting configuration". It remains to be seen whether such an approach may be useful in an intracavity configuration.

The length of the Mg:$LiNbO_3$ crystal is a parameter that can be optimised in order to reduce the impact of THz absorption, and to understand this, we consider the spatial overlap of the fundamental and Stokes resonator modes, i.e. the region where THz radiation is generated. Clearly it is desirable to have these beams overlapping as close as possible to the side of the Mg:$LiNbO_3$ through which the THz radiation is out-coupled. The range of angles between the intersecting beams, in combination with the length of the crystal and diffraction losses sets a limit to how close these beams can be to the side of the crystal. Based on geometric considerations and assuming mode diameters of 450 μm for the fundamental and Stokes fields, we have calculated the crystal length in which the fundamental and Stokes beams interact to range between 18.0 and 9.5 mm for external angles between 1.5 and 3.0 degrees respectively. Accordingly, the system could be improved by using a shorter crystal of say 20 mm length so that THz generation can take place closer to the side of the crystal without clipping of the Stokes beam at the ends of the crystal. Additional benefits associated with shorter crystals include lower cavity round trip times and reduced resonator losses.

There are also prospects for reducing the amount of THz absorption by considering material properties. Previous studies have shown that the SPS gain is dependent upon composition and purity of the Mg:$LiNbO_3$ crystal. For example, the use of stiochiometric $LiNbO_3$ compositions as opposed to congruent compositions (as used in this work) exhibit higher SPS gain and better separation of the targeted A_1 transverse optical mode with adjacent modes [41], both factors that would contribute to better SPS generation efficiency. Also,

stoichiometric Mg:$LiNbO_3$ crystals exhibit significantly lower THz absorption in comparison to congruent Mg:$LiNbO_3$ [42], lower scattering losses, and they can be doped with lower levels of MgO in order to achieve the same damage resistance as congruent crystals (typically <1% vs 5%) [30], [43]. The relative abundance of Li^6 and Li^7 is another factor that has been reported to influence SPS gain [44].

The key design challenge for the THz laser presented here, is to design a laser resonator which will simultaneously enable efficient generation of the fundamental field in the laser crystal, and efficient generation of the Stokes and THz fields through SPS in the Mg:$LiNbO_3$ crystal. In so doing, it is also important to manage thermal lensing in the laser crystal to maintain reasonable intracavity mode-sizes, and maintain resonator stability, minimise back conversion, minimise extraction losses and maximise tunability, while avoiding optical damage. There are inevitably trade-offs between these various priorities, and these need to be understood and managed, depending on the desired input/output powers for a particular laser. For example, increasing the mode size in the Mg:$LiNbO_3$ could lead to higher THz powers being generated (by increasing the pump power level at which strong fundamental depletion occurs), however this larger mode size may also be detrimental to the extraction efficiency, because the THz beam has to travel further to exit the crystal, and would also reduce the THz frequency tuning range due to clipping.

V. Conclusion

In this work, we have demonstrated an efficient and compact source of frequency-tunable THz radiation based on stimulated polariton scattering in Mg:$LiNbO_3$. By making use of small intracavity mode sizes, high-Q cavities, and a short SPS crystal, we have achieved THz generation at only 2.4 W incident diode pump power, which to the best of our knowledge, is the lowest diode pump threshold reported for the generation of THz radiation from an SPS system. Also, we have achieved a maximum average THz power of 6.45 μW for a diode pump power of only 5 W. There is significant scope to further increase THz output power through using stoichiometric Mg:$LiNbO_3$ crystals which exhibit higher Raman gain and lower THz absorption. The ability to generate tunable THz emission from a system little more complex than a solid-state Raman laser, and for only 5 W diode pump power represents a significant step towards realising a low-cost THz source suitable for "out of the lab" applications.

Acknowledgment

The authors would like to thank Dr. P. Browne (Macquarie University) and Dr. G. Malcolm (M Squared Lasers Inc.) for their advice and valuable discussions during the early stages of the project.

References

[1] B. Ferguson and X.-C. Zhang, "Materials for terahertz science and technology," *Nature Mater.*, vol. 1, no. 1, pp. 26–33, 2002.

[2] P. H. Siegel, "Terahertz technology," *IEEE Trans. Microw. Theory Tech.*, vol. 50, no. 3, pp. 910–928, Mar. 2002.

[3] D. M. Mittleman, M. Gupta, R. Neelamani, R. G. Baraniuk, J. V. Rudd, and M. Koch, "Recent advances in terahertz imaging," *Appl. Phys. B*, vol. 68, no. 6, pp. 1085–1094, 1999.

[4] J. Ahn, A. V. Efimov, R. D. Averitt, and A. J. Taylor, "Terahertz waveform synthesis via optical rectification of shaped ultrafast laser pulses," *Opt. Exp.*, vol. 11, no. 20, pp. 2486–2496, 2003.

[5] M. Tonouchi, "Cutting-edge terahertz technology," *Nature Photon.*, vol. 1, no. 2, pp. 97–105, 2007.

[6] L. Ho, M. Pepper, and P. Taday, "Terahertz spectroscopy signatures and fingerprints," *Nature Photon.*, vol. 2, no. 9, pp. 541-543, 2008.

[7] P. H. Siegel, "Terahertz technology in biology and medicine," *IEEE Trans. Microw. Theory Technol.*, vol. 52, no. 10, pp. 2438–2447, Oct. 2004.

[8] P. C. Achworth, E. Pickwell-MacPherson, E. Provenzano, S. E. Pinder, A. D. Purushotjam, M. Pepper, and V. P. Wallace, "Terahertz spectroscopy freshly excised human breast cancer," *Opt. Lett.*, vol. 17, no. 15, pp. 12444–12454, 2009.

[9] G. Davies, A. D. Burnett, W. Fan, E. H. Linfield, and J. E. Cunningham, "Terahertz spectroscopy of explosives and drugs," *Mater. Today*, vol. 11, no. 3, pp. 18–26, 2008.

[10] K. Kawase, M. Mizuno, S. Sohma, H. Takahashi, T. Taniuchi, Y. Urata, S. Wada, H. Tashiro, and H. Ito, "Difference-frequency terahertz-wave generation from 4-dimethylamino-N-methyl-4-stilbazolium-tosylate by use of an electronically tuned Ti:sapphire laser," *Opt. Lett.*, vol. 24, no. 15, pp. 1065–1067, 1999.

[11] K. Suizu, K. Miyamoto, T. Yamashita, and H. Ito, "High-power terahertz-wave generation using DAST crystal and detection using mid-infrared powermeter," *Opt. Lett.*, vol. 32, no. 19, pp. 2885–2887, 2007.

[12] K. Kawase, M. Sato, T. Taniuchi, and H. Ito, "Coherent tunable THz-wave generation from LiNbO3 with monolithic grating coupler," *Appl. Phys. Lett.*, vol. 68, no. 18, pp. 2483-2485, 1996.

[13] J. Shikata, K. Kawase, K. Karino, T. Taniuchi, and H. Ito, "Tunable terahertz-wave parametric oscillators using $LiNbO_3$ and MgO:$LiNbO_3$ crystals," *IEEE Trans. Microw. Theroy Tech.*, vol. 48, no. 4, pp. 653–660, Apr. 2000.

[14] K. Kawase, J. Shikata, and H. Ito, "Terahertz wave parametric source," *J. Phys. D: Appl. Phys.*, vol. 34, pp. R1–R14, Dec. 2001.

[15] K. Kawase, H. Minamide, K. Imai, J. Shikata, and H. Ito, "Injection-seeded terahertz parametric generator with wide tunability," *Appl. Phys. Lett.*, vol. 80, no. 2, pp. 195–197, 2002.

[16] M. Scheller, J. M. Yarborough, J. V. Moloney, M. Fallahi, M. Koch, and S. W. Koch, "Room temperature continuous wave milliwatt terahertz source," *Opt. Exp.*, vol. 18, no. 26, pp. 27112–27117, 2010.

[17] M. Yarborough, S. S. Sussman, H. E. Puthoff, R. H. Pantell, and B. C. Johnson, "Efficient, Tunable optical emission from LiNbO3 without a resonator," *Appl. Phys. Lett.*, vol. 15, no. 3, pp. 102–105, 1969.

[18] J. Gelbwachs, R. H. Pantell, H. E. Puthoff, and J. M. Yarborough, "A tunable stimulated Raman oscillator," *Appl. Phys. Lett.*, vol. 14, no. 9, pp. 258–262, 1969.

[19] S. S. Sussman, "Tunable light scattering from transverse optical modes in lithium niobate," Stanford Univ., Stanford CA, USA: Microw. Lab. Rep., 1851, 1970.

[20] M. A. Piestrup, R. N. Fleming, and R. H. Pantell, "Continually Tunable Submillimeter Wave Source," *Appl. Phys. Lett.*, vol. 26, no. 8, pp. 418–421, 1975.

[21] D. L. Mills and E. Burstein, "Polaritons: The electromagnetic modes of media," *Rep. Progr. Phys.*, vol. 37, no. 7, pp. 817–926, 1974.

[22] M. Rokni, L. S. Wall, E. Amzallag, and T. S. Chang, "Temperature study of the polariton associated with the 248cm^{-1} soft mode in $LiNbO_3$," *Solid State Commun.*, vol. 10, no. 1, pp. 103–105, 1972.

[23] J. L. Servoin and F. Gervais, "Soft vibrational mode in $LiNbO_3$ and $LiTaO_3$," *Solid State Commun.*, vol. 31, no. 5, pp. 387–391, 1979.

[24] H. E. Puthoff, R. H. Pantell, B. G. Huth, and M. A. Chacon, "Near-forward Raman scattering in $LiNbO_3$," *J. Appl. Phys.*, vol. 39, no. 4, pp. 2144–2146, 1968.

[25] T. D. Wang, Y. Y. Lin, S. Y. Chen, A. C. Chiang, S. T. Lin, and Y. C. Huang, "Low-threshold, narrow-line THz-wave parametric oscillator with an intra-cavity grazing-incidence grating," *Opt. Exp.*, vol. 16, no. 17, pp. 12571–12576, 2008.

[26] B. Sun, S. Li, J. Li, E. Li, and J. Yao, "Terahertz-wave parametric oscillator with a misalignment-resistant tuning cavity," *Opt. Lett.*, vol. 36, no. 10, pp. 1845–1847, 2011.

[27] S. Hayashi, T. Shibuya, H. Sakai, T. Taira, C. Otani, Y. Ogawa, and K. Kawase, "Tunability enhancement of a terahertz-wave parametric generator pumped by a microchip Nd:YAG laser," *Appl. Opt.*, vol. 48, no. 15, pp. 2899–2902, 2009.

[28] T. J. Edwards, D. Walsh, M. B. Spurr, C. F. Rae, M. H. Dunn, and P. G. Browne, "Compact source of continuously and widely-tunable terahertz radiation," *Opt. Exp.*, vol. 14, no. 4, pp. 1582–1589, 2006.

[29] D. A. Bryan, R. R. Rice, R. Gerson, H. E. Tomaschke, K. L. Sweeney, and L. E. Halliburton, "Magnesium-doped lithium niobate for higher optical power applications," *Opt. Eng.*, vol. 24, no. 1, pp. 241138–241143, 1985.

[30] L. Palfalvi, J. Hebling, G. Almasi, A. Peter, K. Polgar, K. Lengyl, and R. Szipocs, "Nonlinear refraction and absorption of Mg doped stoichiometric and congruent $LiNbO_3$," *J. Appl. Phys.*, vol. 95, no. 3, pp. 902–908, 2004.

[31] K. Kawase, M. Sato, K. Nakamura, T. Taniuchi, and H. Ito, "Unidirectional radiation of widely tunable THz wave using a prism coupler under noncollinear phase matching condition," *Appl. Phys. Lett.*, vol. 71, no. 6, pp. 753–755, 1997.

[32] E. Yablonovitch, D. M. Hwang, T. J. Gmitter, L. T. Florez, and J. P. Harbison, "Van der Waals bonding of GaAs epitaxial liftoff films onto arbitrary surfaces," *Appl. Phys. Lett.*, vol. 56, no. 24, pp. 2419-2421, 1990.

[33] *Lascad-Software for Laser Cavity Analysis and Design.* [Online]. Available: www.las-cad.com

[34] R. L. Sutherland, *Handbook of Nonlinear Optics*, 2nd ed, New York, USA: Marcel Dekker, Inc. 2003.

[35] J. E. Pearson, U. Ganiel, and A. Yariv, "Rise time of pulsed parametric oscillators," *IEEE J. Quantum Electron.*, vol. 8, no. 5, pp. 433–440, May 1972.

[36] T. Debuisschert, "Nanosecond optical parametric oscillators," *Quantum Semiclass. Opt.*, vol. 9, no. 2, pp. 209–219, 1997.

[37] G. Rustad, G. Arisholm, and O. Farsund, "Effect of idler absorption in pulsed optical parametric oscillators," *Opt. Exp.*, vol. 19, no. 3, pp. 2815–2830, 2011.

[38] D. Grischkowsky, S. Keiding, M. van Exer, and C. Fattinger, "Far-infrared time-domain spectroscopy with terahertz beams of dielectrics and semiconductors," *J. Opt. Soc. Amer. B*, vol. 7, no. 10, pp. 2006–2015, 1990.

[39] X. Xin, H. Altan, A. Saint, D. Matten, and R. R. Alfano, "Terahertz absorption spectrum of para and ortho water vapors at different humidities at room temperature," *J. Appl. Phys.*, vol. 100, no. 9, pp. 094905-1–094905-4, 2006.

[40] T. Ikari, R. Guo, H. Minamide, and H. Ito, "Energy scalable terahertz-wave parametric oscillator using surface-emitted configuration," *J. Eur. Opt. Soc.-Rapid Publications*, vol. 5, pp. 10054-1–10054-4, Nov. 2010.

[41] U. T. Schwarz and M. Maier, "Damping mechanisms of phonon polaritons, exploited by stimulated Raman gain measurements," *Phys. Rev. B*, vol. 58, no. 2, pp. 766–775, 1998.

[42] L. Palfalvi, J. Hebling, J. Kuhl, A. Peter, and K. Polgar, "Temperature dependence of the absorption and refraction of Mg-doped congruent and stiochiometric $LiNbO_3$ in the THz range," *J. Appl. Phys.*, vol. 97, no. 12, pp. 123505-1–123505-6, 2005.

[43] M. Nakamura, S. Higuchi, S. Takekawa, K. Terabe, Y. Furukawa, and K. Kitamura, "Optical damage resistance and refractive indices n near-stoichiometric MgO-doped $LiNbO_3$," *Jpn. J. Appl. Phys.*, vol. 41, no. 2, pp. L49–L51, 2002.

[44] W. D. Johnston, I. P. Kaminow, and J. G. Bergman, "Stimulated Raman gain coefficients for Li^6NbO_3, $Ba_2NaNb_5O_{15}$, and other materials," *Appl. Phys. Lett.*, vol. 13, no. 5, pp. 190–193, 1968.

Andrew Lee received his Bachelors degree (Honors First Class) in optoelectronics and the Ph.D. degree in physics from Macquarie University, Sydney, Australia, in 2001 and 2007, respectively.

He is currently an Australian Research Council Postdoctoral Fellow at Macquarie University, and is working on the development of new Terahertz source technologies and Raman laser technologies. His current research interests include development of high power continuous-wave crystalline Raman laser sources, fabrication of optical micro- and nano-structures using laser-based processes, and terahertz generation.

Dr. Lee is the recipient of an Australian Research Council Post Doctoral Fellowship.

Yabai He was born and educated in China, before his Ph.D. studies at Universität Bonn (Germany) and a postdoctoral period at ETH, Zürich (Switzerland). Since 1997, he has worked at Macquarie University in Sydney, Australia. His current research interests include laser-based spectroscopic gas sensing, development of tunable nonlinear optical coherent sources, and precision laser spectroscopy.

Helen Pask was awarded her Ph.D. in Physics by Macquarie University, Sydney, Australia in 1992. She currently holds an Australian Research Council Future Fellowship at Macquarie University, with research interests in crystalline Raman lasers, THz generation and applications, remote sensing, and Raman spectroscopy.

A.2. First publication resulting from this work: Tiago Ortega, Helen Pask, David Spence and Andrew Lee, Stimulated polariton scattering in an intracavity RbTiOPO4 crystal generating frequency-tunable THz output," Opt. Express 24, 10254-10264 (2016)

This paper is related to the work reported in Chapter 4 (Section 4.4) and was the first publication resulting from this PhD research.

Stimulated polariton scattering in an intracavity $RbTiOPO_4$ crystal generating frequency-tunable THz output

Tiago A. Ortega,* Helen M. Pask, David J. Spence, and Andrew J. Lee

MQ Photonics Research Centre, Department of Physics and Astronomy, Macquarie University, NSW 2109, Australia
*tiago.ortega@students.mq.edu.au

Abstract: A high power, frequency-tunable THz source based on intracavity stimulated polariton scattering (SPS) in $RbTiOPO_4$ (RTP) is demonstrated for the first time. Frequency tunable THz output was obtained from 3.10 to 4.15 THz, with a gap at 3.17 to 3.49 THz, arising from the 104 cm^{-1} A_1 mode in RTP. A maximum average output power of 16.2 μW was detected at 3.8 THz. This is the highest average output power ever reported for an intracavity polariton laser.

OCIS codes: (190.5890) Scattering, stimulated; (190.4410) Nonlinear optics, parametric processes; (140.3070) Infrared and far-infrared lasers.

References and links

1. P. H. Siegel, "Terahertz technology in biology and medicine," IEEE Trans. Microw. Theory Tech. **52**(10), 2438–2447 (2004).
2. G. Davies, A. D. Burnett, W. Fan, E. H. Linfield, and J. E. Cunningham, "Terahertz spectroscopy of explosive and drugs," Mater. Today **11**(3), 18–26 (2008).
3. R. M. Woodward, B. E. Cole, V. P. Wallace, R. J. Pye, D. D. Arnone, E. H. Linfield, and M. Pepper, "Terahertz pulse imaging in reflection geometry of human skin cancer and skin tissue," Phys. Med. Biol. **47**(21), 3853–3863 (2002).
4. S. J. Oh, J. Choi, I. Maeng, J. Y. Park, K. Lee, Y. M. Huh, J. S. Suh, S. Haam, and J. H. Son, "Molecular imaging with terahertz waves," Opt. Express **19**(5), 4009–4016 (2011).
5. B. B. Hu and M. C. Nuss, "Imaging with terahertz waves," Opt. Lett. **20**(16), 1716–1718 (1995).
6. K. B. Cooper, R. J. Dengler, N. Llombart, T. Bryllert, G. Chattopadhyay, E. Schlecht, J. Gill, C. Lee, A. Skalare, I. Mehdi, and P. H. Siegel, "Penetrating 3-D imaging at 4- and 25-m range using submillimeter-wave radiation," IEEE Trans. Microw. Theory Tech. **56**(12), 2771–2778 (2008).
7. K. Kawase, Y. Ogawa, Y. Watanabe, and H. Inoue, "Non-destructive terahertz imaging of illicit drugs using spectral fingerprints," Opt. Express **11**(20), 2549–2554 (2003).
8. E. Brundermann, H. Hubers, and M. F. Kimmitt, *Terahertz Techniques* (Springer, 2012).
9. K. Kawase, J. Shikata, and H. Ito, "Terahertz wave parametric source," J. Phys. D Appl. Phys. **35**(3), R1–R14 (2002).
10. S. S. Sussman, *Tunable Light Scattering from Transverse Optical Modes in Lithium Niobate* (Stanford Univ., 1970).
11. K. Kawase, M. Sato, T. Taniuchi, and H. Ito, "Coherent tunable THz-wave generation from LiNbO3 with monolithic grating coupler," Appl. Phys. Lett. **68**(18), 2483–2485 (1996).
12. K. Kawase, H. Minamide, K. Imai, J. Shikata, and H. Ito, "Injection-seeded terahertz parametric generator with wide tunability," Appl. Phys. Lett. **80**(2), 195–197 (2002).
13. T. Edwards, D. Walsh, M. Spurr, C. Rae, M. Dunn, and P. Browne, "Compact source of continuously and widely-tunable terahertz radiation," Opt. Express **14**(4), 1582–1589 (2006).
14. D. Walsh, S. J. M. Stothard, T. J. Edwards, P. G. Browne, C. F. Rae, and M. H. Dunn, "Injection-seeded intracavity terahertz optical parametric oscillator," J. Opt. Soc. Am. B **26**(6), 1196–1202 (2009).
15. A. J. Lee and H. M. Pask, "Continuous wave, frequency-tunable terahertz laser radiation generated via stimulated polariton scattering," Opt. Lett. **39**(3), 442–445 (2014).
16. W. Wang, X. Zhang, Q. Wang, Z. Cong, X. Chen, Z. Liu, Z. Qin, P. Li, G. Tang, N. Li, C. Wang, Y. Li, and W. Cheng, "Multiple-beam output of a surface-emitted terahertz-wave parametric oscillator by using a slab MgO:$LiNbO_3$ crystal," Opt. Lett. **39**(4), 754–757 (2014).
17. D. J. M. Stothard, T. J. Edwards, D. Walsh, C. L. Thomson, C. F. Rae, M. H. Dunn, and P. G. Browne, "Line-narrowed, compact, and coherent source of widely tunable terahertz radiation," Appl. Phys. Lett. **92**(14), 141105 (2008).
18. J. Shikata, K. Kawase, K. Karino, T. Taniuchi, and H. Ito, "Tunable terahertz-wave parametric oscillators using LiNbO3 and MGO:LiNbO3 crystals," IEEE Trans. Microw. Theory Tech. **48**(4), 653–661 (2000).

#260259 Received 29 Feb 2016; revised 30 Mar 2016; accepted 6 Apr 2016; published 2 May 2016

19. W. Wang, Z. Cong, X. Chen, X. Zhang, Z. Qin, G. Tang, N. Li, C. Wang, and Q. Lu, "Terahertz parametric oscillator based on $KTiOPO_4$ crystal," Opt. Lett. **39**(13), 3706–3709 (2014).
20. C. Yan, Y. Wang, D. Xu, W. Xu, P. Liu, D. Yan, P. Duan, K. Zhong, W. Shi, and J. Yao, "Green laser induced terahertz tuning range expanding in KTiOPO4 terahertz parametric oscillator," Appl. Phys. Lett. **108**(1), 011007 (2016).
21. W. Wang, Z. Cong, Z. Liu, X. Zhang, Z. Qin, G. Tang, N. Li, Y. Zhang, and Q. Lu, "THz-wave generation via stimulated polariton scattering in KTiOAsO4 crystal," Opt. Express **22**(14), 17092–17098 (2014).
22. Y. Y. Wang, Z. X. Li, J. Q. Li, C. Yan, T. N. Chen, D. G. Xu, W. Shi, H. Feng, and J. Q. Yao, "Energy scaling of a tunable terahertz parametric oscillator with a surface emitted configuration," Laser Phys. **24**(12), 125402 (2014).
23. A. Hildebrand, F. Wagner, J. Natoli, M. Commandre, H. Albrecht, and F. Theodore, "Laser damage investigation in RbTiOPO4 crystals: a study on the anisotropy of the laser induced damage threshold," Proc. SPIE **6403**, 64031W (2006).
24. J. Y. Wang, L. Li, S. Liu, Y. Liu, and J. Wei, "The inelastic light scattering of RbTiOAsO4 single crystal," Ferroelectrics **132**(1), 197–202 (1992).
25. P. Dekker, H. M. Pask, D. J. Spence, and J. A. Piper, "Continuous-wave, intracavity doubled, self-Raman laser operation in Nd:GdVO4 at 586.5 nm," Opt. Express **15**(11), 7038–7046 (2007).
26. K. Kawase, J. Shikata, H. Minamide, K. Imai, and H. Ito, "Arrayed silicon prism coupler for a terahertz-wave parametric oscillator," Appl. Opt. **40**(9), 1423–1426 (2001).
27. I. Hosako, N. Sekine, K. Fukunaga, Y. Kasai, P. Baron, T. Seta, J. Mendrok, S. Ochiai, and H. Yasuda, "At the dawn of a new era in terahertz technology," Proc. IEEE **95**(8), 1611–1623 (2007).
28. A. Lee, Y. He, and H. Pask, "Frequency-tunable THz source based on Stimulated Polariton Scattering in Mg:LiNbO3," IEEE J. Quantum Electron. **49**(3), 357–364 (2013).
29. V. Nikolaev, Deputy General Manager, Tydex LLC, 16 Domostroietelnaya str, St. Petersburg, Russia 194292 (personal communication, 2015).

1. Introduction

Spectroscopy and spectral imaging utilizing THz radiation have successfully demonstrated the potential to address a wide variety of revolutionary applications in industry, homeland security and medical sciences [1,2]. Human skin cancer detection [3], tumor detection and differentiation in mice [4], non-destructive testing for industrial quality control [5], concealed weapons detection [6] and toxic substances indentification [7] are among the numerous examples reported in the literature [1,8].

While the number of applications continue to build, their translation into mainstream use has been limited and this is due, in large part, to the lack of practical THz sources. Most of the available sources utilize a time-domain THz spectroscopy configuration (TDS-THz), in which a femtosecond laser pulse irradiates a photoconductive antenna, emitting a very short, broadband THz pulse (typically spanning several terahertz) [2]. These TDS-THz systems rely on high power and expensive laser systems, as well as complex optomechanics and computer-controlled delay lines for detection. Development of reliable, robust and cost-effective THz sources with narrow band and frequency tunable output which can be interfaced with conventional THz detectors is then imperative, and the approach considered here uses a conventional diode-pumped Nd laser to produce such frequency-tunable THz radiation via stimulated polariton scattering (SPS) in nonlinear optical crystals [9].

Interaction of a fundamental laser (ω_f) with a polariton mode of a crystal may generate, via SPS, Stokes (ω_S) and THz (ω_T) fields. Conservation of energy ($\omega_f = \omega_S + \omega_T$) and momentum ($k_f = k_S + k_T$) in the process yields angle dependent frequencies for Stokes and THz radiation. As a result, variation in the interaction angle enables frequency-tunable THz output [10]. Stimulated polariton scattering is a versatile technique to access the THz portion of the electromagnetic spectrum, and various pulsed systems using both extra-cavity and intra-cavity configurations have been developed [11–14]. Recently, a continuous-wave, frequency-tunable THz source based on intracavity SPS in lithium niobate ($LiNbO_3$) crystals has also been reported [15], further demonstrating the flexibility of the technique for generating THz emission with different output modalities. The vast majority of SPS THz systems demonstrated to-date have been based on polariton modes in Mg:$LiNbO_3$ [16–18], typically generating output between 0.6 to 3.2 THz. This tuning range is determined by the material properties of the Mg:$LiNbO_3$, in particular the dispersion curve and absorption characteristics.

#260259 Received 29 Feb 2016; revised 30 Mar 2016; accepted 6 Apr 2016; published 2 May 2016

By employing different SPS-active crystals, different THz frequency ranges can be accessed, which may lead to enhanced uptake of these THz systems. In this context, extracavity SPS systems have been developed utilizing KTP ($KTiOPO_4$) [19,20] and KTA ($KTiOAsO_4$) [21] crystals. In KTP, three tunable bands were obtained when pumping with a 1064 nm, near-infrared laser: 3.17 to 3.44 THz, 4.19 to 5.19 THz and 5.55 to 6.13 THz. Also in KTP, four tunable bands were reported pumping using a laser at 532 nm: 5.7 to 6.1, 7.4 to 7.8, 11.5 to 11.8 and 13.3 to 13.5 THz. Similar THz emission was observed in KTA, with output tunable in five discrete bands between 3.59 to 6.43 THz. Discontinuities in emitted THz spectra are attributed to infrared absorption by A_1 crystalline modes in the crystal. The efficiency of these KTP and KTA extracavity systems was broadly similar to extracavity systems based on $Mg:LiNbO_3$ [22].

Rubidium titanyl phosphate ($RbTiOPO_4$, RTP) is another SPS-active nonlinear crystal with high transparency range and higher damage threshold then KTP, making it ideal for high-power intracavity systems [23]. An isomorph to KTP, RTP is orthorhombic at room temperature and belongs to C2υ (mm2) point group, with 47 A_1 transverse optical modes both Raman and infrared active in the crystallographic z-axis direction. Polariton A_1 modes are located at 104, 142.0, 159, 163, 211 and 269 cm^{-1} [24], and can be used for polariton scattering in RTP. Similar to what is observed in its isomorphs, the RTP crystal is expected to produce THz radiation in frequency tunable bands, with gaps located at the A_1 modes below 269 cm^{-1}.

With a desire to produce compact, efficient and diode-pumped THz sources that generate THz output beyond what is achieved with $Mg:LiNbO_3$, in this work we report a frequency-tunable THz source based on intracavity SPS in an RTP crystal. This is the first time a nonlinear material different from lithium niobate has been used for intracavity SPS, and the maximum average THz power we report is in fact higher than has been previously reported for any intracavity SPS laser. This SPS laser produces THz output with tunability extending to 4.15 THz, well beyond what can be achieved in $Mg:LiNbO_3$, in a simple and compact layout, and pumped with only 8 W from a laser diode. It represents a significant improvement towards broadening the spectral coverage of THz sources.

2. Experimental setup

The laser resonator is represented in Fig. 1. The fundamental field at 1064 nm was produced in a conventional diode end-pumped, Nd:YAG Q-switched laser resonator, containing an intracavity RTP crystal. The Stokes field was resonated in a separate laser cavity formed around the RTP. Wavelength tunability for Stokes and THz radiation was achieved by adjusting the angle θ_{ext} between fundamental and Stokes resonator axes.

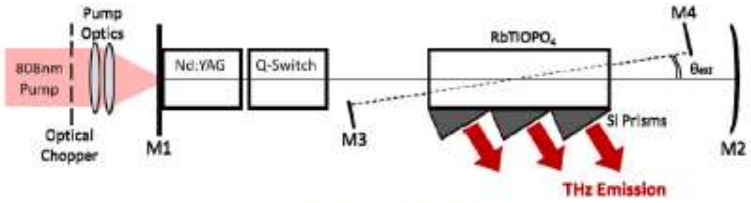

Fig. 1. Experimental setup.

The fundamental resonator was end-pumped by a continuous-wave fiber coupled diode laser (100 μm core diameter, 0.22 NA) operated at maximum output power of 10 W at 808 nm. To reduce thermal lensing, the laser diode was chopped by an optical chopping wheel at 200 Hz and 50% duty cycle [25]. Pump optics produced an approximate 300 μm diameter spot inside the 5 mm long, 5 mm diameter 1 a.t. % Nd:YAG crystal, which was anti-reflection (AR) coated for 808 and 1064 nm. The fundamental cavity was formed by flat mirror M1 (T > 99% at 808 nm and R > 99.99% at 1064nm) and concave (1000 mm ROC) mirror M2 having

#260259 Received 29 Feb 2016; revised 30 Mar 2016; accepted 6 Apr 2016; published 2 May 2016

16 May 2016 | Vol. 24, No. 10 | DOI:10.1364/OE.24.010254 | OPTICS EXPRESS 10256

a high reflectivity (HR) coating (R = 99.4% at 1064 nm), separated by 230 mm. Pulsed operation was achieved with an acousto-optic Q-switch at 3 kHz repetition rate (a repetition rate much higher than diode laser chopping frequency to avoid any influence of the pump duty cycle on the Q-switching operation). An intracavity x-cut RTP crystal, 4x4x20 mm^3 (Crystal Laser S. A.) with end faces AR coated for 1064-1100 nm (R < 0.1% at 1064 nm) was used as the SPS-crystal (fundamental laser field polarized parallel to the crystal z-axis).

The Stokes resonator was 85 mm in length, formed by two flat mirrors M3 and M4 coated HR from 1064 to 1090 nm (R>99.9%). Mirrors M3 and M4 were D-shaped to avoid clipping of the fundamental beam, and were mounted on a rotational stage, enabling fine tuning of the angle between Stokes and fundamental resonator axes (θ_{ext}), promoting the consequent frequency tuning in Stokes and THz outputs [9]. To avoid total internal reflection of the THz field inside the RTP, the crystal side face (y-surface) was polished and three high resistivity Silicon prisms (R > 10 kΩ/cm; 7 mm hypotenuse, 32°/58°/90° internal angles) were bonded [26].

Fundamental and Stokes output power leaking from M2 and M4, respectively, were monitored with a laser power meter (Thorlabs PM100D). Spectral content was detected with a high resolution fiber coupled grating spectrometer (Ocean Optics HR4000), and temporal profiles were measured with silicon photodiodes (Thorlabs DET10A/M; 1 ns rise time). A Golay cell (Tydex, GD-1P) in combination with a long pass filter (Tydex, LPF 14.3) and a 50 mm focal length collecting lens (Tydex, 50 mm EFL TPX lens) was used to measure the THz output from the Si prism array.

3. Results

3.1 THz and Stokes fields frequency tunability

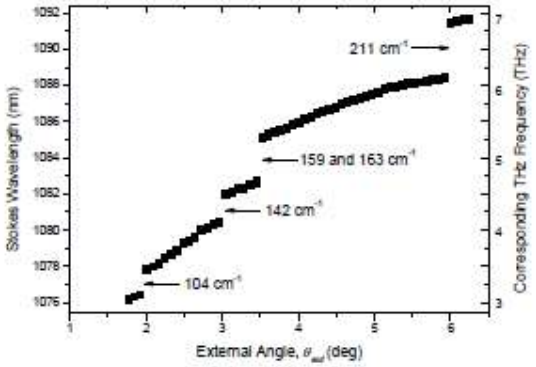

Fig. 2. Stokes wavelength output versus external angle in RTP. The absorbing A_1 modes that give rise to discontinuities in the Stokes and THz tuning are indicated.

The external angle (θ_{ext}) between fundamental and Stokes resonator axes was adjusted from ~1.8 to 6.3° (~1 to 3.6° internal angle), and a corresponding Stokes wavelength tunable from 1076.2 to 1091.7 nm was measured. From this, we calculated the corresponding THz frequencies to range from 3.10 to 7.03 THz. This is plotted in Fig. 2. This data was collected with the system operating with an incident diode pump power of 7 W; the fundamental laser wavelength was 1064.4 nm. Discontinuities in the Stokes wavelength tuning range were observed (Fig. 2), and these correlate with RTP infrared absorbing A_1 modes at 104, 142, 159, 163 and 211 cm^{-1}. Fine tuning of the external angle was performed close to these modes and the Stokes radiation spectra were collected. As this tuning was performed, a clear jump was

#260259 Received 29 Feb 2016; revised 30 Mar 2016; accepted 6 Apr 2016; published 2 May 2016

16 May 2016 | Vol. 24, No. 10 | DOI:10.1364/OE.24.010254 | OPTICS EXPRESS 10257

observed at each mode, with the coexistence of dual-Stokes wavelengths either side of the gaps, as depicted in Fig. 3. This particular behavior suggests simultaneous, dual-terahertz output, which could be explored for applications involving differential transmission with THz radiation.

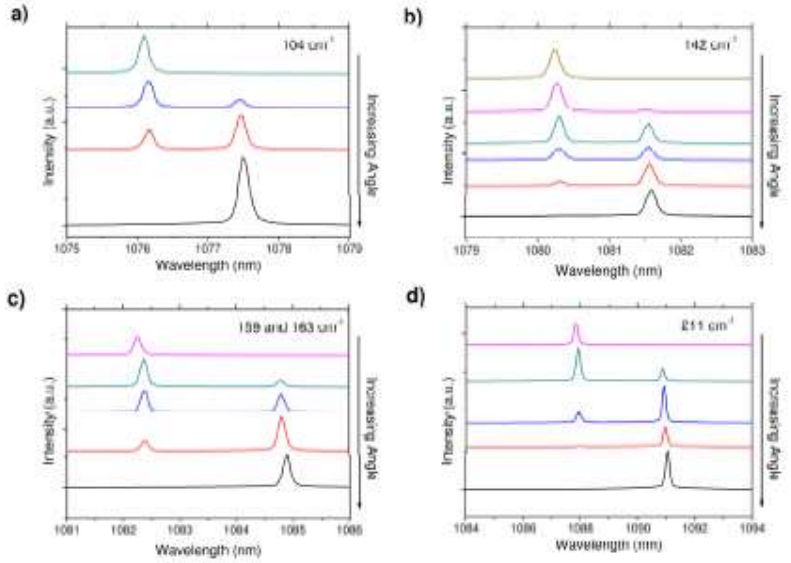

Fig. 3. Fine angle tuning showing evolution of the Stokes wavelength in the region of RTP absorption features at (a) 104 cm^{-1}, (b) 142 cm^{-1}, (c) 159 and 163 cm^{-1} and (d) 211 cm^{-1}.

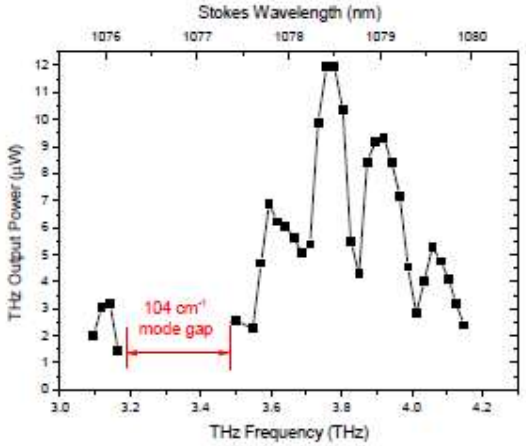

Fig. 4. Average THz power exiting the silicon prisms as a function of THz frequency.

The THz frequency tuning curve is shown in Fig. 4, in which the THz frequency has been inferred from the Stokes wavelength. THz radiation was detected for Stokes wavelengths in the range of 1076.6 to 1080.3 nm, corresponding to a tunable range from 3.10 to 4.15 THz.

#260259 Received 29 Feb 2016; revised 30 Mar 2016; accepted 6 Apr 2016; published 2 May 2016

16 May 2016 | Vol. 24, No. 10 | DOI:10.1364/OE.24.010254 | OPTICS EXPRESS 10258

The reported THz output power from the laser has been corrected for the frequency-dependent transmission loss of the filter and lens attached to the Golay cell, using data supplied by Tydex, and corresponds to the free space THz field after exiting the prisms. As expected, no THz emission was observed in the 104 cm^{-1} gap (THz frequencies between 3.16 THz and 3.5 THz). The significant dips in power observed around 3.68, 3.84 and 4.01 THz match water vapor absorption lines [27], and are attributed to the presence of water vapor in our laboratory environment. No efforts had been made taken to exclude water vapor. Somewhat surprisingly, no THz power was detected above 4.15 THz, the possible reasons for which are discussed later in this paper.

3.2 Laser power scaling

The most efficient THz emission was obtained at 3.80 THz, and power scaling measurements at this frequency are plotted in Fig. 5 for fundamental, Stokes and THz fields. The efficiency of the SPS process can be inferred from the fundamental field depletion, because it is related to the amount of fundamental power channeled into the SPS process. The fundamental field depletion was calculated by measuring the 1064 nm laser power with Stokes cavity enabled and disabled, as shown in Fig. 6. The Stokes output power versus fundamental field depletion is also shown as an inset in Fig. 6. The temporal profiles of the fundamental (depleted and undepleted, that is with and without SPS activity, respectively) and Stokes fields were measured when the system was pumped at 6 W, and are plotted in Fig. 7.

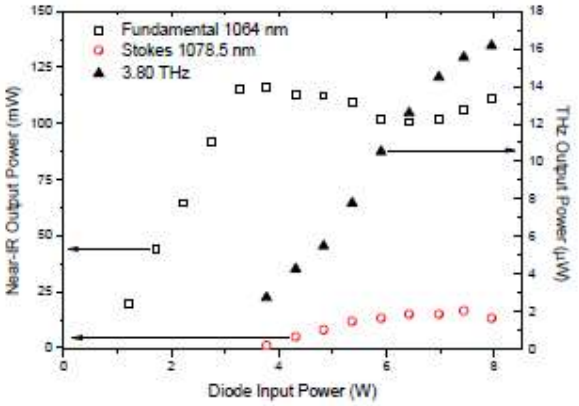

Fig. 5. Average output powers measured for fundamental, 1078.5 nm Stokes and 3.80 THz fields as a function of incident diode power.

#260259 Received 29 Feb 2016; revised 30 Mar 2016; accepted 6 Apr 2016; published 2 May 2016

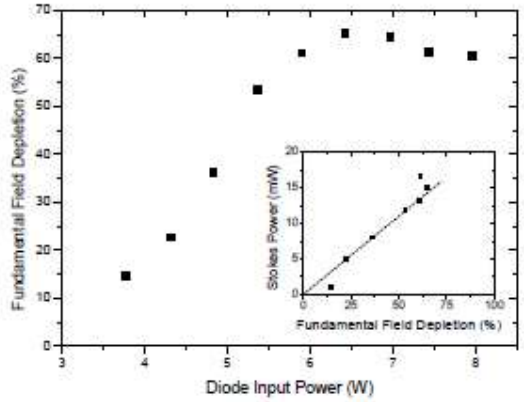

Fig. 6. Fundamental field depletion as a function of incident diode power at 3.80 THz output.

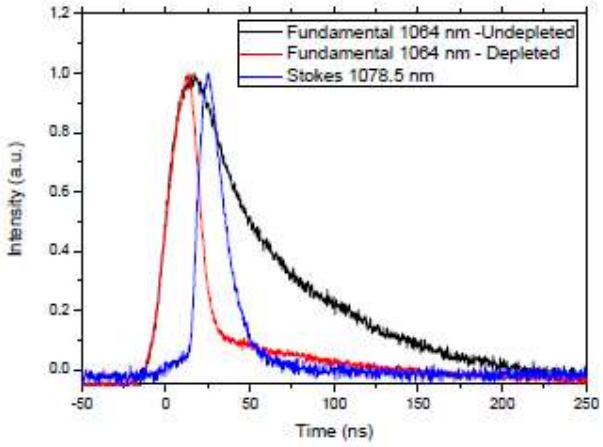

Fig. 7. Temporal profiles of the fundamental field (depleted and undepleted) and Stokes field at 1078.5 nm, for 6 W diode pump power. At this Stokes wavelength, terahertz radiation at 3.8 THz is generated.

A maximum average power of 16.2 μW was obtained at 3.80 THz, with fundamental field depletion in excess of 60%. This is, to our knowledge, the highest average THz output power, and the highest fundamental field depletion ever reported for an intracavity SPS laser, suggesting very good mode matching between interacting fields. Within our data range, there is a near-linear relation between the Stokes output power and fundamental field depletion as can be observed in the inset of Fig. 6. At 6 W pump power, the fundamental field pulse width decreased from ~50 ns to ~21 ns (FWHM) when the SPS process was enabled, and a pulse width of ~17 ns was measured for the Stokes radiation.

#260259 Received 29 Feb 2016; revised 30 Mar 2016; accepted 6 Apr 2016; published 2 May 2016

16 May 2016 | Vol. 24, No. 10 | DOI:10.1364/OE.24.010254 | OPTICS EXPRESS 10260

4. Limiting factors on THz frequency tuning range

Tuning to higher THz frequencies resulted in a considerable reduction in detected THz output power, and no power could be detected for frequencies above 4.15 THz. This was somewhat surprising, given that the external cavity systems using KTP and KTA reported in [19,21] had generated THz output as high as 6.13 and 6.43 THz, respectively. To explore this further, we now consider the various factors relating to the generation of THz frequencies above 4.15 THz in RTP, including the efficiency with which it can be extracted, and the efficiency with which it propagates to, and is detected by the Golay cell.

4.1 THz generation efficiency

An indicator of how efficiently the THz field is being generated is to monitor the fundamental and Stokes output power across the tuning range. For each fundamental photon experiencing SPS, we assume that one Stokes and one THz photon must be generated. Therefore, the Stokes laser output power is, in theory, linearly proportional to the number of generated THz photons, in the absence of other processes. The Stokes laser output power and fundamental field depletion versus Stokes wavelength were measured, and are shown in Fig. 8, with the horizontal dashed line representing the Stokes output power detected at 1078.5 nm, the Stokes wavelength corresponding to 3.8 THz, which is the frequency at which the highest power was detected.

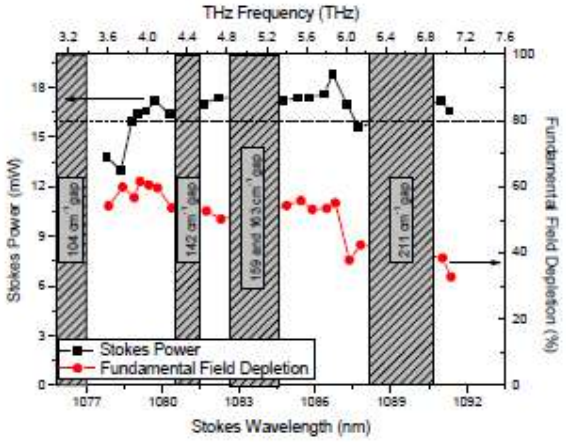

Fig. 8. Stokes field average output power and fundamental field depletion versus Stokes wavelength, at 6 W diode input power. The horizontal dashed line corresponds to the Stokes output power detected when the system is generating output at 3.8 THz.

It can be observed in Fig. 8 that the detected Stokes output power is greater than that measured at 1078.5 nm for almost all Stokes wavelengths. This result suggests that the number of THz photons generated should be similar to or exceed that at 3.8 THz across the entire tuning range. Fundamental field depletion is high over the same range, with values between 50% and 55% until 1086.7nm, which corresponds to output at 5.7 THz. As described above, we expect that the THz power should scale similarly to the Stokes power, yet this is clearly not what we detect from our system. This suggests that there are other factors affecting our measurement of the THz field above 4.15 THz.

4.2 THz detection efficiency

The THz field is generated inside the nonlinear crystal, and travels through multiple materials and interfaces in order to be coupled out and detected. The efficiency with which THz

#260259 Received 29 Feb 2016; revised 30 Mar 2016; accepted 6 Apr 2016; published 2 May 2016

photons are extracted from the laser and propagated to the Golay cell for power measurement is affected by THz absorption and Fresnel reflection losses associated with the various media in their path. Hence it is important to analyze the transmission for each step individually, starting with THz extraction from the laser, which involves propagation through the RTP and the silicon prisms), propagation through free space, and finally propagation through the detection optics in front of the Golay cell.

The first step in extraction is the propagation of the THz photons generated within the RTP to the crystal edge (to which the silicon prims are previously bonded). This THz field generated inside the crystal is outside the transparency range of RTP (0.35 - 4.5 μm), and therefore strong absorption of the THz field during propagation inside the crystal is expected. To quantify this, a direct measurement of the absorption coefficient in RTP at different THz frequencies was performed using the same method described in [28]. In this technique, THz output power is measured versus THz field propagation distance inside the nonlinear crystal, and absorption coefficient is obtained according to Beer's Law. The RTP crystal was mounted on a translation stage having micron-scale resolution, and the distance travelled by the THz beam inside the crystal was varied by translating the RTP across the fundamental beam propagation direction. At each position, the detected THz signal was recorded, and found to follow an exponential dependence, as shown in Fig. 9.

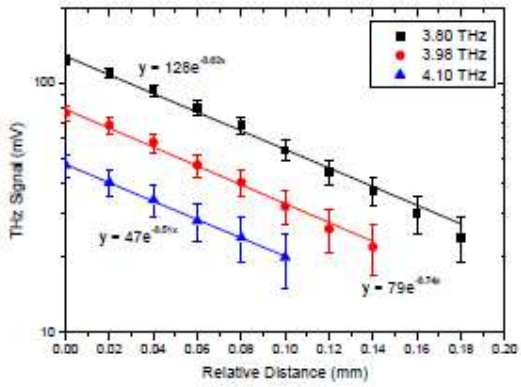

Fig. 9. Power output versus propagation distance inside RTP crystal for output at 3.8, 3.98 and 4.10 THz. The corresponding absorption coefficient at each THz frequency were determined with best-fit exponential decay.

The absorption coefficients obtained from the exponential decay curves were 86 cm^{-1} at 3.80 THz, 87 cm^{-1} at 3.98 THz and 85 cm^{-1} at 4.10 THz, with estimated uncertainties of 10 cm^{-1}. No values could be found in the literature for comparison. As expected, the material exhibits high absorption at THz frequencies, and minimizing the THz field propagation distance inside the RTP is therefore crucial. To this end, we always ensure that the fundamental beam resonates as close to the RTP crystal edge as possible. However, in order to avoid clipping of the Stokes beam, the minimum distance between the fundamental laser beam and RTP edges is around 500 μm. Taking this to be the average THz propagation distance inside the crystal, we find that more than 98% of the generated THz photons are absorbed inside the RTP for these three THz frequencies. It is difficult to predict the absorption losses for higher frequencies due to the shortage of reported material data. We expect, however, the absorption coefficient to generally increase as the THz frequency

#260259 Received 29 Feb 2016; revised 30 Mar 2016; accepted 6 Apr 2016; published 2 May 2016

16 May 2016 | Vol. 24, No. 10 | DOI:10.1364/OE.24.010254 | OPTICS EXPRESS 10262

increases towards the strong 269 cm^{-1} resonance, with additional absorption in the vicinity of the weaker 142.0, 159, 163 and 211 cm^{-1} modes.

After propagation inside RTP, the transmitted THz photons are extracted with the silicon prisms, a process consisting of refraction in the crystal-prism interfaces, propagation inside the prisms, and a second refraction at the prism-air interfaces. Absorption in the high resistivity silicon prisms is known to increase considerably at higher THz frequencies [8], and therefore losses in the range of 10% at 4 THz are expected, increasing to 25% at 7 THz, given the 2 mm average propagation distance for the prisms used. At the crystal-prism and prism-air interfaces, the combined Fresnel reflection loss is estimated to be approximately 30% from 3 to 7 THz, given refractive indices for Si of 3.41, and assuming that for RTP it would be similar to that reported for KTP [19].

After being refracted out of the prism, the THz beam propagates in free space, and could experience absorption in air, particularly in water vapor. However, these discrete lines would generate dips and fine structure in THz spectra similar to what is observed in Fig. 4, and would not suppress a wide THz frequency band.

Finally, the THz beam impinges on the detection system, which is composed of a long pass filter, a TPX lens, and the Golay cell TPX entrance window. Each of these materials has a transmission loss that increases substantially with THz frequency [29]. Table 1 lists the estimated transmission through each component, and it is seen that the total transmission (31%) for 4 THz radiation is around 10 times higher than the total transmission (3%) at 7 THz. As a consequence, the minimum detectable power depends strongly on the THz frequency. Given that the minimum detectable power at 3.8 THz was ~2 μW, we estimate the minimum detectable power would increase with frequency, up to 20 μW at 7 THz.

Table 1. THz Transmission in Detection Optics[a]

	Transmission	
	4 THz	7 THz
Long pass filter	61%	17%
TPX 50mm EFL Lens	65%	30%
Golay cell TPX window	78%	58%
Total transmission	31%	3%

[a]From Tydex material data sheet [29].

We believe that the absence of a detectable THz signal above 4.15 THz in our system is due to a combination of the expected increase in the absorption coefficient in RTP at higher frequencies (due to the tuning towards the strong absorbing mode at 269 cm^{-1}), and the increasing losses in the outcoupling prisms and detection system with frequency above 4 THz. These effects attenuate the THz signal to a level which is below the minimum detectable signal level. A reduction in total transmission losses in the system is therefore necessary, and could be achieved either via optimizing the THz extraction from the RTP crystal, or reducing the losses in the detection system.

It is interesting to compare our findings to those in [19–21] where THz output above 6 THz was observed. First we note the higher pulse energies employed in [19–21], however the other significant difference was the surface-emitted configuration employed. In that configuration, the nonlinear crystal is cut at an angle to avoid total internal reflection of the THz beam at the crystal-air interface, enabling the THz field to be refracted out of the crystal without the silicon prisms. In the surface-emitted configuration the THz field is generated at the crystal-air interface, reducing absorption losses due to THz propagation inside the nonlinear material, and eliminating losses associated with Si prisms. An additional benefit is that the Golay cell can be positioned close to the nonlinear crystal, eliminating the need for a focusing lens, with its associated loss. In future work, we will explore the use of such a surface-emitting configuration in our intracavity system.

#260259 Received 29 Feb 2016; revised 30 Mar 2016; accepted 6 Apr 2016; published 2 May 2016

5. Conclusion

A frequency-tunable and high power THz source based on intracavity stimulated polariton scattering in RTP is demonstrated for the first time to the best of our knowledge. Frequency tunable THz output was obtained from 3.10 to 4.15 THz, with a gap from 3.17 to 3.49 THz, corresponding to the 104 cm^{-1} absorption mode in RTP. High output power levels were obtained, with a maximum average output power of 16.2 μW being detected at 3.80 THz, higher than that previously reported for an intracavity THz laser based on SPS. Our ongoing research aims overcome problems in extracting and detecting THz output above 4 THz, and thereby extend the tuning range of the system to around 6 THz. This work represents a compelling advance in the development of reliable, cost-effective and compact THz sources for real-world applications.

Acknowledgments

This work was supported under Australian Research Council's Linkage Projects funding scheme (project number LP140100724) and was performed in part at the OptoFab node of the Australian National Fabrication Facility (ANFF), using NCRIS and NSW state government funding. Assoc. Prof. Pask is the grateful recipient of an Australian Research Council Future Fellowship (project number FT120100294), and Tiago Ortega gratefully acknowledges receipt of a scholarship from the Commonwealth of Australia under the International Postgraduate Research Scheme (IPRS). The authors would like to thank M Squared Lasers Inc. for their support.

#260259 Received 29 Feb 2016; revised 30 Mar 2016; accepted 6 Apr 2016; published 2 May 2016

A.3. Second publication resulting from this work: Tiago Ortega, Helen Pask, David Spence and Andrew Lee, "THz polariton laser using an intracavity Mg:$LiNbO_3$ crystal with protective Teflon coating," Opt. Express 25, 3991-3999 (2017)

This paper is related to the work reported in Chapter 5 (Section 5.1) and was the second publication resulting from this PhD research.

Research Article | Vol. 25, No. 4 | 20 Feb 2017 | OPTICS EXPRESS 3991

Optics EXPRESS

THz polariton laser using an intracavity Mg:$LiNbO_3$ crystal with protective Teflon coating

TIAGO A. ORTEGA,* HELEN M. PASK, DAVID J. SPENCE, AND ANDREW J. LEE

MQ Photonics Research Centre, Department of Physics and Astronomy, Macquarie University, NSW 2109 Australia
*tiago.ortega@students.mq.edu.au

Abstract: An enhancement in the performance of a THz polariton laser based on an intracavity magnesium-doped lithium niobate crystal (Mg:$LiNbO_3$) in surface-emitted (SE) configuration is demonstrated resulting from the deposition of a protective Teflon coating on the total internal reflection surface of the crystal. In this cavity geometry the resonating fields undergo total internal reflection (TIR) inside the lithium niobate, and laser damage to that surface can be a limiting factor in performance. The protective layer prevents laser damage to the crystal surface, enabling higher pump power, yielding higher THz output power and wider frequency tuning range. With the unprotected crystal, narrow-band THz output tunable from 1.50 to 2.81 THz was produced, with maximum average output power of 20.1 μW at 1.76 THz for 4 W diode pump power (limited by laser damage to the crystal). With the Teflon coating, no laser damage to the crystal was observed, and the system produced narrow-band THz output tunable from 1.46 to 3.84 THz, with maximum average output power of 56.8 μW at 1.76 THz for 6.5 W diode pump power. This is the highest average output power and the highest diode-to-terahertz conversion efficiency ever reported for an intracavity terahertz polariton laser.

OCIS codes: (190.4410) Nonlinear optics, parametric processes; (130.3730) Lithium niobate; (310.1515) Protective coatings; (140.3330) Laser damage; (040.2235) Far infrared or terahertz; (140.3580) Lasers, solid-state.

References and links

1. I. Hosako, N. Sekine, M. Patrashin, S. Saito, K. Fukunaga, Y. Kasai, P. Baron, T. Seta, J. Mendrok, S. Ochiai, and H. Yasuda, "At the dawn of a new era in terahertz technology," Proc. IEEE 95(8), 1611–1623 (2007).
2. S. J. Oh, J. Choi, I. Maeng, J. Y. Park, K. Lee, Y.-M. Huh, J.-S. Suh, S. Haam, and J.-H. H. Son, "Molecular imaging with terahertz waves," Opt. Express 19(5), 4009–4016 (2011).
3. J. I. Shikata, K. Kawase, K. I. Karino, T. Taniuchi, and H. Ito, "Tunable terahertz-wave parametric oscillators using $LiNbO^3$ and $MgO:LiNbO^3$ crystals," IEEE Trans. Microw. Theory Tech. 48(4), 653–661 (2000).
4. K. Kawase, J. I. Shikata, and I. Hiromasa, "Terahertz wave parametric sources," J. Phys. D Appl. Phys. 35(3), R1–R14 (2002).
5. Y. Taira, S. R. Tripathi, K. Murate, K. Nawata, H. Minamide, and K. Kawase, "A Terahertz Wave Parametric Amplifier With a Gain of 55 dB," IEEE Trans. THz. Sci. Technol. 4, 753–755 (2014).
6. Y. Takida, T. Ohira, Y. Tadokoro, H. Kumagai, and S. Nashima, "Tunable picosecond terahertz-wave parametric oscillators based on noncollinear pump-enhanced signal-resonant cavity," IEEE J. Sel. Top. Quantum Electron. 19(1), 8500307 (2013).
7. A. Lee, Y. He, and H. Pask, "Frequency-tunable THz source based on stimulated polariton scattering in $Mg:LiNbO^3$," IEEE J. Quantum Electron. 49(3), 357–364 (2013).
8. A. J. Lee and H. M. Pask, "Continuous wave, frequency-tunable terahertz laser radiation generated via stimulated polariton scattering," Opt. Lett. 39(3), 442–445 (2014).
9. K. Kawase, J. Shikata, H. Minamide, K. Imai, and H. Ito, "Arrayed silicon prism coupler for a terahertz-wave parametric oscillator," Appl. Opt. 40(9), 1423–1426 (2001).
10. X. Wu, C. Zhou, W. R. Huang, F. Ahr, and F. X. Kärtner, "Temperature dependent refractive index and absorption coefficient of congruent lithium niobate crystals in the terahertz range," Opt. Express 23(23), 29729–29737 (2015).
11. T. Ikari, X. Zhang, H. Minamide, and H. Ito, "THz-wave parametric oscillator with a surface-emitted configuration," Opt. Express 14(4), 1604–1610 (2006).

#283267 https://doi.org/10.1364/OE.25.003991
Journal © 2017 Received 6 Jan 2017; revised 8 Feb 2017; accepted 9 Feb 2017; published 14 Feb 2017

Optics EXPRESS

12. W. Wang, X. Zhang, Q. Wang, Z. Cong, X. Chen, Z. Liu, Z. Qin, P. Li, G. Tang, N. Li, C. Wang, Y. Li, and W. Cheng, "Multiple-beam output of a surface-emitted terahertz-wave parametric oscillator by using a slab MgO:$LiNbO_3$ crystal," Opt. Lett. 39(4), 754–757 (2014).
13. Y. Y. Wang, Z. X. Li, J. Q. Li, C. Yan, T. N. Chen, D. G. Xu, W. Shi, H. Feng, and J. Q. Yao, "Energy scaling of a tunable terahertz parametric oscillator with a surface emitted configuration," Laser Phys. 24(12), 125402 (2014).
14. Y. Y. Wang, D. G. Xu, H. Jiang, K. Zhong, and J. Q. Yao, "A high-energy, low-threshold tunable intracavity terahertz-wave parametric oscillator with surface-emitted configuration," Laser Phys. 23(5), 055406 (2013).
15. M.-H. Wu, Y.-C. Chiu, T.-D. Wang, G. Zhao, A. Zukauskas, F. Laurell, and Y.-C. Huang, "Terahertz parametric generation and amplification from potassium titanyl phosphate in comparison with lithium niobate and lithium tantalate," Opt. Express 24(23), 25964–25973 (2016).
16. R. House, J. Bettis, and A. Guenther, "Surface roughness and laser damage threshold," IEEE J. Quantum Electron. 13(5), 361–363 (1977).
17. D. W. Camp, M. R. Kozlowski, L. M. Sheehan, M. A. Nichols, M. Dovik, R. G. Raether, and I. M. Thomas, "Subsurface damage and polishing compound affect the 355-nm laser damage threshold of fused silica surfaces," Proc. SPIE 3244, 356–364 (1998).
18. R. J. Shine, Jr., A. J. Alfrey, and R. L. Byer, "40-W cw, TEM(00)-mode, diode-laser-pumped, Nd:YAG miniature-slab laser," Opt. Lett. 20(5), 459–461 (1995).
19. Y. Furukawa, A. Yokotani, T. Sasaki, H. Yoshida, K. Yoshida, F. Nitanda, and M. Sato, "Investigation of bulk laser damage threshold of lithium niobate single crystals by Q-switched pulse laser," J. Appl. Phys. 69(5), 3372–3374 (1991).
20. Y. Sun, C. F. Li, Z. Y. Li, and F. Gan, "Investigation of nonlinear absorption and laser damage on lithium niobate single crystals," Proc. SPIE 1848, 594–598 (1993).
21. "Lascad-Software for Laser Cavity Analysis and Design," https://www.las-cad.com/.
22. T. Ikari, R. Guo, H. Minamide, and H. Ito, "Energy scalable terahertz-wave parametric oscillator using surface-emitted configuration," J. Eur. Opt. Soc. 5, 1–4 (2010).
23. F. Albiol, S. Navas, and M. V. Andres, "Microwave experiments on electromagnetic evanescent waves and tunneling effect," Am. J. Phys. 165, 165–169 (2006).
24. N. J. Bazin, J. E. Andrew, and H. A. McInnes, "Formation of Teflon AF Polymer Thin Films as Optical Coatings in the High Peak Power Laser Field.," Proc. SPIE 3492, Third Int. Conf. Solid State Lasers Appl. to Inert. Confin. Fusion 3492, 964–969 (1999).
25. E. Bründermann, H. W. Hübers, and M. F. G. Kimmitt, *Terahertz Techniques* (2012), Vol. 151.
26. D. J. M. Stothard, T. J. Edwards, D. Walsh, C. L. Thomson, C. F. Rae, M. H. Dunn, and P. G. Browne, "Line-narrowed, compact, and coherent source of widely tunable terahertz radiation," Appl. Phys. Lett. 92(14), 141105 (2008).
27. Q. Meng, B. Zhang, S. Zhong, and L. Zhu, "Damage threshold of lithium niobate crystal under single and multiple femtosecond laser pulses: theoretical and experimental study," Appl. Phys., A Mater. Sci. Process. 122(6), 582 (2016).

1. Introduction

The potential for electromagnetic radiation at terahertz frequencies to address a wide variety of real-world applications in life-sciences, medicine and homeland security has been known for decades [1,2]. Terahertz laser sources with frequency tunable output based on stimulated polariton scattering (SPS) have experienced continuous improvement over the years, with particular attention to terahertz parametric oscillators (TPO) [3,4], injection-seeded terahertz parametric generators (is-TPGs) [5], picosecond TPOs (ps-TPO) [6], and THz polariton lasers [7,8]. In these sources, a fundamental laser field (with frequency ν_f) interacts with a polariton mode of a nonlinear crystal generating via SPS both Stokes (ν_S) and polariton fields (with terahertz frequency ν_T) in a non-collinear phase matching configuration. In such sources, the frequency ν_T is the difference between ν_f and ν_S and can be modified by adjusting the interaction angle between the fundamental and Stokes fields [7].

Magnesium-doped lithium niobate (Mg:$LiNbO_3$) is the most used nonlinear material in terahertz sources based on SPS, and generally yields frequency tunable output from ~1 to 3 THz. Its widespread use is largely due to its high nonlinear coefficients, wide transparency range and photorefractive damage resistance promoted by the magnesium doping [4]. Extraction of the THz field from the nonlinear material is a challenging procedure. The polariton field is generated at approximately 65° to the fundamental field, and the incidence angle of approximately 25° on the crystal's side face is larger than the critical angle for total internal reflection (TIR) on the crystal-air interface. To avoid TIR, silicon (Si) prisms are typically bonded to the material's side face [9] through which the THz field exits. However,

this extraction technique introduces inherently high losses: Fresnel reflection losses are of the order of 30% at the prism/air interface at the THz frequencies generated. This is in addition to the strong absorption the polariton field experiences inside the crystal during its propagation from the SPS interaction region to the crystal's side face: the absorption coefficient ranges between 10 to 50 cm^{-1} from 1 - 2 THz, increasing even further at higher frequencies [10]. Another shortcoming of this technique is wave front discontinuities in the output THz beam, when multiple prisms are used.

A method which effectively overcomes many of these shortcomings is to use a surface-emitting (SE) configuration, in which total internal reflection of the pump and Stokes fields takes place at a crystal surface. In this configuration, also referred to as a bounce resonator geometry, the phase matching angles result in the polariton field being generated at an angle approximately normal to the reflecting surface, and so the THz output is refracted directly from the material into the air [11]. The SE configuration has been demonstrated in various systems using non-resonated pump fields such as TPOs [12], is-TPGs [13], and ps-TPOs [6]. These configurations yield high THz-output with relatively small beam sizes when compared with the Si-prism approach. This design has also been demonstrated in an intracavity system [14], utilizing a kW-level diode side-pumped resonator, Q-switched at low repetition rate, and with relatively low quality factor, resulting in a diode-to-THz conversion efficiency of 4.8×10^{-5}%. In the intracavity configuration the nonlinear material is placed inside the fundamental resonator, utilizing the inherently high intracavity field intensity to achieve SPS threshold in a simple and compact design, in contrast to the more complex and expensive pump lasers required in extra-cavity TPOs and is-TPGs.

The laser damage threshold of the lithium niobate crystal limits how high these systems can be power scaled, representing a limiting factor in the performance of these terahertz sources [14,15], and a technique to overcome this issue is required. The laser damage threshold of a crystal surface does not depend solely on the material composition, but is also influenced by the surface roughness [16,17], therefore a high-quality surface may result in an increase in laser damage resistance. In the case of the SE emitted configuration, a protective coating can be applied to the TIR surface in order to minimize the interaction of the evanescent wave with surface defects and impurities which may result in surface damage [18].

In this work, we report an enhancement in the laser damage resistance of an Mg:$LiNbO_3$ crystal in an intracavity surface-emitting configuration after the deposition of a protective Teflon coating on the TIR surface of the material. As a result, the pump power could be substantially increased, and the system yielded higher THz output power and wider frequency-tuning range. Prior to the coating, the system produced frequency-tunable output from 1.50 to 2.81 THz, with a maximum average output power of 20.1 μW at 1.76 THz for 4 W diode pump power, with the maximum diode pump power limited by surface damage on the TIR surface. After the Teflon deposition on the TIR surface of the crystal, no laser damage was observed, and the system produced terahertz radiation tunable over a wider range from 1.46 to 3.84 THz, and delivered a maximum average output power of 56.8 μW at 1.76 THz for 6.5 W diode pump power. This represents the most efficient intracavity THz polariton laser reported to-date, with the highest average THz output power ever reported for an intracavity system. This research outcome is part of our pathway to producing compact and affordable THz sources with narrow-band frequency-tunable output.

2. Experimental setup

The resonator for the intracavity surface-emitted THz polariton laser is outlined in Fig. 1. In this system, a trapezoidal Mg:$LiNbO_3$ crystal was placed inside a conventional diode-pumped Q-switched Nd:YAG laser, forming a bounce resonator for the fundamental 1064 nm field. A separate pair of mirrors formed the Stokes resonator around the nonlinear crystal, also in a bounce configuration. The SPS crystal geometry and the bouncing angle of the resonator

modes were designed to produce a polariton field at ~90° incidence angle on the TIR surface, enabling the terahertz radiation to be directly refracted out by the crystal. The terahertz frequency was tuned by adjusting the angle (θ_{ext}) between the fundamental and Stokes resonator axes [7].

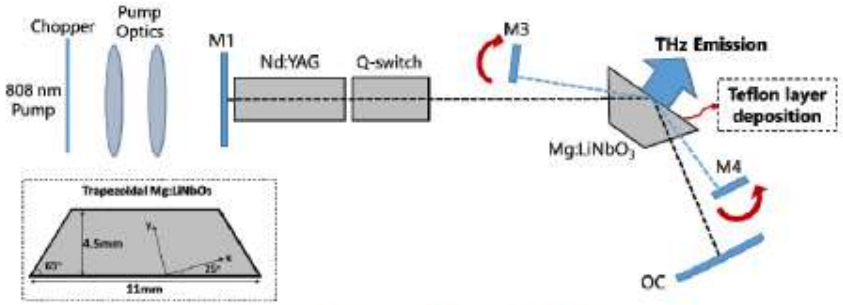

Fig. 1. Intracavity surface-emitted resonator layout.

In the fundamental resonator, a 1 at.% Nd:YAG crystal (5 mm length, 5 mm diameter; anti-reflection coated for 808 and 1064 nm) was end-pumped by a fiber coupled diode laser (100 μm core diameter, 0.22 NA; 10 W maximum output power) operating at 808 nm and chopped at 200 Hz with a 50% duty-cycle to reduce thermal lensing and enable the laser to operate further above threshold. A pair of aspheric lenses produced a ~300 μm diameter pump spot inside the laser crystal. A flat input mirror (T > 99% at 808 nm and R > 99.99% at 1064nm) and a concave output coupler (OC) (radius of curvature = 1000 mm; R = 99.4% at 1064 nm) delimited the fundamental resonator which had a cavity length of 250 mm. Total internal reflection of the fundamental and Stokes fields occurred inside a trapezoidal 5 at.% Mg:$LiNbO_3$ crystal (Castech Inc.; base angle of 65°; longer base length of 11 mm, 4.5 mm height and 8 mm thickness in the crystallographic z axis direction). The crystallographic xy plane orientation with respect to the trapezoidal geometry is also represented in Fig. 1. The nonlinear crystal end faces were polished with high-quality (10/5 scratch/dig) and anti-reflection coated for the fundamental and Stokes wavelengths (1060 to 1090 nm). Initially, the TIR surface was optically polished by the manufacturer (80/50 scratch/dig). As will be detailed below, a protective Teflon (AF Amorphous Fluoroplastic Solutions; AF 2400; Chemours) layer was spin-coated and cured onto the bounce surface, and a comparative evaluation was performed using the crystal with and without this coating. An acousto-optic Q-switching cell was responsible for pulsed operation at 3 kHz, a repetition rate sufficiently higher than the diode laser chopping frequency to avoid any significant influence of the chopped pump on the Q-switching operation.

The Stokes resonator was formed by a pair of flat mirrors (M3 and M4) separated by 70 mm, and coated for high reflectivity from 1060 to 1090 nm (R>99.9% at M3 and R>99% at M4). Both Stokes mirrors were D-shaped to avoid clipping of the fundamental beam, and were mounted on independent rotation stages enabling high precision angle tuning of θ_{ext}, which promotes fine adjustment of the THz frequency.

The average output power of the Q-switched fundamental and Stokes fields leaking respectively from OC and M4, were measured with a laser power meter (Thorlabs PM100D), and spectral content was monitored with a high-resolution optical spectrometer (Ocean Optics HR4000). Temporal behavior of the near-infrared fields was monitored with fast photodiodes (Thorlabs DET10C/M). The terahertz frequency was calculated from the energy difference between the fundamental and Stokes photons. The terahertz emission was chopped with a separate optical chopping wheel (10 Hz), and the average THz output power was measured with a Golay cell (Tydex GC-1T; 116.14 kV/W @10 Hz) in combination with a long pass

filter (Tydex, LPF 14.3) and a 50 mm focal length TPX lens (Tydex) to ensure that all the generated terahertz radiation was collected. As an additional check to ensure the detected THz radiation was not contaminated with scattered near-infrared light, whenever a terahertz signal was detected it was checked that a BK7 would completely suppress the signal being measured, validating it as purely THz radiation (the BK7 window blocks the THz but not near infrared).

In describing the performance of the Q-switched laser, we refer to the average output power, to distinguish from the peak pulse power. Moreover, we note that the laser operated at 50% duty-cycle, and the powers presented are those obtained during the laser-on periods.

3. Results and discussion

3.1 Laser performance with unprotected TIR surface

The laser performance was evaluated without the Teflon layer on the optically polished TIR surface of the lithium niobate. The fundamental field was obtained first, optimizing the fundamental resonator without the presence of the Stokes mirrors. Thereafter, the Stokes mirrors were inserted and aligned, and the SPS fields measured: undepleted fundamental, depleted fundamental, Stokes and terahertz. With the onset of the SPS action, the fundamental field energy is channeled to the generated Stokes and THz fields. As a consequence, there is a reduction in power from the undepleted (i.e. without SPS) to the depleted fundamental field, and the percentage of depletion at each diode pump level relates to the SPS conversion efficiency, and can be determined from the difference between the depleted and undepleted fundamental field output powers, measurements that were made by blocking/unblocking the Stokes resonator.

Fundamental field threshold was reached for an incident diode pump power of 0.6 W (determined by extrapolating the power scaling data points), and SPS field threshold was reached for an incident diode pump power of 2.75 W, above which Stokes and THz fields were detected. The diode pump power was set to 3 W, and the frequency-tuning range of the resonator was explored. When the external angle (θ_{ext}) between the fundamental and Stokes fields was adjusted from ~1.5° to 3°, tunable Stokes radiation from 1070.1 to 1075.1 nm was detected, and a corresponding terahertz field tunable from 1.50 to 2.81 THz was measured. Power scaling of the fundamental (depleted and undepleted), Stokes and THz fields were performed at 1.76 THz, the frequency at which the most efficient THz emission was observed and this data is plotted in Fig. 2. The maximum diode pump power tolerated by the crystal during power scaling was 4 W with or without SPS action, and above this value, damage to the TIR surface of the $MgLiNbO_3$ crystal was observed.

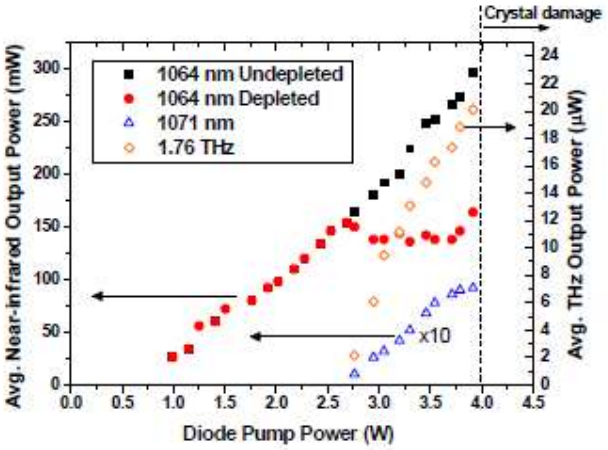

Fig. 2. Power scaling for the fundamental (1064 nm), Stokes (1071 nm, magnified 10 times) and THz (1.76 THz) fields without Teflon coating on Mg:$LiNbO_3$ crystal. The laser was operated at 50% duty-cycle.

A maximum average output power of 20.1 μW was detected at 1.76 THz at 4 W incident diode pump power. From the graph in Fig. 2 a fundamental field depletion in excess of 44% can be calculated. It is anticipated that the average output of the THz field power will increase even further at higher pump levels, because there was no evidence of saturation or roll-over of the stokes or terahertz fields when pumping up to 4 W. The horizontal beam profile of the THz radiation propagating in free space was measured after 1 mm propagation from the crystal's TIR surface. Using a knife-edge mounted on a high precision translation stage, a 2.0 mm horizontal beam diameter was measured.

From the results reported here it is evident that the THz output power is limited by surface damage to the TIR face of the Mg:$LiNbO_3$ crystal. The literature concerning laser-induced damage of lithium niobate is complicated by the occurrence of photorefractive damage (mainly in the bulk), and that dopants such as MgO which are added to reduce photorefractive damage, are found to actually reduce the laser induced damage threshold [19]. For the doping concentration utilized here (5% MgO:$LiNbO_3$) a bulk damage threshold around 2.5 J/cm^2 was reported in [19] (at 1053 nm, 25 ns pulses). It is common for the surface damage threshold in lithium niobate to exceed the bulk damage threshold, and in [20] these were reported to be 22 J/cm^2 and 12 J/cm^2 respectively (1064 nm, 10 ns pulses) in $LiNbO_3$. We were unable to find corresponding data for MgO:$LiNbO_3$.

The laser spot size at the TIR surface was determined through ABCD resonator analysis (using LASCAD® software [21]) to be an ellipse with horizontal and vertical dimensions of ~1.14 and 0.48 mm respectively. With the laser spot size, the average output power of the fundamental field, and the transmission of the output coupler, we estimate that the fluence of the fundamental field at the TIR surface was around 3 J/cm^2 at 4 W diode pump. We note that damage to the TIR surface occurred more frequently during alignment, prior to the onset of the SPS process. When the SPS process is stable, the fluence is lower, at around 2 J/cm^2, owing to depletion of the fundamental field. These observations are consistent with those in [22], where surface damage was found to occur for powers of about 2.6 J/cm^2.

Surface roughness is also known to influence the surface damage threshold [16,17], and we also note that the Mg:$LiNbO_3$ crystal input faces, which had been polished to a higher standard (10/5 scratch/dig, versus 80/50 for the TIR surface), were not damaged during power

scaling. However, we were informed by the manufacturer that improving the surface figure of the TIR surface of the existing crystal was not possible, and to remove the damaged spots, the TIR surface was re-polished to an optical standard (80/50 scratch/dig).

3.2 Laser performance with Teflon-coated TIR surface

To improve the laser damage resistance of the TIR surface, we investigated the application of a protective Teflon layer to the surface. This coating is believed to prevent interaction of the evanescent wave of the totally internally reflected field with impurities and imperfections on the TIR surface, and is a technique which has been used in other solid state laser systems [18]. Utilizing the evanescent wave decay coefficient [23], the optical properties of Teflon (refractive index of 1.3) [24], and the incidence angle at the TIR surface (65°), it was calculated that a 120 nm thick Teflon layer would be sufficient to result in a evanescent field amplitude at the Teflon/air interface of 1/e of its amplitude at the $MgLiNbO_3$/Teflon interface. A solution of Teflon (AF Amorphous Fluoroplastic Solutions; AF 2400; Chemours) was deposited on the TIR surface using spin-coating [24] and the crystal was heated to evaporate the solvent present in the deposited layer. The lithium niobate crystal was spin coated with Teflon AF2400 solution at 2000 rpm for 60 s, and heated at 112° for 5 minutes. Using a surface profiler (Tencor Alphastep 500), we measured a ~150 nm thick single Teflon layer. The interaction of the THz fields with the Teflon layer this thick can be neglected. The absorption coefficient of Teflon at the THz frequency range of interest here is sufficiently low ($\leq 4\ cm^{-1}$) [25] to absorb less than 0.01% of the incident radiation. Moreover, the wavelength of the terahertz radiation (~75 to 200 μm) is around 3 orders of magnitude higher than the layer thickness, which prevents the Teflon of acting as a thin-film interference coating.

The lithium niobate crystal with the protective Teflon coating on the TIR surface was re-inserted in the fundamental resonator, and the system was re-optimized following the methodology adopted previously. No laser-induced damage was observed for pump powers of 4 W and higher. However, the power of the undepleted fundamental field rolled over above 6 W diode pump power due to strong thermal lensing, despite the pump diode being chopped. The power scaling for the fundamental, Stokes and THz fields is plotted in Fig. 3 for the most efficient THz emission at 1.76 THz (1071 nm Stokes). Within the context of this experiment, the laser damage threshold for the Teflon coated material could not be determined, yet it can be inferred that it increased by at least 50% comparing the maximum 1064 nm average output power tolerated on each case: 450 mW and 300 mW with and without Teflon, respectively. The fundamental field threshold was not affected by the re-polishing and Teflon-coating procedure. The SPS threshold was reached at 3.3 W. This slight increase in threshold may originate from the interaction of the fundamental field with a slightly different region of the crystal bulk (and local variations in the SPS gain throughout the crystal due to impurities, local defects, etc.). As expected, an increase in the measured terahertz output was observed, and a maximum average output power of 56.8 μW was detected at 1.76 THz at 6.5 W incident diode pump power. From the graph in Fig. 3 a fundamental field depletion in excess of 55% can be calculated in this case at 6.5 W pump, with a diode-to-THz conversion efficiency of 8.7×10^{-4}%, an order of magnitude increase over [14]. From these results, there is scope for further increasing the THz output power by redesigning the fundamental cavity to better manage the effects of thermal loading in the laser crystal.

Optics EXPRESS

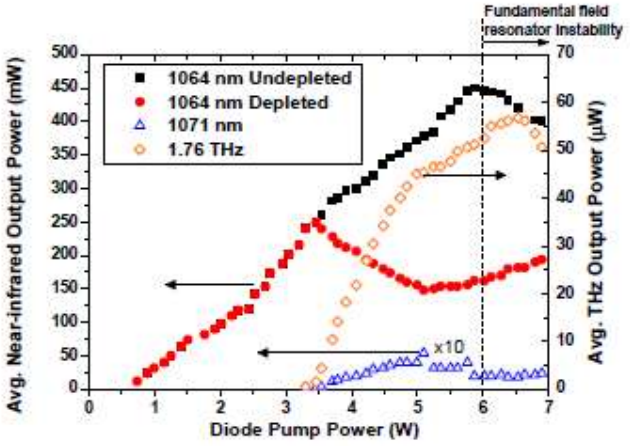

Fig. 3. Teflon-coated Mg:$LiNbO_3$ crystal: Power scaling for the fundamental (1064 nm), Stokes (1071 nm, magnified 10 times) and THz (1.76 THz) fields after the Teflon deposition on the crystal. The laser was operated at 50% duty-cycle.

The temporal behavior of the near-infrared fields were characterized near SPS threshold (3.5 W diode pump power) and in the high depletion regime (>50%), at 4.5 W diode pump power. The full width half maximum (FWHM) pulse width of the undepleted fundamental field was around 130 ns in both regimes. Near SPS threshold the depleted fundamental field exhibited similar pulse widths, and a 41 ns (FWHM) Stokes pulse width was measured. In the high depletion regime, significant pulse shortening occurred, with typical depleted fundamental and Stokes pulses durations being ~54 and 20 ns (FWHM) respectively. The difference between the areas under the pulse shapes of the depleted and undepleted fundamental pulses correlate well with the amount of fundamental power converted in the SPS process, and our previously calculated percentage of depletion. The spatial profiles of the fundamental and Stokes beams were observed qualitatively to be close to Gaussian. Measurement of the linewidth is a challenging task that we have not yet undertaken. However, we anticipate that it will be around several tens of gigahertz [26].

The frequency-tuning range of the resonator with the Teflon-coated lithium niobate was also explored. When the external angle (θ_{ext}) was adjusted from ~1.5° to 4°, tunable Stokes radiation from 1070.0 to 1079.2 nm was detected, and a corresponding terahertz field tunable from 1.46 to 3.84 THz was measured. The plot in Fig. 4 shows the terahertz frequency-coverage of the system with and without the Teflon coating, with the diode pump optimized for maximum terahertz output at each frequency. The diode pump value at each point would slightly vary due to the complex interplay between fields and the dependence on the SPS gain with frequency. For the unprotected crystal, this was performed adjusting the diode pump power from 3 to 4 W and for the Teflon coated material the diode pump was varied between 5 and 7 W. The substantial 83% increase in the frequency-tunability with the Teflon coating is attributed to the ability to pump the system harder, enabling us to reach threshold at terahertz frequencies with lower SPS gain. The THz beam profile in the horizontal plane was not measured but it is expected to remain similar to the previous value of 2.0 mm.

Optics EXPRESS

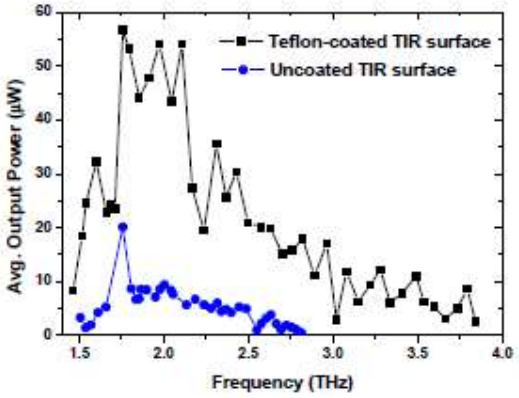

Fig. 4. Comparative plot of terahertz frequency-coverage of the system before and after the protective Teflon layer deposition on the lithium niobate total internal reflection surface. In each case, the diode pump power was adjusted to maximize the average THz output power.

The average terahertz output powers reported in this experiment exhibited a maximum fluctuation of 10% (as observed in the Golay cell signal output), when running for more than an hour, despite the lack of active feedback loop of any nature. It is anticipated that with active feedback control of the pump diode, the system would exhibit even better stability in the THz output for applications outside the laboratory environment.

4. Conclusion

Lithium niobate is likely the most important nonlinear crystal in THz generation via SPS sources. However, laser damage to the crystal has been a recurring topic in the literature [14,15,27] and this limits performance. In this report, we demonstrated that a single layer of Teflon can be applied to the crystal's total internal reflection surface with a simple spin-coating procedure, this resulting in a higher pump capacity, and yielding higher THz average output power and wider frequency-tunability. The Teflon-coated crystal delivered 56.8 μW average output power at 1.76 THz (against 20.1 μW without Teflon), and the frequency coverage also improved, spanning from 1.46 to 3.84 THz (against 1.50 to 2.81 THz without Teflon). The terahertz source described here represents the most efficient intracavity THz polariton laser reported to-date (8.7×10^{-4}% diode-to-THz conversion efficiency), with the highest average THz output power ever reported for an intracavity system. The enhancement in performance obtained here in an intracavity SPS system can be readily translated to other configurations layouts such as TPOs, is-TPGs, and ps-TPOs.

Funding

Australian Research Council's Linkage Projects (LP140100724); Australian Research Council Future Fellowship (project number FT120100294);

Acknowledgment

The authors would like to thank M Squared Lasers Ltd. for their support and acknowledge that the crystal polishing was performed at the OptoFab node of the Australian National Fabrication Facility (ANFF). Tiago Ortega acknowledges the receipt of an Australian Government Research Training Scholarship.

A.4. Third publication resulting from this work: Tiago Ortega, Helen Pask, David Spence and Andrew Lee, “Tunable 3-6 THz polariton laser exceeding 0.1 mW average output power based on crystalline RbTiOPO4,” IEEE J. Sel. Top. Quantum Electron. DOI: 10.1109/JSTQE.2018.2810380 (2018)

This paper is related to the work reported in Chapter 5 (Section 5.3) and was the third publication resulting from this PhD research.

Tunable 3-6 THz polariton laser exceeding 0.1 mW average output power based on crystalline $RbTiOPO_4$

Tiago A. Ortega, Helen M. Pask, David J. Spence and Andrew J. Lee

***Abstract*—We report a diode-pumped, intracavity THz laser source based on stimulated polariton scattering in crystalline $RbTiOPO_4$ using a surface-emitting configuration. The system was continuously tunable in four regions, from 3.05 – 3.16 THz, from 3.50 – 4.25 THz, from 4.57 – 4.75 THz and from 5.40 – 5.98 THz. The laser delivered 124.7 μW average output power at 4.10 THz for only 6.0 W diode pump power at 808 nm, corresponding to a diode-to-THz conversion efficiency of 2.1×10^{-5}. The horizontal and vertical beam quality parameters were $M_x^2 < 1.6$ and $M_y^2 < 1.1$ and the linewidth of the terahertz field was 28 GHz at 4.10 THz. The results demonstrate that the surface-emitting configuration is a very efficient technique to produce high power THz laser sources with frequency-tunable output suitable for real world applications.**

***Index Terms*— Nonlinear optics, parametric devices, Raman scattering, solid-state lasers, stimulated polariton scattering (SPS), terahertz lasers.**

I. Introduction

TERAHERTZ spectroscopy and spectral imaging techniques have demonstrated great potential to address important real-world applications in various fields, particularly in medicine[1]–[3], homeland security[4]–[6] and non-destructive testing across a wide range of industries[7]–[9]. However, further development of robust, reliable and cost-effective THz sources with sufficient output power is crucial to produce commercially viable systems.

A prominent technique for THz generation is stimulated polariton scattering (SPS) which has been demonstrated in nonlinear crystals such as MgO:$LiNbO_3$ (MgO:LN), $KTiOPO_4$ (KTP), $KTiOAsO_4$ (KTA), and more recently $RbTiOPO_4$ (RTP)[10]–[15]. In SPS, a fundamental laser field (frequency ν_f) interacting with a polariton mode of a nonlinear crystal parametrically generates two other fields, a Stokes (frequency ν_s) and a polariton field (with terahertz frequency ν_{THz}), in a non-collinear phase matching configuration[10]. The frequency of the polariton field is the difference between ν_f and ν_s, in keeping with the conservation of energy. To satisfy momentum conservation, a noncollinear phase matching scheme is used, and the frequency of the Stokes and THz fields can be modified by adjusting the interaction angle between the fundamental and Stokes fields[10].

A key design consideration for SPS lasers is how to efficiently extract the generated terahertz radiation from the crystal. Here there are two key challenges. First, strong THz absorption by the nonlinear material makes it necessary to minimize the length over which the THz field must propagate before exiting the crystal. Second, the high refractive indices for THz radiation can lead to total internal reflection (TIR) if the angle of incidence of the THz beam exceeds the critical angle. For this reason high-resistivity silicon prisms are typically bonded to the crystal's side face, enabling the THz radiation to refract into the silicon and exit the prism at near-normal incidence, into the air[16]. There are substantial Fresnel reflection losses and significant absorption of the THz field during its propagation through the silicon prism. A more efficient extraction mechanism is the surface-emitting (SE) configuration, in which the fundamental and Stokes fields experience TIR inside the nonlinear crystal, and the phase matching angles result in a polariton field generated in close proximity and at near-normal incidence to the crystal-air interface. Hence, the THz radiation generated at the TIR surface is refracted directly into the air. The SE configuration has been reported using several polariton crystals including MgO:LN, KTP and KTA[13], [14], [17] where it was found to be effective at producing higher THz outputs and smaller beam sizes when compared to the performance of linear resonators in combination with silicon prisms.

SPS has been demonstrated for externally-pumped and intracavity nonlinear crystals. Reaching SPS threshold for externally-pumped crystals however, require the use of high energy pulsed laser systems, which are generally complex, often expensive and lack compactness. This can be contrasted to the intracavity design, in which the SPS crystal is placed inside the resonator of what is typically a diode-pumped Nd laser, making use of the intense intracavity fields to reach SPS threshold for very modest (typically a few Watts at 808 nm) diode pump powers[18]. The resulting devices are typically compact and cost-effective, and can be pumped by

This work was supported by the Australian Research Council through the Discovery Project scheme (DP110103748), Linkage Project scheme (LP140100724) and Future Fellowship Scheme (Pask, FT120100294).

The Authors are with the MQ Photonics Research Centre, Department of Physics and Astronomy, Macquarie University, Sydney NSW 2109, Australia (email: tiago.ortega@students.mq.edu.au; helen.pask@mq.edu.au; david.spence@mq.edu.au; andrew.lee@mq.edu.au)

Color versions of one or more of the figures in this paper are available online at http://ieeexplore.org.

conventional laser diodes. They exhibit very low SPS threshold, high average THz output powers and outstanding diode-to-THz efficiency when compared with externally pumped systems[12], [18]. Most intracavity SPS terahertz lasers have used MgO:$LiNbO_3$ to generate terahertz fields continuously tunable in the ~1 – 3 THz range in both linear[18], [19] and SE configurations[20], [21]. Recently, our group sought to extend the THz frequency coverage of these sources, and reported the first intracavity SPS source based on a different nonlinear material, RTP, which was implemented in a linear configuration[15].

Rubidium titanyl phosphate (RTP) is an excellent nonlinear crystal widely used in electro-optical devices, due to its high nonlinear coefficient, high laser damage threshold, low-switching voltage and high transparency range[22]. These attributes make RTP a very attractive material for SPS, and the system reported in [15] produced detectable terahertz radiation ranging from 3.10 – 4.15 THz, with a maximum average output power of 16.2 μW at 3.80 THz. However, while the Stokes lasing indicated THz fields up to 7.05 THz were being generated inside the material, no emission above 4.15 THz could be detected, and this was attributed to increased THz extraction losses and reduced detection efficiencies associated with the higher THz frequencies. The use of an intracavity RTP crystal in a SE configuration was proposed as a potential means for increasing the range of THz frequencies that could be detected.

In this manuscript we report, for the first time to our knowledge, a THz polariton laser based on an intracavity RTP in a surface-emitting configuration which produces terahertz radiation in four tunable bands between 3.05 THz and 5.98 THz, providing much better spectral coverage compared to the 3.10-4.15 THz reported previously using a linear configuration[15]. The lack of continuous tunability is associated with infrared absorbing modes in the material[15]. Moreover, the SE configuration promoted a substantial increase of more than 7 times in THz output power and in one order of magnitude in diode-to-THz efficiency. A maximum average output power of 124.7 μW was detected at 4.10 THz for a diode pump power of just 6 W, resulting in a diode-to-THz efficiency of 2.1×10^{-5}. This result represents an important milestone because it is not only the highest average THz output power and diode-to-THz efficiency ever reported for any intracavity SPS laser, but also the first time an intracavity SPS source has exceeded the 0.1 mW average output power level.

II. Experimental Details

The THz polariton laser with the intracavity RTP crystal in SE configuration is outlined in Fig. 1. The RTP crystal was cut with a trapezoidal geometry, and was placed inside the cavity of a conventional diode-pumped Q-switched Nd:YAG laser. Within this cavity, the fundamental 1064 nm field underwent TIR inside the RTP crystal, forming a folded cavity. The Stokes field also underwent TIR inside the RTP crystal, in a separate folded cavity formed by an independent pair of mirrors. The internal angles of the RTP trapezoid and the folding angles of the fundamental and Stokes resonators were designed to produce a polariton field which was generated at an incidence angle close-to-normal on the TIR surface. This enabled the terahertz radiation to be directly refracted out of the RTP crystal. The internal angle θ between the fundamental and Stokes fields was adjusted to produce frequency-tunable THz radiation[12].

The fundamental resonator was end-pumped by a fiber

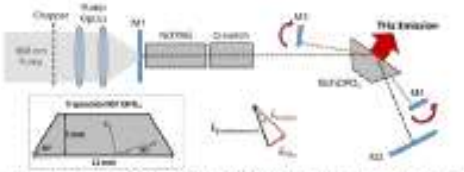

Fig. 1. Resonator layout for the THz polariton laser with intracavity RTP in a surface-emitting configuration.

coupled diode laser operating at 808 nm (100 μm core diameter, 0.22 NA; 10 W maximum output power). The diode laser was chopped at 200 Hz with a 50% duty-cycle to reduce thermal lensing. A pair of aspheric lenses produced a ~300 μm diameter pump spot inside a 1 at.% Nd:YAG crystal (5 mm length, 5 mm diameter; anti-reflection coated for 808 and 1064 nm). The fundamental resonator was 250 mm-long and was composed of a flat input mirror M1 (T > 99% at 808 nm and R > 99.99% at 1064 nm) and a concave output coupler M2 (radius of curvature = 1000 mm; R = 99.4% at 1064 nm). The fundamental field was Q-switched by an acousto-optic cell at a repetition rate of 3 kHz. This was substantially higher than the diode laser chopping frequency and hence was not affected by the chopped pump diode. The trapezoidal RTP crystal (Crystech Inc.) had base angle of 60° with longer base length of 12 mm, 5 mm height and 8 mm thickness in the crystallographic z axis direction. The orientation of the crystallographic xy plane with respect to the crystal geometry is shown inset in Fig. 1 and the laser fields were polarized in the z-direction. Total internal reflection of the fundamental and Stokes fields occurred at the uncoated long base of the trapezoid, and the crystal end faces were anti-reflection coated for the fundamental and Stokes wavelengths (R<0.3% from 1060 to 1090 nm).

The pair of flat mirrors M3 and M4 were separated by 85 mm and coated for high reflectivity from 1060 to 1090 nm (R>99.99% for M3 and R>99.9% for M4) and formed the Stokes resonator. Each Stokes mirror was mounted on an independent rotation stage, which enabled high-precision tuning of the internal angle θ, and consequently fine adjustment of the THz frequency. To avoid clipping of the fundamental field when adjusting the Stokes resonator, both mirrors M3 and M4 were D-shaped.

The average fundamental field power leaking from M2 and the average Stokes power leaking from M4 were measured with a laser power meter, and their temporal characteristics were measured with a fast silicon photodiode. The wavelength of the fundamental and Stokes fields were monitored with a spectrometer, and the difference between the energy of these fields was used to calculate the terahertz frequency. The average terahertz output power was measured with the same apparatus described in[15], an optical chopper (10 Hz) and a Golay cell (Tydex GC-1T; 116.14 kV/W @10 Hz), in combination with a long pass filter (Tydex, LPF 14.3) and a 50 mm focal length TPX lens (Tydex), to ensure that all the generated terahertz radiation was collected. The laser operated with the pump laser diode at 50% duty-cycle, and it is important to note that all the average output power levels presented in this manuscript are those obtained during the laser-on periods.

III. Results and Discussion

The fundamental resonator was optimised first, producing a 1064.4 nm field. Adjusting the interacting angle from $\theta = 1 - 2.8°$, wavelength-tunable Stokes radiation from 1076.1 to 1087.5 nm was measured, corresponding to polariton fields from 3.05 – 5.98 THz being generated internally. For interacting angles below 1° the Stokes mirrors clipped the fundamental field, preventing oscillation of the fundamental field, and for angles above 2.8° no SPS fields could be detected, this being attributed to a decreasing overlap between the fundamental and Stokes cavity modes, resulting in decreasing SPS gain. The 2.8° upper limit for the interacting angle is below that observed for the linear resonator, in which SPS activity was present at angles as high as 3.6° inside RTP[15]. The frequency-coverage of the THz polariton laser based on RTP in linear (adapted from[15]) and in SE configurations are plotted in Fig. 2 for a 5.5 W diode pump input. In the figure, the average THz output power measured with the Golay cell, emitted from the TIR surface of the RTP crystal is plotted together with the average Stokes power measured leaking from M4. The SE resonator was continuously tunable in four regions, from 3.05 – 3.16 THz, from 3.50 – 4.25 THz, from 4.57 – 4.75 THz and from 5.40 – 5.98 THz, a substantially wider range when compared to the linear configuration in which terahertz detection was limited to 3.10 – 3.17 THz and 3.50 – 4.15 THz. The gaps in THz emission correspond to polariton modes in RTP located around 106, 143 and 161 cm^{-1} [15] and result from the increase in absorption close to resonance. It is important to

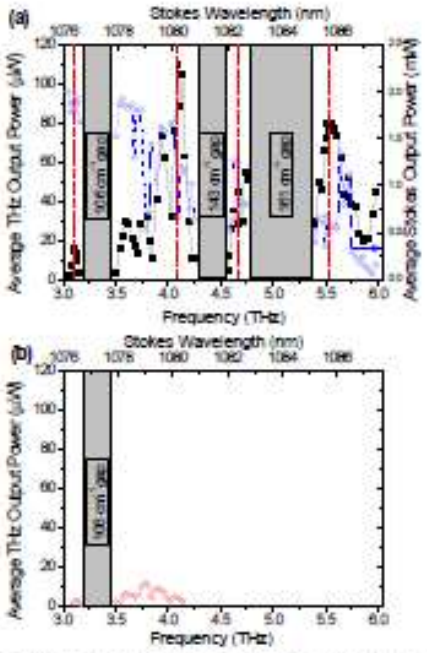

Fig. 2. Average THz output power and average Stokes power measured for a 5.5 W diode pump input (a) from the SE configuration. (b) from the linear configuration (adapted from[15]). The higher THz powers and expanded spectral coverage achieved by using the SE configuration are clearly apparent. The significant dips in THz power are attributed to water vapor absorption present in the laboratory environment[23].

note that the emission from RTP fills the emission gap from sources based on KTP and KTA[13], [14], and vice-versa. In the experimental setup, the output frequency was manually adjusted with the translation stages; this can be easily automated with motorized stages for rapid frequency scanning, envisioning future applications.

From Fig. 2 it should be noted that with the RTP in SE configuration, frequency-tunable THz radiation was detected for all interacting angles producing wavelength-tunable Stokes fields. This was not the case with the same crystal in linear configuration previously reported in[15], in which the highest detectable THz frequency was 4.15 THz, whilst frequencies as high as 7.05 THz were generated inside the nonlinear material. The frequency-tuning results obtained from the RTP in SE configuration confirms that extraction of the THz fields from the SPS crystal were the limiting factor for the linear configuration, and this can be avoided with the SE geometry. This is because the SE geometry virtually eliminates THz absorption losses for the fields generated at the TIR surface, producing measurable THz signal across the entire SPS tuning range.

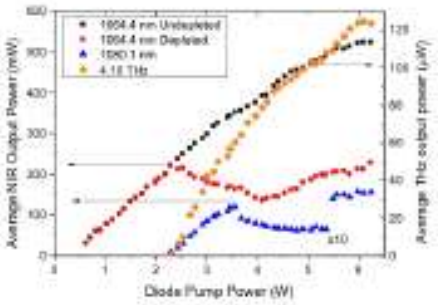

Fig. 3. Power scaling for the fundamental (undepleted and depleted), 1080.1 nm Stokes (magnified 10 times) and 4.10 THz fields.

The system was power scaled at the most efficient SPS frequency on each emitting band, 3.12 THz, 4.10 THz, 4.69 THz and 5.53 THz. The power scaling curves for the 4.10 THz, 1080.1 nm Stokes and 1064.4 nm fundamental (undepleted and depleted) fields are shown in Fig. 3, as a representation of the general power scaling response of the system. The undepleted fundamental field power corresponds to the 1064.4 nm output with the Stokes cavity blocked (i.e. no SPS action), and the depleted value correspond to the output leaking from M2 with the SPS process active (i.e. Stokes cavity unblocked). The decrease in power from the undepleted to the depleted fundamental field for a given diode pump level is related to the amount of energy channeled to the SPS process, and the percentage of depletion calculated from this difference in power is an indication of the SPS conversion efficiency[12].

Threshold for generating the fundamental field was 0.6 W diode pump power, while the lowest pump power required to achieve SPS threshold was 2.3 W, for a THz frequency of 4.10 THz (1080.1 nm Stokes). Considering the average output power at 1064 nm at this pump level (200 mW), the transmission of mirror M4 at 1064 nm (0.6%), the calculated cavity mode size inside the crystal (230 μm radius), and the measured pulse width at this pump level (270 ns full width half-maximum (FWHM)), a SPS threshold intensity of 27 MW/cm^2 can be calculated. This figure is comparable to that observed in other intracavity systems, which are typically lower than those observed in externally pumped resonators[12], [15], [18].

At 4.10 THz, a maximum average terahertz output power of 124.7 μW was measured for only 6.0 W diode pump power (pump depletion in excess of 60%), corresponding to a diode-to-THz conversion efficiency of 2.1×10^{-5}. This represents a 7-fold increase in power over the 16.2 μW previously obtained for the linear THz polariton laser[15], and one order of magnitude improvement in diode-to-THz efficiency, this demonstrating another great advantage of the SE configuration. The system maintained similar SPS thresholds and a high level of average output power at the other three frequencies evaluated, with a maximum average output power

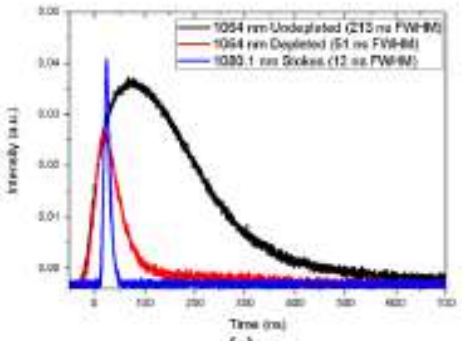

(a)

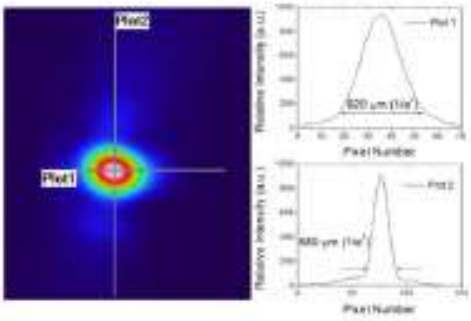

(b)

Fig. 4. (a) Temporal profiles of the depleted and undepleted 1064 nm, and 1080.1 nm Stokes fields at 6.0 W diode pump power; and (b) terahertz signal at 4.10 THz focused to a 920×680 μm spot (horizontal×vertical; $1/e^2$) with a 50 mm focal length spherical lens into the THz camera.

of 62.3 μW at 3.12 THz, 47.1 μW at 4.69 THz and 78.6 μW at 5.53 THz for a maximum 6.0 W diode pump input. The SPS threshold for the surface-emitting configuration is comparable to that of the linear cuboid crystal, suggesting similar gains for both configurations. Hence, the substantial increase in the THz signal detected from the surface-emitting configuration can be attributed to a much higher extraction efficiency. When comparing RTP with MgO:LN, the most explored SPS crystal, RTP yielded more than double the amount of THz output which suggests that the materials properties of RTP may be more favourable to nonlinear conversion via SPS. Moreover, in RTP laser damage to the TIR surface did not occur, as opposed to what at observed in MgO:LN, which required a protective Teflon coating to the TIR surface[21].

The temporal profile of the fundamental (undepleted and depleted) and 1080.1 nm Stokes fields were measured at 6.0 W diode pump as shown in Fig. 4. Close inspection of Fig. 4(a) shows that the rising edge of the Stokes pulse (blue line) coincides with the point at which depletion of the fundamental

commences. The full-width at half maximum (FWHM) of the fundamental field pulse decreased from 213 ns undepleted to 51 ns when depleted, and the Stokes pulse width was measured to be 12 ns (FWHM). The area under the undepleted and depleted fundamental field pulses are related to the energy output of these fields, and the ratio between the pulse area of the depleted and undepleted pulses is another indication of the fundamental field depletion. From this ratio, a 65% depletion was calculated, a value comparable to that measured from the power scaling curves.

The linewidth of the free-running terahertz field was estimated from the coherence length of the 4.10 THz field, measured with a Fabry-Perot interferometer[24] constructed from two silicon windows (0.5 mm thick, 50.8 mm diameter, Tydex). From the interferometric measurements, a coherence length of around 3.4 mm was measured, corresponding to a 28 GHz (±1 GHz) linewidth estimated at 4.10 THz, considering a Lorentzian spectrum[25]. This is similar to the free-running linewidth measured for other intracavity SPS systems, and could potentially be reduced with the insertion of etalons in the fundamental and Stokes cavities[19]. The polarization of the terahertz output was measured with a linear polyethylene polarizer (Tydex) to be vertically polarized, parallel to the crystal z-axis.

The terahertz output at 4.10 THz was collected with a 50 mm focal length TPX lens (Tydex) placed at ~100 mm from the TIR surface, and focused on a camera sensitive to THz radiation (IRV-T0831, NEC Corporation), as also shown in Fig. 4(b). A 920×680 μm (horizontal×vertical; $1/e^2$; ±50 μm) spot was formed in the focal plane array of the camera, demonstrating the ability of the source to produce uniform and tightly-focused beams. The small asymmetry of the focused spot is a consequence of the ellipsoid mode shape at the TIR surface, and may be corrected with customized optics. The horizontal and vertical beam quality parameters (M^2) for the free-space propagating terahertz field at 4.10 THz was calculated with the knife-edge method, similarly to what was reported in[21], and assuming a close-to-Gaussian THz beam profile. From these measurements, horizontal and vertical beam quality parameters were calculated respectively to be $M_x^2 < 1.6$ and $M_y^2 < 1.1$. These values are substantially lower than that reported for an intracavity SPS laser in a linear configuration, using silicon prisms to extract the THz field, in which the beam quality was measured to be $M_x^2 \sim 6.7$ and $M_y^2 \sim 2.3$[26], indicating that the SE configuration can increase the brightness of the THz output when compared to the linear configuration.

IV. Conclusion

In this manuscript we reported the development of the first THz polariton laser based on RTP in SE configuration. The combination of the good material properties of RTP in an intracavity surface-emitting configuration resulted in a record-high terahertz output, with an average output power of 124.7 μW detected at 4.10 THz. Furthermore, it was continuously tunable in four regions, from 3.05 – 3.16 THz, from 3.50 – 4.25 THz, from 4.57 – 4.75 THz and from 5.40 – 5.98 THz, significantly extending the frequency coverage of THz sources based on intracavity SPS, and filling the emission gaps of other nonlinear materials. The diode-to-THz conversion efficiency was 2.1×10^{-5}, the highest ever reported for an intracavity SPS laser, to the best of our knowledge. The horizontal and vertical beam quality parameters were $M_x^2 < 1.6$ and $M_y^2 < 1.1$, and the linewidth of the terahertz field was 28 GHz at 4.10 THz. When compared to the linear approach which uses silicon prisms to extract the THz fields, the surface-emitting configuration yielded a substantial increase in the range of terahertz frequencies detected and a notable increase in the average output power levels measured, this being a consequence of the superior extraction efficiency and the elimination of absorption losses for the THz fields generated at the TIR surface. Also, the M^2 parameters of the THz output in the horizontal and vertical directions were superior to what is typically obtained in the linear configuration. The results reported here suggest that the intracavity surface-emitting configuration is extremely advantageous, and represents a compelling advance towards producing practical THz sources with frequency-tunable output for real-world applications.

V. References

[1] A. Rammdo Orlando and G. P. Gallerano, "Terahertz radiation effects and biological applications," *J Infrared, Millimeter, Terahertz Waves*, vol. 30, no. 12, pp. 1308–1318, 2009.

[2] A. J. Fitzgerald, E. Berry, R. E. Miles, C. B. Reid, A. Fitzgerald, G. Reese, S. Fan, Y. He, B. S. Ung, W. L. Chan, J. Deibel, D. M. Mittleman, B. Fergnson, S. Wang, D. Gray, R. M. Woodward, B. E. Cole, and V. P. Wallace, "Terahertz pulse imaging in reflection geometry of human skin cancer and skin tissue," *Phys. Med. Biol.*, vol. 47, pp. 3853–3863, 2002.

[3] S. J. Oh, J. Choi, I. Maeng, J. Y. Park, K. Lee, Y. Huh, J. Suh, S. Hasm, and J. Son, "Molecular imaging with terahertz waves," *Opt. Express*, vol. 19, no. 5, pp. 4009–4016, 2011.

[4] K. Kawase, Y. Ogawa, Y. Watanabe, and H. Inoue, "Non-destructive terahertz imaging of illicit drugs using spectral fingerprints," *Opt. Express*, vol. 11, no. 20, pp. 2549–2554, 2003.

[5] M. R. Leahy-hoppa and M. J. Fitch, "Terahertz spectroscopy techniques for explosives detection," *Anal. Bioanal. Chem.*, vol. 395, pp. 247–257, 2009.

[6] J. Federici, B. Schulkin, F. Huang, D. Gedy, R. Barat, F. Oliveira, and D. Zimdars, "THz imaging and sensing for security applications — explosives , weapons and drugs," *Semicond. Sci. Technol.*, vol. 20, pp. S266–S280, 2005.

[7] M. Yahyapour, N. Vieweg, T. Göbel, H. Roehle, and A. Deninger, "Non-Contact Contact Thickness Measurements with Terahertz Pulses," *Proc. World Conf. Non-Destructive Test.*, pp. 1–8, 2016.

[8] S. Krimi, J. Klier, J. Jonuscheit, G. Von Freymann, R. Urbansky, and R. Beigang, "Highly accurate thickness

measurement of multi-layered automotive paints using terahertz technology," *Appl. Phys. Lett.*, vol. 109, p. 21105, 2016.
[9] R. K. May, M. J. Evans, S. Zhong, I. A. N. Warr, L. F. Gladden, Y. Shen, and J. A. Zeitler, "Terahertz In-Line Sensor for Direct Coating Thickness Measurement of Individual Tablets During Film Coating in Real-Time," *J. Pharm. Sci.*, vol. 100, no. 4, pp. 1535–1544, 2011.
[10] K. Kawase, J. Shikata, and H. Ito, "Terahertz wave parametric source," *J. Phys. D. Appl. Phys.*, vol. 35, no. 3, pp. R1–R14, Feb. 2002.
[11] S. Hayashi, K. Nawata, K. Kawase, and H. Minamide, "Terahertz parametric oscillator sources," *Advanced Solid State Lasers, OSA Technical Digest (online) paper AW2A.1. Optical Society of America*, 2014.
[12] A. Lee, Y. He, and H. Pask, "Frequency-tunable THz source based on stimulated polariton scattering in Mg:LiNbO3," *IEEE J. Quantum Electron.*, vol. 49, no. 3, pp. 357–364, 2013.
[13] W. Wang, Z. Cong, X. Chen, X. Zhang, Z. Qin, G. Tang, N. Li, C. Wang, and Q. Lu, "Terahertz parametric oscillator based on $KTiOPO_4$ crystal.," *Opt. Lett.*, vol. 39, no. 13, pp. 3706–3709, 2014.
[14] W. Wang, Z. Cong, Z. Liu, X. Zhang, Z. Qin, G. Tang, N. Li, Y. Zhang, and Q. Lu, "THz-wave generation via stimulated polariton scattering in $KTiOAsO_4$ crystal," *Opt. Express*, vol. 22, no. 14, pp. 17092–17098, 2014.
[15] T. A. Ortega, H. M. Pask, D. J. Spence, and A. J. Lee, "Stimulated polariton scattering in an intracavity $RbTiOPO_4$ crystal generating frequency-tunable THz output," *Opt. Express*, vol. 24, no. 10, pp. 10254–10264, 2016.
[16] K. Kawase, J. Shikata, H. Minamide, K. Imai, and H. Ito, "Arrayed silicon prism coupler for a terahertz-wave parametric oscillator," *Appl. Opt.*, vol. 40, no. 9, pp. 1423–1426, 2001.
[17] T. Ikari, X. Zhang, and H. Minamide, "THz-wave parametric oscillator with a surface- emitted configuration," *Opt. Express*, vol. 14, no. 4, pp. 1604–1610, 2006.
[18] T. Edwards, D. Walsh, M. Spurr, C. Rae, M. Dunn, and P. Browne, "Compact source of continuously and widely-tunable terahertz radiation," *Opt. Express*, vol. 14, no. 4, pp. 1582–1589, 2006.
[19] D. J. M. Stothard, T. J. Edwards, D. Walsh, C. L. Thomson, C. F. Rae, M. H. Dunn, and P. G. Browne, "Line-narrowed, compact, and coherent source of widely tunable terahertz radiation," *Appl. Phys. Lett.*, vol. 92, no. 14, pp. 3–5, 2008.
[20] Y. Wang, Z. Li, J. Li, C. Yan, T. Chen, D. Xu, W. Shi, H. Feng, and J. Q. Yao, "Energy scaling of a tunable terahertz parametric oscillator with a surface emitted configuration," *Laser Phys.*, vol. 24, no. 12, p. 125402, 2014.
[21] T. Ortega, H. Pask, D. Spence, and A. Lee, "THz polariton laser using an intracavity Mg : LiNbO 3 crystal with protective Teflon coating," *Opt. Express*, vol. 25, no. 4, pp. 1604–1610, 2017.
[22] A. Hildenbrand, F. Wagner, J. Y. Natoli, M. Commandré, H. Albrecht, and F. Theodore, "Laser damage investigation in RbTiOPO4 crystals: A study on the anisotropy of the laser induced damage threshold," *Laser-Induced Damage Opt. Mater.*, vol. 6403, no. 0, p. 64031W, 2006.
[23] I. Hosako, N. Sekine, M. Patrashin, S. Saito, K. Fukunaga, Y. Kasai, P. Baron, T. Seta, J. Mendrok, S. Ochai and H. Yasuda, "At the dawn of a new era in terahertz technology," *Proc. IEEE*, vol. 95, no. 8, pp. 1611-1623, 2007.
[24] A. Siegman, *Lasers*. University Science Books, 1986.
[25] I. V. Hertel and C. P. Schulz, "Coherence and Photons," in *Atoms, Molecules and Optical Physics 2. Graduate Texts in Physics*. Springer, Berlin, Heidelberg, 2015.
[26] D. Walsh, "Intracavity Terahertz Optical Parametric Oscillators," (Doctoral dissertation). University of St. Andrews, 2010.

Tiago A. Ortega was born and educated in Brazil, receiving his Bachelor's degree in Physics and MSc. in Applied Physics from University of Sao Paulo, Sao Carlos, Brazil, in 2007 and 2011, respectively.

He worked on the development of solid state lasers and optical systems for the medical industry from 2007 to 2014, and currently is a Ph.D. at Macquarie University, working on the development of compact and frequency-tunable THz polariton lasers.

Tiago is the recipient of a scholarship from the Commonwealth of Australia under the Research Training Program (RTP) scheme.

Helen Pask was awarded a Ph.D. in Physics by Macquarie University, Sydney, Australia in 1992. She currently holds an Australian Research Council Future Fellowship at Macquarie University, with research interests in crystalline Raman lasers, THz generation and applications, remote sensing, and Raman spectroscopy.

David J. Spence was born in Birmingham, U.K., in 1975. He received the M.Phys. and D.Phil. degrees in Physics from Oxford University, Oxford, U.K., in 1997 and 2001, respectively.

After a year in industry and two years as a Research Assistant at Oxford, he moved to Sydney, Australia in 2004. Following an Australian Research Council Postdoctoral Fellowship, he won a Lectureship at Macquarie University, Sydney, where he is currently Associate Professor. His research interests include lasers and nonlinear optics, including Raman lasers and frequency conversion, and visible and ultraviolet laser materials.

Andrew J. Lee received his Bachelor's degree (Honours First Class) in optoelectronics and the Ph.D. degree in Physics from Macquarie University, Sydney, Australia, in 2001 and 2007, respectively.

He is currently a Macquarie University Vice-Chancellors

Innovation Fellow at Macquarie University. His current research interests include development of high-power THz sources and their applications; development of high-power continuous wave Raman lasers and vortex lasers.

A.5. Optical coatings for 1064 nm fundamental field

This appendix contains the transmission spectra for the laser mirrors utilised for the fundamental and Stokes resonators operating with a 1064 nm fundamental field. Initially the output coupler OC1 was being utilised, when competition effects were identified as reported in Section 4.2. A new output coupler OC2 was specified and resulted in a pure 1064 nm and Stokes fields as reported from Section 4.3.

Summary of the laser mirrors utilised in 1064 nm fundamental and Stokes resonators.

Mirror			Specification	Manufacturer
Fundamental resonator	M1		HR>99.9%@1064 nm HT>98%@808 nm	ATF
	M2	OC1	98.5%<R<99.5%@1064 nm	CVI
		OC2	98.5%<R<99.5%@1064 nm HT>40%@1090-1200 nm	LASEROPTIK
Stokes resonator	M3		HR>99.99%@1064 nm	ATF
	M4		HR>99.9%@1064 nm	VLOC

M1 and M3 mirror coatings

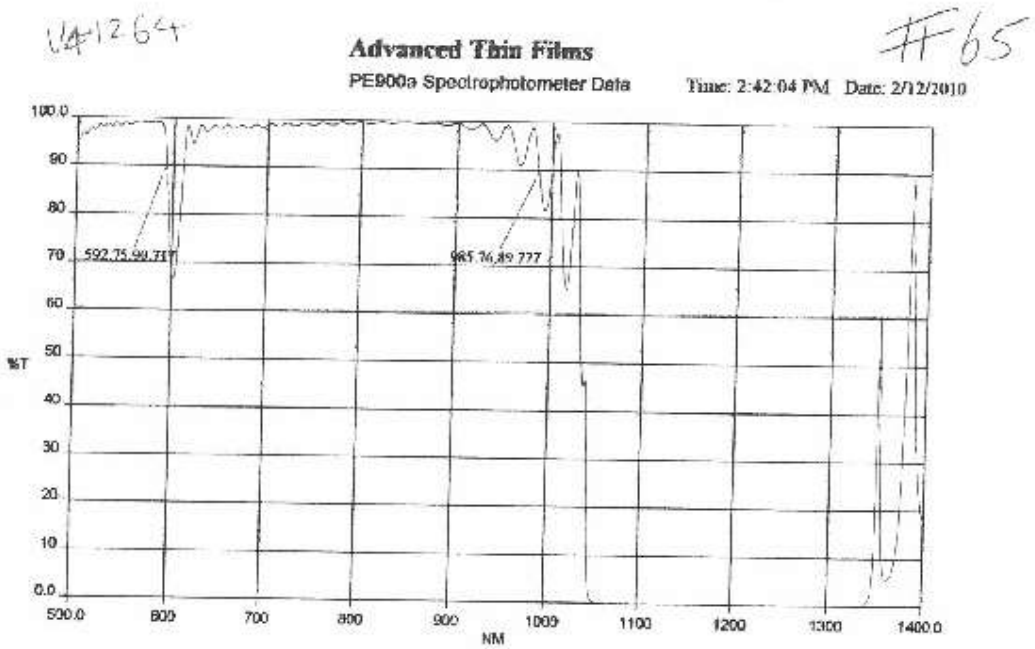

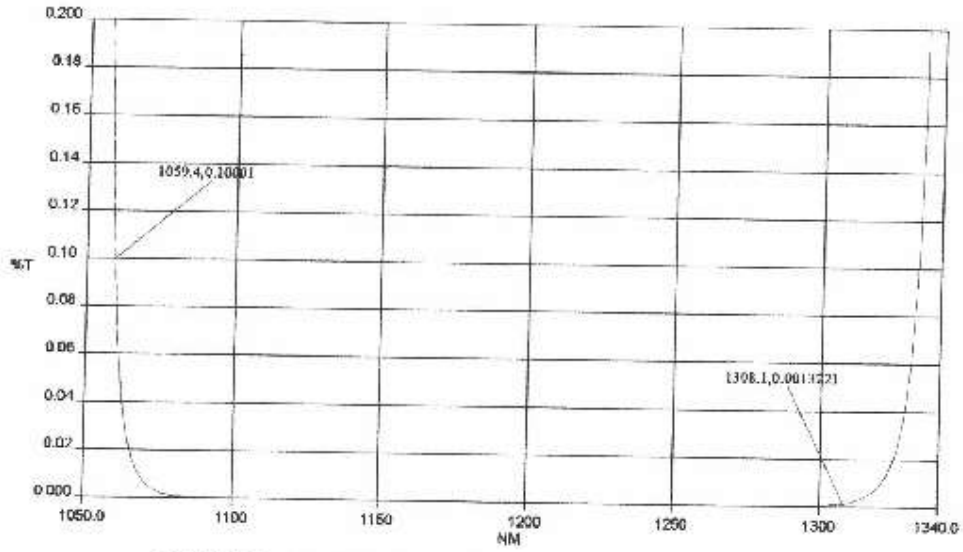

M4 mirror coatings

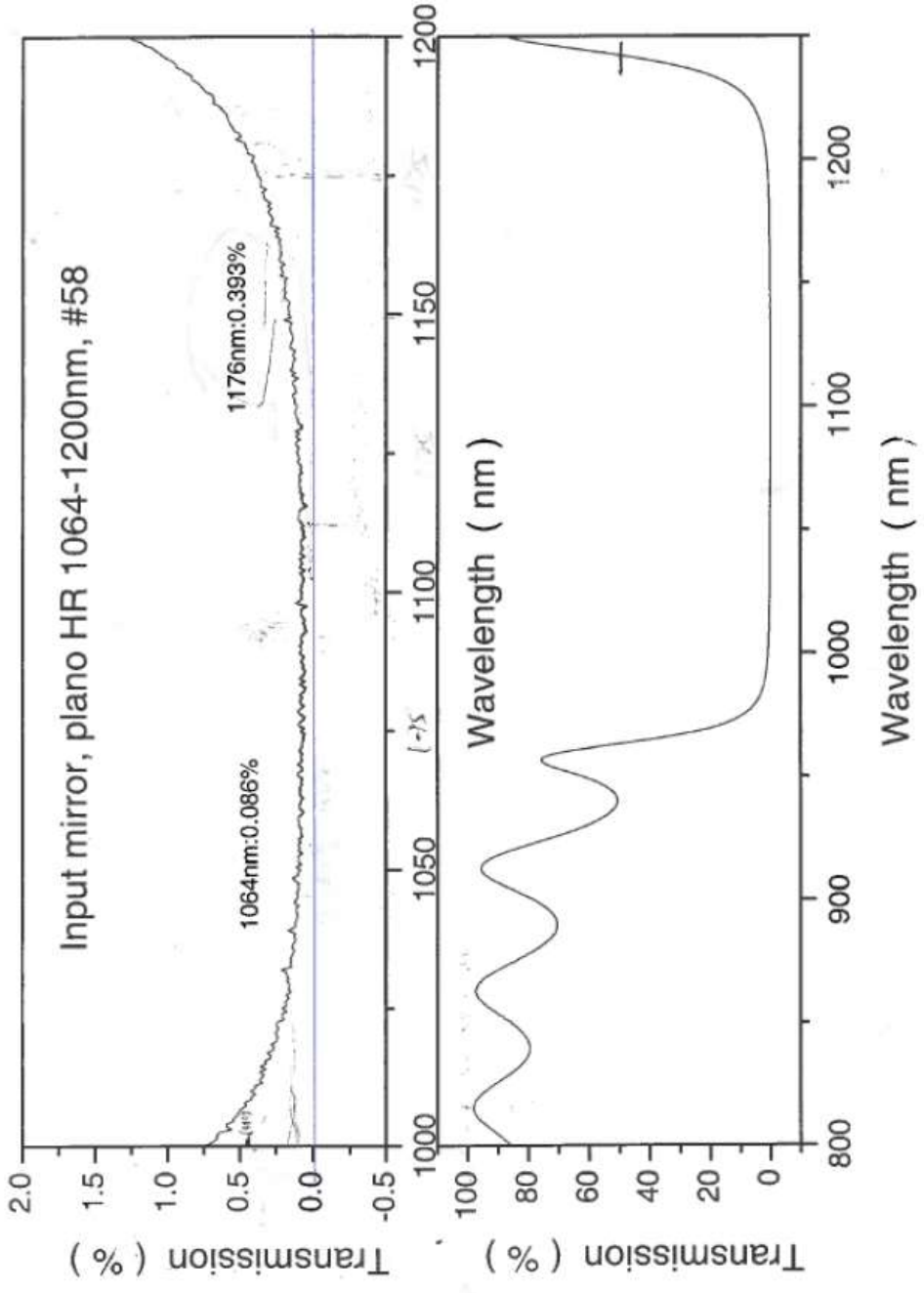

M2 (OC1) – Initial output coupler for 1064 nm fundamental field

MACQUARIE UNIV
Part PR1-1064-99-1025-1.00CC
PO F15P4-0219

Side 1-99.149664 %
R >98.5 %, and < 99.5 %at 1064Side 1
Pol N/A
AOI 0 deg

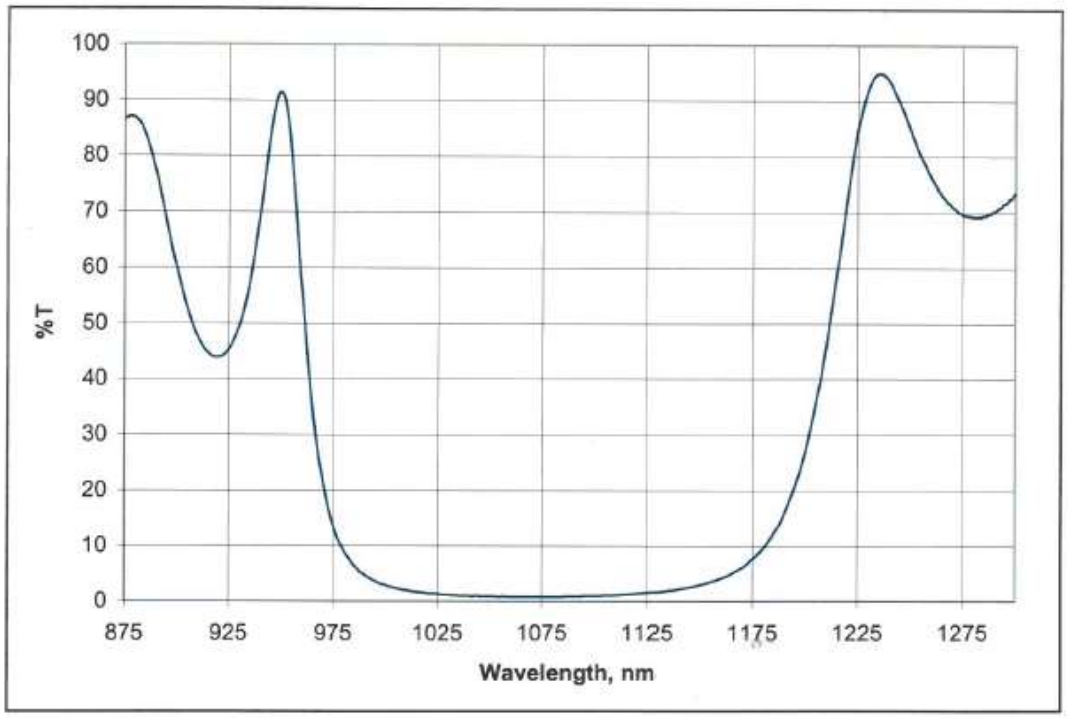

M2 (OC2) – New design for output coupler for 1064 nm fundamental field

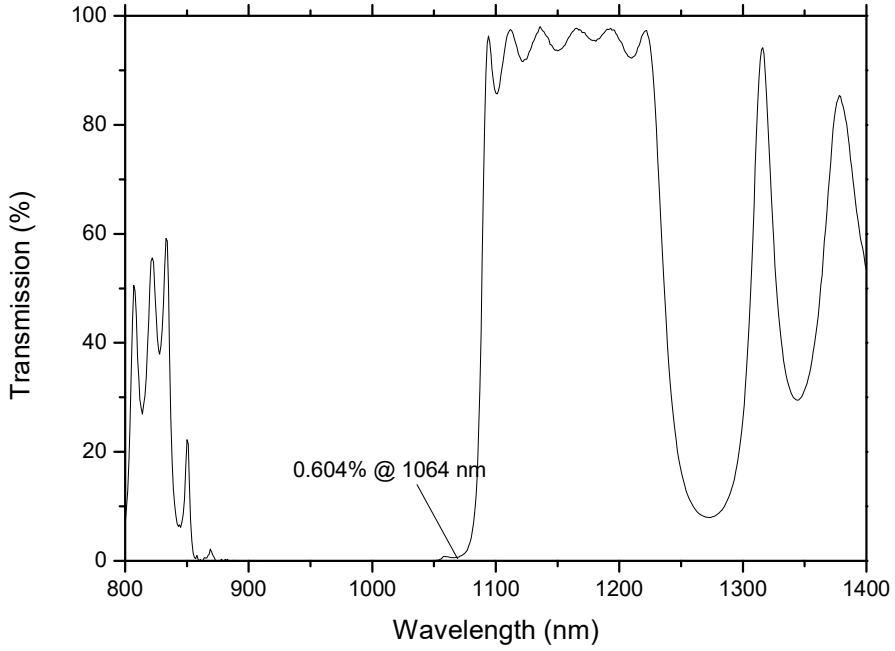

A.6. Optical coatings for 1342 nm fundamental field

This appendix contains the transmission spectra for the laser mirrors utilised for the fundamental and Stokes resonators operating with a 1342 nm fundamental field reported in Section 4.4.3.

Summary of the laser mirrors utilised in 1064 nm fundamental and Stokes resonators.

Mirror		Specification	Manufacturer
Fundamental resonator	M5	HR>99.9%@1342 nm HT>95%@1064 nm HT>99%@808 nm	Layertec
	M6	HR>99%@1280 – 1520 nm	
Stokes resonator	M7, M8	HR>99%@1280 – 1520 nm	

M5 mirror coating for 1342 nm fundamental field

batch G0311036 - transmission measurement 0°

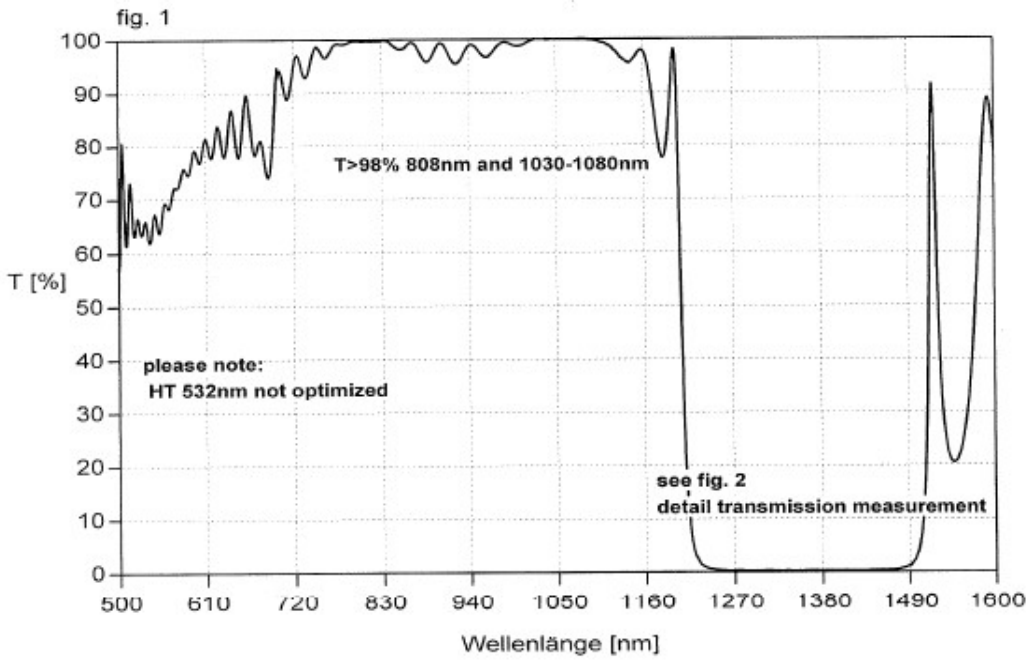

detail transmission HR-region

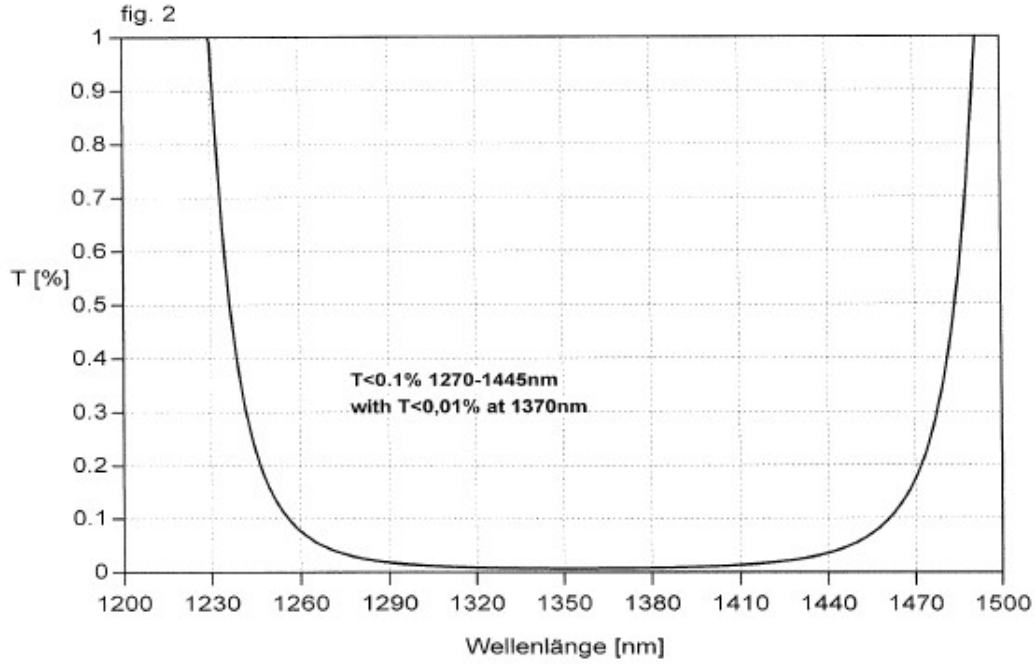

M6, M7 and M8 mirrors – Output coupler for 1342 nm fundamental field and Stokes mirrors

Layertec batch R0110002

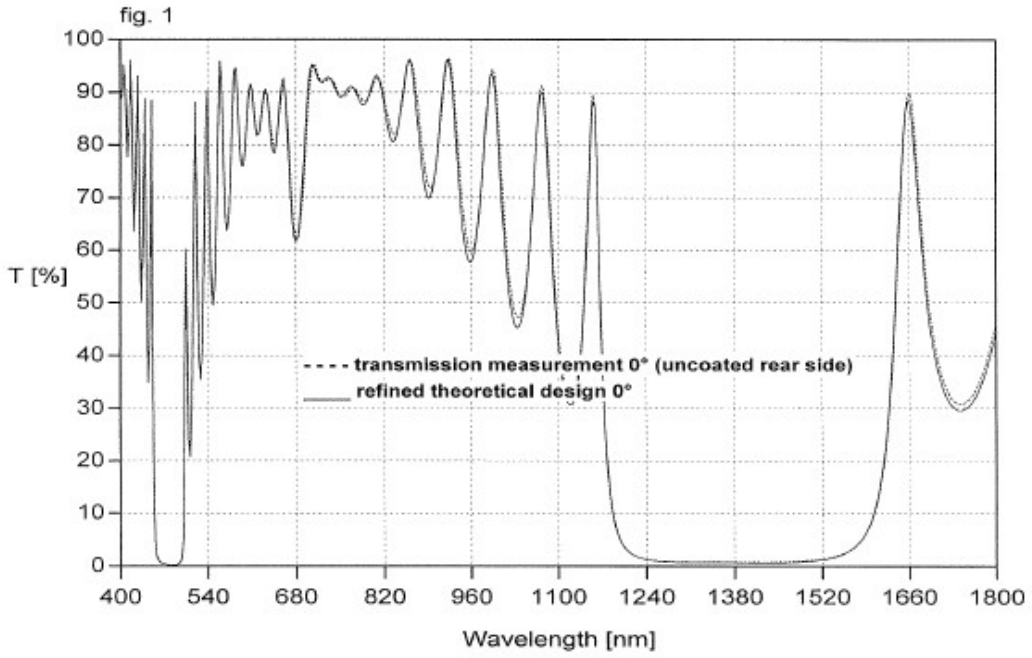

calculated reflection at 0° (based on refined th. design fig. 1)

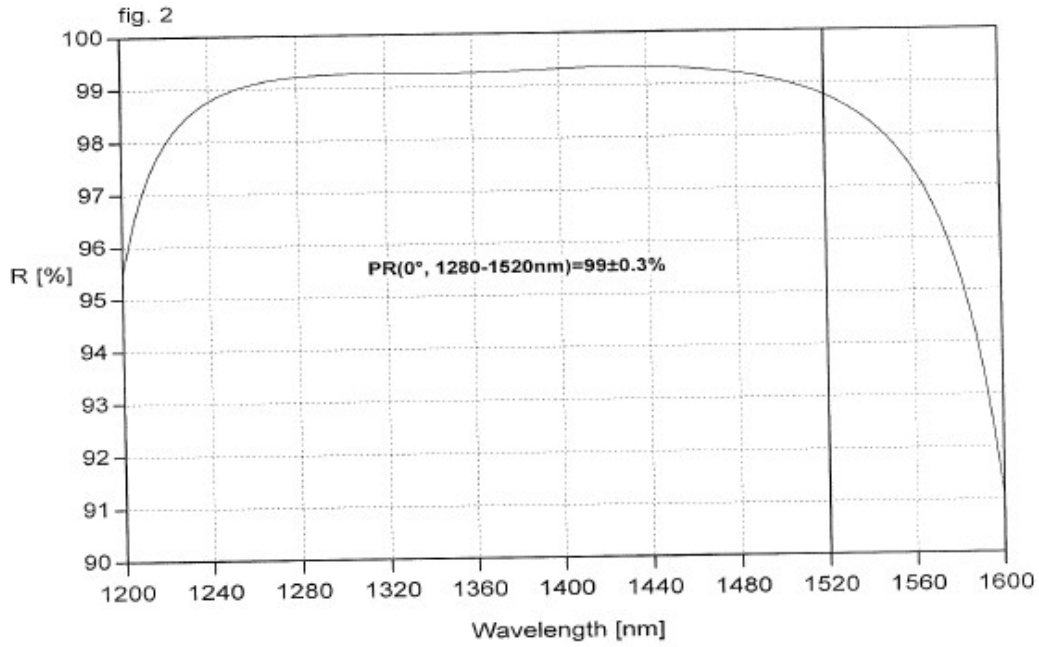

1520 nm : 98.765 %

A.7. Terahertz optics transmission curves

Bandpass filter LPF 14.3

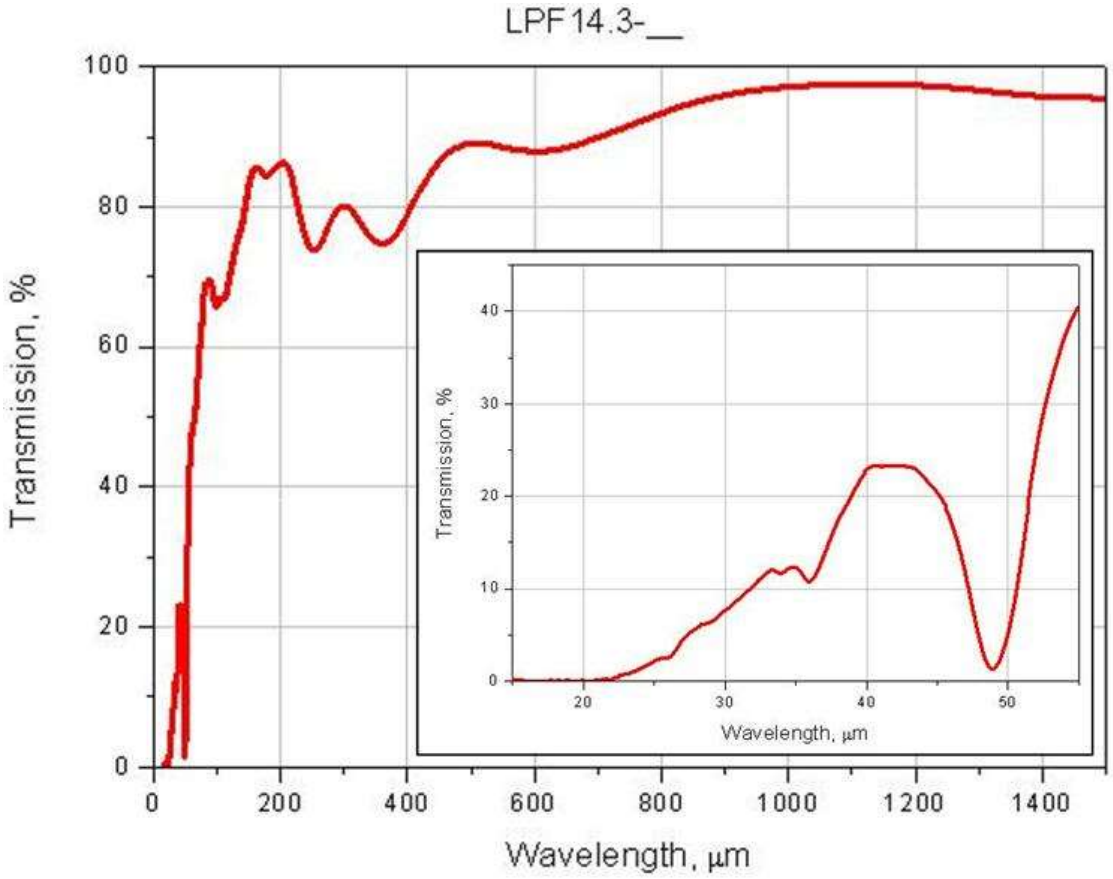

TPX window (2 mm thick)

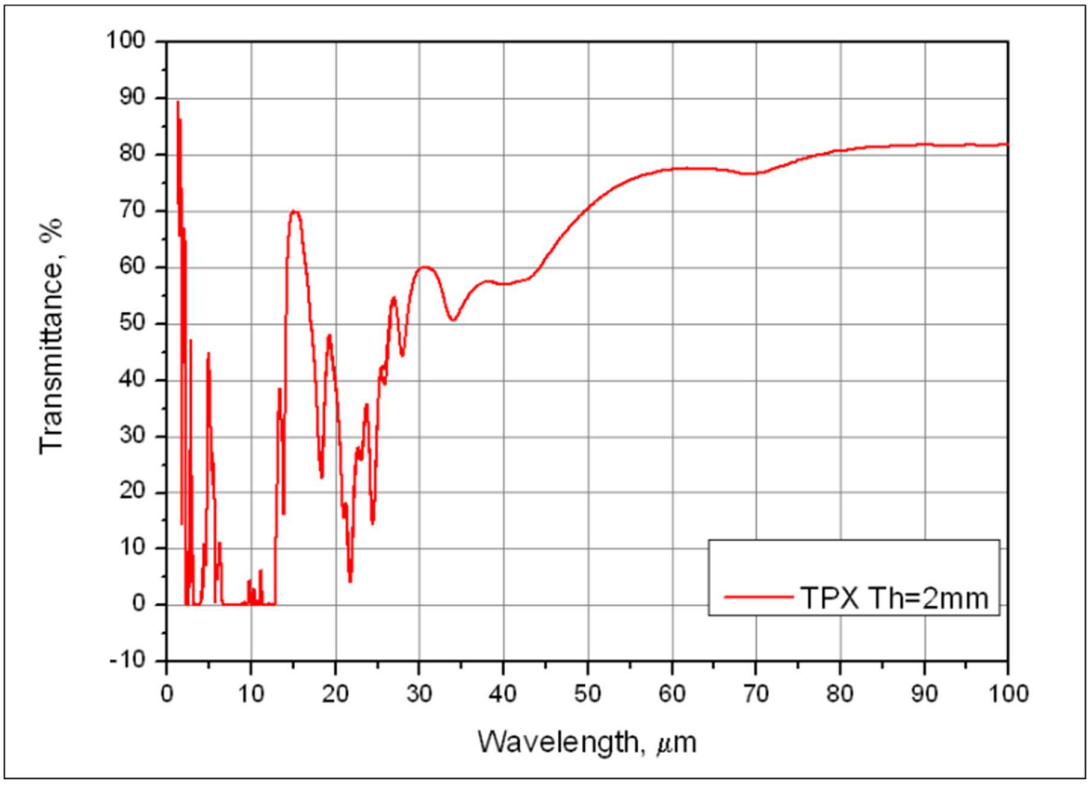

A.8. Matlab® codes

The same Matlab® algorithm was utilised to determine the oscillator strengths for all different SPS crystals, with the difference that each crystal had a different number of modes with specific positions and linewidths measured from their respective Raman spectra (Section 3.3). To simplify for the reader, only the codes for MgO:$LiNbO_3$ are detailed in this appendix because it is the material with the smaller number of modes, and consequently the smaller number of code lines. The same is valid for the codes to plot the dispersion curve, refractive index and absorption coefficient.

Genetic Algorithm

A genetic algorithm was written in Matlab® to determine the oscillator strengths according to the methodology described in Section 3.2. It is completely out of the scope of this thesis to provide a deep understanding of the programming tools, however a brief overview of the algorithm technique is provided to the reader.

The genetic algorithm is a clever programming tool for solving both constrained and unconstrained optimization problems, and it is based on 'natural selection'. The genetic algorithm starts with an initial set of individuals (initial population) which will be called the first generation. The population is then modified to create a new generation, and these modifications include *crossovers* (combining two 'parent' individuals to generate a 'child' for the next generation) and *mutations* (random changes to individuals). The new generation is compared with an optimization goal and *selection rules* are applied to appoint which individuals are best fitted. The genetic material of the best individuals is then utilised to start a new generation, and the iterative process continues until the population "evolves" towards an optimal solution. For more information on genetic algorithm the following literature is recommended:

[1] https://au.mathworks.com/help/gads/what-is-the-genetic-algorithm.html

[2] W. Banzhaf, P. Nordin and R. Keller, *Genetic Programming – An Introduction* (Morgan Kaufmann, 1998).

Genetic Algorithm to determine the oscillator strengths for MgO:LN

```
clear all;
close all;

FTIR=xlsread('LN'); %load FTIR data
FTIR_T=transpose(FTIR);
w=FTIR_T(1,:);
I=FTIR_T(2,:);

geracao=1; %generation=1 (first generation)
e_HF=4.6; %initial guess for the high frequency component of the dielectric
function

%mode position measured from Raman spectra
W1=254;
W2=268;
W3=325;
W4=632;

%linewidth measured from Raman spectra
L1=17;
L2=20;
L3=31;
L4=29;

%Initial guess for oscilator strength
S1=16;
S2=0.5;
S3=0.15;
S4=2.5;

%variable limits
S_min=0;
S_max=1;
Sm_max=5;
Ss_max=30;
eHF_min=0;
eHF_max=10;
max_lim=[Ss_max Sm_max S_max Ss_max eHF_max];
min_lim=[S_min S_min S_min S_min eHF_min];

%creates 15 random individuals and calculates A and the error for each
individual
for i=1:15
    coef1=rand(1,5);
    coef(i,:)=[S_min+(Ss_max-S_min)*coef1(1) S_min+(Sm_max-S_min)*coef1(2)
S_min+(S_max-S_min)*coef1(3) S_min+(Ss_max-S_min)*coef1(4)
eHF_min+(eHF_max-eHF_min)*coef1(5)];
    A(i,:)=abs((sqrt(coef(i,5)+(coef(i,1)*W1.^2)./(W1.^2-w.^2-
1i*w*L1)+(coef(i,2)*W2.^2)./(W2.^2-w.^2-1i*w*L2)+(coef(i,3)*W3.^2)./(W3.^2-
w.^2-1i*w*L3)+(coef(i,4)*W4.^2)./(W4.^2-w.^2-1i*w*L4))-
1)./(sqrt(coef(i,5)+(coef(i,1)*W1.^2)./(W1.^2-w.^2-
1i*w*L1)+(coef(i,2)*W2.^2)./(W2.^2-w.^2-1i*w*L2)+(coef(i,3)*W3.^2)./(W3.^2-
w.^2-1i*w*L3)+(coef(i,4)*W4.^2)./(W4.^2-w.^2-1i*w*L4))+1)).^2;
    Erro(i)=sum(abs(I-A(i,:)));
end
```

```
%Veryfies which 2 individuals exhibited lower errors and stores them in
index1 and index2
erro_total=inf;
erro_menor=inf;
i_plot=1001;
while erro_total>25 %relative error to be minimised; adjustable parameter

    if erro_menor>erro_total
       erro_menor=erro_total;
       i_plot=1001;
    end

   geracao=geracao+1;

     if erro_total<50
            peso_mutacao=0.005;
        else if erro_total<100
                peso_mutacao=0.01;
            else
                peso_mutacao=0.05;
            end
        end

    index1=0;
    index2=0;
    erro_max=inf;
    erro_total=min(Erro);
    for i=1:15
        if(Erro(i)<erro_max)
          index1=i;
          erro_max=Erro(i);
          erro_k=erro_max;
          coef_salvo=coef(index1,:);
        end
    end
    Erro(index1)=inf;
    erro_max=inf;
    for i=1:15
        if(Erro(i)<erro_max)
          index2=i;
          erro_max=Erro(i);
        end
    end

    %Generates a cross-link individual from  index1 and index2
    clear Erro A coef_permut;
    coef_permut(1,:)=[coef(index1,1) coef(index2,2) coef(index1,3)
coef(index2,4) coef(index1,5)];

    A(i,:)=abs((sqrt(coef_permut(1,5)+(coef_permut(1,1)*W1.^2)./(W1.^2-
w.^2-1i*w*L1)+(coef_permut(1,2)*W2.^2)./(W2.^2-w.^2-
1i*w*L2)+(coef_permut(1,3)*W3.^2)./(W3.^2-w.^2-
1i*w*L3)+(coef_permut(1,4)*W4.^2)./(W4.^2-w.^2-1i*w*L4))-
1)./(sqrt(coef_permut(1,5)+(coef_permut(1,1)*W1.^2)./(W1.^2-w.^2-
1i*w*L1)+(coef_permut(1,2)*W2.^2)./(W2.^2-w.^2-
1i*w*L2)+(coef_permut(1,3)*W3.^2)./(W3.^2-w.^2-
1i*w*L3)+(coef_permut(1,4)*W4.^2)./(W4.^2-w.^2-1i*w*L4))+1)).^2;
    Erro(1)=sum(abs(I-A(1,:)));
    %generates 14 new mutations
    for i=2:15
```

```
        coef1=rand(1,5);
        coef_aux1=[S_min+(Ss_max-S_min)*coef1(1) S_min+(Sm_max-
S_min)*coef1(2) S_min+(S_max-S_min)*coef1(3) S_min+(Ss_max-S_min)*coef1(4)
eHF_min+(eHF_max-eHF_min)*coef1(5)];
        coef_aux2_meta = rand(1, 5) < 0.5;
        for j=1:5
            if coef_aux2_meta(j)==0
                coef_aux2(j)=-1;
            else
                coef_aux2(j)=1;
            end
        end

coef_permut(i,:)=coef_permut(1,:)+(coef_aux1.*coef_aux2*peso_mutacao);

        for d=1:5
            if coef_permut(i,d)>max_lim(d);
                coef_permut(i,d)=max_lim(d);
            end
               if coef_permut(i,d)<min_lim(d);
                   coef_permut(i,d)=min_lim(d);
            end
        end

        A(i,:)=abs((sqrt(coef_permut(i,5)+(coef_permut(i,1)*W1.^2)./(W1.^2-
w.^2-1i*w*L1)+(coef_permut(i,2)*W2.^2)./(W2.^2-w.^2-
1i*w*L2)+(coef_permut(i,3)*W3.^2)./(W3.^2-w.^2-
1i*w*L3)+(coef_permut(i,4)*W4.^2)./(W4.^2-w.^2-1i*w*L4))-
1)./(sqrt(coef_permut(i,5)+(coef_permut(i,1)*W1.^2)./(W1.^2-w.^2-
1i*w*L1)+(coef_permut(i,2)*W2.^2)./(W2.^2-w.^2-
1i*w*L2)+(coef_permut(i,3)*W3.^2)./(W3.^2-w.^2-
1i*w*L3)+(coef_permut(i,4)*W4.^2)./(W4.^2-w.^2-1i*w*L4))+1)).^2;
        Erro(i)=sum(abs(I-A(i,:)));
    end
    clear coef;
    coef=coef_permut;
    disp(sprintf('Menor Erro = %d, Erro = %d,
geracao=%d',erro_menor,erro_total,geracao));

end

%Final values calculated for the oscillator strengths
S1_empirico=coef_salvo(1);
S2_empirico=coef_salvo(2);
S3_empirico=coef_salvo(3);
S4_empirico=coef_salvo(4);
e_HF_empirico=coef_salvo(5);

%Theoretical FTIR spectra calculated with mode postion and linewidth from
%Raman and calculated oscillator strengths
A_empirico=abs((sqrt(e_HF_empirico+(S1_empirico*W1.^2)./(W1.^2-w.^2-
1i*w*L1)+(S2_empirico*W2.^2)./(W2.^2-w.^2-
1i*w*L2)+(S3_empirico*W3.^2)./(W3.^2-w.^2-
1i*w*L3)+(S4_empirico*W4.^2)./(W4.^2-w.^2-1i*w*L4))-
1)./(sqrt(e_HF_empirico+(S1_empirico*W1.^2)./(W1.^2-w.^2-
1i*w*L1)+(S2_empirico*W2.^2)./(W2.^2-w.^2-
1i*w*L2)+(S3_empirico*W3.^2)./(W3.^2-w.^2-
1i*w*L3)+(S4_empirico*W4.^2)./(W4.^2-w.^2-1i*w*L4))+1)).^2;
erro_final=sum(abs(I-A_empirico))
```

```
 plot(w,I,'b')%plot experimental FTIR
 hold on;
 plot(w,A_empirico,'r')%plot calculated FTIR spectra with calculated
oscillator strenghts
```

Algorithm to calculate dispersion curve:

```
clear all;
close all;

FFTIR=xlsread('LN_Dispersion');
FTIR_T=transpose(FTIR);%load FTIR data
w=FTIR_T(1,:);%range of wavenumbers from 1-650cm-1 with same step size as
FTIR spectra
e_inf=4.2; %epslon_infinity obtained from model

%mode position measured from Raman spectra
W1=254;
W2=268;
W3=325;
W4=632;

%linewidth measured from Raman spectra
L1=17;
L2=20;
L3=31;
L4=29;

%calculated oscilator strengths
S1=19.89;
S2=1.30;
S3=0.52;
S4=4.42;

%'Theta-lines' parameters
f=1064.43E-9;%fundamental wavelength
wf=0.01/f;%fundamental frequency in wavenumbers
s=1./(100*(wf-w));%stokes wavlength
ws=0.01./s;%Stokes frequency in wavenumber
a=2.4272;%Sellmeier coefficient
b=0.01478; %Sellmeier coefficient
c=1.4617; %Sellmeier coefficient
d=0.05612; %Sellmeier coefficient
e=9.6536; %Sellmeier coefficient
F=371.216; %Sellmeier coefficient

%calculation of sqrt of dielectric funcion 'epslon' and wavevector 'k'
epslon=sqrt(e_inf+(S1*W1.^2)./(W1.^2-w.^2-1i*w*L1)+(S2*W2.^2)./(W2.^2-w.^2-
1i*w*L2)+(S3*W3.^2)./(W3.^2-w.^2-1i*w*L3)+(S4*W4.^2)./(W4.^2-w.^2-
1i*w*L4));
k=real(2*pi.*w.*epslon);

%calculation of near-infrared refractive indicessing Sellmeier equation
%from ZELMON at. al., JOSAB 14(12) 1997
nf=sqrt(1+a*(f*1000000)^2/((f*1000000)^2-b)+c*(f*1000000)^2/((f*1000000)^2-
d)+e*(f*1000000)^2/((f*1000000)^2-F));%refractive index at 1064nm
ns=sqrt(1+a*(s*1000000).^2./((s*1000000).^2-
b)+c*(s*1000000).^2/((s*1000000).^2-d)+e*(s*1000000).^2/((s*1000000).^2-
F));%refractive index at Stokes wavelength


%calculation of 'theta-curves' - phase matching curves
k0=sqrt(4*pi^2*(wf*nf-ws.*ns).^2+8*pi^2*wf.*ws*nf.*ns*(1-cos(0)));%phase-
matching curve at zero degrees
```

```
k1=sqrt(4*pi^2*(wf*nf-ws.*ns).^2+8*pi^2*wf.*ws*nf.*ns*(1-
cos(1*pi/180)));%phase-matching curve at one degree
k2=sqrt(4*pi^2*(wf*nf-ws.*ns).^2+8*pi^2*wf.*ws*nf.*ns*(1-
cos(2*pi/180)));%phase-matching curve at two degrees
k3=sqrt(4*pi^2*(wf*nf-ws.*ns).^2+8*pi^2*wf.*ws*nf.*ns*(1-
cos(3*pi/180)));%phase-matching curve at three degrees
k4=sqrt(4*pi^2*(wf*nf-ws.*ns).^2+8*pi^2*wf.*ws*nf.*ns*(1-
cos(4*pi/180)));%phase-matching curve at four degrees
k5=sqrt(4*pi^2*(wf*nf-ws.*ns).^2+8*pi^2*wf.*ws*nf.*ns*(1-
cos(5*pi/180)));%phase-matching curve at five degrees

%plot of dispersion curve and phase-matching curves
f1=figure;
 plot(w,I,'b')
 f2=figure;
 plot(k,w,'r')
 hold on
 plot(k0,w,'k')
 hold on
 plot(k1,w,'b')
 hold on
 plot(k2,w,'m')
 hold on
 plot(k3,w,'g')
 hold on
 plot(k4,w,'y')
 hold on
 plot(k5,w,'c')
 hold on
```

Algorithm to calculate the refractive index:

```
clear all;
close all;

FTIR=xlsread('LN_Dispersion');
FTIR_T=transpose(FTIR);%load FTIR data
w=FTIR_T(1,:);%range of wavenumbers from 1-650cm-1 with same step size as
FTIR spectra
e_inf=4.2; %epslon_infinity obtained from model

%mode position measured from Raman spectra
W1=254;
W2=268;
W3=325;
W4=632;

%linewidth measured from Raman spectra
L1=17;
L2=20;
L3=31;
L4=29;

%calculated oscilator strengths
S1=19.89;
S2=1.30;
S3=0.52;
S4=4.42;

%calculation of sqrt of dielectric funcion 'epslon' and ref index 'n'
epslon=sqrt(e_inf+(S1*W1.^2)./(W1.^2-w.^2-1i*w*L1)+(S2*W2.^2)./(W2.^2-w.^2-
1i*w*L2)+(S3*W3.^2)./(W3.^2-w.^2-1i*w*L3)+(S4*W4.^2)./(W4.^2-w.^2-
1i*w*L4));
n=real(epslon);

%Plot the calculated refractive index
f1=figure;
 plot(n,w,'r')
 hold on
```

Algorithm to calculate the THz absorption coefficient (α_T):

```
clear all;
close all;

FTIR=xlsread('LN_Dispersion');
FTIR_T=transpose(FTIR);%load FTIR data
w=FTIR_T(1,:);%range of wavenumbers from 1-650cm-1 with same step size as
FTIR spectra
e_inf=4.2; %epslon_infinity obtained from model

%mode position measured from Raman spectra
W1=254;
W2=268;
W3=325;
W4=632;

%linewidth measured from Raman spectra
L1=17;
L2=20;
L3=31;
L4=29;

%calculated oscilator strengths
S1=19.89;
S2=1.30;
S3=0.52;
S4=4.42;

%calculation of sqrt of dielectric funcion 'epslon' and absorption 'Abs'
epslon=sqrt(e_inf+(S1*W1.^2)./(W1.^2-w.^2-1i*w*L1)+(S2*W2.^2)./(W2.^2-w.^2-
1i*w*L2)+(S3*W3.^2)./(W3.^2-w.^2-1i*w*L3)+(S4*W4.^2)./(W4.^2-w.^2-
1i*w*L4));
Abs=2*imag(2*pi.*w.*epslon);

%Plot the calculated absorption coefficient
f1=figure;
 plot(Abs,w,'r')
 hold on
```

A.9. Polarised Raman at $Y(XX)\bar{Y}$ and FTIR spectra at $(\vec{E} \perp c)$ configurations

Magnesium oxide-doped lithium niobate - $MgO:LiNbO_3$:

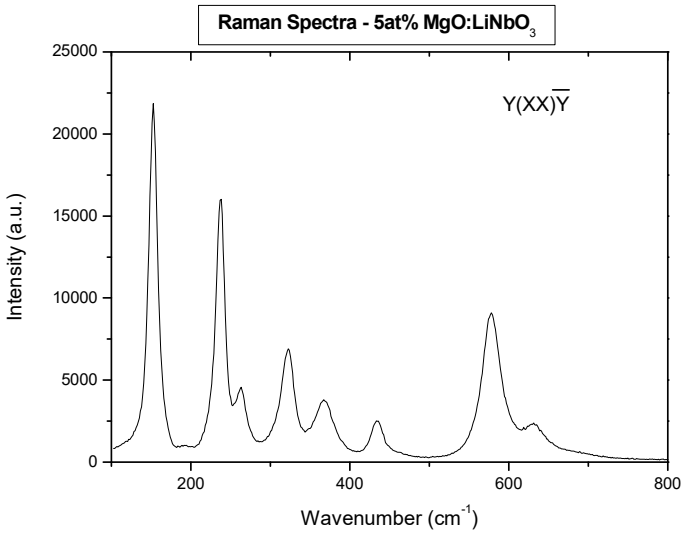

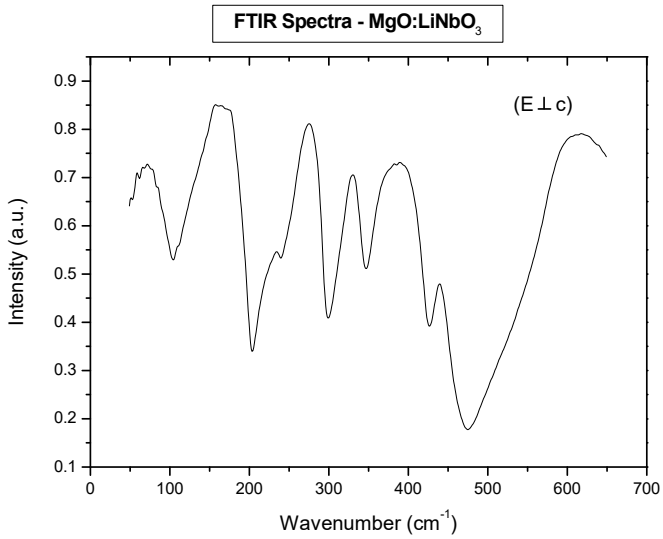

Table A.1 – Mode location (ω_{0j}) and linewidth (Γ_{0j}) in 5 at.% $MgO:LiNbO_3$ extracted from polarised Raman spectra in $Y(XX)\bar{Y}$ configuration $(\vec{E} \perp c)$.

Mode location, ω_{0j} (± 1 cm^{-1})	**Linewidth, Γ_{0j} (± 1 cm^{-1})**
152	12
238	16
263	18
322	24
367	32
434	20
578	30
631	26

Potassium titanyl phosphate - $KTiOPO_4$:

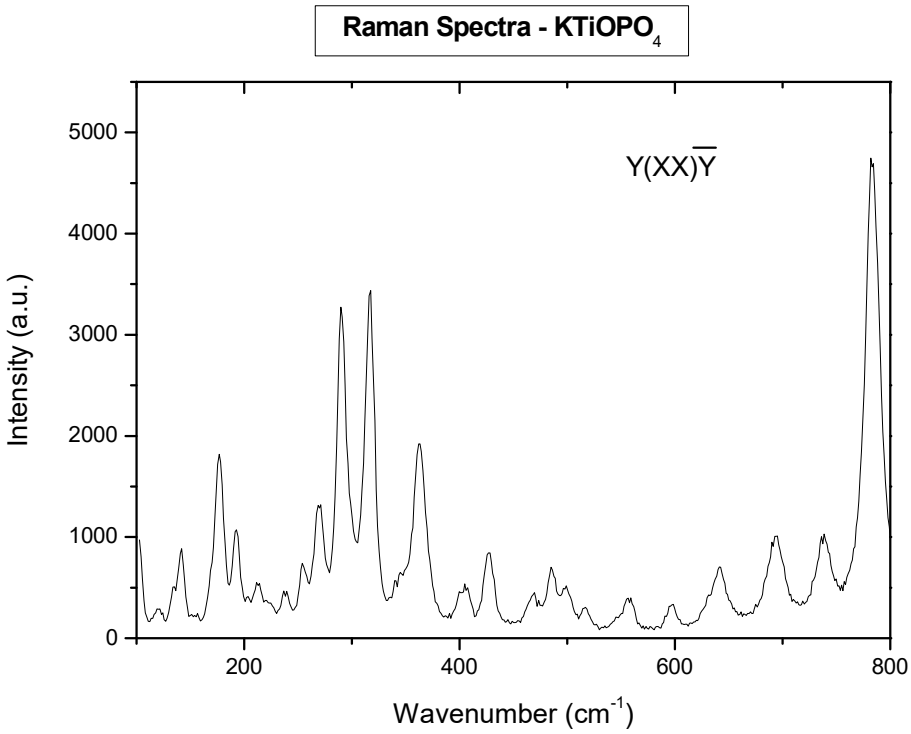

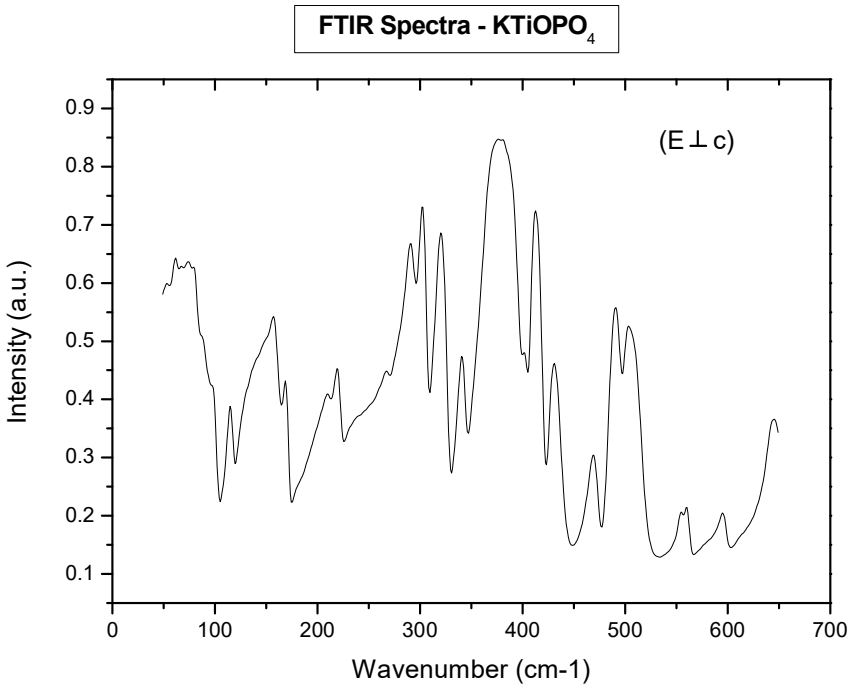

Table A.2 – Mode location (ω_{0j}) and linewidth (Γ_{0j}) in $KTiOPO_4$ extracted from polarised Raman spectra in $Y(XX)\bar{Y}$ configuration $(\vec{E} \perp c)$.

Mode location, ω_{0j} ($\pm$1 cm^{-1})	**Linewidth, Γ_{0j} ($\pm$1 cm^{-1})**
103	6
141	8
176	10
192	8
212	8
238	8
253	4
269	5
289	8
317	10
362	18
404	8
427	12
469	10
484	6
498	6
516	10
557	14
597	16
641	24
694	20
737	16
783	18

Rubidium titanyl phosphate - $RbTiOPO_4$:

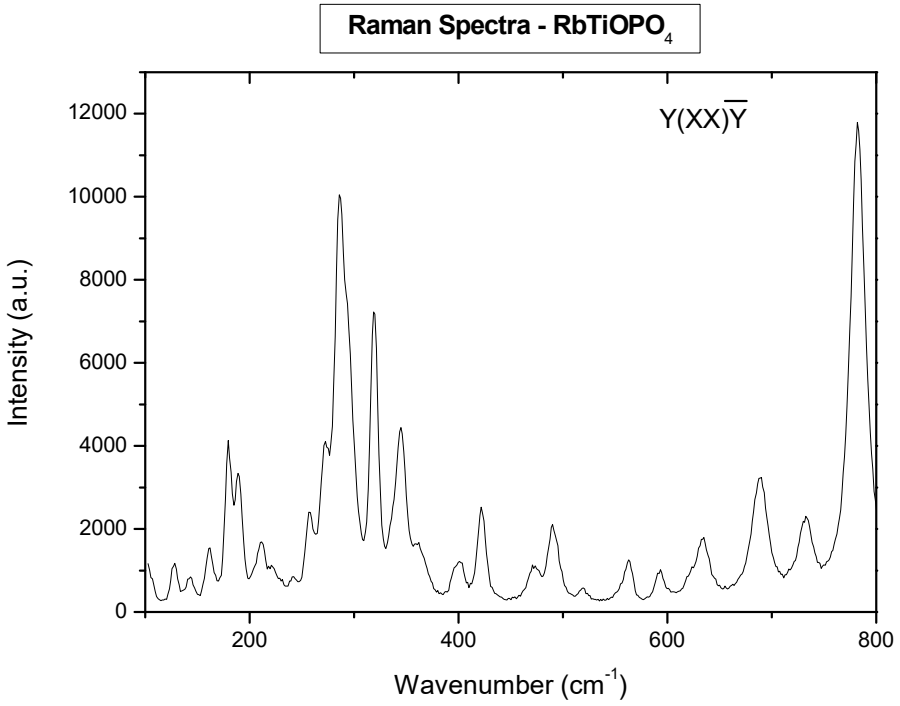

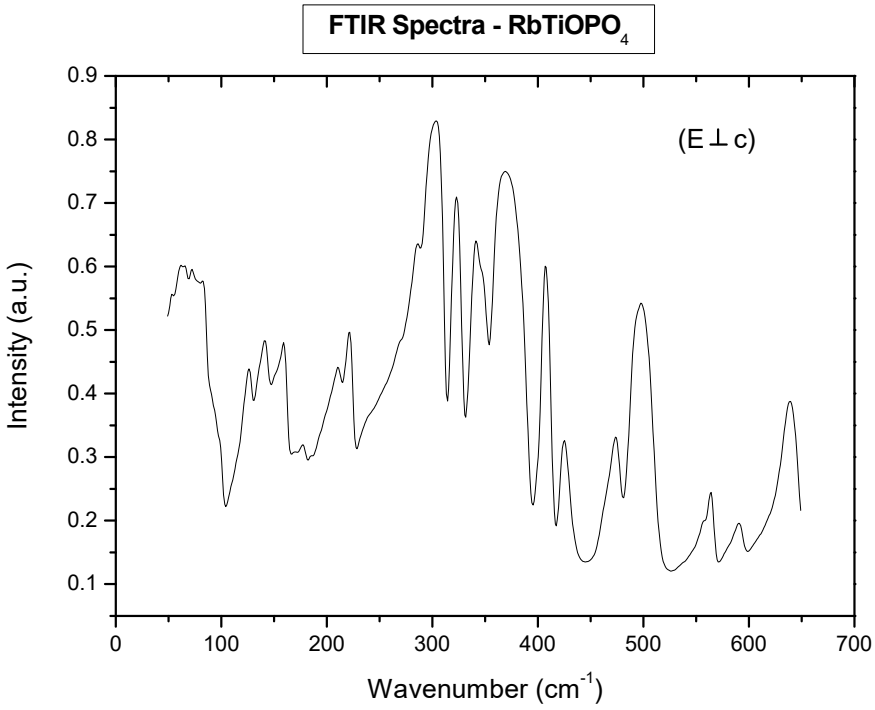

Table A.3 – Mode location (ω_{0j}) and linewidth (Γ_{0j}) in $RbTiOPO_4$ extracted from polarised Raman spectra in $Y(XX)\bar{Y}$ configuration $(\vec{E} \perp c)$.

Mode location, ω_{0j} (± 1 cm^{-1})	**Linewidth, Γ_{0j} (± 1 cm^{-1})**
128	8
143	4
157	8
179	8
189	10
211	10
257	6
272	4
285	10
293	14
319	6
344	10
400	18
421	8
471	15
489	14
518	7
562	12
593	10
634	15
688	18
732	16
782	20

A.10. Calculated absorption spectra of $MgO:LiNbO_3$, $KTiOPO_4$ and $RbTiOPO_4$

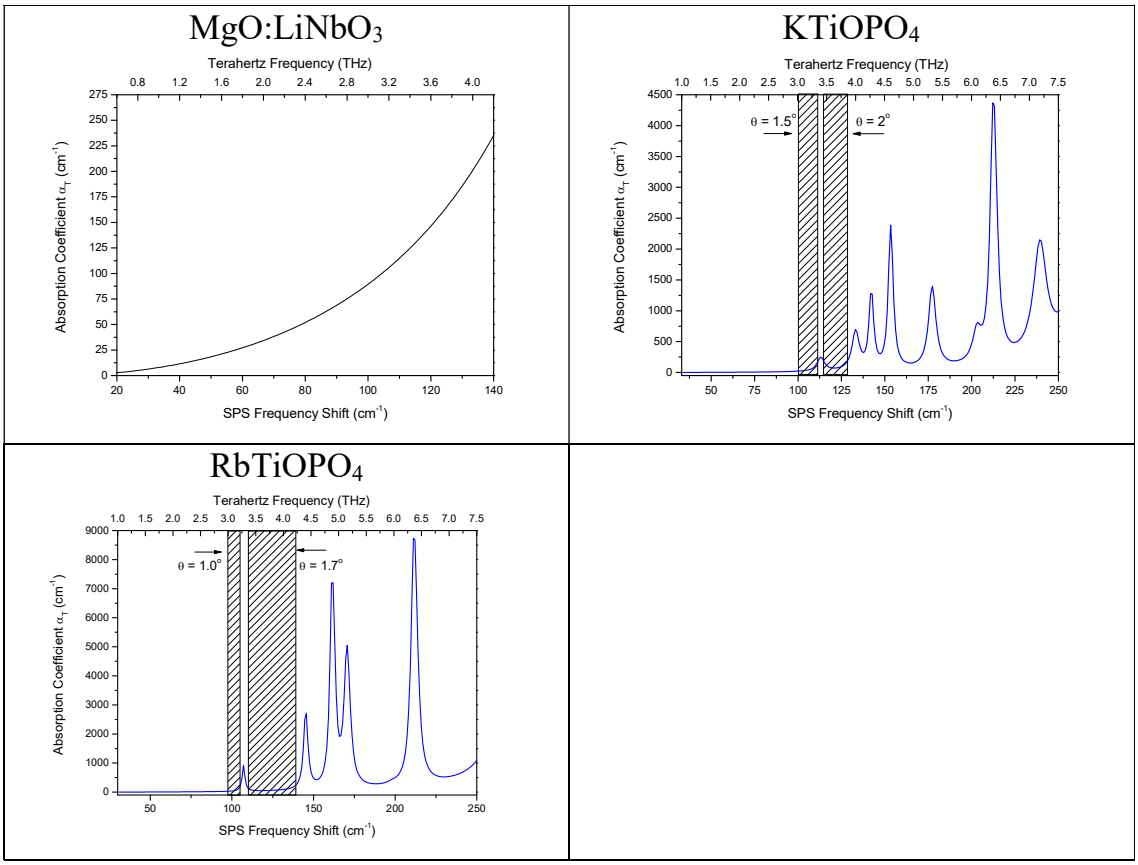

A.11. Liquid Teflon material datasheet

Safety Data Sheet

Chemours™

AF Amorphous Fluoroplastic Solutions

Version 3.0

Revision Date 12/19/2015 Ref. 150000000912

This SDS adheres to the standards and regulatory requirements of the United States and may not meet the regulatory requirements in other countries.

SECTION 1. PRODUCT AND COMPANY IDENTIFICATION

Product name	:	AF Amorphous Fluoroplastic Solutions
Product Grade/Type	:	AF 601S2-100-6, AF 601S2-1-6, AF 601S2-1-18, AF 601S2-100-18 (AF 1601 SOL FC), AF 1601 X Sol AF 400S2-100-1 (AF 2400 SOL FC), AF 2400 X SOL
Product Use	:	Coatings, For industrial use only.
Restrictions on use	:	Do not use in medical applications involving permanent implantation in the human body., See Section 16
Manufacturer/Supplier	:	The Chemours Company FC, LLC 1007 Market Street Wilmington, DE 19899 United States of America
Product Information	:	1-844-773-CHEM (outside the U.S. 1-302-773-1000)
Medical Emergency	:	1-866-595-1473 (outside the U.S. 1-302-773-2000)
Transport Emergency	:	CHEMTREC: +1-800-424-9300 (outside the U.S. +1-703-527-3887)

SECTION 2. HAZARDS IDENTIFICATION

Not classified as a hazardous substance or mixture according to the Occupational Safety and Health Administration (OSHA) Hazard Communication Standard 2012.

Other hazards
No applicable data available.

SECTION 3. COMPOSITION/INFORMATION ON INGREDIENTS

This product does not contain any components that require disclosure according to OSHA Hazard Communication Standard 2012.

SECTION 4. FIRST AID MEASURES

General advice	:	No applicable data available.
Inhalation	:	Move to fresh air. If victim has stopped breathing: Artificial respiration and/or oxygen may be necessary. Call a physician immediately.
Skin contact	:	Wash off immediately with soap and plenty of water. Wash contaminated clothing before re-use.
Eye contact	:	Rinse with plenty of water. Get medical attention immediately.
Ingestion	:	Call a physician or poison control centre immediately. If swallowed, DO NOT induce vomiting unless directed to do so by medical personnel. Never give anything by mouth to an unconscious person.
Most important symptoms/effects, acute and delayed	:	No applicable data available.
Protection of first-aiders	:	No applicable data available.
Notes to physician	:	No applicable data available.

SECTION 5. FIREFIGHTING MEASURES

Suitable extinguishing media	:	Water, Foam, Dry chemical, Carbon dioxide (CO2)
Unsuitable extinguishing media	:	No applicable data available.

Specific hazards	:	Hazardous thermal decomposition products: Hydrofluoric acid...% Carbon monoxide Hexafluoroacetone Perfluoroisobutylene potentially toxic fluorinated compounds
Special protective equipment for firefighters	:	In the event of fire, wear self-contained breathing apparatus. Wear suitable protective equipment. Wear neoprene gloves during cleaning up work after a fire.
Further information	:	Protect from hydrogen fluoride fumes which react with water to form hydrofluoric acid.

SECTION 6. ACCIDENTAL RELEASE MEASURES

NOTE: Review FIRE FIGHTING MEASURES and HANDLING (PERSONNEL) sections before proceeding with clean-up. Use appropriate PERSONAL PROTECTIVE EQUIPMENT during clean-up.

Safeguards (Personnel)	:	Wear personal protective equipment. Evacuate personnel to safe areas. Ventilate the area. Wear respiratory protection.
Environmental precautions	:	No applicable data available.
Spill Cleanup	:	Soak up with inert absorbent material (e.g. sand, silica gel, acid binder, universal binder, sawdust).
Accidental Release Measures	:	For disposal considerations see section 13.

SECTION 7. HANDLING AND STORAGE

Handling (Personnel)	:	Avoid contact with skin, eyes and clothing. Avoid contamination of cigarettes or tobacco with dust from this material. Do not breathe vapours or fumes that may be evolved during processing. Do not use a torch to clean this material from equipment without local exhaust ventilation and respirator.

Do not contaminate tobacco products.

Handling (Physical Aspects)	:	No applicable data available.
Dust explosion class	:	No applicable data available.
Storage	:	Keep in a well-ventilated place. Keep tightly closed. Keep away from food and drink.
Storage period	:	No applicable data available.
Storage temperature	:	No applicable data available.

SECTION 8. EXPOSURE CONTROLS/PERSONAL PROTECTION

Engineering controls	:	Use local exhaust to completely remove vapors and fumes liberated during hot processing from the work area.

Personal protective equipment

Respiratory protection	:	Use respirator when performing operations involving potential exposure to vapour of the product. Wear a positive-pressure supplied-air respirator.
Eye protection	:	Wear coverall chemical splash goggles and face shield when the possibility exists for eye and face contact due to splashing or spraying of material. Safety glasses with side-shields conforming to EN166
Skin and body protection	:	Impervious clothing Apron Boots Recommended preventive skin protection Neoprene

Exposure Guidelines

Exposure Limit Values

This product does not contain any exposure limits that require disclosure according to OSHA Hazard Communication Standard 2012.

Non-Constituent(s)

Hexafluoroacetone			
TLV	(ACGIH)	0.1 ppm	TWA

SECTION 9. PHYSICAL AND CHEMICAL PROPERTIES

Appearance		
Physical state	:	liquid
Form	:	liquid
Color	:	colourless
Odor	:	none
Odor threshold	:	No applicable data available.
pH	:	No applicable data available.
Melting point/range	:	No applicable data available.
Boiling point/boiling range	:	Boiling point/boiling range 102 - 221 °C (216 - 430 °F)
Flash point	:	does not flash
Evaporation rate	:	No applicable data available.
Flammability (solid, gas)	:	No applicable data available.
Upper explosion limit	:	No applicable data available.
Lower explosion limit	:	No applicable data available.
Vapour Pressure	:	No applicable data available.
Vapour density	:	No applicable data available.
Specific gravity (Relative	:	1.8 - 1.9

density)

Water solubility	:	insoluble
Solubility(ies)	:	No applicable data available.
Partition coefficient: n-octanol/water	:	No applicable data available.
Auto-ignition temperature	:	No applicable data available.
Decomposition temperature	:	No applicable data available.
Viscosity, kinematic	:	No applicable data available.
Viscosity, dynamic	:	No applicable data available.
% Volatile	:	75 %

SECTION 10. STABILITY AND REACTIVITY

Reactivity	:	No applicable data available.
Chemical stability	:	Stable under normal conditions.
Possibility of hazardous reactions	:	No applicable data available.
Conditions to avoid	:	Temperature > 200 °C (> 392 °F) Heating can release hazardous gases.
Incompatible materials	:	Powdered metals Finely divided aluminium, Magnesium, Strong oxidizing agents, Contact with incompatible materials can cause fire and explosion.
Hazardous decomposition products	:	Hazardous decomposition products: Hydrogen fluoride, Hexafluoroacetone, perfluoroisobutylene

SECTION 11. TOXICOLOGICAL INFORMATION

Further information : The product contains no substances classified as hazardous to health in concentrations which should be taken into account.

Carcinogenicity

The carcinogenicity classifications for this product and/or its ingredients have been determined according to HazCom 2012, Appendix A.6. The classifications may differ from those listed in the National Toxicology Program (NTP) Report on Carcinogens (latest edition) or those found to be a potential carcinogen in the International Agency for Research on Cancer (IARC) Monographs (latest edition).

None of the components present in this material at concentrations equal to or greater than 0.1% are listed by IARC, NTP, or OSHA, as a carcinogen.

SECTION 12. ECOLOGICAL INFORMATION

Additional ecological information : The product contains no substances classified as hazardous to the environment in concentrations which should be taken into account.

SECTION 13. DISPOSAL CONSIDERATIONS

Waste disposal methods - Product : In accordance with local and national regulations. Incinerate only if incinerator is capable of scrubbing out hydrogen fluoride and other acidic combustion products.

Contaminated packaging : No applicable data available.

SECTION 14. TRANSPORT INFORMATION

Not classified as dangerous in the meaning of transport regulations.

SECTION 15. REGULATORY INFORMATION

TSCA	:	On the inventory, or in compliance with the inventory
SARA 313 Regulated Chemical(s)	:	This material does not contain any chemical components with known CAS numbers that exceed the threshold (De Minimis) reporting levels established by SARA Title III, Section 313.
California Prop. 65	:	WARNING! This product contains a chemical known to the State of California to cause birth defects or other reproductive harm.Hexafluoroacetone

SECTION 16. OTHER INFORMATION

Restrictions for use	:	Do not use or resell Chemours™ materials in medical applications involving implantation in the human body or contact with internal body fluids or tissues unless agreed to by Seller in a written agreement covering such use. For further information, please contact your Chemours representative.

Revision Date : 12/19/2015

The information provided in this Safety Data Sheet is correct to the best of our knowledge, information and belief at the date of its publication. The information given is designed only as a guidance for safe handling, use, processing, storage, transportation, disposal and release and is not to be considered a warranty or quality specification. The information relates only to the specific material designated and may not be valid for such material used in combination with any other materials or in any process, unless specified in the text.

Significant change from previous version is denoted with a double bar.